UNIVERSITY OF CAPE TOWN

IYUNIVESITHI YASEKAPA • UNIVERSITEIT VAN KAAPSTAD

Degradation Behaviour of the Mechanical Properties of Bovine Cortical Bone

Nicholas Daras

Department of Mechanical Engineering

University of Cape Town

South Africa

June 2024

This thesis is being presented in fulfilment of the requirements for the degree of Doctor of Philosophy in the Department of Mechanical Engineering at the University of Cape Town

If you can keep your head when all about you
Are losing theirs and blaming it on you,
If you can trust yourself when all men doubt you,
But make allowance for their doubting too;
If you can wait and not be tired by waiting,
Or being lied about, don't deal in lies,
Or being hated, don't give way to hating,
And yet don't look too good, nor talk too wise:

If you can dream—and not make dreams your master;
If you can think—and not make thoughts your aim;
If you can meet with Triumph and Disaster
And treat those two impostors just the same;
If you can bear to hear the truth you've spoken
Twisted by knaves to make a trap for fools,
Or watch the things you gave your life to, broken,
And stoop and build 'em up with worn-out tools:

If you can make one heap of all your winnings
And risk it on one turn of pitch-and-toss,
And lose, and start again at your beginnings
And never breathe a word about your loss;
If you can force your heart and nerve and sinew
To serve your turn long after they are gone,
And so hold on when there is nothing in you
Except the Will which says to them: 'Hold on!'

If you can talk with crowds and keep your virtue,
Or walk with Kings—nor lose the common touch,
If neither foes nor loving friends can hurt you,
If all men count with you, but none too much;
If you can fill the unforgiving minute
With sixty seconds' worth of distance run,
Yours is the Earth and everything that's in it,
And—which is more—you'll be a Man, my son!

- Rudyard Kipling

Abstract

Cortical bone, is subject to extensive mechanical characterization, yet the literature reveals notable discrepancies in reported mechanical properties, in particular concerning the elastic modulus. This variability is attributed to the intricate nature of bone and the diverse experimental factors influencing its performance, notably specimen preparation, including machining techniques and storage protocols. Additionally, the manner in which machine compliance is accounted for is not always reported, particularly concerning the quasi-brittle nature of cortical bone. Even when compliance is accounted for, the methods are not elaborated on in great detail. A further critical observation is the absence of an intermediary step in bone testing simulations, bridging the gap between specimen-scale material characterization and full bone testing. An intermediate stage would provide validation data for a nuanced understanding of material behaviour while mitigating computational expense associated with full bone simulations.

To address these gaps, this thesis develops solutions that enhance the accuracy and reliability of the mechanical testing of bone. A custom subpress has been designed and commissioned to minimize machine compliance during quasi-static compression tests on small cortical bone specimens. By quantifying machine compliance through novel methodologies, this research has unveiled its significant impact on mechanical property measurements.

Furthermore, this investigation delves into the effects of long-term storage, particularly frozen storage, on bovine cortical bone properties. Three distinct storage protocols were evaluated over a one-year period, revealing significant degradation of fresh bone samples beyond six months irrespective of storage method. This study sheds light on the practical implications of specimen storage protocols in preserving bone integrity.

In parallel, the efficacy of cross-section bone specimen tests as an intermediary validation step for simulations is presented. Dynamic strain rate tests using a three-point bending split Hopkinson bar yield rich datasets, indicating clear trends applicable for numerical validation. Simulations utilizing dynamic compression and cross-section data exhibit encouraging correlations with experimental observations. A comparison between the material model for cortical bone in the commonly used 'Total Human Model for Safety' (THUMS) and a strain-rate dependent plasticity material model highlights the advantages of the latter, emphasizing the potential for enhanced simulation accuracy.

Declaration

I, Nicholas Daras, hereby:

(a) grant the University of Cape Town free license to reproduce this thesis in whole, or in part, for the purpose of research;

(b) declare that:

(i) I know that plagiarism is wrong. Plagiarism is to use another's work and pretend that it is one's own.

(ii) I have used the IEEE convention for citation and referencing. Each significant contribution to, and quotation in, this report/project from the work(s) of other people has been attributed and has been cited and has been referenced.

(iii) I have not allowed and will not allow anyone to copy my work with the intention of passing it off as his or her own work.

(iv) this thesis is my own unaided work, both in concept and execution, and that apart from the normal guidance from my supervisor, I have received no assistance apart from that explicitly stated in the Acknowledgements.

(v) neither the substance nor any part of this thesis has been submitted in the past, or is being, or is to be submitted for a degree at this university or at any other university.

I am now presenting the report for examination for the degree of PhD (Mechanical Engineering).

Acknowledgements

Dr. Trevor Cloete, my supervisor for my undergraduate final year project, my (short-lived) MSc and my PhD. Over the last five years I have been lucky enough to get a glimpse into the mind of a truly passionate and ingenious academic. Trevor, thank you for the countless 'nuggets of knowledge' that you bestowed upon me, and thank you for never ceasing to push me to achieve more than I thought I was capable. I value your expertise and mentorship more than I can describe, and I am truly grateful to have had you as my supervisor for this journey.

To my co-supervisor, Professor Nurick, thank you for all that you did for me. I cannot even begin to explain how much your advice and assistance guided me through this PhD. Your input and seemingly endless proof-reading is immensely appreciated. Thank you, not only for your academic input, but for always checking in on how life outside of the PhD is going. I will forever cherish our chats; thank you.

To my BISRU friends that I made along the way, I truly could not have got through this without you. To Aashir, Matt and Pierre, who started this journey with me, thank you for the countless laughs and few too many dart games. To the new comers, Malcom and Lia, thank you for bringing a new life into the lab and for all of the good times. Finally, to Sherlyn, thank you. You truly helped me get through the toughest parts of this degree and your encouragement, patience and generosity is something I do not think I will ever be able to repay. To each of you, thank you so much for being a part of this journey.

I would like to thank the BISRU staff members for their input into my work and for the effort they put into making BISRU what it is. To Sa-aadat Parker, thank you for all of the laughs and good times. Dr. Reuben Govender, thank you for taking the time to answer my questions and for making the time to check-in on how I was doing. To Shivasi Mashau, thank you for the endless conversations about cars and for making me a cyclist. Finally, to Prof. Steeve Chung Kim Yuen, thank you for always putting a smile on my face and for your genuine interest in my project and my life.

A massive thank you must be extended to all of the staff members in the workshop that machined all of the apparatuses and specimens in this study. Pierre, Grant, Thulani, Cam and Wayne, none of this is possible without you and I truly cannot thank you enough for all of the hard work you do. Apart from the professional help, thank you all for your friendship and guidance you gave me throughout this journey. I truly appreciate you all.

I have to thank my CME family for making my testing a fun and enjoyable experience. Thank you all your time, input and friendship. I truly enjoyed spending time with you all and this PhD would have not been the same without you.

To my friends and loved ones who were always there for me, offering an ear to listen and for your words of encouragement, you are all immensely appreciated and I could never have got through any of this without each and every one of you.

Finally, to my father, Chris, my mother, Catherine and my brother, Perry, you guys have always supported me in everything I do; no matter how outrageous. I could write a whole other thesis thanking each of you for all you do for me. So, to summarize, none of this could have been done without you and I can't even begin to describe how much I appreciate you guys. Thank you for giving me this opportunity and thank you for being the best family a guy could ask for.

Contents

List of Figures

List of Tables

Glossary

BISRU	Blast Impact and Survivability Research Unit
CiT	Cone-in-tube
FEA	Finite Element Analysis
FMF	Specimens that have been machined from bones which were frozen whole, stored for a certain time frame and then frozen again as specimens prior to being tested
fps	Frames per second
ISR	Intermediate strain-rate
MF	Specimens that have been machined fresh prior to being frozen
MR	Specimens that have been machined fresh prior to being refrigerated
OPL	Objective power law
PMMA	Polymethyl methacrylate
QS	Quasi-static
RMS	Root mean square
SG	Strain gauge
SHB	Split Hopkinson bar
THUMS	Total human model for safety
UCS	Ultimate compressive strength
UCT	University of Cape Town
VE	Visual extensometer

Nomenclature

A	Cross-sectional area
c	Material wave speed
E	Elastic modulus
EV	Excitation voltage of the power supply
F	Force
GA	Gain amplitude of the amplifier
GF	Gain factor of the strain gauge
I	Second moment of inertia
K	K-factor
k	Stiffness
N	Number of bridges in the Wheatstone bridge
p	Statistical significance
R^2	Coefficient of determination
t	Time
v	Velocity
$\beta_n l$	Normal mode of a uniform beam
δ	Deflection
ϵ	Strain
$\dot{\epsilon}$	Strain rate
ρ	Density
σ	Stress
ω_n	Natural frequency of a uniform beam

Chapter 1

Introduction

1.1 Background

Bone, as an engineering material, has been documented, and its properties quantified, for over a half century [1]. However, despite being the focus of so much research over such an extended period of time, there appears to be significant scatter in the literature pertaining to the mechanical properties of bone [2–6]. It is hypothesized in the literature that these conflicting results stem from the highly complex nature and structure of bone, as well as a lack of a standard approach with regards to the testing and storage protocols amongst researchers. In particular, the specimen storage procedures of studies pertaining to bone are not fully documented in the literature. For example, certain studies have stored specimens in frozen storage, for example van Haaren *et al.* [7], while other studies, for example by Sedlin *et al.* [8] and Öhman *et al.* [9], stored specimens in a storage medium, such as saline or formalin. Furthermore, there is no consensus on whether storage duration has an effect of the measured mechanical properties of bone specimens, with a number of studies reporting differing results in this regard. Furthermore, there does not appear to be any specific investigation wherein fresh bones (i.e. within 24 hours of death of the donor) are tested. This raises the question whether extended periods of time in storage can skew the results recorded during testing.

The characterization of bone is further complicated due to the relatively low failure strain [6, 10]. A highly accurate testing apparatus is required to precisely measure properties, such as the failure strain of relatively small specimens, and reaching this level of accuracy does not appear to have received sufficient attention in the literature. Although testing machines are rated to a specific accuracy, the inherent compliance of

the large machines relative to the small specimens has a significant effect on the measured properties. As a result, the machines typically used to measure the mechanical properties of bone specimens require additional systems or techniques to allow for sufficiently accurate displacement measurements to be recorded. Furthermore, the existence of after-market measurement systems, such as a visual extensometer, highlights the need to eliminate compliance effects. However, these systems are susceptible to external influences, such as vibrations from the surrounding environment, which is detrimental to the consistency of these systems over a number of tests; particularly when considering small displacements.

One focus of the Blast Impact and Survivability Research Unit (BISRU) at the University of Cape Town (UCT) is to conduct research pertaining to the mechanical properties of bone, particularly in the intermediate strain rate (ISR) range, to a level of accuracy that does not appear to have been attempted elsewhere. This will allow for further research to be conducted with the ultimate aim of being able to generate patient-specific numerical models that will accurately predict and describe the reaction of a skeleton under loads across a range of strain rates (10^1 - 10^2 s^{-1}).

However, before such a complex model can be generated, accurate material properties for bone must be characterized and satisfactorily representative material models must be developed to capture the highly variable nature of bone. The 'Total Human Model for Safety', or THUMS [11, 12], appears to be the 'gold standard' when it comes to numerical models of human occupants, although the chosen material model for cortical bone lacks strain-rate dependence. As such, it would appear that this material model does not accurately simulate the physical behaviour of cortical bone and a model that is capable of capturing this strain-rate dependence may demonstrate benefits over the current choice.

In an effort to extensively validate these material models, real-world experiments on small specimens are conducted in order to determine the mechanical properties of the material. Once satisfactorily characterized, the introduction of a more complex geometry into experiments allows for the effects of geometry and complex structures to be observed. However, the step from small, material characterization specimens to full bones could mask certain shortcomings of material models when conducting numerical work. The highly complex geometry of a full bone could be masking certain material behaviours, which would only be observed with smaller, less complicated geometries. As

a result, an intermediary step between small specimen tests and full bone tests could potentially offer a solution.

1.2 Purpose and Scope

The primary purpose of this research is to characterize the degradation behaviour of bovine cortical bone in an effort to determine how the storage protocol, which includes storage method and duration, has an effect on the measured properties. To conduct this degradation study, a new quasi-static subpress was developed and validated, and a novel means of determining machine compliance was developed to improve the accuracy of measured properties. Furthermore, a unique bone cross-section test was developed as an intermediary step between small specimen tests and full bone tests in an effort to decrease the leap in complexity and effect of geometry on measured results between these types of tests. Finally, a comparison between the THUMS material model for cortical bone and a proposed strain-rate dependent material model will be made. While only bovine bone will be tested in this thesis and THUMS is modelled for human bone, a direct comparison is justified as cortical bone from both species cover a similar mechanical material performance regime, and this will be elaborated on in upcoming sections of this thesis.

This work will not include the development and implementation of a custom material model for the numerical simulation of cortical bone.

1.3 Objectives and Novel Contributions

The objectives and novel contributions of this thesis are:

Quasi-Static Subpress
Develop and validate the quasi-static compression subpress for small specimen material characterization tests. Discussed in Chapter 3.

Machine Compliance
Determine the effects of machine compliance on the measured results of a number of apparatuses that will be used for future cortical bone material characterization tests. Discussed in Chapter 3.

Degradation Study
Determine the effect of a long-term frozen storage protocol on the measured mechanical properties of bovine cortical bone. Introduced in Chapter 4 and elaborated on in the chapters that follow.

Cross-Section Tests
Conduct cortical bone cross-section tests to observe the complex geometry behaviour of the biomaterial and determine if this testing technique is an appropriate validation test for numerical work. Introduced in Chapter 4 and elaborated on in the chapters that follow.

Numerical Results
Compare the numerical results from simulating both dynamic tests on small specimens and dynamic tests on cross-section specimens, with the THUMS cortical bone material model and a proposed strain-rate dependent material model. Discussed in Chapter 6.

1.4 Thesis Outline

This thesis is divided into the following chapters:

Chapter 2 - Literature Review
The literature review begins with a summary of the physiological description of bone, which is followed by an outline of the current engineering material description of bone, with particular focus on the cortical regions. A section will be dedicated to the response of cortical bone to strain specifically, as this forms a core aspect of the tests conducted in this study. The content of the literature review will then be shifted to identify influential factors that have been highlighted in the literature as having effects on the measured mechanical properties of cortical bone. The review will then highlight the apparent gaps in the literature pertaining to the preparation of cortical bone specimens and the seeming inconsistencies in the storage and testing protocols of such specimens. Focus will then be placed upon the various methods used to characterize and test bone over a range of strain rates. Finally, the literature review will briefly summarize the relevant aspects of numerical work conducted pertaining to cortical bone.

Chapter 3 - Experimental Apparatus
This chapter will be an outline of the various experimental apparatuses used in this study. A large portion of this chapter will be dedicated to the **quasi-static subpress** developed for this study. The calibration process for this subpress will be described and a comparison will be made of the results from the subpress to those obtained using readily apparatuses, as a means of validating the operation of the subpress. In this chapter, a technique to determine the **machine compliance** is introduced, and is expanded upon in later chapters. Finally, this chapter will close with the introduction of the dynamic apparatuses, and the theory behind the operation of such apparatuses. Particular focus will be placed on the Cone-in-Tube (CiT) striker, which allows for testing in the ISR regime, and the unique three-point bending split Hopkinson bar (SHB), which was trialled for the first time in this study.

Chapter 4 - Methodology
This chapter begins with the outlining of the methods used to prepare the cortical bone specimens, with a particular focus on the specimen machining process and specimen naming convention for this study. A focus is placed on obtaining fresh bone samples, i.e. retrieved, machined and tested within 24 hours of the death of the donor. The **degradation study** is introduced in this chapter, with explanations of the various

storage protocols and the timeline of the tests. The chapters then shifts focus to the data capture and processing steps for each of the experimental testing methods. The unique bone **cross-section tests** are introduced, following by explanations of the intended testing techniques. Finally, the numerical methodology is discussed in the closing sections of this chapter, including the development process of the full SHB model, which involves basic validation tests, mesh convergence and final geometry implementation.

Chapter 5 - Results
This chapter will summarize the results obtained from the various experiments and numerical simulations of this study. The chapter begins with the results from the various apparatus validation tests, wherein the apparatus validation process yields results that highlight the advantages of the various experimental apparatuses. The results from the degradation study follow, and clearly demonstrate the degradation behaviour of bovine cortical bone when stored under long-term frozen protocols. This section also includes the explanations of various statistical concepts, which are required for the upcoming discussion. The results from the bone cross-section tests are then reported here, along with the introduction of the term 'robustness', which, as will be discussed in the chapters that follow, is a useful term for later validation simulations. Finally, the chapter concludes with the reporting of numerical results for the dynamic compression specimen simulations as well as the dynamic cross-section simulations.

Chapter 6 - Discussion
The results presented in the previous chapter will be investigated in more detail in this chapter. The chapter begins with the interpretation of the apparatus validation tests results, and elaborates on the explanations of the shortcomings of that experimental apparatuses that these tests highlighted. The chapter shifts focus to the results from the degradation study, with statistical analysis being used to identify particular phases of degradation behaviour observed in each of the three storage protocols. The relationships with apparent elastic modulus, ultimate compressive strength, and strain at ultimate compressive strength to storage duration demonstrate the unique degradation behaviour of bovine cortical bone when stored under different storage protocols. The chapter elaborates on the results from the bone cross-section tests, and the correlation between various specimen parameters and 'robustness'. The high correlation of the specimen stiffness, and maximum experienced force to specimen 'robustness' suggest that these types of tests could be valuable validation for numerical simulations of cortical bone. The chapter presents the discussion of numerical results from the dynamic compression

specimen simulations and the dynamic cross-section simulations. A comparison is then made between the experimental cross-section test results and the numerical cross-section simulation results. Finally, a comparison is made between the **numerical results** of the cross-section simulations using the cortical bone material model from the commonly used THUMS, and an alternative strain-rate dependent material model, with the material parameters set to those obtained from fresh specimens.

Chapter 7 - Conclusions and Recommendations
The final chapter of the thesis highlights the various novel contributions made in this thesis by consolidating the conclusions from the various aspects of this study. Firstly, conclusions regarding the pre-testing aspects of this study are made; specifically the commissioning of the new subpress and the implementation of the apparatus validation techniques. Secondly, conclusions pertaining to the degradation study are highlighted in particular, with this being the primary objective of this thesis. Thirdly, conclusions are made regarding the numerical aspects of this study. This chapter closes with the presentation of recommendations for future work.

Chapter 2

Literature Review

2.1 The Structure of Bone

In this section the physiology of bone, the structures of the material, as well as the constituents of said structures, will be considered. Being a biological material, bone is complex and is typically divided into five main hierarchical levels as seen in Figure 2.1; macro-, micro-, sub-micro-, nano- and sub-nanostructures [13]. As these structural levels are distinct, they all demonstrate unique properties [13], however as **the research in this thesis is focused on the macroscopic level**, only the macrostructures and microstructures will be dealt with in depth in this section.

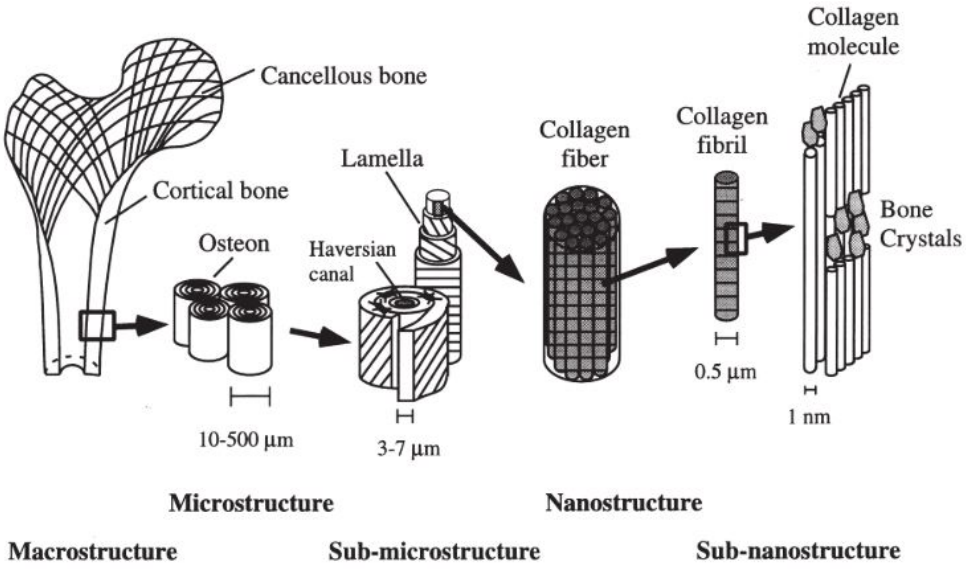

Figure 2.1 Hierarchical structure of bone [13].

2.1.1 Macrostructures of Bone

The macrostructures of bone are divided into two categories; the hard, brittle, outer cortical region (also known as compact bone) and the softer, sponge-like inner trabecular region (also known as cancellous bone) [13]. The cortical bone is found on the outer regions of a bone and forms the primary load-bearing portion of the skeletal system, while also serving the function of protecting the softer trabecular bone [14]. It also provides attachment points for muscles, which, in turn, allow for movement to occur and protects the vital organs sheltered within the skeleton [15]. Trabecular bone, conversely, is typically found within the bone and serves as a supportive core material for the surrounding cortical bone [16]. Additionally, trabecular bone serves a number of metabolic functions in the body, such as maintaining mineral homoeostasis, ensuring a balance of acids and bases in the body and the secretion of hormones [3, 15, 17]. The total mass of an adult skeleton consists of approximately 80% cortical bone and 20% trabecular bone, but this ratio does not hold for each individual bone [15]. For example, a load-bearing bone with few contact points, such as a femur, will contain more cortical bone than a more metabolically active bone with more contact points, such as a vertebra [15].

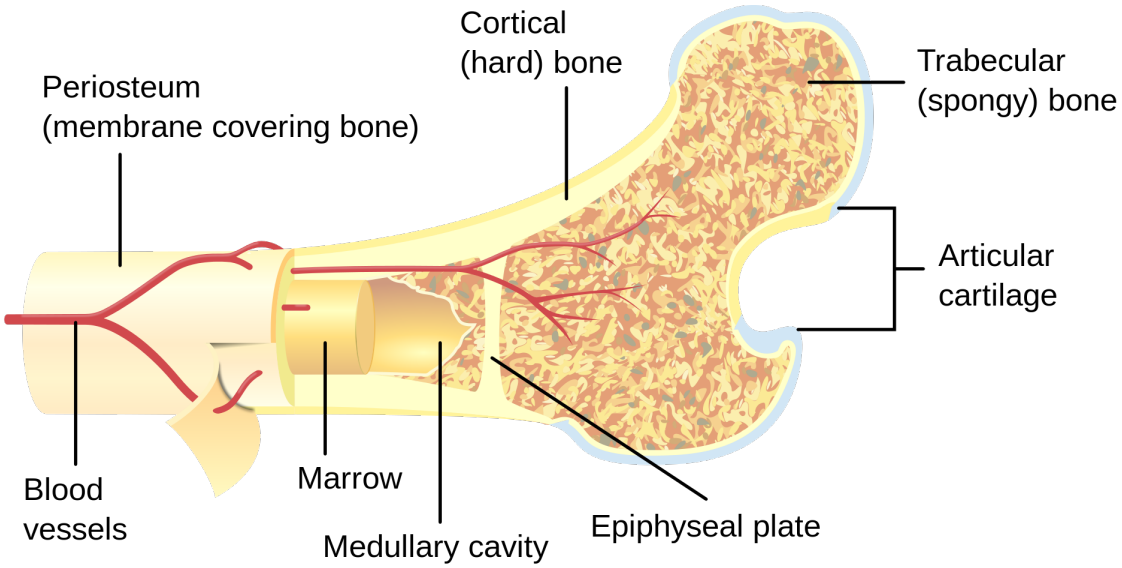

Figure 2.2 Macrostructure of bone [18].

The chemical compositions of bone macrostructures are relatively similar, as both consist of roughly 73% calcium and 27% phosphorus [14]. Beyond this similarity, the two structures share little in common. The major difference between the two structures is their degrees of porosity, as the cortical bone is significantly more dense than the trabecular bone. Cortical bone has a porosity of between 5% to 15%, while the trabecular bone has a porosity of between 40% to 95% [3].

From Figure 2.2, cortical bone is found on the diaphysis (the shaft of the bone), metaphysis (the neck of the bone) and epiphysis (the head of the bone); and forms the outer layer of the entire perimeter of the bone [3]. Trabecular bone, however, is found solely in the epiphysis of the long bone, but can be found partially in the metaphysis [3]. This distinction changes, for flat bones, such as a rib or clavicle, where one would observe a core of trabecular bone between outer layers of cortical bone [13], i.e. a structure similar to composite sandwich panels.

The structural make-up of each macrostructure is also a point of differentiation. Cortical bone has dense and solid structure with a relatively uniform surface, while trabecular bone appears as a connection of various struts, pillars and plates, and appears as a micro-lattice or sponge-like material [15].

The relative maturity differentiates the two macrostructures further. The relative age of the trabecular bone is much less than that of cortical bone due to trabecular bone being more metabolically active and thus undergoing remodelling more frequently than cortical bone [13, 15]. As a result, the mechanical behaviour of the cortical bone could be due to its relative age, as it is not being remodelled as frequently as its trabecular counterpart [13].

2.1.2 Microstructures of Bone

Each of the aforementioned macrostructures have their own microstructural constituents as shown in Figure 2.3.

In cortical bone, mineralized collagen fibres form planar arrangements referred to as lamellae [13] and form the fundamental constituents for all bone types [16]. The most abundant type of cortical bone in large mammals is lamellar bone, which consists of parallel mineralized collagen fibres that form planar sheets [13, 16]. Cortical bone in mature human is additionally observed in the form of osteonal bone, which is shown prominently in Figure 2.3. These microstructures are formed when the collagen fibres are laid down in concentric layers around a central canal of blood vessels [13, 14]. In mammals, these systems, typically, have been measured to have a diameter around 250 μm and run parallel to the main axis of the shaft of the bone [13, 20]. Such systems were not observed in this form in reptiles or birds, rather, these species feature unique systems that appear to have adapted in order to facilitate the habits of said species [20]. Finally, cortical bone can be arranged in what is referred to as woven bone, and this is

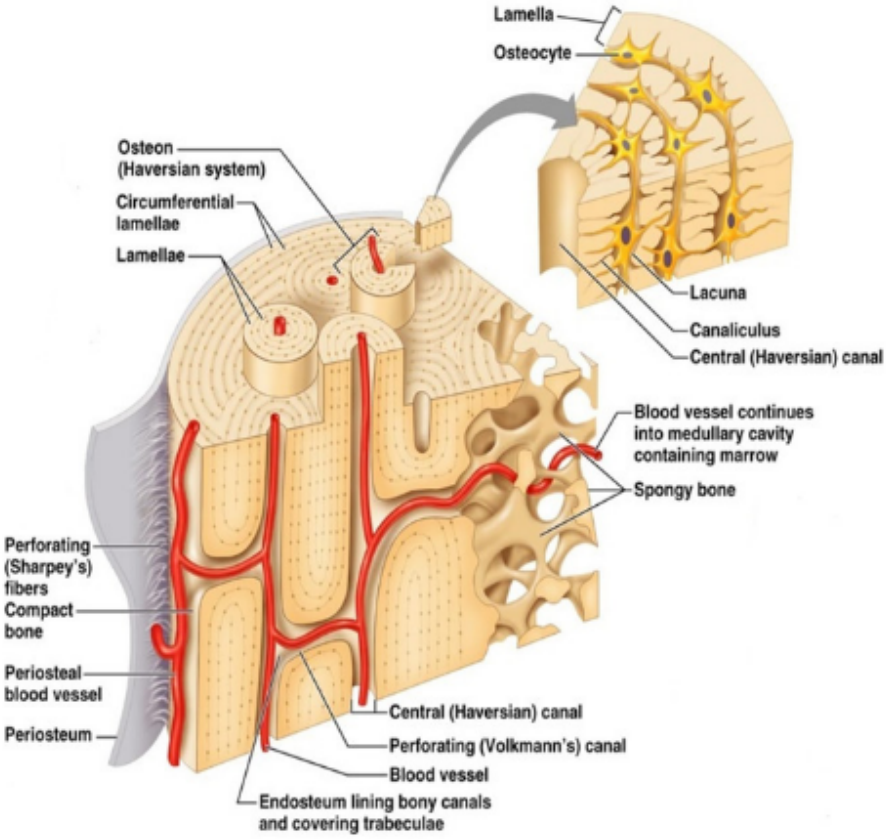

Figure 2.3 Microstructure of human bone [19].

when the collagen fibres are oriented in a random manner such that no discernible pattern can be found in the structure [13]. This is typically observed in bone that are undergoing growth [21], and is replaced by mature lamellar bone during bone remodelling [22].

The trabecular bone is made up of an interconnected network of trabeculae arrangements, which consist of rod- and plate-like structures that are found in a number of combinations, all forming an open cell foam [13, 14]. This is shown in the central channel of the bone depicted in Figure 2.3, labelled *Trabeculae of spongy bone*. These trabecular rods are about 50 μm to 300 μm in diameter [13], and fill approximately 20% of the trabecular region [17]. The remaining 80% of this region is filled with bone marrow and other living cells, such as fat [14, 17].

2.1.3 Sub-Microstructures of Bone

Below the microscopic level, bone consists of individual, mineralized collagen fibrils, which have been shown to have higher stiffness, strength and toughness when compared to pure

collagen fibrils [14]. These fibrils have been found to be either oriented in a uniform manner, to form lamellar bone, or in a random manner, to form woven bone, however the mechanism through which this organization takes place is not well known [13, 14].

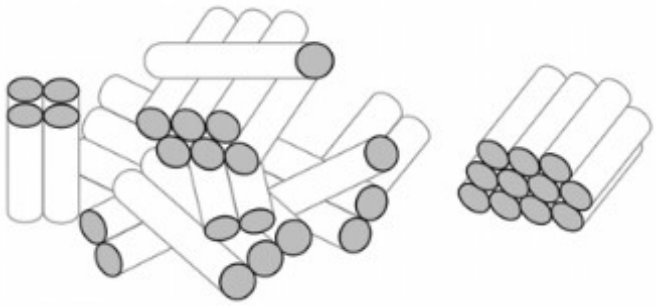

Figure 2.4 Randomly oriented collagen fibrils in woven bone (Left) and parallel aligned fibrils in lamellar bone (Right) [14].

Below this level, these fibrils are made up of smaller collagen constituents, mineral crystals and proteins [13]. The nanoscopic mineral crystals and the collagen constituents align to form the microscopic collagen fibrils, while the proteins are thought to facilitate growth of these fibrils [13]. The mineral regions are related to the overall stiffness of the bone, while the collagen regions relate to the toughness of the bone [14].

2.2 Current Material Description of Cortical Bone

Over a number of decades, many researchers have attempted to define bone as a material and the results have varied across many of the studies, as is evident by the scatter in the summary presented by Johnson *et al.* [2]. More recently, bone is categorized as a viscoelastic, anisotropic, composite biomaterial, which is continually remodelled depending on its environment. In this section the various material properties of bone will be discussed and will be defined more clearly in terms of its mechanical properties.

2.2.1 Elastic and Shear Moduli

As will be a recurring point in this literature review, the elastic modulus, or stiffness of bone is highly variable. The density of bone, which is a topic that will be dealt with later in Section 2.4.1, has proven to be a pivotal property when considering a number of other characteristics of bone [4]. Despite this significant scatter, both Morgan *et al.* [3] and Rho *et al.* [5] reported independently that in a healthy adult human, the elastic modulus of cortical bone is approximately 17 GPa in the longitudinal direction and approximately 10 GPa in the transverse direction. With this being said, it must be noted that a number of studies have found that the elastic modulus can decrease by as much as 40% when loading the bone transversely as opposed to longitudinally [3, 4].

Both Wirtz *et al.* [4] and Rho *et al.* [5] reported that the elastic modulus of a bone sample can vary as much as 62% when looking at highly dense bone samples in particular, and as much as 33% in lower density regions along a whole bone. These are noteworthy statistics as they demonstrate the vast variability in the measured properties of bone. Research has also been conducted on the elastic modulus of a bone sample where nanoindentation was used to test at different locations on a whole bone [24]. This method revealed that the elastic moduli did in fact differ along the length of the same bone sample, with the highest modulus reported as being in the diaphysis of the bone [24]. Furthermore, the shear modulus of bone has been reported to be approximately 3.3 GPa [4]. However, both Zysset *et al.* [24] and Wirtz *et al.* [4] report that the density of the sample does not have as prominent of an effect when measuring the shear modulus as it does when measuring the elastic modulus.

A distinction must be made between apparent and effective properties of a material. According to Lawrence [25], apparent properties of a specimen account for both material and structural influences, while effective properties assume an infinite structure, free of boundary conditions effects. Due to the inherent geometric constraints of machining

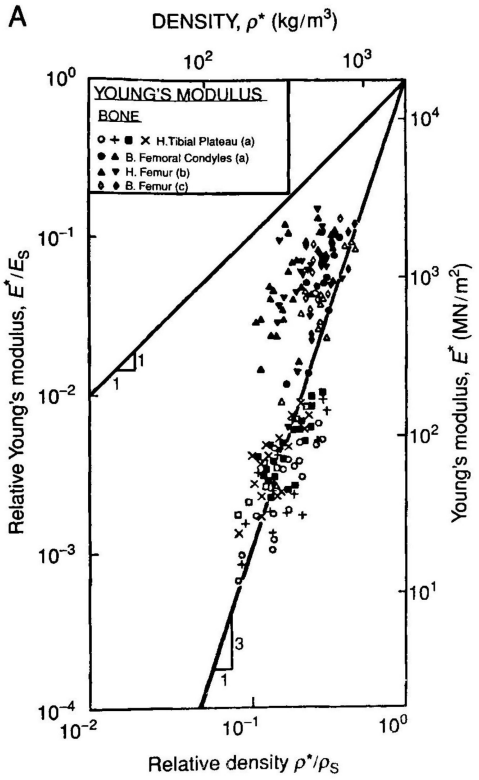

Figure 2.5 Graph demonstrating the relationship between elastic modulus of bone samples and density [23]. In this graph the 'Relative' terms are relative to a solid or non-porous piece of trabecular bone would have the same properties as cortical bone, namely $\rho_s = 1800kg/m^3$, and elastic modulus $E_s = 17GPa$.

specimens from bone, it can be difficult to obtain bone specimens that would be considered immune to the effect of boundary conditions [25] . Hence, many of the properties reported on cortical bone are apparent and not effective [25].

2.2.2 Strength

Bone behaves differently when subjected to tensile and compressive loads [3, 4, 6]. In the literature surveys of Hart *et al.* [6] and Keaveny *et al.* [26] found that cortical bone is stiffer and stronger under compression than under tension and is stronger under longitudinal loads than under transverse loads. It must be noted that there was no mention of compliance of the testing apparatus being taken into account during these tests. As was the case with stiffness, Wirtz *et al.* [4] report that the compressive strength of the bone increases with density, but this cannot be said for tensile and torsional strengths. This is of particular interest, but little evidence is offered as to why

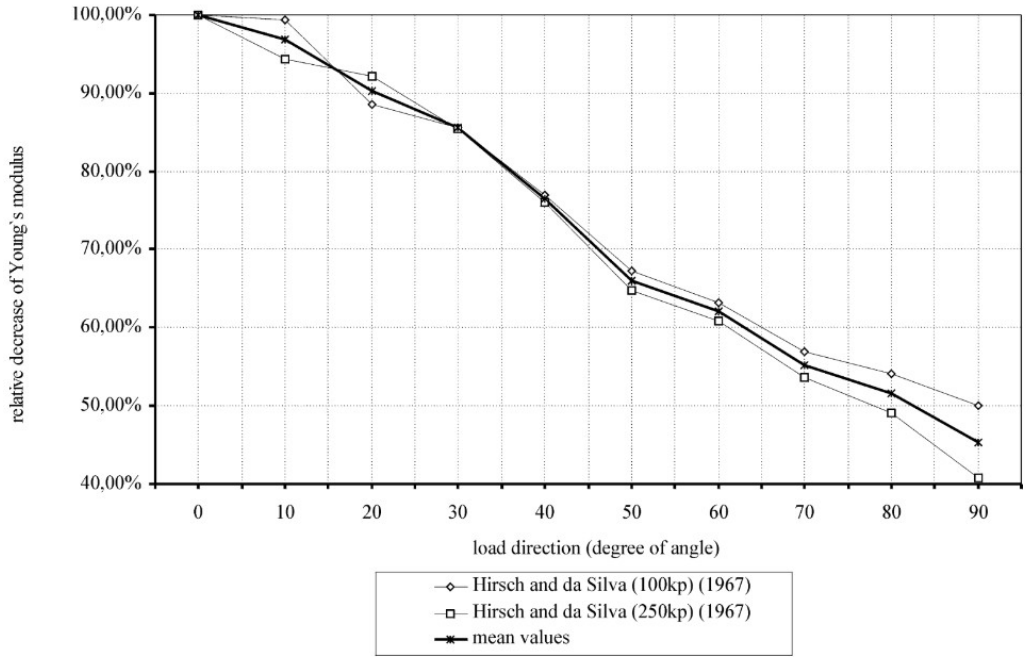

Figure 2.6 Graph demonstrating the relationship between elastic modulus of bone samples and loading angle relative to the axis of the bone from various studies [4].

this is the case and no proposed theory was given for this outcome. As for the actual values, in the longitudinal direction, Morgan *et al.* [3] found that the compressive yield strength of cortical bone is around 115 MPa and a tensile yield strength of roughly 72 MPa. They also reported the ultimate compressive strength of cortical bone to be between 150 MPa and 200 MPa, while the ultimate tensile stress was recorded as being closer to 100 MPa. Additionally Morgan *et al.* [3] found that in the transverse direction, bone was observed to have a compressive yield strength of 42 MPa, and an ultimate compressive strength ranging from 62 MPa and 131 MPa. In tensile loading, the yield strength could not be found, but the ultimate tensile strength was recorded at around 53 MPa.

2.2.3 Anisotropy

The anisotropic characteristics of bone do not appear to have been specifically studied in the literature, however values have been determined through other research and are reported. As can be extracted from the previous sections, bone behaves differently if loaded longitudinally or transversely, and Turner *et al.* [27] attribute this anisotropy to the orientation of the collagen fibres that make up the bone tissue.

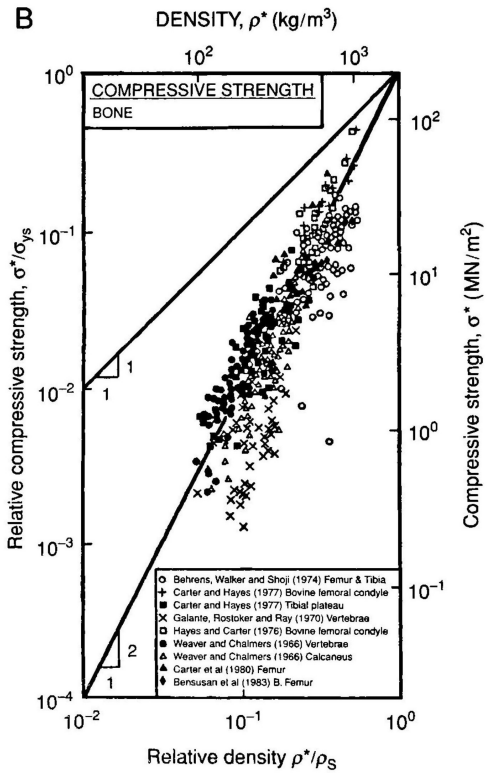

Figure 2.7 Graph demonstrating the relationship between compressive strength of bone samples and density [23]. In this graph the 'Relative' terms are relative to a solid or non-porous piece of trabecular bone would have the same properties as cortical bone, namely $\rho_s = 1800kg/m^3$ and yield stress $\sigma_{ys} = 193MPa$.

One will observe bone widening when under a compressive load and narrowing when loaded under tension, which is typical behaviour of most materials [6]. For the case of cortical bone, the literature varies notably with values for Poisson's ratio quoted as ranging between 0.2 and 0.62, an extremely wide range of values [3–6]. As with the Young's modulus, research has been conducted and it has been reported by Rho *et al.* [13] that the Poisson's ratio of a bone sample is in fact a function of position along the bone. This highly variable anisotropy has been noted as a major hindrance to finite element analyses of bone [4], but the use of the 'Rule of Mixtures' from composite materials has been put forward as a possible solution while models are being further developed [13]. With this being said, the use of computer tomography is now being used to accurately image the bone samples, in-vivo (non-invasively), and from that information the morphology and density of the sample can be interpreted [28]. With bone destiny being such a core characteristic to many of the other properties of bone, it is apparent that this information could be useful with regards to developing accurate patient specific computer-based material models of bone [28].

2.2.4 Viscoelasticity

Across the literature, bone is classified as a viscoelastic material [14, 29, 30]. The degree of this viscoelasticity has been attributed to a number of factors, such as the level of hydration of the bone, where a more hydrated specimen offers more ductility than a dryer bone, and the collagen content, which differs between sexes [29, 31].
This strain rate dependency has been quantified and it was found that a six-fold increase in the normal physiological range of strain rates results in a two-fold increase on the modulus of the bone samples tested [3]. This same increase in strain rate also resulted in a three-fold increase in the strength of the tested bone samples [3]. These values are relevant as impact events, such as falling or in a sports injury, often exceed normal strain rates, that would be experienced during walking, for example, by a factor of ten [3].
The exact mechanisms that induce this viscoelastic response are not fully understood, but it is suggested that the microscopic collagen fibres in the bone sample are the key [6, 13]. In a review article, Hart *et al.* [6] concluded that collagen in bone is a severely neglected topic in the literature, and this neglect has led to the gap wherein these viscoelastic mechanics could fall. One of the early attempts to quantify this viscoelastic behaviour was made by Carter and Hayes [32], resulting in:

$$\sigma_{comp} = 68\dot{\varepsilon}^{0.06}\rho^2 \tag{2.1}$$

where σ_b is the ultimate compressive strength of the bone, $\dot{\varepsilon}$ is the strain rate and ρ is the apparent density [4].

2.2.5 Composite Nature

In the literature, bone has been described as a natural, bi-phasic composite material [6,14, 27,29,31,33]. The two macroscopic phases of bone in the form of the cortical and cancellous bone have been discussed in Section 2.1.1. Cortical bone at a microscopic level also exhibits this composite-like structure, in the form of the mineral matrix and the collagen fibres [13]. Although there is not a distinct phase boundary between the two phases of the bone, which is characteristic of a typical engineering composite, bone is far more complex than one of the man-made composite materials [13]. Bone consists of approximately 40% organic constituents and 60% inorganic constituents and the interaction between these two components has a profound effect on the mechanical behaviour of the bone [6, 34].
As with other composite materials, the reinforcing constituent acts to strengthen the material and impede crack propagation, and bone is no exception. The osteons in the

bone act as the reinforcing fibres, which do not only increase the strength of the bone in the direction along their axes, but also act as barriers to crack propagation in the cortical bone [35]. It was found that the bone specimens exhibited a few microcracks after 10 000 cycles in a fatigue test, but between 10 000 and 50 000 cycles, these microcrack encountered osteons which prevented further propagation for a limited amount of time [35]. This observation is typical in other engineering composites, such as fibreglass, where cracks have a large number of sites to initiate, but once a fibre is encountered the propagation is hindered [35].

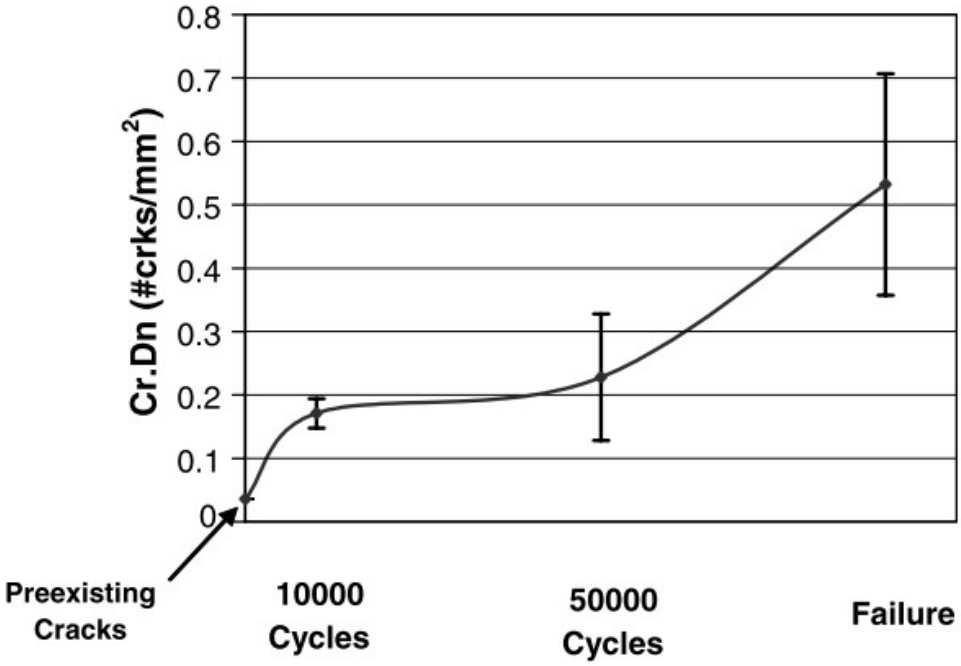

Figure 2.8 Graph demonstrating the relationship between crack density in bone samples and the number of loading cycles [35].

2.2.6 Remodelling Capabilities

Another unique characteristic of bone is that it is capable of repair and remodelling depending on its environment [6, 10, 14, 15, 31, 34, 35]. This remodelling is reported to be a removal and replacement of old, damaged bone with new, mechanically stronger bone [15]. As an example, when the bone is subjected to many cycles of loading, as it would be during walking for example, microcracks will form and begin to propagate, but this damage stimulates the repair mechanism of the bone, through which it is capable of replacing old, damaged cells with newer, more mineral-rich cells [14, 35].
The microstrucutres responsible for this remodelling are known as the osteoclasts and osteoblasts, which absorb old, damaged bone and create new regions of bone, respectively

[14, 15].

Fatima *et al.* [14] reported that remodelling is not strictly for repair, as the bone needs to grow throughout the lifetime of an organism, thus this remodelling also allows for the bones to grow. In humans, during adolescence, this growth, which is associated with bone mass increase, appears to follow a linear pattern with time until about the age 25 to 30 years old, at which point the bone growth and mass increase peaks. Beyond this point, the metabolic activity of the bone begins to slow down, and bone decay begins.

Additionally, bone has the ability to remodel itself according to the load it experiences; increasing the bone mass at regions of high stress and this increases the strength of the bone by making these more densely packed regions [14, 34]. The inverse has also been proven, whereby when remodelling has been suppressed, the material properties of the bone decreased [31].

Bone remodelling is also essential in regulating the calcium homeostasis in the body, as reported by Feng *et al.* [34], as bone is the major reservoir for calcium in the body. Thus, when calcium intake is low, the bones are able to release their stored calcium to maintain homeostasis within the body.

2.3 Response to Strain

As has been discussed previously, bone and its characteristics are highly dependent on the density of the sample as well as the load it experiences. Due to this dependency on load, and therefore stress, there is an important relationship between characteristics of bone and the strain the material experiences. The strain dependency of bone has been extensively documented in literature and will be the focus of this section of this literature review.

2.3.1 Stress and Strain

Bone, like the vast majority of other materials, is capable of two types of deformation; elastic and plastic deformation. As Beaupied *et al.* [36] reported, below its yield strength, bone has the ability to elastically deform and return to the original state when the load is removed, while above the yield point, the bone will deform to the point where irreversible damage will occur. This plastic deformation is not true plastic deformation, as bone typically does not remain in a deformed state, rather pores begin to collapse in the bone and micro-cracks start to form. Thus, a significantly bent bone will not often be observed, however if a finer analysis were to be performed, permanent damage would be noted. In their review, Hart *et al.* [6] reported that these stress-strain characteristics are unique to each macrostructure of the bone as a result of their differing microstructural constituents. The stiffer cortical bone is able to withstand significantly higher stresses when compared to trabecular bone. Kopperdahl *et al.* [10] stated that the strain at yield of cortical bone is recorded as being around 2%, while Hart *et al.* found that trabecular bone is capable of withstanding strains of up to 50% prior to failure. This link between the microstructural constituents and the properties of the macrostructural systems can also been seen when one considers the mineral content of these microstructural constituents, as reported by Spatz *et al.* [37] and Currey *et al.* [21]. The modulus, or stiffness, of the cortical bone has been correlated to the mineral content of the bone sample, in both humans and other animals.

High stiffness is not always a desirable property, as bones will need some flexibility in order to withstand impact events without breaking. For example, in the case of a femur, the bone will need to flex when an individual lands from a jump, but the bones in the ear need to be extremely stiff for acoustical reasons [21]. As a result, bones with drastically different stiffnesses in the same skeletal system can be observed, and this difference in stiffness is as a result of the stress and strains the bones experience.
Finally, it has also been observed by Currey [21] that the younger bones are more

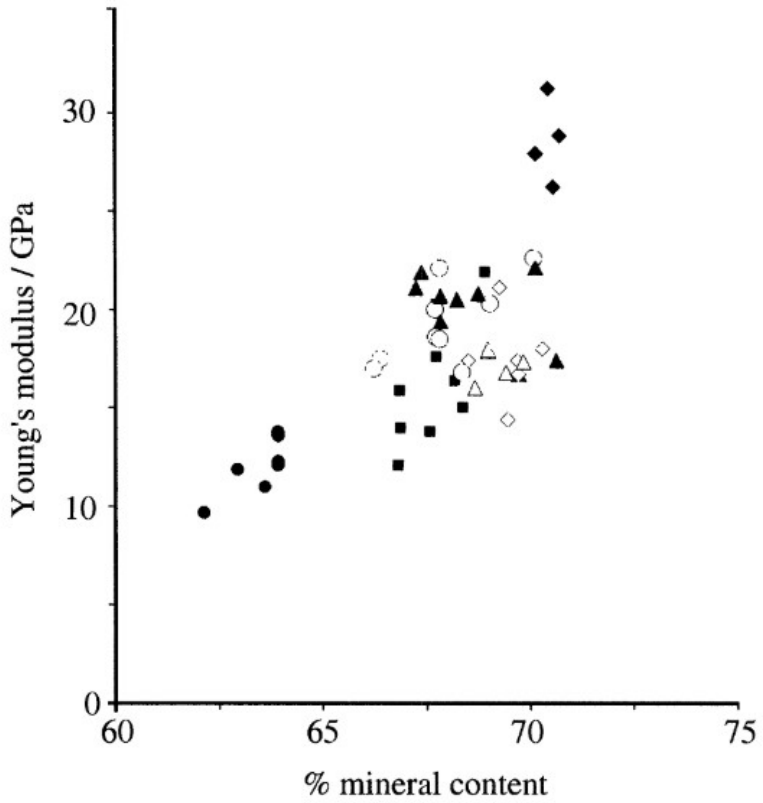

Figure 2.9 Graph demonstrating the relationship between the elastic modulus of bone samples and their ash mineral content percentage in various species [37].

compliant and flexible when compared to older bones. The exact reason for this is not clear, but it is hypothesized that the flexibility is a more desirable property at these younger ages than the stiffness.

2.3.2 Strain Magnitude

When considering the strains that bone experiences, the most common would be the strains associated with those resulting from muscular contraction and gravitational effects, and these two aspects are thought to be the most influential in bone adaptation as reported by Hart *et al.* [6] and Frost [38, 39]. This is with the exception of trauma, nevertheless, bone typically experiences rather uniform and constant strains during normal operation [38, 39].

The *Mechanostat* is a qualitative theory developed by Frost [38] to describe the responses of bone to differing strain magnitudes. The *Mechanostat* describes the resorptive, regenerative and formative responses bone exhibits when subjected to various magnitudes of strain. Figure 2.10 represents the *Mechanostat* theory pictorially and

highlight the relative strengths the remodelled bone depending on the amount of strain experienced. The horizontal axis represents the magnitudes of the strains and is split up into four regions; The disuse window (DW), the adapted window (AW), the mild overload window (MOW) and the pathologic overload window (POW). The vertical axis represents the strength of the remodelled bone as a result of the experienced strains.

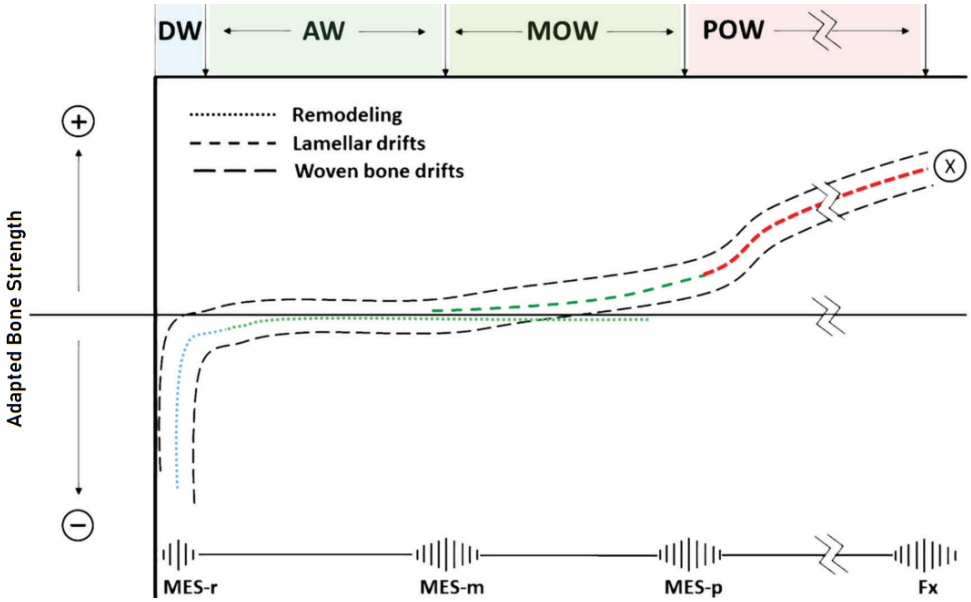

Figure 2.10 Mechanostat [6].

Frost [38] describes the central dotted line seen in the DW (Blue) and AW (Green) of Figure 2.10 represents the remodelling period of disused bone. Bone that experiences strains below the mild overload threshold will eventually be removed and replaced by bone marrow. The central dashed line seen in the MOW (Green) of Figure 2.10 represents highly strained bone, which exhibits an increase in bone strength. Finally, the central dashed line seen in the POW (Red) of Figure 2.10 represents the period wherein the bone structure changes from lamellar bone to woven bone, at which point the bone exhibits its peak strength.

This theory can be used as a tool to represent how bone can undergo remodelling depending on the amount of strain it experiences. However, this bone strength is not as highly correlated to strain magnitude as it is to strain frequency and strain rate, as reported by Hart *et al.* [6].

2.3.3 Strain Frequency

Frequency refers to the number of loading cycles per second on the bone, and it has been found to be a rather influential factor for osteogenesis (bone production) [6].

Linking back to the *Mechanostat*, it has been reported by Cullen *et al.* [40] that at higher frequencies of strain, the stress and strain thresholds for bone formation are significantly lowered. Additionally, Cullen *et al.* [40] reported an increase in loading frequency from $1Hz$ to $30Hz$ can reduce the strain threshold for osteogenesis from $1200\mu\epsilon$ to $100\mu\epsilon$.

The above relationship is not linear, but both Hsieh *et al.* [41] and Warden *et al.* [42] reported that for frequencies greater than 10 Hz the correlation begins to fall off. Additionally, when conducting strain frequency tests on live rats, Warden *et al.* [42] observed that beyond the 10 Hz point, the signal gets saturated and the bone is not able to respond any faster.

A fine balance between strain magnitude and strain frequency needs to be met in order to form optimal adaptations [6]. Low magnitude strains administered at low frequencies will not be sufficient to elicit bone remodelling and the bone will be broken down, while high magnitude strains administered at high frequencies will likely result in failure [6].

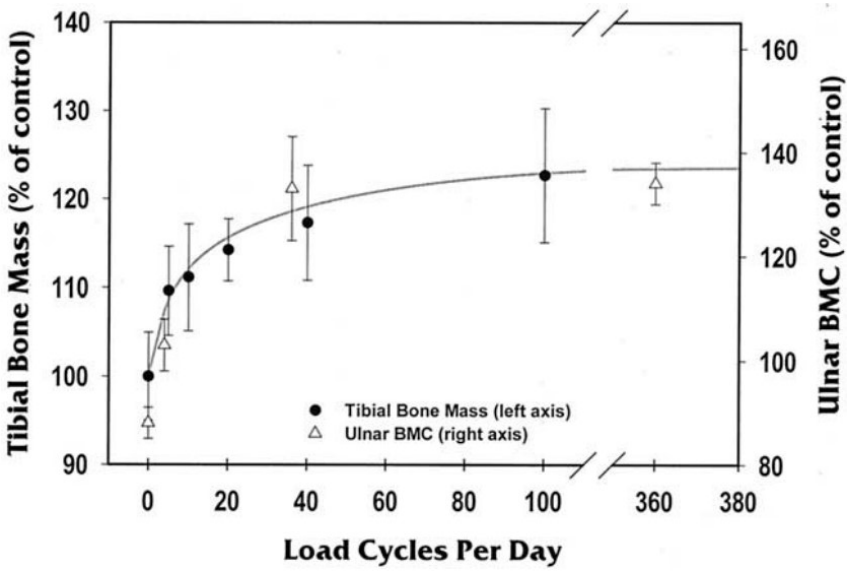

Figure 2.11 Graph demonstrating the relationship between bone mass concentration (BMC) and the number of loading cycles [43].

2.3.4 Strain Rate

Strain rate describes rapidity of the change in the magnitude of an applied strain in one cycle [6]. For example, in an impact event, such as jumping from a 1.5m height, when the strain experienced by the bones occurs in an extremely short timeframe, the strain rate is considered to be high. In the literature, strain rate has been reported to be a highly influential factor when looking at osteogenesis, irrespective of the strain magnitude [44]. Judex *et al.* [44] reported that keeping the strain magnitudes to levels similar to regular,

biological loading, but with higher strain rates greatly increased osteogenesis. Judex *et al.* additionally reported that regular strains, such as those experienced when taking part in aerobic activities like running, showed little increase in bone production when compared to higher impact activities, such as jumping. This once again demonstrates that bone is highly adaptive and is capable of altering itself to achieve its intended function.

A study by Burr *et al.* [43] reported that although exposure to high strain frequencies is important when inducing osteogenesis and for the prevention bone loss, reducing exposure of the bone to high strain magnitudes can be equally as important. Burr *et al.* reported that in order to reach an optimal rate of osteogenesis, recovery periods of between four and eight hours are needed in order to allow the bone to completely re-establish its homeostasis. Finally, Burr *et al.* also reported that high strain magnitudes are not required in order to induce osteogenesis if sufficiently high strain rates were used, which confirms the same conclusions made by Judex *et al.* [44].

2.4 Influential Factors

As has been discussed, bone is a highly variable material, and the slightest change in one particular aspect can have significant repercussions to the properties and characteristics of bone. This section aims to explicitly state these aspects and highlight the effect they have on the measured material properties. The vast majority of these influential aspects are intrinsic, but are susceptible to influence from external factors and this will be dealt with in this section.

2.4.1 Porosity

Cooper *et al.* [45] stated that cortical regions at the end of some long bones can bear between 30% and 90% of the axial loads experienced, thus one could imagine that the presences of pores and voids in such regions would have an impact on the mechanical properties of the bone. In one instance, Cooper *et al.* [45] reported that cortical porosity was the reason for 76% of the variance observed in bone ultimate tensile strength. In addition, it was reported by Cooper *et al.* [45] that with an increase in porosity, bone experiences a decrease in elastic modulus, toughness, elasticity and capacity to absorb impact energy, and this conclusion was reinforced by Currey [46].
With regards to elastic modulus in particular, Cooper *et al.* [45] reported that it was related to porosity to the 11^{th} power (i.e. $E_{cortical} \propto (1-p)^{11}$), which means that if the bone exhibits a change in porosity from 10% to 15%, one could expect a reduction of 46% in elastic modulus values.
With the ever-improving field of medical imaging, much focus has been placed on the ability to accurately determine the degree of porosity of bone sample, in vivo, in order to estimate the properties and strength of bone according to McCalden *et al.* [47] and Engelke *et al.* [48]. This would allow medical professionals to identify individuals with a high risk of bone fracture, and this will allow them to put cautionary measures into place to prevent any major damage [47]. These non-invasive assessment methods, such as advanced computer tomography, have shown to accurately determine bone porosity levels as well as bone structure, and from this information, this method has been able to accurately predict bone strength [48].

2.4.2 Mineral Content

The mineral content in a bone has a significant effect on the properties it exhibits [49–51]. However, as reported by Donnelly *et al.* [50], the actual effect of the mineral content has

on the bone properties is poorly documented when compared to the reported effect the mineral content has on the structure of bone. The reason for this is due to the extensive list of minerals seen in bone; there are simply too many constituents to consider and not enough means of accurately testing the resulting effects [50].

Considering the ash content in particular, Currey [49] reported that very high values of mineralization result in high stiffness, but consequently, low fracture toughness and the converse has also been proven for low values of ash content. The reason for this low fracture toughness has been related to the numerous crack-stopping mechanisms, which develop when bone crystals have *not* formed, failing due to the high mineral content in the bone inducing more bone crystallization [49].

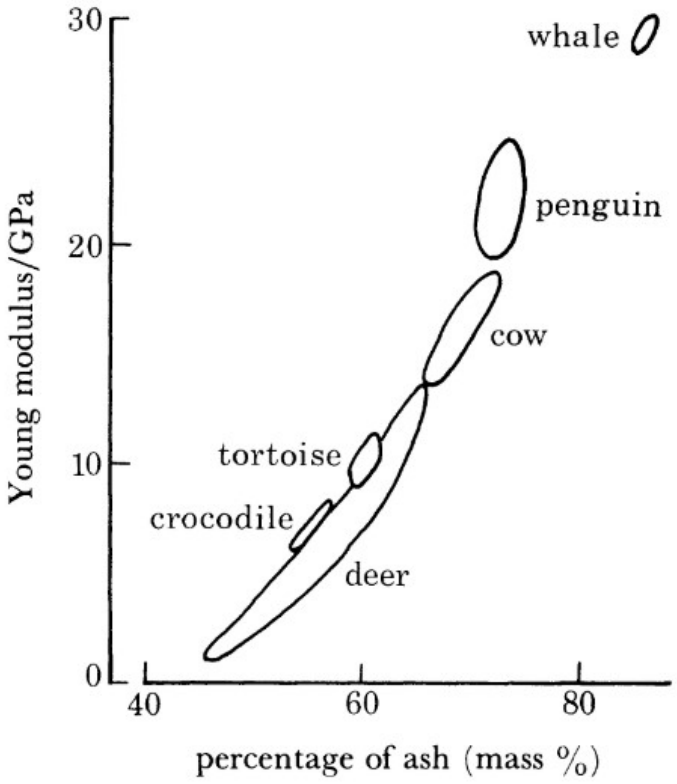

Figure 2.12 Graph demonstrating the relationship between elastic modulus and ash content in the bone [49].

The effects of vitamin D on the properties of bone has been investigated by Donnelly *et al.* [50], who reported that by reducing the vitamin D in a young male rat resulted in a halving of the stiffness and strength of the bone. Vitamin D deficiency has been associated with the development of rickets and osteomalacia (otherwise known as 'soft bones').

Low mineral content has also been identified as the primary cause for osteoporosis in elderly individuals and it is estimated that this bone-related disease will affect a significant portion of the population, as reported by Wang *et al.* [51]. Faibish *et al.* [52] reported

that this disease is characterized by structural deterioration and a lowering of bone mass, which results in an increased risk of fracture.

2.4.3 Degree of Hydration

When in the body, bone maintains a certain degree of hydration, and it has been noted drying a bone prior to conducting tests has a noticeable effect on the measured material properties [53]. As reported by Rho *et al.* [53], there is an increase in the stiffness of the bone when drying out, which consequently reduces the toughness and strain at failure.
Few studies have been conducted pertaining to the specific effects that the dryness has on the properties of bone. Adharapurapu *et al.* [54], Lucksanasombool *et al.* [55] and Sedlin *et al.* [8] all reported that the influence hydration has on the bone agreed that a hydrated and dry bone do in fact display different properties, with the major focus being on the stiffness and fracture toughness.

2.4.4 Age and Sex

As has been alluded to in previous sections, bone is also dependent on the age and sex of the individual. This results from a decrease in metabolic activity as one gets older, as well as from differing sex-related mechanisms in male and female bodies.
With regards to age, it has been reported by Faibish *et al.* [52] that osteoporosis is a major factor to consider regarding the mechanical performance of bone in elderly people. This comes as a result of the aforementioned decreased metabolic activity, and this consequently decreases the strength of the bones [52].
Nirody *et al.* [56] reported that metrics describing porosity, pore number and pore size were all larger in the older of two cohorts of test subjects, irrespective of sex. The cohorts in this study differed in age by over three decades, thus accounting for a significant difference in age between them [56]. From Figure 2.13, a correlation between total pore area and age can be noted.

With regards to sex, there is a difference between the various mechanical properties of the bone between the two sexes. Females display sex age-related porosity changes when compared to males [56]. From a chemical perspective, a difference in the exhibited properties of bone is reported by Toth *et al.* [57], specifically bone morphogenic protein-2 (BMP2), which is a protein associated with bone formation. The deficiency of this protein will result in a reduction in bone mass and overall bone strength. Toth *et al.* [57] report that BMP2 operates in a sex-related manner, for example, it was found that the same BMP2 polymorphism resulted in increased bone mass density in

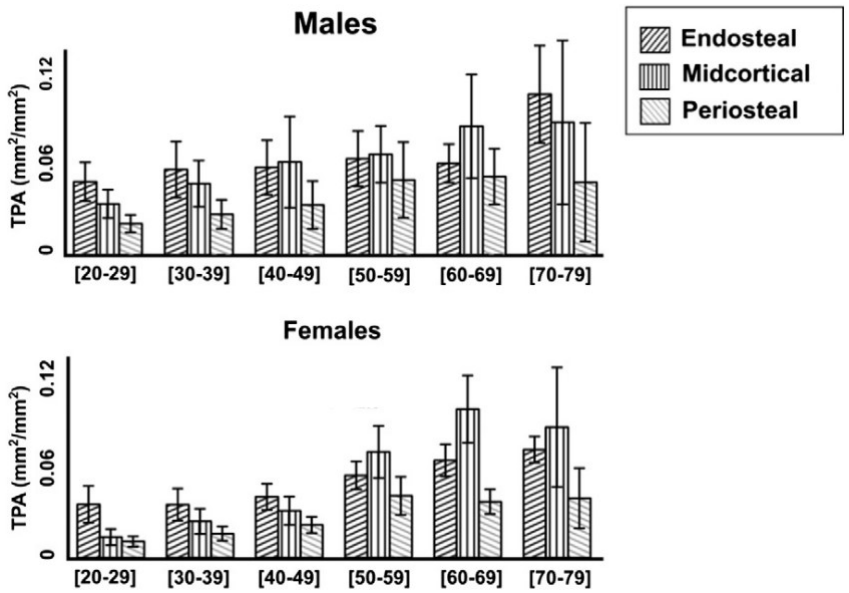

Figure 2.13 Graph demonstrating the relationship between age and total pore area (TPA) in the bone [56].

males and a decrease in females. It was also reported that BMP2-deficient mouse subjects were noticeably smaller than their control cohorts.

2.4.5 Activity Level

Counter-intuitively to what one might imagine, increased activity levels in individuals does not have a strong correlation to bone properties [58, 59].

Montoye *et al.* [58] reported that there was a slight increase in the cortical area of the bone in fitter men when compared to a control group. This was only reported to be at the 5% significance level, so it was not a significant finding, and this low correlation was also reported in a second study of a similar content.

In the second study, Dalén *et al.* [59] reported that the mineral content at various points along a bone were slightly higher in the group of cross-country runners when compared to a control group. In addition, it was reported that there was no increase in mineral content in the bones of a cohort of male office employees subjected to a three-month period of increased physical activity.

2.5 Specimen Preparation

During this literature review it was noticed that the field of bone specimen preparation is not as well documented as other aspects, such as the actual properties or characteristics of bone. This begs the question of whether or not the preparation protocols used for these various tests have any bearing on the actual results generated. This section of this review aims to highlight the inconsistent procedures used when conducting tests on bones and hopes to emphasize the need to conduct further research into this aspect of the testing. A discussion regarding the specimen geometry choices made for this research is dealt with in Section 3.1.2.

2.5.1 Pre-Testing Protocols

Bone retrieval was an aspect of research that has been particularly sparsely documented. Some papers specifically state that the bones were retrieved via professional orthopaedic facilities, such as those by Sedlin *et al.* [8], Ebacher *et al.* [60] and Lin *et al.* [22]. While papers by Kopperdahl *et al.* [10], Kim *et al.* [61] and Yamada *et al.* [62] failed to mention any retrieval protocols at all. This could be problematic from the perspective that if the bones were not retrieved in as delicate of a manner as possible, the damage experienced could have an effect on the properties exhibited during testing. As an example, if a surface crack were to be sustained by the specimen, for example via damage from a saw used to retrieve the bone, it could act as a stress raiser during bending tests. The use of harsh, inaccurate tools for bone retrieval is seen throughout the literature, and few tests even mention the fact that this damage has been taken into consideration [7, 8, 22, 62, 63].

Specimen designs are also an aspect where there is little agreement with regards to standardized protocols. Some tests, for example, have highly detailed protocols of specimen manufacturing [30, 53, 61, 63, 64], while other tests by Currey *et al.* [46], Ebacher *et al.* [60] and van Haaren *et al.* [7] were conducted on whole bone. Furthermore, Lin *et al.* [22] reported their specimen manufacturing process with little detail. This variability could have some impact of the results found, and it justifies the need to specifically consider these preparation protocols to identify if they do indeed have an impact on the results obtained.

2.5.2 Dry VS Hydrated

The degree of hydration has been discussed previously, and, once again, there is a noticeable amount of conflicting information regarding how this degree of hydration is maintained in the bone. Ideally, one would want to preserve the in vivo characteristics of bone during any mechanical tests, as this data is relates to how the bone would react if it were still in the body. This means retaining the moisture content of the bone during tests, but in the few papers that did look into this aspect, each employed a different means achieving this state.

In their study, Rho *et al.* [53] reported that the dry specimen was simply air-dried for an extended period of time, while the hydrated specimen was stored in deionized water. The modulus of the dried bone was reported to be around 10% higher than the hydrated bone, while the hardness also increased by roughly 14%.

Another study, by Borchers *et al.* [64], considered the number of procedures to induce this varying degree of hydration. Out of the six treatments considered, only the use of boiling, to induce hydration, and autoclaving, to induce dryness, showed significant results. The dry specimens were heated at 127°C for ten minutes, while hydration was induced by boiling the specimens in normal saline at 100°C for half an hour. The drier specimens showed a 58% reduction in strength and a 59% reduction in compressive modulus, while the more hydrated specimens only demonstrated a reduction of 26% in their strength.

Finally, in their study Sedlin *et al.* [8] considered dryness in particular, and specimens were subjected to air-drying for differing lengths of time, ranging from five minute to one hour, while one other group was incubated at 105°C for a week. It was reported that after just ten minutes of being air-dried, specimens started to show an increase in strength, while modulus showed no change after an hour of air-drying. But the incubated specimens showed significant increase in modulus and decrease in toughness after the week long incubation.

These few studies demonstrate the susceptibility of bone to dryness, and it is definitely an aspect that needs to be considered when conducting tests on bone. Despite this, some consensus is beginning to emerge in more recent reviews. For example, the drying and rehydrating of bone specimens is not advised. In their extensive review of over 150 published articles, Zhao *et al.* [65] stated that the testing of rehydrated cortical bone specimens compared to never dehydrated specimens yields significantly different results. Similarly, Sanborn *et al.* [66] and Weerasooriya *et al.* [67], state that the comparison of non-embalmed bone to embalmed specimens is not viable, as the embalming and drying process effects the microstructure and constituents of the bone specimens. This is

attributed by both Sanborn *et al.* and Weerasooriya *et al.* to the hydration-dependent behaviour of the organic phase of the bone (i.e. the collagen fibres).

2.5.3 Temperature

Many of the studies cited in this literature review either did not mention temperature as a factor in their research, or simply stated that tests were conducted at room temperature [4, 7, 10, 22, 24, 35, 42].
However, Sedlin *et al.* [8] did attempt to observe the effects of testing at different temperatures, and it was reported to have little impact on the properties. Groups of specimens were tested at 21°C and others were tested at 37°C, and a difference of modulus, strength, energy absorption and failure strain were reported to be insignificant. One other study, by Kim *et al.* [61] did mention that fatigue tests were conducted at different temperatures, but the results of this aspect were not recorded.

2.5.4 Post-Mortem Duration

A noteworthy finding regarding bone testing is that information such as the post-mortem age of the donor bone and the time between specimen manufacture and testing are typically not reported. The vast majority of the papers found for this review did not mention the time between the retrieval from the donor and the testing, nor the time between specimen preparation and testing. However, a paper published by Gustafson *et al.* [68] pertaining to horse bone did find that after six days of the specimens being stored in an unbuffered saline solution, a deterioration in elastic modulus was observed. It must be noted that this paper reported that the bones were dried at $100°C$ for 24 hours after retrieval.
Intuitively, one could imagine this aspect being crucial to the properties being tested in the various papers, but the lack of conclusive evidence in regard to this is a noticeable gap in the literature.
A distinction must be made between the age of the donor at death and the post-mortem age of the bone. While the age of the donor is often reported in the literature, the age of the bone after retrieval from the donor, i.e. the post-mortem age of the bone, is seldom reported. Furthermore, the time between machining and testing is also seldom reported.

2.5.5 Storage Conditions

There are two fields of thought for storage conditions of bone specimens; the first being storage in a solution and the other being freezing. Storage solutions range from saline,

to formalin and alcohol-based solutions, each with unique effects on the properties of the bone.

Four studies considered the effects of formalin, which is the aqueous form of formaldehyde, as a storage medium in particular, and they all came to different conclusions. After three weeks of storage, Sedlin *et al.* [8] reported that there was no difference in modulus when compared to a control group, while Öhman *et al.* [9] reported a significant decrease in modulus, with no change in strength or hardness after eight weeks in formalin solution. Goh *et al.* [69] reported that after 21 days in formalin solution there was an increase in brittleness, while Stefan *et al.* [70] only noted a minor change in properties after six months of storage. Other tests in this regard, conducted by Currey *et al.* [71] and van Haaren *et al.* [7] also reported that after as long as a year in storage, there was no significant difference in the properties of the bone. However, Currey *et al.* [71] failed to report the age of the specimens before formaldehyde treatment, and the treatment process also took a number of days. While van Haaren *et al.* [7] failed to state the age of the specimens after extraction. In addition to these studies, two articles concerned with investigating the loading rate effects of cortical bone through the use of digital image correlation (DIC), by Sanborn *et al.* [66] and Weerasooriya *et al.* [67], both explicitly state that the comparison of fresh bone to bones that have undergone an embalming process would not be effective, as the embalming process causes significant effects on the microstructure and constituents of the bone.

Considering alcohol-based solutions, there are differing results reported in the literature. Stefan *et al.* [70] recorded no significant difference in the properties after six months of storage, while Lucksanasombool *et al.* [55] observed significant changes in brittleness after storing the specimens in an alcohol-based solution for one week. Lucksanasombool *et al.* [55] proposed that this difference was due to the alcohol dehydrating the specimens prior to testing, thus inducing the brittleness which has been mentioned previously. Notably in the study by Lucksanasombool *et al.* [55], the dehydration could be reversed by storing the specimens in saline for the same amount of time as they were stored in alcohol, thus restoring the properties of the specimens to the positions if stored purely in saline.

A notable finding by Zhao *et al.* [65] is that freezing appears to be the most popular storage method. Despite this, the reported effects as a result of freezing bone samples are contradictory. It was reported that a number of studies froze their specimens between $-30°C$ and $-20°C$, without specifically considering the impact the freezing had on the properties of the bone [22, 60, 61]. Sedlin *et al.* [8] did report that freezing bone after retrieval for four weeks had no significant effect on the average strength of the specimens and no effect at all on other mechanical properties. These findings were

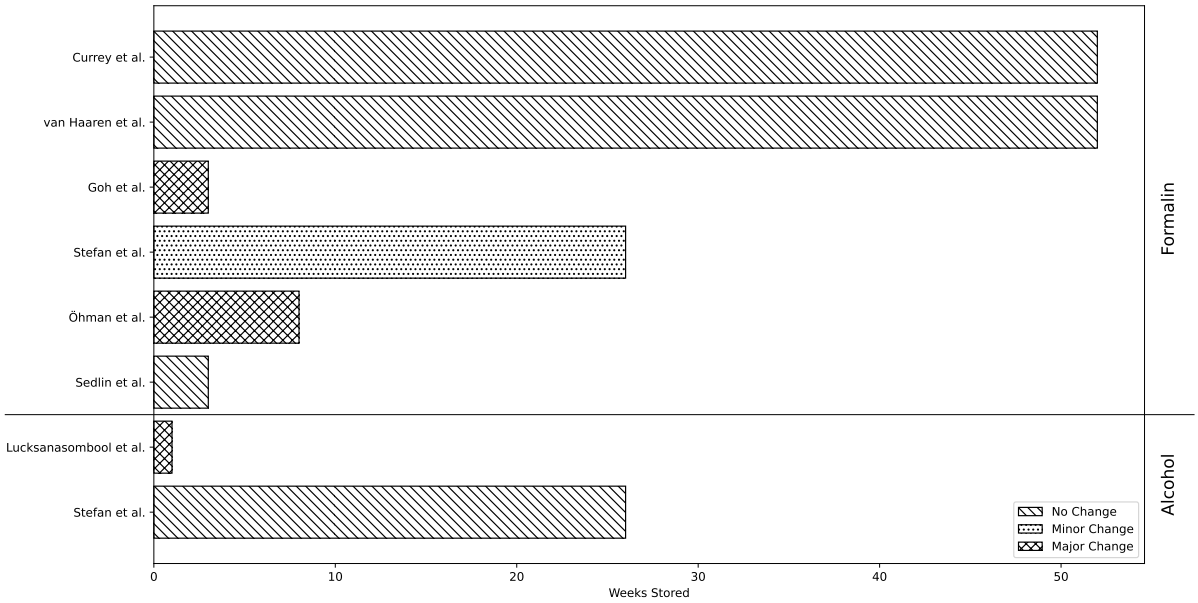

Figure 2.14 Comparison of the results of storage protocols studies.

confirmed by van Haaren *et al.* [7], that froze specimens at −20°C for up to one year and no significant difference was recorded in any mechanical property. Contrary to this, Lee *et al.* [72] reported that the effects of long-term freezing on porcine trabecular bone resulted in approximately a 40% decrease in the apparent modulus after one year of storage. Borchers *et al.* [64] attempted to determine if the temperature of freezing had an effect on the properties of the bone, and it was reported that even with temperature as low as −70°C, there was no significant effect on the properties of the bone. Finally, Kaye *et al.* [73] conducted tests pertaining to the fracturability of bone specimens which were frozen for up to 20 days at −20°C. Kaye *et al.* [73] reported that the freezing had no effect on the properties. Notably, the tests in the van Haaren [7], Borchers *et al.* [64] and Kaye *et al.* [73] studies were all conducted after allowing the specimens to thaw with the hope of returning to the recently retrieved state, and this aspect was not mentioned elsewhere in the literature.

2.6 Testing Methods

As has been discussed previously in Section 2.3, strain rate is a particularly important aspect to take into consideration when conducting tests on bones. As a result, tests in particular strain rate regimes have been the focus of many studies attempting to quantify the mechanical properties of bone, and this section aims to bring to light these various techniques and explain the importance of the strain rate requirements of bone related studies.
This section will focus on the testing techniques used for this study and will highlight the principles behind the design of the testing apparatus.

2.6.1 Digital Image Correlation

The use of DIC to observe the deformation of a specimen is a relatively common practise in current material testing. However, the dependency of this technique to have an accurate speckle pattern renders is difficult to implement in the case of cortical bone specimens. Although a number of studies have attempted to use DIC for cortical bone material tests [66, 67, 74, 75], none of these studies claim to be determining the mechanical properties of fresh bone. The reason for this is that the specimens tested in these studies underwent extensive speckling processes, which resulted in the specimens drying out prior to testing. While the studies by Nguyen *et al.* [74] and Pereira *et al.* [75] do not state any rehydration processes, the studies by Sanborn *et al.* [66] and Weerasooriya *et al.* [67] do state that their specimens were rehydrated after speckling using Hank's Buffered Salt Solution (HBSS). In those same studies, Sanborn *et al.* and Weerasooriya *et al.* state that the drying out of specimens does have an effect on the measured properties due to the collagen fibres in the bone being hydration-dependent.
This brings into question the viability of using DIC to investigate the mechanical properties of bone specimens. The DIC method requires sufficiently accurate and clear speckle patterns to achieve a high resolution, but this process requires that the specimen, firstly, be dried and then secondly, potentially have to undergo surface treatment, like the specimens in the previously mentioned Nguyen *et al.* study. This drying out and surface treatment could potentially alter the performance of the specimens, thus, for the case of determining the mechanical properties of fresh bone (i.e. still being representative of an in-vivo state), the use of DIC appears to not be viable.

2.6.2 Quasi-Static Apparatus

The quasi-static (QS) strain rates regime is generally defined within the range of 0.001 s^{-1} to 0.1 s^{-1} [16]. This regime has been the focus of the majority of studies, as this is the most accessible strain rate regime with respect to the use of standardized machinery [32,46,54,71]. These tests can be conducted in either tension, compression or bending and the machines that conduct such tests, such as servo-hydraulic or screw-driven machines, are capable of operating at a wide range of strain rates, thus allowing for easy repeatability of tests [46, 54].

Furthermore, the versatility of these QS testing methods is another attractive aspect of testing in this strain rate regime. As will be discussed later in this section, custom rigs can be designed in which tests can be conducted which will cater for any type of loading; be it compression, tension or bending, as reported by Currey *et al.* [46, 71]. This allows for all loading circumstances to be accounted for and tested, all with the benefit of only needing to operate one machine.

Currey *et al.* [46] stated that conducting tests on bones at QS strain rates might yield irrelevant results as it is rare that bones will fracture at such low strain rates. Despite this, a high QS yield strength has been linked to improved fatigue characteristics, thus these results are not without merit.

2.6.3 Dynamic Apparatus

The primary apparatus used for bone testing in the dynamic strain rate regime is the Split Hopkinson Bar (SHB), with Adharapurapu *et al.* [54], Cloete *et al.* [16], Prot *et al.* [76] and Teja *et al.* [77] all using the SHB. The typical setup of a SHB consists of a gas gun, a striker, an incident bar and a transmission bar, shown Figure 2.15.

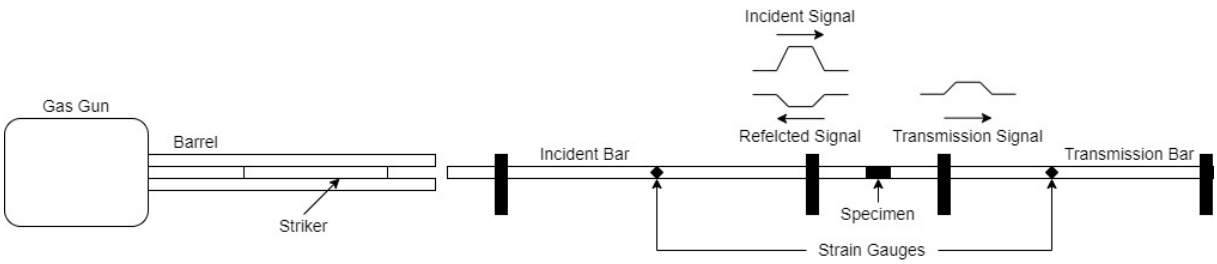

Figure 2.15 Labelled schematic of a simple SHB.

Gas is pressurized in the gas gun, and at a critical pressure, the gas is released which propels the striker forwards, into the incident bar. The striker impacts the incident bar, which in turn impacts the specimen. At this point, due to the free-boundary condition

that is induced at the incident-specimen interface, a portion of the incident stress wave is reflected back into the incident bar and the rest is transmitted through the specimen, into the transmission bar. The stress waves are captured using diametrically opposed strain gauge pairs bonded to both the incident and transmission bars, and are connected to a data capture device.
The governing principle upon which the SHB is based on is the theory of one-dimensional stress wave propagation. The theory is summarized by:

$$c = \sqrt{\frac{E}{\rho}} \tag{2.2}$$

Equation 2.2 describes the speed at which the stress wave traverses the bar and equation 2.3 describes the stress induced in the bar as a result of its impact with the striker.
The compressive stress induced in the incident bar after its impact with the striker results in a compressive zone that moves along the bar at a constant speed of sound, c [79]. Hence, it can be seen that the velocity of the stress wave through the bar is a result of the material properties of the bar from:

$$\sigma = \rho c v \tag{2.3}$$

where v is the particle velocity of the material after impact. A Lagrangian Wave Propagation Diagram represents the various stress waves that traverse the bars, with respect to time, as shown in Figure 2.16. The full derivations of these equations are presented in the literature [78, 79].

The traditional SHB is a compression testing machine, however adapted versions have been developed to test other loading types, such as bending [81–83]. A common alteration is one in which the interfaces between the SHB and the specimen are changed through either a radical alteration, seen in Figures 2.17a and 2.17b, or a more minimal alteration, shown in Figure 2.17c.

In all the cases found, either the bars themselves have been the focus of the development, while the specimens have remained rather simple, while in other cases the specimens have been radically changed and the bars have been kept simple.
It was also noted in the literature that both the incident and transmission bars did not necessarily need to be altered in order to develop a SHB for dynamic bending, as in two cases only the transmission bar was adapted [83, 84].
It was reported by Jiang *et al.* [82] that there appears to be little to no difference

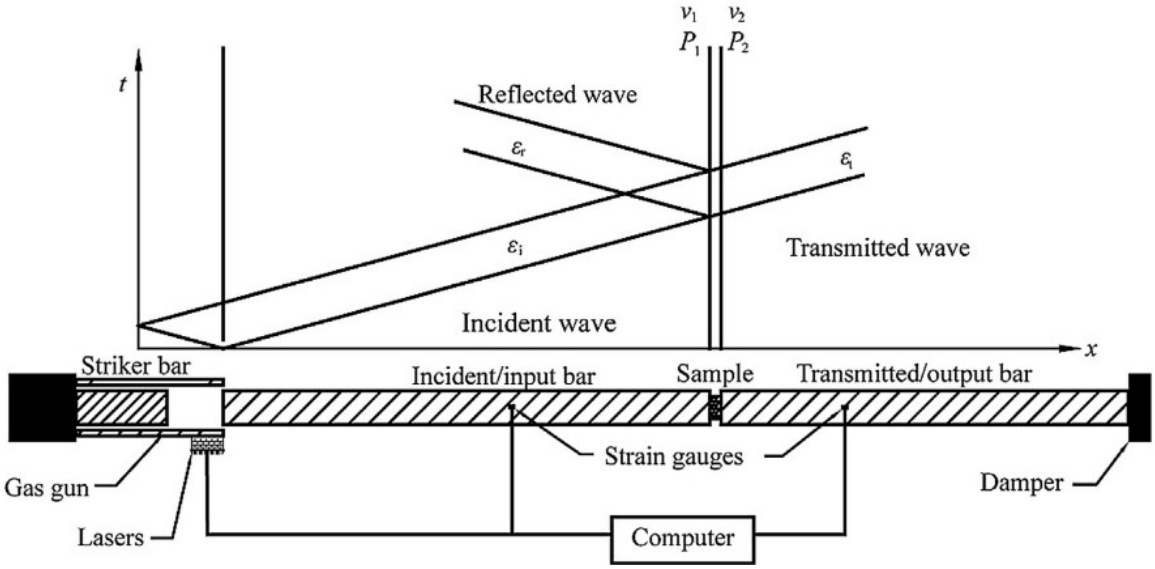

Figure 2.16 Schematic of Lagrangian wave propagation of a split hopkinson bar [80].

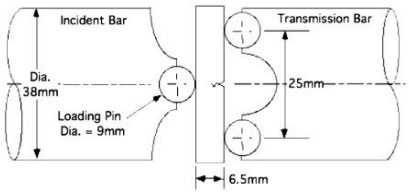

(a) Radical 3-Point bending SHB alteration [81].

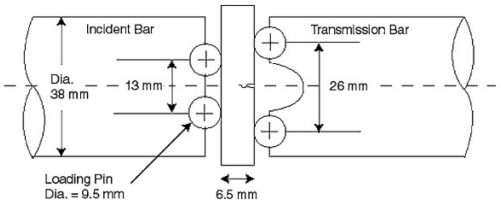

(b) Radical 4-Point bending SHB alteration [82].

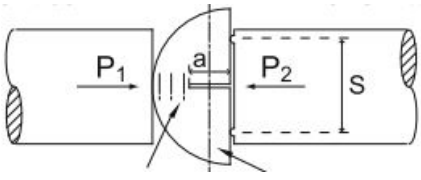

(c) Simple 3-Point bending SHB alteration [83].

Figure 2.17 Bending SHB alteration comparison.

between the results generated from the three- and four-point bending tests, except that in the four-point bending tests the fracture time can be increased through wave shaping. Furthermore, Jiang *et al.* [82] also reported that the four-point setup can be used to reduce the effects of dispersion and it can extend the rise time of the initial pulse, thus allowing more time for the specimen to reach the required stress-state equilibrium.

As reported by Sanborn *et al.* [66], a few studies have attempted to secure SG's directly to the specimens in an effort to improve the accuracy of these dynamic tests. Apart from having to determine a means of accurately positioning a set of SG's to a small bone specimen, the primary issue with this method is that the specimen must be dry for an adhesive to satisfactorily secure the SG to the surface of the specimen. This would involve the artificial drying of the specimen, which, Sanborn *et al.* report, has an effect on the measured mechanical properties of the specimen.

2.6.4 Intermediate Strain Rates

Due to the viscoelastic properties of bone, it is anticipated to react differently when subjected to different strain rates, and the need to conduct tests across a wide range of strain rates of bone is necessary in order to fully quantify the properties of the material. As a result, many tests have been conducted at lower, or quasi-static strain rates [32,46,54,71], and higher, otherwise known as dynamic, strain rates [41,43,44,51,54]. These lower strain rates are considered to typically lie within the range of 0.001 s^{-1} to 0.1 s^{-1}, while the dynamic range lies above 300 s^{-1} [16]. These lower strain rates are akin to what would be experienced during walking or running, while the dynamic range is similar to what would be experienced during an impact event such as a bullet wound or a severe vehicle accident [2, 16, 44, 85].
Testing in these two regimes has been the preference of the vast majority of previous bone studies. This is due to the fact that current testing apparatuses are readily capable of testing in these domains and special adaptations are needed to test in the intermediate strain rate (ISR) regime [16]. Furthermore, due to the viscoelastic nature of bone, tests in the ISR regime requires testing at near-constant strain rates [16]. This will prevent false results that would result from the testing of a strain-stiffening material, such as cortical bone [16].
As a result, the ISR regime is significantly less populated than these other two regions, as illustrated in Figure 2.18, which was taken from a thorough review on the various strain rates at which bone testing has been conducted [2].

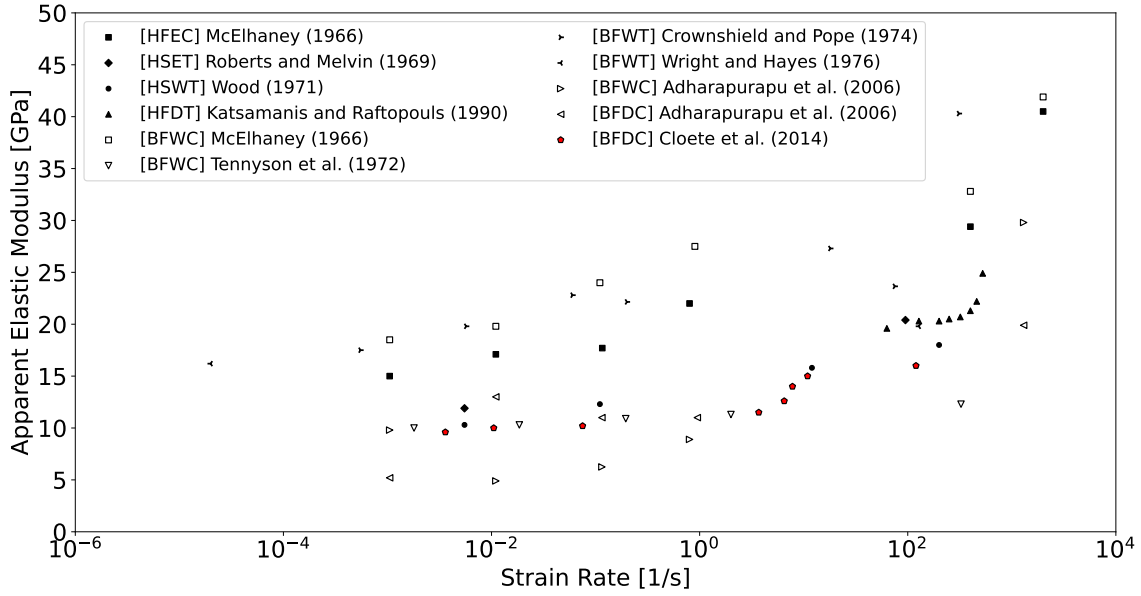

Figure 2.18 An adaptation of the graph generated by Johnson *et al.* [2] demonstrating the relationship between the modulus and strain rate.

In Figure 2.18, the region between 1 s^{-1} and 100 s^{-1} is significantly less populated with data when compared to the outer two regions. The reason for this is due to this range being on the upper limit of what is capable by most QS testing machines and at the lower limit of the common dynamic testing apparatuses [86]. These strain rates are faster than the QS equilibrium of controlled testing machines, but slower than the single wave mechanics used in a SHB test [86]. Additionally, these strain rates are in the range of what would be experienced during a motor vehicle accident or during a sports injury, and these are typically the most common instances where bone fractures occur [87–90]. Furthermore, only until recently had the matter of ensuring constant strain rate throughout the duration of the test been considered [54, 91]. The need for ensuring constant strain rate is required so that the results obtained through a test are not showing information from a range of strain rates, but rather for one particular strain rate, as the strain-stiffening cortical bone will react differently when subjected to different strain rates [54, 91]. Additionally, the testing procedure will need to reach this constant strain rate quickly, as bone is recorded as failing at relatively low strain [16]. This means that the testing apparatus needs to reach the desired strain rate without sustained periods of time in the undesirable strain rates [16].

This near constant strain rate has been achieved via two noteworthy means, one of which was through adapting the geometry of the striker while the other uses a sacrificial material between the striker and the incident bar to shape the stress wave [16, 54, 91].

This sacrificial material is referred to as a pulse shaper and it is simply a small piece of soft material that sits between the striker and the incident bar. When the impact between the two aforementioned bars takes place, the pulse shaper deforms and reduces the sharpness of the ramp-up of the incident stress wave in the incident bar [80, 91]. If shaped correctly, this increases the loading time of the specimen, which allows the specimen to be in stress-state equilibrium for a longer period of time, thus increasing the testing time [80, 91]. Without the pulse shaper the incident wave would be a rectangular shape and there would not be sufficient time for the specimen to reach equilibrium [80, 91].

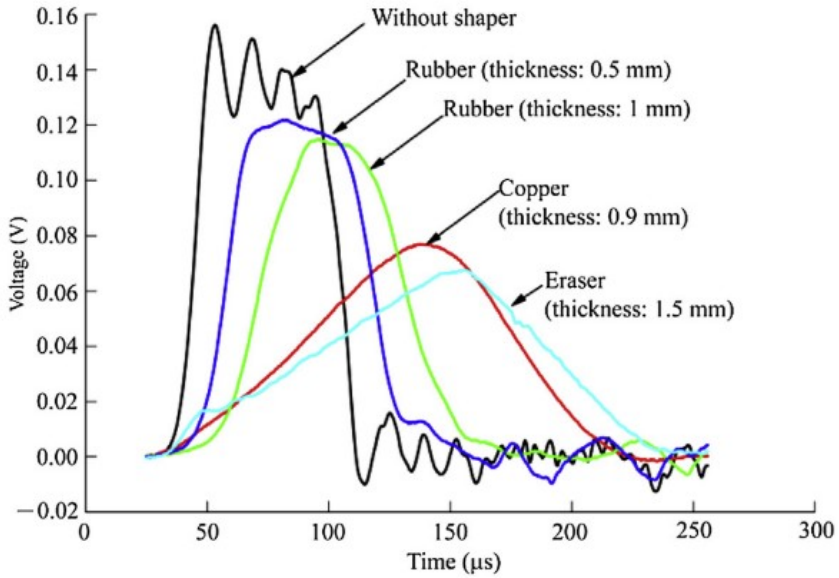

Figure 2.19 Plot demonstrating the different incident stress wave shapes resulting from the use of different pulse shaping materials.

Ideally, a pulse similar to the one seen by the copper load line in Figure 2.19 is desirable. The favourable traits of this incident pulse are the longer ramp-up time, seen by the gradual increase in the voltage magnitude, and the reduced oscillations at the peak of the load [16, 80]. This stress-state equilibrium ensures that the entire specimen is loaded with the same stress, which is critical when conducting a split hopkinson bar analysis [80]. The oscillations observed at the peak of the unshaped load line are representative of the specimen not having the same forces at either of its ends, which also means it is not in a state of stress equilibrium [80].

The alternative means of conducting tests are near-constant strain rates was reported by Cloete *et al.* [16] whereby a conical striker was used in place of a traditional cylindrical striker. The conical striker was placed inside a hollow tube of the same material, shown

in Figure 2.20, and this outer tube acted as a momentum trap to sharply truncate the end of the stress wave.

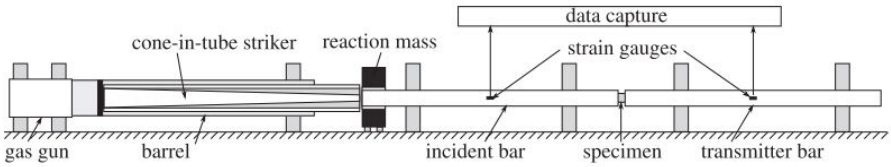

Figure 2.20 Cone-in-Tube modified SHB [16].

The intention of this design was to generate a incident pulse that featured a steeply rising slope with the same gradient as that of the specimen response [16]. This near-constant strain rate, along with a steep incident wave that is sharply truncated which results from the use of this apparatus, would allow for the test time to be maximized and for dynamic recovery tests to be conducted [16]. This technique generated promising results, with constant strain rates at the upper limit of the ISR regime being achieved across a number of tests [16].

2.6.5 Intermediate Strain Rate Testing of Polymers

As has been presented in Section 2.6.4, the testing within the ISR regime is difficult, even when attempting to test relatively stable materials, such as metals. Being both viscoelastic and highly temperature-dependant, as reported by a number of authors [92–96], polymers, specifically for this work PMMA, offer even more of a challenge when attempting to conduct dynamic tests in this strain rate regime.

A number of studies can be found focused on the strain rate sensitivity of polymers, however, many of those studies report results for strain rates below 1^{-1} and above 300^{-1}. Even so, many of these studies describe the stress, strain and failure characteristics of the tested materials, but fail to explicitly state findings pertaining to the elastic modulus. Although trends are mentioned and results can be inferred from the graphs and results, very few studies are focused primarily on the elastic modulus of polymers in this strain rate regime.

For example, Nasraoui *et al.* [93], Jin *et al.* [97], Acharya *et al.* [98], Hu *et al.* [94] and Hoolquist *et al.* [99] all do not mention elastic modulus in their results, while Li *et al.* [95] and Richeton *et al.* [96] state conclusions about the elastic modulus but do not quote any values. Additionally, only Richeton *et al.* and Acharya *et al.* reported results from tests conducted in the ISR regime; all other studies conducted tests well above this strain rate regime.

Furthermore, due to the nature of dynamic material testing, it is difficult to conduct tests at near-constant strain rates, as was discussed in Section 2.6.4. Hence, despite many of the aforementioned studies reporting results, these results may not be truly representative of the viscoelastic material. As shown in Figure 2.21 from Acharya *et al.* , despite being able to conduct tests in the ISR regime, those results are not obtained from periods of time where the specimen was being loaded at a near-constant strain rate. Being a viscoelastic material, ensuring this criteria is met is crucial for quoting results for polymer material characteristics; particularly elastic modulus.

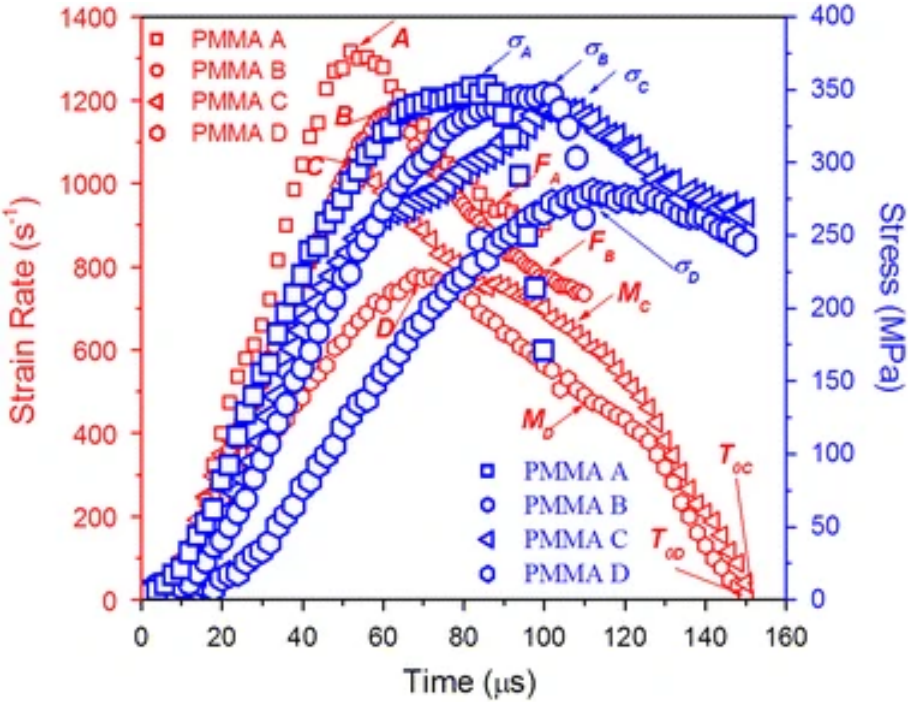

Figure 2.21 Graph of strain rate vs time from Acharya *et al.* [98] highlighting the non-constant strain rate of dynamic compression tests conducted on PMMA specimens.

2.7 Computational Simulations

Viscoelastic material models have generally been the basis of many bone material models to date [100, 101]. Despite numerous viscoelastic models having been developed, the vast majority of the models do not account for the strain rate sensitivity that typical viscoelastic materials exhibit [101]. Despite this, a number of models do attempt to account for this strain rate sensitivity, and this section will focus on these two prominent examples of such models. Furthermore, this section will highlight the THUMS finite element model which is a commonly used human occupant model for traffic accidents.

2.7.1 Shim Model

The viscoelastic model developed by Shim *et al.* [100] utilised a combination of Voigt and Maxwell elements, which are simply parallel and series arrangements of springs and dampers, respectively. These models that consist of such elements, are typically used to demonstrate the viscoelastic response of materials, while also taking into account the non-linear dependence of the material with regards to strain rate. Shim *et al.* [100] were able to achieve an accurate fit to their experimental data using their proposed model, across strain rates ranging from 0.01 s^{-1} and 0.1 s^{-1}. The Shim model used a parallel arrangement of a Voigt element and a Maxwell element, shown in Figure 2.22.

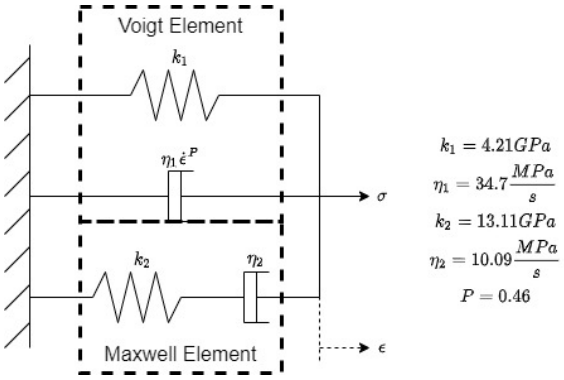

Figure 2.22 Diagram of the Shim model highlighting the individual Voigt and Maxwell elements.

This model is unique when compared to other viscoelastic bone material models as it takes into account the effect of both density and strain rate [102].

2.7.2 Objective Power Law (OPL) Model

The Shim model [100] was chosen by Bekker *et al.* [102] to develop further after comparing it to eight other viscoelastic models. All nine viscoelastic models were compared to a collection of experimental datasets and Bekker reported that the Shim model demonstrated the lowest relative error and scatter [102]. The objective power law (OPL) model is exactly the same as the Shim model in all respects, except for the fact that the OPL model is frame invariant, which allows general power law rate dependence for 3-dimensional cases.

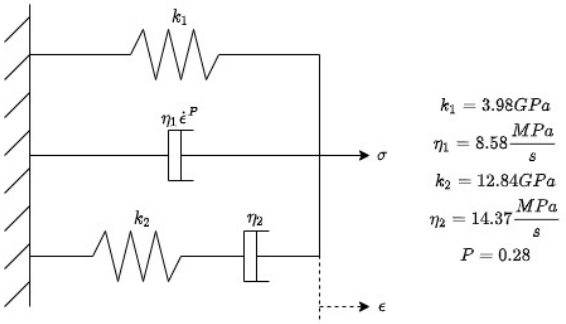

Figure 2.23 Diagram of the OPL model.

Neither Shim *et al.* nor Bekker *et al.* conducted tests in the ISR regime, and as such, it was reported by Paul *et al.* [103], these models could not accurately describe the behaviour of cortical bone in the ISR regime.

2.7.3 SHB Simulations

The operation of a SHB relies on the interaction of the stress waves induced by the striker impact at the various interfaces of the SHB. As such, in order to obtain clean waves from which meaningful data can be extracted, there cannot be any overlap of the waves as they reflect off the various interfaces. As a result, it appears from the literature that SHB tests are typically simulated with the entire length of the various bars being modelled [104–109]. With the typical SHB setup consisting of bars with lengths in the order of metres, having to model the entire bar comes at a great computational expense. A solution to this issue would be the implementation of a set of infinite elements at the ends of the input and output bars which do not interact with the specimen. This would ensure that these ends of the bars do not generate any unwanted reflections that would reload the specimen unintentionally. The use of the infinite elements would additionally, and more importantly, allow for the length of the bars to be greatly reduced as there would be not any undesirable wave interactions as a result of the reflected waves off these ends of

the bars. Kammerer *et al.* [110] appear to be the first to have attempted and successfully implement such a solution in ABAQUS. Despite the successful implementation of the infinite elements, this solution does not appear to yet be adopted as standard practise with only a limited number of papers having been found that attempt to implement the infinite elements in a SHB simulation [111–113]. Weyer [114] was able to successfully implement a similar solution in LS-Dyna using an extra set of elements tied to the ends of the bars, with a non-reflecting boundary condition of the far faces. The distinction between this and what Kammerer *et al.* [110] were able to implement was that the solution by Weyer [114] was applied on a boundary, while the infinite elements are simply added to existing elements on the mesh.

2.7.4 Validation Tests

There appears to be a lack of validation tests of bone with large and rich data sets in the literature. In the studies that were found, validation tests consisted of one loading type or one strain rate, with one paper conducting no validations tests [115–117].
The OPL model, by contrast, was validated using a large sample size, across a range of both QS and dynamic strain rates, however only compression loading was tested [101]. Due to the viscoelastic behaviour bone exhibits [2, 29, 30, 51], testing across a range of strain rates and loading types is necessary to better describe the complex biomaterial. Furthermore, due to the variability of bone properties along a particular donor bone [24], large data sets need to be curated prior to model development if a true representation of a complex whole bone is to be modelled computationally.

2.7.5 THUMS

The 'Total Human Model for Safety', or THUMS, is a finite element model of a human occupant designed with the intention of estimating injuries in motor vehicle accidents in finite element analysis (FEA) codes such as PAM-CRASH and LS-Dyna [11]. Bones, ligaments, tendons, flesh, skins and organs are all modelled in THUMS [11, 12].

Iwamoto *et al.* [11, 119] first introduced this model in the early 2000's through the Toyota Motor Corporation, and THUMS has been supported and developed with updates being made as recently as 2023 [120]. The model has been developed significantly from the first version and currently has a number of different occupant variations, each accounting for different occupant sex, age and body type, as well as different seating and standing positions [118, 120].
Upon inspection of the model, THUMS utilizes the piecewise linear plasticity material

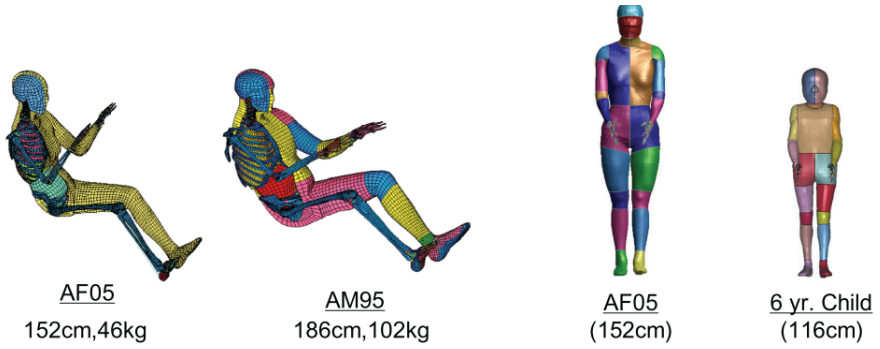

Figure 2.24 Diagrams of the THUMS occupant and pedestrian models highlighting the skeletal and soft tissue systems that are modelled in THUMS [118].

model (MAT_024) in LS-Dyna for the cortical regions of the long bones. This material model is capable of accounting for strain rate effects, however it does not appear that such an option is activated in THUMS. Furthermore, this material model offers a number of failure criteria and the effective plastic strain option is activated in THUMS.

Chapter 3

Experimental Apparatus

This chapter aims to explain the philosophies behind the various apparatuses used to conduct the tests for this research, which includes design and material choices. Additionally, the calibration process for the various apparatuses will be outlined in this chapter, along with the associated calibration errors and factors.

3.1 Quasi-Static Compression

For this study, a custom compression rig was used, which was designed with compliance reduction and micron-level accuracy as the primary goals. The reason for this focus was due to the fact that the anticipated deformations are minimal, in the order of 1 mm, and as such, any error will have a significant impact on the results. The compression rig used for this study is shown in Figures 3.1, 3.2 and 3.3.

The rig was manufactured from plain carbon steel due to the good stiffness properties of the material and low price [121]. It must be noted that the rig used for this study was a first iteration, thus cheaper, more versatile plain carbon steel was preferable for this first iteration of the rig [121]. The rig consists of a number of components, which include a loading platform, a guide, a plunger and a locking nut, and was secured into Zwick Universal Testing Machine to conduct the various QS compression tests.
The reason for the use of a cylindrical design was to allow for manufacturing of the rig to be as accurate as possible through the inherent precision achievable when machining on a lathe. As such, all the various components of the rig can be as concentric as possible, despite them being manufactured from different parent pieces of metal. A high tolerance on the rig was achieved, which, in turn, prevents any undesirable motion other than the compressive motion of the plunger on the specimen. Additionally, this manufacturing

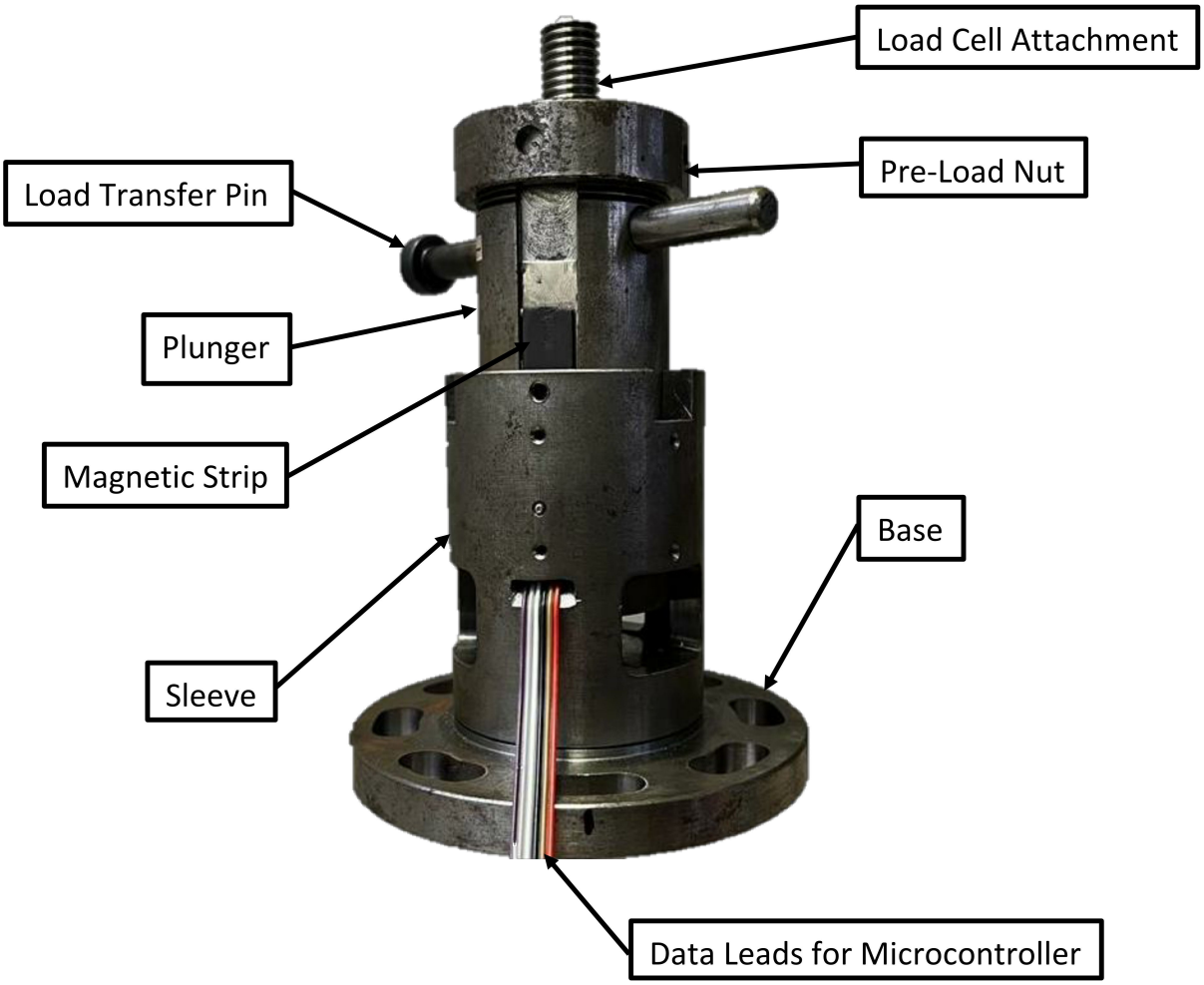

Figure 3.1 Side-on view of the custom quasi-static compression rig.

method ensures that the compression surfaces of the specimen are as parallel as possible during operation.

An important aspect of this rig is the lock nut, which is used to avoid backlash due to the load transfer pin. This is achieved via the use of two threads, each with an opposite thread direction, and a tensioning pin. The upper thread of the lock nut, which attaches to the load cell, is a right-hand thread, while the lower thread, which attaches to the plunger, is a left-hand thread. A hole through the load cell attachment and the plunger was machined to hold the tensioning pin, which is used to facilitate load transfer. However, in order to minimize compliance of this connection point between the load cell and the plunger, the tensioning pin needed to be pre-tensioned, and that is the function of the two threads. The upper thread pulled the load cell attachment towards the plunger and the lower thread pulled the plunger towards the load cell attachment. The pin went through both of these two components, and as a result, load was transferred directly through the load cell attachment, then through the pin and directly into the plunger. This ensures that no

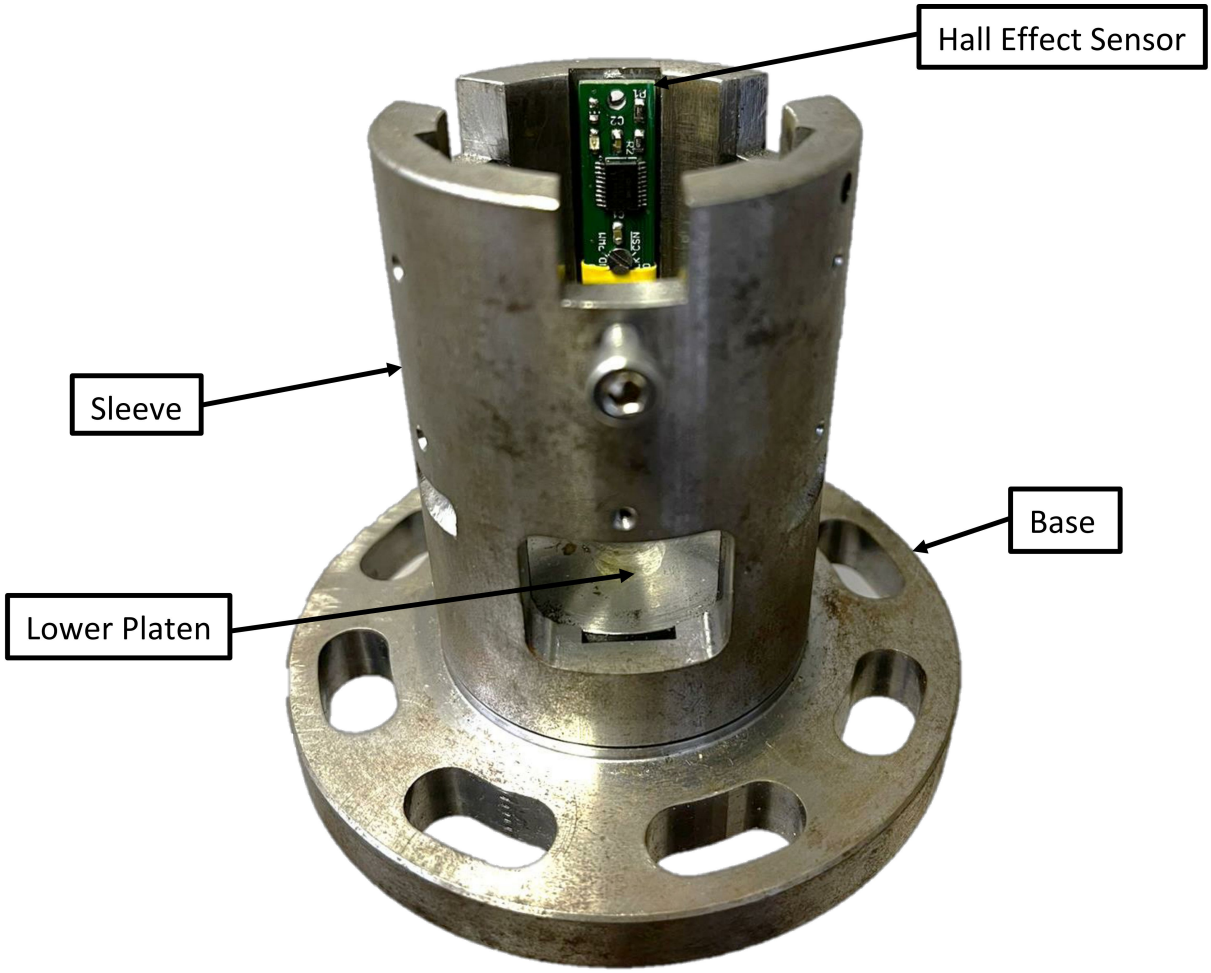

Figure 3.2 The Hall effect sensor of the subpress secured a recessed slot of the sleeve-base assembly.

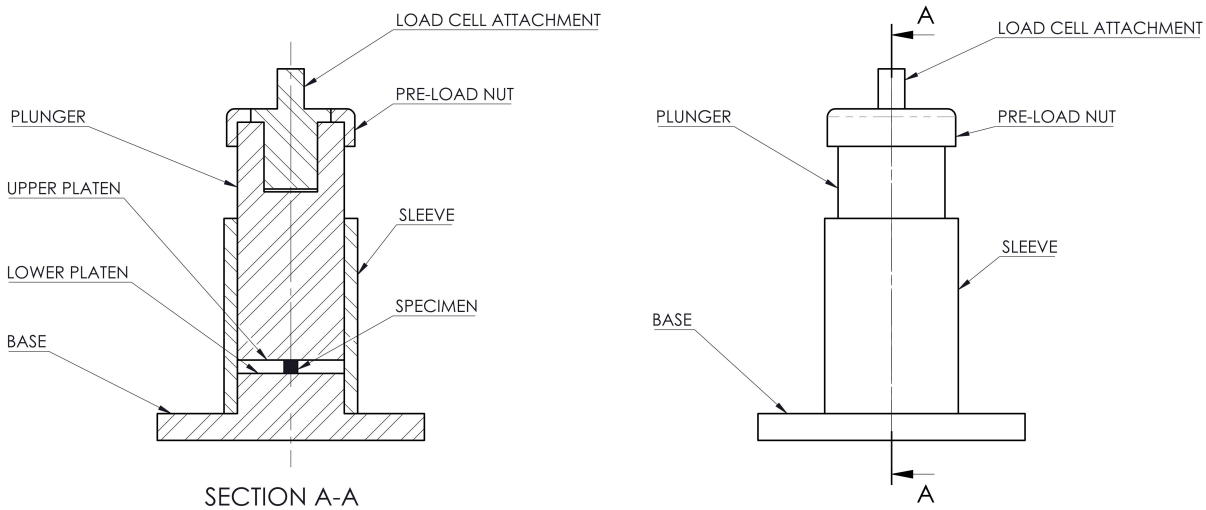

Figure 3.3 A simplified schematic and cross-section of the custom rig with a specimen in the testing location.

load is transferred through the threads, where possible compliance issues could occur.
The displacement is measured using a combination of three AMS AS5311 Hall effect sensors secured to the stationary sleeve and three Bogen MS10-300 Magnetic Multipole Strips with 2 mm pole-to-pole distances, which are secured to the plunger. The Hall effect sensors provide a 12-bit digitization, which results in a displacement resolution of 0.488 μm when paired with the chosen magnetic strips. The signal from the Hall effect sensors is captured using a Pro Micro ATMEGA32U4 microcontroller. The three sensors are secured equidistant around the inner circumference of the sleeve. This allows for non-axial motion to be picked up by the different displacement readings from the sensors and this can be accounted for by averaging the three data streams. In addition to accounting for any non-axial motion using the sensors, the plunger and sleeve were machined with a tight sliding fit tolerance.
The Zwick software captured the force data, which was retrieved via the use of a 10 kN load cell. This meant that the displacement data from the rig and the force data from the Zwick needed to be synchronized before any analysis could be done. This process is dealt with in Section 4.4.2.

3.1.1 Calibration

The base plate was removed and the sleeve of the rig was secured into a custom mount such that all motion was restricted. A Mitutoyo depth micrometer, which is rated to be accurate to 10 μm, was secured to the bottom face of the sleeve and its motion was also restricted. Finally, the plunger was inserted into the sleeve and pushed to bottom dead centre of the sleeve, so it was flush with the depth micrometer. The micrometer was manually incremented by 10 μm at a time over a total distance of 100 μm. Between each step a period of time was allowed to pass to allow for distinct plateaus in the displacement-time data to be recorded. This process was repeated a number of times to ensure consistency and repeatability in results. Figure 3.4 is a typical example of the results from one of these tests.

The rig was able to clearly measure distinct step in the displacement, with averaged difference between the recorded displacements and the expected displacements being 0.087 μm, with a standard deviation of 0.746 μm, across all of the tests. In addition to the overall displacement, Figure 3.4 also shows the noise superimposed on the signal. The inset highlights this noise on a plateau, with all of the noise being present within a 1 μm envelope and all data being distributed amongst five distinct bands. The inset in Figure 3.4 shows 200 data points with an overall skewness of -0.04602, which implies that the noise has a random, normal distribution [122]. The central band contains the

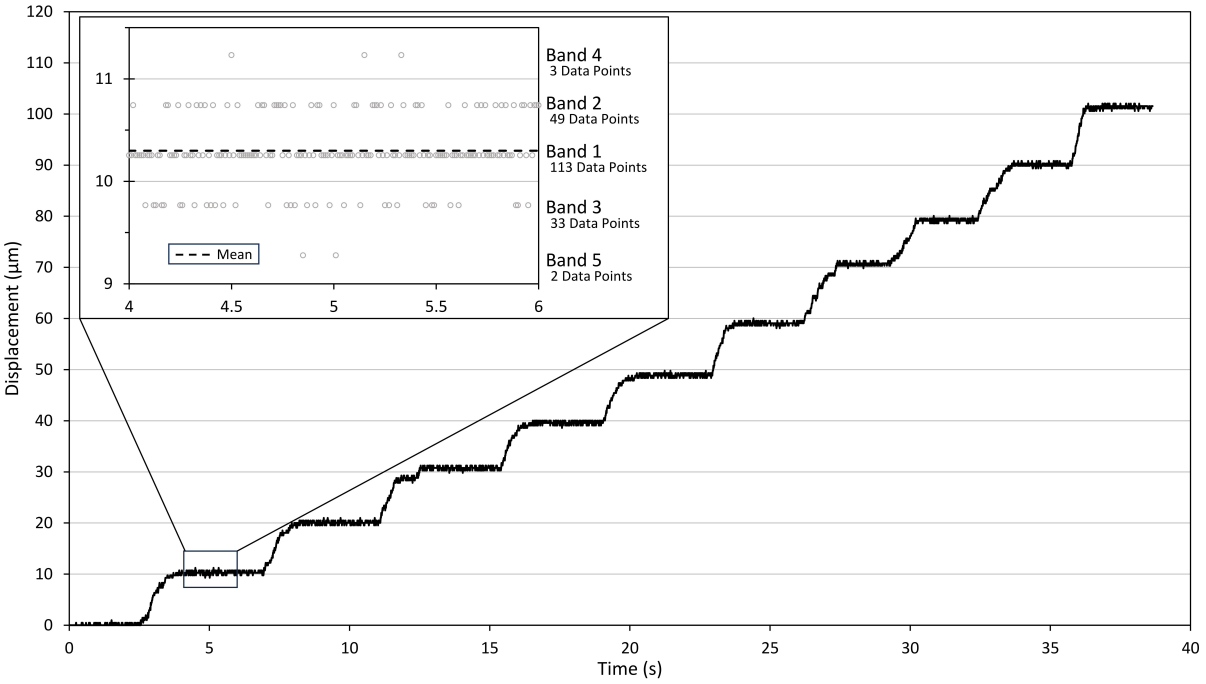

Figure 3.4 Graph showing calibration stepping.

vast majority of the data points (113 points), with the adjacent bands containing less (49 and 33 points) and the outermost bands containing the least (3 and 2 points). Based on this data, it is a reasonable assumption to make that the true position of the plunger lies approximately on the displacement of the central band, with a slight offset to the adjacent band with the most data points. As a result, provided the sample rate is high enough, the moving average of the signal would provided greater accuracy that the resolution of the sensor-strip combination would suggest. This is a similar logic to that behind the concept of 'dithering' in image processing, where sub-pixel accuracy is achieved by utilising the noise in the image [123–125].

3.1.2 Statistical Analysis of Current Apparatus

A series of tests were conducted on polymethyl methacrylate (PMMA) specimens in order to compare the accuracy of the Hall effect sensors in the custom rig to the integrated displacement measurement system of the Zwick, as well as an Allied Vision MG-505B visual extensometer (VE). A loading sequence was used where the specimen was simply compressed until a 6000 N load was measured by the load cell at a strain rate of 0.01 s^{-1}. Data acquisition rates for both the crosshead displacement and the rig displacement was set to 100 Hz. All three systems could not be compared simultaneously as the proprietary software of the Zwick does not allow for displacement to be recorded by the integrated displacement measurement device and the VE at the

same simultaneously.

There do not appear to be any standards outlined for the compressive testing of bone specimens. The most applicable standards that could be applied to these types of tests would be those used for the compressive testing of rigid plastics, for example the ASTM D695 [126] or the ISO D604 [127] standards. However, even these standards are not ideal for the ultimate use case of this subpress, due to the required specimen geometries in these standards being extremely difficult to meet with such a unique material, in the form of cortical bone. These standards require cylindrical specimens of 50.8 mm in height and 12.7 mm in diameter for tests intended to determine elastic modulus [126]. It would be extremely difficult to maintain this 4:1 aspect ratio for cortical bone specimens with a reasonable diameter due to the inconsistent cross-section of the cortical bone region of the donor bone. Furthermore, if only one donor bone is used to manufacture specimens for a test, producing a statistically significant sample size of specimens with this aspect ratio will be impractical. As a result, it is more likely to find cortical bone specimens with height-diameter ratios closer to 1:1 in the literature. Lee *et al.* [72], McElhaney [1] and Rampersadh *et al.* [128] all tested cortical bone specimens, with a maximum aspect ratio of 2:1. This low aspect ratio is reported as desirable by Zhao *et al.* [65], who state that a specimen with an aspect ratio of 1:1 avoids buckling during compression tests and therefore maintains axial load application. Furthermore, due to the viscoelastic dependency of cortical bone, these tests are intended to compliment a series of dynamic tests, wherein this 1:1 specimen aspect ratio is not only desirable, but necessary [16].

For these reasons, the proposed 5 mm by 5 mm cylindrical specimens were deemed appropriate for the bone specimens. However, for the initial commissioning of the subpress, PMMA specimens were manufactured with a 5 mm height and a 8 mm diameter. The barrelling and friction effects of the unique PMMA specimen geometry were not of concern for these tests as the purpose was not to evaluate the properties of PMMA. Rather, these tests were strictly used to compare displacement data between the various measurement devices. Tests for anisotropy were conducted and it was found that the material directions from which the specimens were machined had no effect on the recorded material characteristics.

A total of 13 tests were conducted where the internal displacement measurement system for the crosshead of the Zwick was compared to the displacement recorded by the custom rig. Over all of the tests, the rig recorded an average total displacement of 2436 μm with a standard deviation of 61 μm. The crosshead was recorded as having an average total displacement of 3120 μm across all of the tests with a standard deviation

of 73 μm. These results demonstrate that the internal displacement measurements of the Zwick were offset from the magnetic sensor by an average of 684 μm, but the crosshead displacement was nearly as repeatable as the rig. Figure 3.5 summarizes the results from this series of tests.

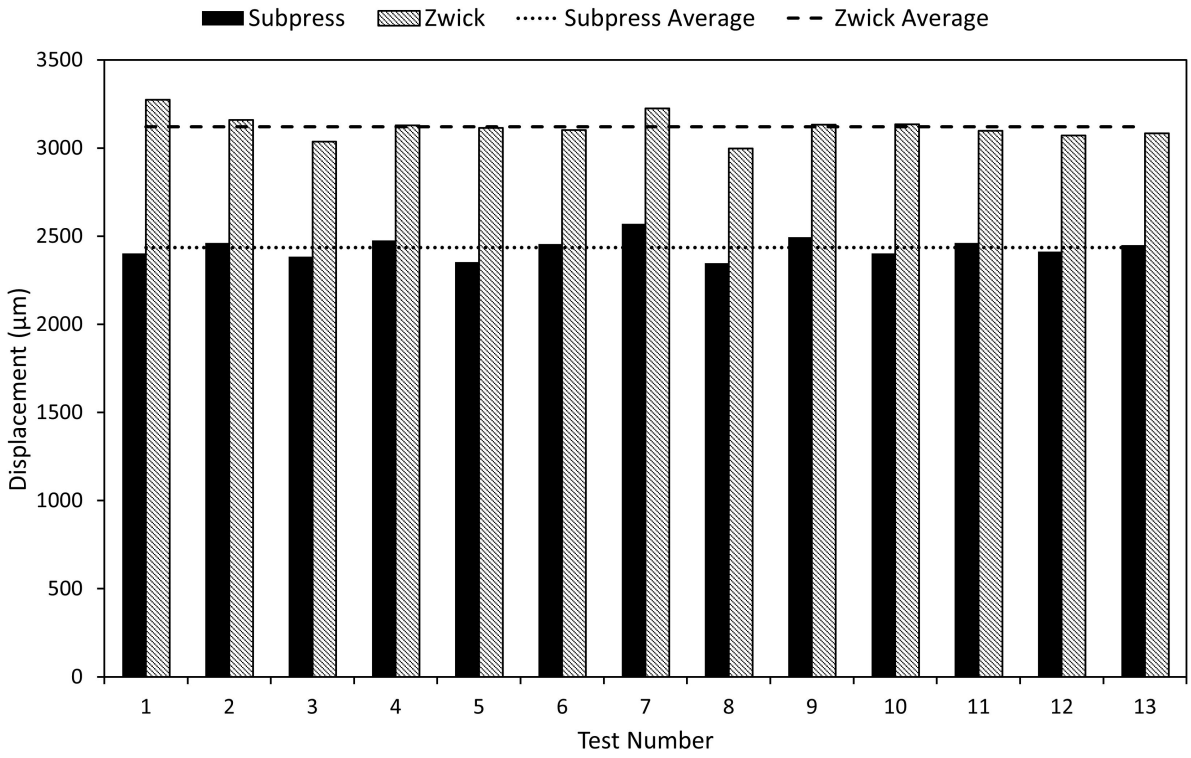

Figure 3.5 Comparison of the custom rig and crosshead displacement measurements for the 13 PMMA specimen tests.

A similar set of four tests were conducted where the displacement recorded by the VE was compared to that of the custom rig. The rig recorded an average total displacement of 2501 μm with a standard deviation of 51 μm. The crosshead was recorded as having an average total displacement of 2582 μm across all of the tests with a standard deviation of 292 μm. With an average difference of 81 μm, these tests suggest that the rig is at least in the same order of accuracy as the VE, but it is more consistent than the VE.

This initial analysis demonstrates that the readily accessible measurement apparatus might not be accurate, nor consistent enough to measure displacements to a micron-level accuracy. Although the Zwick was consistent in its measurements, it was inaccurate when considering even a tenth of a millimetre scale. The visual extensometer is inconsistent, despite it being rated micron-level accuracy, but is more accurate than the Zwick. The custom rig appears to record displacement with the benefit of both of the current systems, and hence was proven to be the best choice for this application.

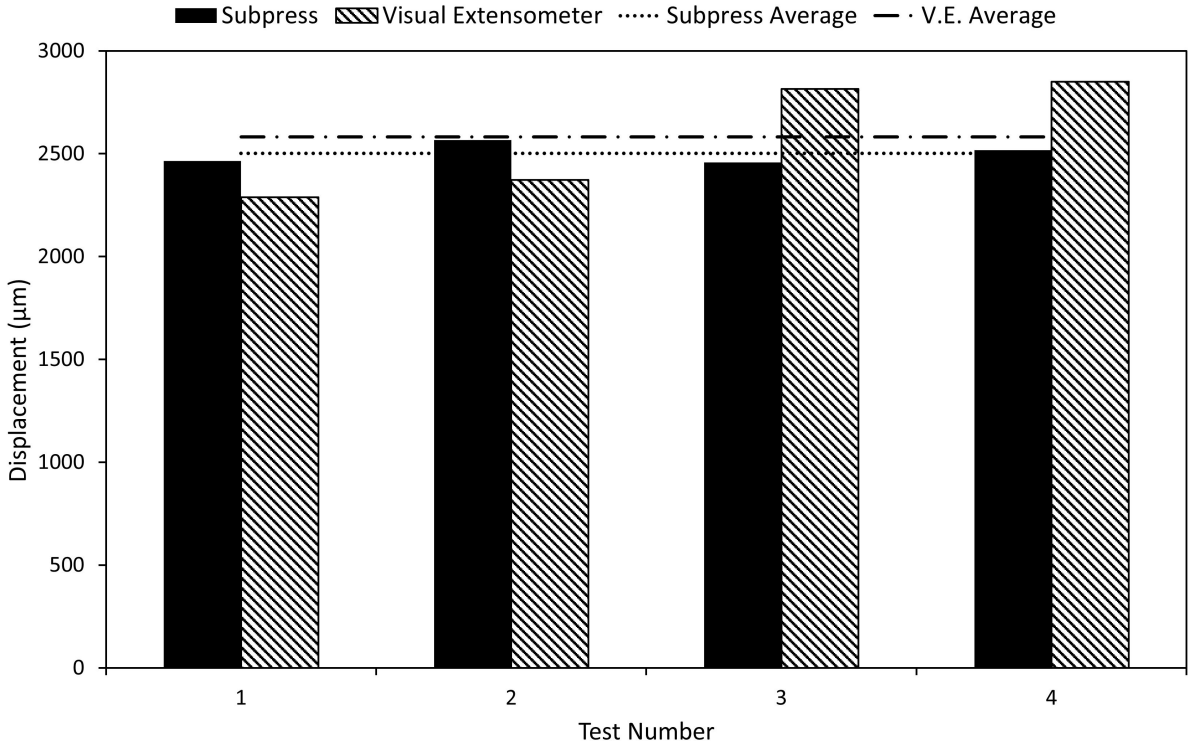

Figure 3.6 Comparison of the custom rig and visual extensometer displacement measurements for the four PMMA specimen tests.

In addition to these benefits of the custom rig over the currently available displacement measurement devices, it was noted that the rig could be used to observe and quantify the compliance of the Zwick. Upon impact of the specimen with the plunger, the Zwick software recorded a continuous, linear displacement as the programmed crosshead speed, which was determined by the desired strain rate of the specimens. However, the rig clearly records the compliance of the Zwick upon specimen impact, as shown by the deviation of the Magnetic Sensor Data in Figure 3.7.

Figure 3.7 clearly demonstrates that the rig and integrated displacement measurement system of the Zwick agree under a no-load condition, while under load (i.e. when the plunger makes contact with the specimen) the Zwick software cannot account for its own inherent compliance. When considering that the expected total specimen deformation will be within 1 mm, not being able to account for such a significant compliance factor will have detrimental effects on the results.

The use of digital image correlation could achieve the desired accuracy for this case, however it is unclear if a speckle pattern could be applied to the hydrated specimens in a timeframe where the effects of drying out would not negatively skew the results. An alternative would be to speckle the rig itself, but, as proven by the results in Figure 3.6,

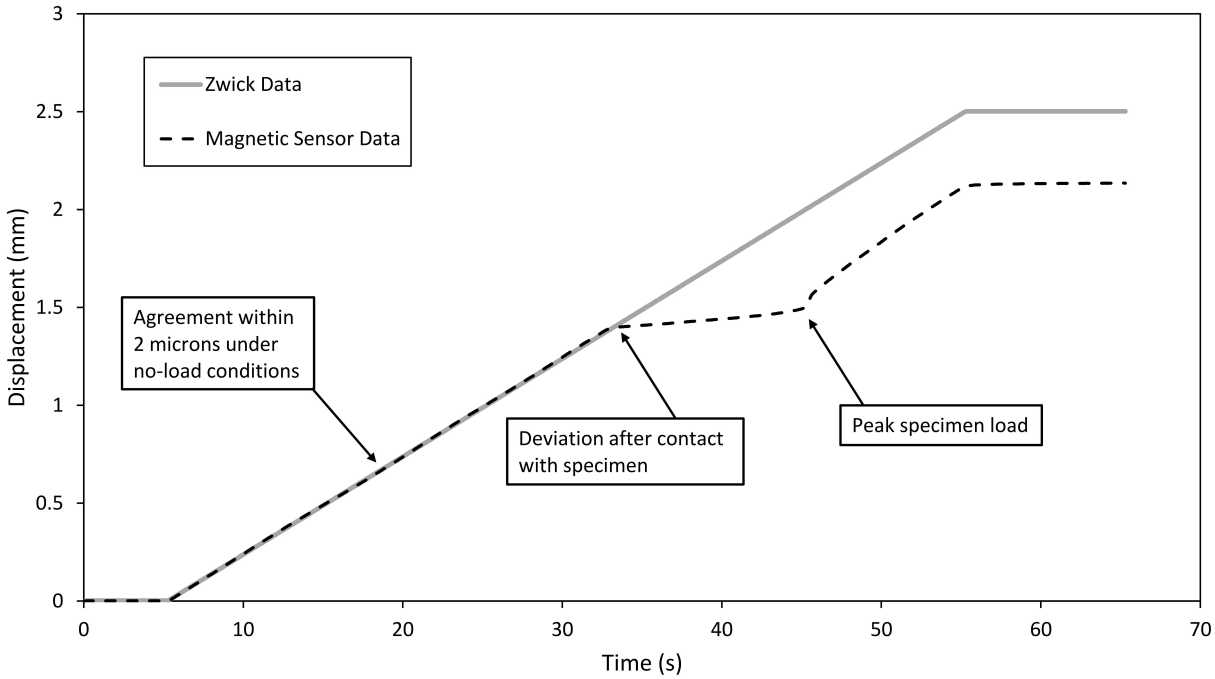

Figure 3.7 Typical comparison of the rig and crosshead displacement vs time data.

it would provide near identical results to the custom rig with a significant increase in cost due to the extra equipment, software and processing time.

The subpress has been designed with the intention of characterizing materials with relatively low elastic moduli, while reducing machine compliance to near-negligible levels. However, a combination of the small specimen geometry and a material much stiffer than the PMMA and bone tested in this study could result in a specimen stiffness in the same order of the local deformation of the plunger and lower platen of the subpress. In this case, more significant local deformation would be expected on the surface of the plunger and lower platen, as well as global deformation of the plunger, between the specimen interface and the point on the plunger where the magnetic sensor is reading displacement.

Modifications could be made to the subpress to better account for these anticipated compliance effects. For example, the subpress could be manufactured from a material stiffer than mild steel, such as tungsten, or inserts of stiffer materials can be integrated into the design of the subpress at the specimen interfaces. However, even with these modifications, the deformations as a result of the compliance could be reduced, but not removed entirely. Nevertheless, these compliance deformations are minimal, typically on the order of less than 10 microns, and can be accounted for theoretically should a stiffer material need to be tested using this subpress. For the cases stated in this study, the

compliance as a result of local and global deformations did not emerge as a primary point of consideration.

This calibration and commissioning process has been elaborated on in a paper by Daras *et al.* [129], which has been referenced in Appendix A.

3.2 Quasi-Static Bending

The QS bending experiments were conducted on a three-point bending setup, in an Instron Universal Testing Machine. A set of custom attachments were used to generate this bending configuration with the two-pronged attachment on the fixed, bottom platform of the Instron, and the single-pronged attachment on the moving, upper cross-head of the Instron. The attachments were designed to allow for testing of small beam specimens with a minimum supportable length of 30 mm, although a larger attachment was also manufactured. The reason for choosing this smaller of the two attachments was due to the fact that machining larger beam specimens would not be possible as a result of the irregular cross-section of the whole donor bones. These attachments were manufactured from stainless steel, due to the rust-resistance of the material, as well as its relative high stiffness and easy availability.

The three-point bending configuration was utilised in this study in an effort to induce tensile failure. In order to more wholistically define the mechanical properties of cortical bone, both compressive and tensile failures were tested. Due to the inherently weaker tensile properties of cortical bone, as outlined in Section 2.2.1, it was reasonable to assume that the three-point bending configuration would result in the desired tensile failure.

The stiffness of the Instron was calculated in order to determine what portion of the recorded displacement was as a result of the compliance of the system and what portion was from the specimen. This stiffness was calculated using spring theory where a widened beam specimen would act as two springs in parallel and regular, square cross-sectioned beam specimens would act as single springs. The widened specimens featured a 8 mm by 4 mm cross-section and 40 mm lengths, while the regular beam specimens featured a 4 mm by 4 mm cross-section and which were also 40 mm in length. These widened specimens would with the longer cross-sectional axis lying perpendicular to the axis of motion of the Instron, and therefore these specimens would have a stiffness double that of the regular specimens.

Considering the total displacements from each test:

$$\delta_1 = \delta_{instron} + \delta_{spec1} = F_1 \left(\frac{1}{k_{instron}} + \frac{1}{k_{spec}} \right) \tag{3.1}$$

$$\delta_2 = \delta_{instron} + \delta_{spec2} = F_2 \left(\frac{1}{k_{instron}} + \frac{1}{2k_{spec}} \right) \tag{3.2}$$

Making the stiffness of the specimen the subject of the formula:

$$k_{spec} = \left(\frac{\delta_1}{F_1} - \frac{1}{k_{instron}} \right)^{-1} \tag{3.3}$$

$$k_{spec} = \left(\frac{2\delta_2}{F_2} - \frac{2}{k_{instron}} \right)^{-1} \tag{3.4}$$

Then using the simultaneous equations and solving for $k_{instron}$, one will obtain:

$$k_{instron} = -\frac{1}{\frac{\delta_1}{F_1} - 2\frac{\delta_2}{F_2}} = -\frac{1}{\frac{1}{k_{single}} - 2\frac{1}{k_{double}}} \tag{3.5}$$

This process was conducted on PMMA specimens, and it was concluded that the Instron setup was approximately 60 times stiffer than the single specimens. Despite this significant stiffness difference between the specimens and the Instron system, the compliance of the system was still taken into account for each test.

3.3 Dynamic Compression

The dynamic compression experiments were conducted using a traditional compression SHB setup. The bars were manufactured from maraging steel bars with a 3/4 inch (19.5 mm) diameter, and were cut to 3 m and 2 m lengths for the incident and output bars, respectively. The choice in material was based on the superior strength properties of the steel, as well as resistance to rust.

Prior to conducting any tests using these bars, a calibration process needed to be conducted. This involved first calibrating the incident bar, then calibrating the output bar. The striker used to conduct these calibration tests was cut from the same stock as the two bars for the SHB setup, and it was reasonable to assume that the striker has the same diameter and density as the bars. This is important to consider when conducting this calibration process as it ensures that the striker is perfectly impedance matched to the bars, thus the stress waves generated by the striker are fully transferred to the bars.

To conduct this calibration process, the incident bar was aligned and set-up with a stopper at the specimen end. This stopper generates a fixed boundary condition, and hence the reflected wave in the incident bar will be of the same magnitude, but will be of the opposite orientation. Thus, the compressive input stress wave would reflect off the fixed boundary condition as a tensile stress wave. This process did not require the use of any pulse shaping, and this decision was made in order to generate a steeply rising stress wave in the bar. This would, in turn, allow for a clear voltage value to be interpreted from the clear plateau in the signal data.

The time between the SG recording the input wave and the reflected wave was determined, and using this along with the distance from the centreline of the strain gauge (SG) to the end of the bar, the speed of sound in the bar was calculated using:

$$c = \frac{2\delta_{SG}}{t} \tag{3.6}$$

Once this value was confirmed to be satisfactorily similar to the theoretical speed of sound in the literature of the bar material, the elastic modulus of the material was calculated using:

$$c = \sqrt{\frac{E}{\rho}} \tag{3.7}$$

This experimental modulus value was then confirmed to be satisfactorily similar to the literature value for the bar material, and finally, an experimental stress value could be determined for the plateaus of the voltage signals, generated by the SG, using the product of the voltage signals and the K-factor, which is determined by:

$$K = \frac{4E}{GF \cdot GA \cdot N \cdot EV} \tag{3.8}$$

where E is the elastic modulus, GF is the gain factor of the SG, GA is the gain amplitude of the amplifier, N is the number of bridges in the Wheatstone bridge for the and EV is the excitation voltage of the power supply. This experimental stress value is compared to the theoretical stress value that should be experienced by the bar, as a result of the impact from the striker. This theoretical stress value is calculated using:

$$\sigma = \frac{\rho c v_{striker}}{2} \tag{3.9}$$

The two stress values should agree if the incident bar is considered to be operating correctly. In the case of the incident maraging steel bar, the error between the theoretical and experimental stress values was 6%, which was deemed to be satisfactory. In order to calibrate the transmission bar, it was aligned with the incident bar, and the stopper was moved to the far end of the transmission bar to generate the fixed boundary condition. Two methods are used in this case to calibrate the transmission bar. The first is the same as the previously mentioned SHB calibration process for the incident bar, while the other uses the difference between input and reflected waves in the incident bar and compares that to the first wave recorded by the SG in the transmission bar. A K-factor is determined in order to scale the output wave to the correct stress, so as to match the stress wave generated by the difference between the input and reflected waves of the incident bar. This approximate K-factor is verified using the K-factor obtain from the first process conducted on the transmission bar, and should they agree, the transmission bar is deemed to be operating correctly.
In the case of the maraging transmission bar, the error between the theoretical and experimental stress values was 4%, and this was deemed to be acceptable.

In order to achieve a constant strain rate during these tests, which is desirable when testing a viscoelastic material, a Cone-in-Tube (CiT) striker was used. The CiT striker, seen in Figure 3.8, has been used previously by Paul in 2014 [103] to induce constant strain rates during the SHB tests on cortical bone specimens.

Figure 3.8 Image of the Cone-in-Tube striker.

The CiT striker consists of a conical striker seated within a constant diameter tube. The intent of this system is to induce a rapid increase in stress on impact with the input bar, thereafter the stress gradually increases with a gradient approximately equal to the elastic modulus of the bone specimens. This can be seen in Figure 3.9.

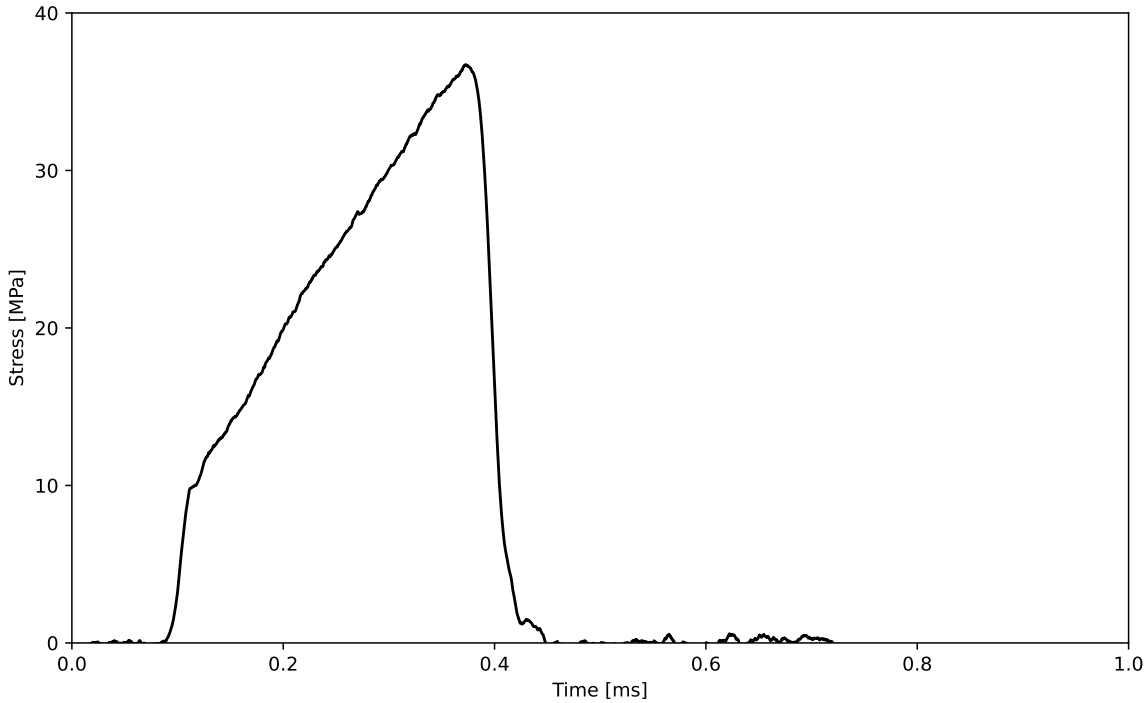

Figure 3.9 Raw output of the SHB test using the CiT striker highlighting the unique loading shape of the CiT striker.

If this gradual rise in stress is the same as the rise in the strain of the specimen, the strain rate will remain constant during the test. The tube interacts with a reaction mass and this impact pull the CiT striker away from the input bar, thus resulting in a sharp truncation of the stress wave. This prevents the possibility of the incident wave overlapping with the reflected wave, which would make analysis difficult, if not impossible. Figure 3.10 shows the CiT system in the SHB setup.

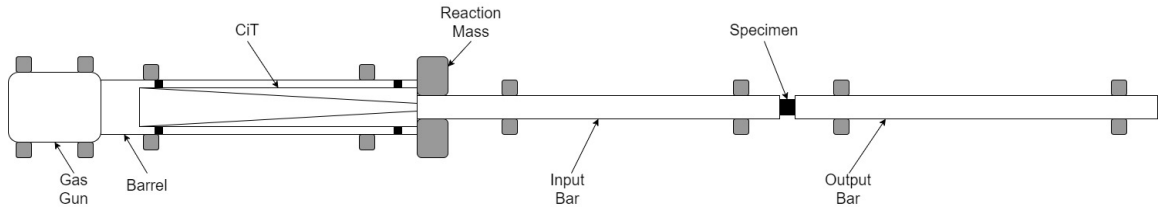

Figure 3.10 Schematic of CiT striker in the compression SHB setup.

3.4 Dynamic Bending

For this study, the concept of a typical compression SHB was altered for bending of the specimens to be tested by using an incident *tube* as opposed to an incident bar. A specimen shaped like a rectangular prism has two points on contact with the incident tube and a third, central point of contact with a transmission bar, and the relative motions between the tube and the bar will induce a bending loading circumstance in the specimen. Bending SHBs have also been developed in order to test four-point bending, however, such configurations were noted as being difficult to accurately set up and aligned. Despite this, four-point setups were noted as reducing time taken for the specimen to achieve a stress-state equilibrium [130]. This stress-state is a requirement for all SHB theory to hold, thus reducing time taken to achieve this state is a desirable advantage of such a configuration [82,130]. The concept of stress-state equilibrium was explored in more detail in Section 2.6.4.

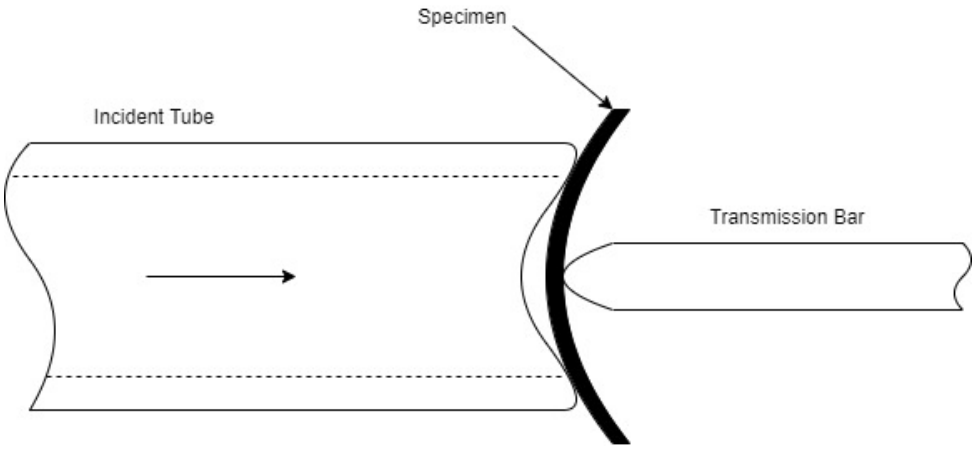

Figure 3.11 Diagram of specimen interaction with the bending split Hopkinson bar for this study.

Another noteworthy aspect of the SHB that will be used in this study is that it will use a load reversal device to ensure that the specimen is not loaded twice, which could result in an undesired loading of the specimen. This device operates due to the principles of stress waves interacting with fixed- and free-end boundaries. At a fixed-end boundary condition, there is no motion, and when a stress wave interacts with such a boundary, a stress wave of the same magnitude and sign (compression or tension) is reflected into the bar. The opposite holds for free-end boundary condition where a stress wave of the same magnitude but opposite sign is reflected. Additionally, in a compressive stress wave, the change in particle velocity of the medium moves in the same direction as the stress wave, while in a tensile stress wave, the particle velocity is in the opposite direction of the stress

wave.

The load reversal device consists of another tube that lies concentrically outside of the incident tube and sits between the barrel of the gas gun and a reaction mass. The cross-section of the outer and incident tubes are impedance matched, thus when the striker impacts the collar on the end of the incident tube, a compressive stress wave of equal magnitude traverses both the incident and outer tubes. However, when the outer tube impacts the reaction mass, due to the effective fixed-end boundary conditions induced here, a *compressive* stress wave reflects back off the reactionary mass, back into the outer tube; thus the particle velocity of the outer tube is also back towards the gas gun. When the compressive, incident stress wave interacts with the specimen, due to the free-end boundary condition induced here, a *tensile* stress wave is reflected from this location, and as a result, the incident tube moves towards the specimen after the initial impact. This would reload the specimen and an undesired failure would occur.

However, the outer tube will dominate the impact and would pull the incident tube, via the collar, away from the specimen. When considering the stress waves traversing the various tubes in this impact event, a compressive stress wave traverses the outer tube after the impact with the striker. The outer tube then impacts the reaction mass, which acts as a fixed boundary, resulting in a reflected compressive stress wave moving back along the outer tube. Remembering that in a compressive stress wave, the particle velocity of the material moves in the same direction as the stress wave, thus, the outer tube moves away from the reaction mass. This will, in turn, pull the incident tube away from the specimen, via the collar, therefore preventing reloading of the specimen. This is the basic function and operation of the load reversal device, but it forms a core aspect of this SHB.

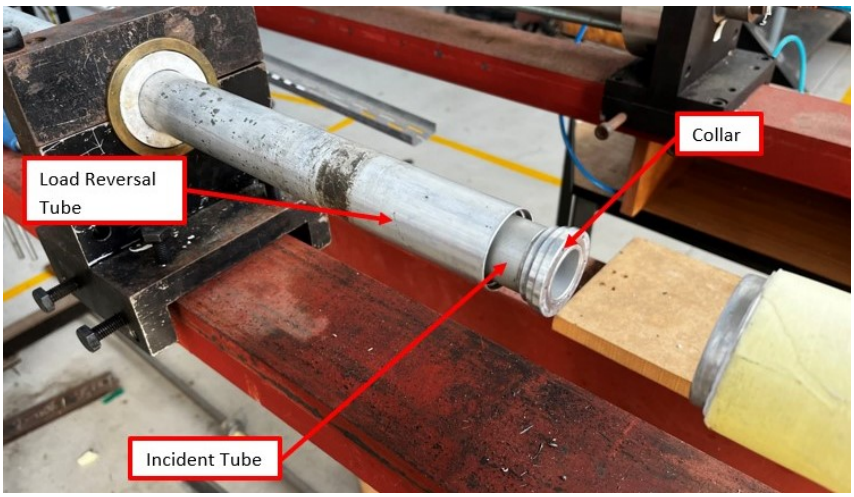

Figure 3.12 Isometric view of load reversal device over incident tube with collar attached.

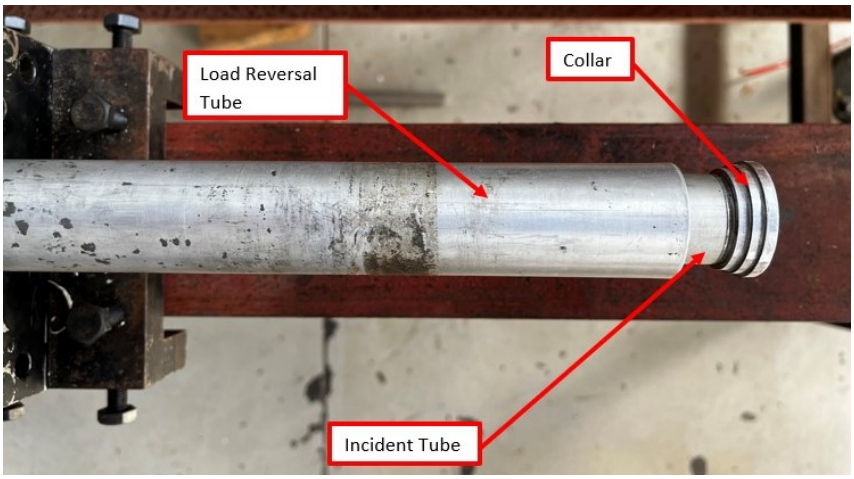

Figure 3.13 Top view of load reversal device over incident tube with collar attached.

The same calibration process was used for this bending SHB as was used for the compression SHB. The incident tube was found to have an error of 3% and the transmission bar had a calculated error of 5%, and these were both deemed to be acceptable.

Chapter 4

Methodology

This chapter will cover the specimen preparation and storage procedures, as well as the methods used to capture the data in both the quasi-static and dynamic strain rate regimes, and it will also include an account on the data processing steps used to refine the data to useful information.

4.1 Specimen Preparation and Storage

This section of this chapter will summarize the means by which the bone specimens were machined and stored. The storage procedure and storage periods are a significant focus of this thesis.

Whole humeri were acquired from *Bill & Riley Meats Co.*[1] and ensured that the bones were obtained from animals from the same farm and from mature bovine cattle (i.e. the cattle were confirmed to be of breeding age but no dental age identification could be conducted as the carcasses were decapitated before the point on bone retrieval). Humeri were chosen for this study since they are generally robust, which was desirable to obtain a large number of specimens from a single donor bone. This reduced the need to use more donor bones than the four used in this study, as that would introduce further variability to consider between specimens. This minimizes the chances that the animals were subjected to different environments and diets which has been shown to have impact on the measured properties of the bones, as discussed in Section 2.4.

The carcasses were obtained from *AH Meat Abattoirs*[1], however, for legal and health reasons, the carcasses were not allowed to leave the slaughter site on the day of slaughter. The carcasses were refrigerated from slaughter until delivery to ensure that

[1]Permission obtained to identify source.

harmful bacteria were killed before any meat was removed from the bone. The carcasses were transported to *Bill & Riley Meats Co.* early the next morning. Any significant soft tissue was removed from the bones on-site before collection, and the bones were transferred to the UCT campus for machining in a cooled, insulated container that same morning.
Upon arrival at the machining site, any remaining soft tissue was removed from each of the whole donor bones and the epiphyses were removed using a band saw. The whole donor bones were stored in a saline solution (0.9% sodium content), in a fridge until machining commenced. No buffer was incorporated into the storage solution as it has been reported by Thorat *et al.* [131] that the freezing of the commonly used phosphate buffered saline results in a 'pronounced pH shift' which could cause potential instabilities for biologics.

4.1.1 Machining

The cylindrical specimens were machined to a nominal height of 5 mm and diameter of 5 mm, while the bending specimens were intended to have a height and width of 4 mm and a length of 40 mm.

The epiphyses of the whole bones were removed with the use of a band saw and were then sliced, also using the band saw into three sections, after which the marrow was simply pushed out of the sections.

(a) Images of whole bone after epiphysis removal and prior to final cleaning.

(b) Images of bone sections with dislodged bone marrow.

Figure 4.1 Images of initial machining steps for whole bone.

From here the sections were cut into four sectors, which were machined into slices that could fit into a lathe, in the case of the compression specimens, and into a mill, in the case of the bending specimens.

(a) Images of bone section divided into sectors.

(b) Images of slices removed from bone sectors.

Figure 4.2 Images of final machining steps for whole bone.

The slices were machined into cylinders using the lathe, which were in turn cut along their length, using the lathe, into as many specimens as possible. Specimens were then visually inspected for surface damage and from there were stored with respect to their designated storage protocols.

(a) Images of slice in lathe prior to final shaping.

(b) Images of cylinder of bone in lathe at final dimensions.

Figure 4.3 Images of final machining steps for bone specimens.

A similar process was conducted for the bending specimens, however these specimens were secured into a vice on the mill, and were machined to the desired dimensions. Upon completion of the machining, the specimens were inspected for any obvious damage and placed into the saline solution.

The specimens tested in this study did not adhere to standards developed for the characterization of elastic moduli of materials, such as ISO604 [127] and ASTM D695 [126]. The specimens in these standards designed to measure elastic modulus have an aspect ratio of 4:1 with relation to the height and diameter respectively. Bone specimens with such aspect ratios, particularly if the specimens are to have acceptable diameters, are difficult to produce in large numbers from a single donor bone due to the inconsistent cross-section of the cortical region. Therefore, in an effort to obtain a significant number of specimens from a single donor bone with reasonable dimensions, as well as ensuring a significant population of specimens, the proposed standard aspect ratios could not be adhered to for the specimens of this study. This decision is supported by the extensive review of Zhao *et al.* [65] which states that a specimen with

an aspect ratio of 1:1 avoids buckling during compression tests and therefore maintains axial load application. Furthermore, due to the viscoelastic dependency of cortical bone, these tests are intended to compliment a series of dynamic tests, wherein this 1:1 specimen aspect ratio is not only desirable, but necessary [16]. For these reasons, the proposed 5mm by 5mm cylindrical specimens were deemed appropriate.
The bias in specimens being orientated in the longitudinal direction stems from the fact that machining a statistically significant number of specimens from a single donor bone is already troublesome, let alone attempting to machine a large enough sample size in two orientations. As a result, specimens were only machined in the longitudinal orientation.

4.1.2 Naming Convention

A thorough and comprehensive naming convention was needed to ensure each specimen could be uniquely identified. As such, the naming convention took into account the biological location of the specimen when the specimen was in the bone, the storage and machining process the specimen underwent and the bone from which it was retrieved.
The convention consists of a series of numbers and letters, each representing a respective aspect of the specimen as mentioned above. As a number of whole bones were used for this study, the first parameter identified each bone numerically via a number ranging from one to four and a letter referring to the appendage (Left or right) from where the bone was retrieved. The second parameter designated where along the bone shaft the specimen was retrieved. This consisted of a letter representing the proximal, middle or distal sections of the whole bones. The third parameter designated which sector of the sectioned bone the specimen was machined. Each section was divided into four sectors, similar to a compass and this parameter consisted of two letters which represented the anterior, posterior, medial and lateral halves of the bone section. The fourth parameter was a number, ranging from one to three, which simply represented the number of the specimen which was machined from a particular sector of a bone. The final parameter came from the machining and storage process that the specimen underwent, and this was a two letter parameter which represented the fresh specimens, the frozen and then machined specimens and the machined then frozen specimens.

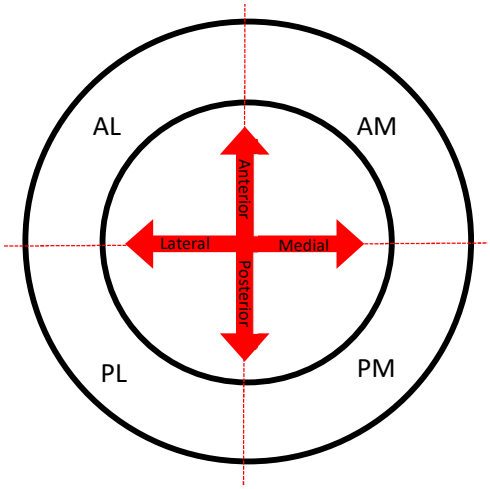

Figure 4.4 Division of bone section into four sectors in a compass-like manner.

Table 4.1 summarizes the various parameters.

Table 4.1 *Table summarizing the naming convention parameters.*

Parameter	Meaning	Definition
1-4	N/A	The number of the whole bone sample.
L, R	Left, Right	Which appendage the bone came from.
P	Proximal	The section along the length of the whole bone.
M	Middle	
D	Distal	
A	Anterior	The sector of the bone section.
P	Posterior	
L	Lateral	
M	Medial	
1-5	N/A	The number of the specimen from a particular region.
MR	Machined-Refrigerated	The machining and storage protocols.
MF	Machined-Frozen	
FMF	Frozen-Machined-Frozen	

An example of the naming convention would be as follows.
A specimen was retrieved from whole bone number two (2), which was a left appendage (L), from the proximal section (P). This specimen was retrieved from the posterior-lateral sector (PL) and was the third specimen from this sector (3). This specimen would be under the 'Machined-Frozen' protocol (MF), which will be explained in Section 4.3. The naming convention of such a specimen would be 2L-P-PL-3-MF.

4.2 Log-Normal Analysis

It was anticipated that the datasets resulting from each testing date would not be normally distributed but rather negatively skewed, and simply calculating the mean of each testing day would not reliably represent this data. The elongated negative tail is to be expected because variations in both bone quality (e.g. canals for blood vessels) and specimen manufacture (e.g. abrasions due to tool wear) are more likely to produce anomalously weak specimens. Conversely, there is no known mechanism by which anomalously strong specimens can be produced, hence the lack of a positive tail. Therefore, for a mean-based analysis to provide a representative result, these anomalously weak specimens would have to be rejected from the data set. However, no objective criteria for data rejection was found in the literature and removing data points from the already limited data sets could reduce the reliability of the modal values. Hence, the three-parameter log-normal approach [132–135] was chosen as it does not require any data rejection but still captures a representative modal value (subsequently referred to as 'Mode').

The benefit of the three-parameter log-normal approach over a mean-based approach is demonstrated in Figure 4.5, which shows a histogram of experimental apparent modulus results. The skewed nature of the data is evident as the mean value does not represent the most frequent modulus value, while the mode captures the most representative value in the data set. The mean value is offset by the longer negative tail of low modulus values.

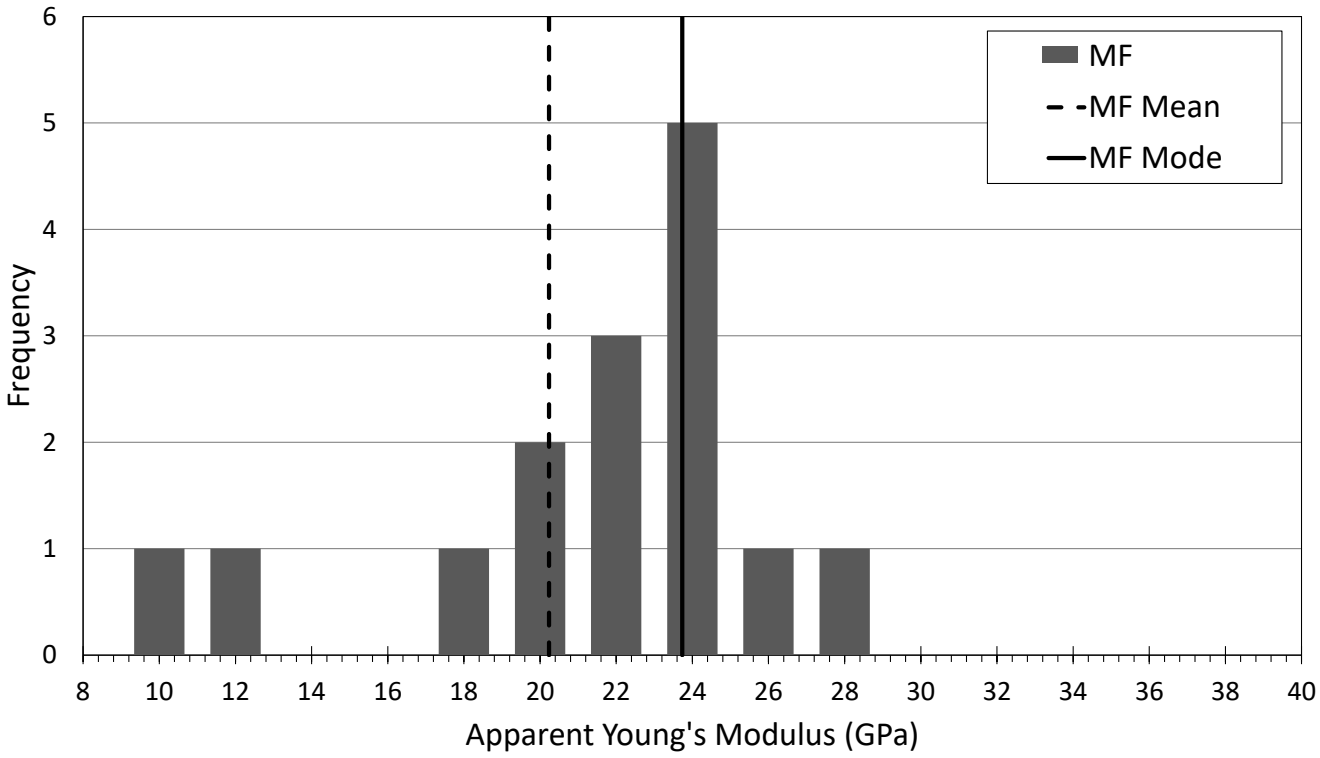

Figure 4.5 Histogram of the apparent elastic moduli measured for the MF specimens during the first week of testing. This highlights the skewness of the data by comparing the mean to the mode, which was obtained using the three-parameter log-normal analysis.

The two low data points shown in Figure 4.5 were obtained from specimens which exhibited a partial trabecular region, which is consistent with the lower elastic moduli. With that said, these two specimens still exhibited a primarily cortical bone structure, and the densities of these two specimens were in-line with the other specimens. In other words, if the presence of a minor trabecular region could not be visually detected, these specimens would have been deemed representative of cortical bone. Hence, Figure 4.5 demonstrates the benefit of the mode-based analysis method over the mean-based method, i.e. the mode-based analysis can account for outliers independent of researcher influence. A mean-based analysis would require a researcher to employ subjective criteria to identify outliers for removal, which will inherently influence the overall results. A mode-based analysis method is presented in detail by Welgemoed [136] and in Appendix B.

4.3 Degradation Study

The aim of this aspect of this research was to identify a period of time, after the bone has been removed from the animal, in which the bone can be considered as fresh, and thus, representative of an in-situ condition. Additionally, this study aimed to identify if altering the storage protocol that the specimens are stored in, after retrieval from the animal, has an impact on the measured mechanical properties of the bone.

The specimens have been split into three main storage protocol groups. The first, making up the majority of the specimens, will be machined on the day of acquisition, or the day after, and then frozen, while a slightly smaller group will be frozen as whole bones, machined after a designated time period of being frozen, and will then be frozen once again after being machined. A final, small group of specimens will be fresh specimens, and tested without being frozen at all.

All the specimens, once machined, were stored in a 0.9% concentrated saline solution and the specimens that were to be frozen were stored at a temperature of $-32°C$. The whole bones were frozen at $-20°C$ in the saline solution, and specimens machined from these bones were also stored in saline for the desired storage time.

As for the fresh specimens (MR), these specimens were stored in a fridge at $4°C$ and tests were conducted on these specimens for one week. This shortened testing timeline for the MR specimens was proposed as such a time period would not allow for significant decay of the specimens.

Tests occurred at regular, eight-week intervals over the span of twelve months, with more frequent tests in the first four-week period. Three tests were conducted in the first week, with a total of seven tests occurring in the first eight-week period and a total of 12 testing days occurring across the entire study. The reason for biasing the number of tests in the beginning of the study was to ensure that any rapid degradation of the properties of the bone at the beginning of the storage phase was captured, along with degradation due to more time in storage.

The machined then frozen (MF) specimens were tested across the entire timeline of the study, while the frozen then, machined, then re-frozen (FMF) specimens were tested only from the week-eight. Additionally, the FMF specimens were split into two further groups, namely the FMF (2M) and FMF (11M), where the 2M specimens were machined from a whole donor bone which was frozen fresh and then machined after two months in frozen storage, and the 11M specimens were machined from a whole donor bone which was frozen fresh for 11 months prior to being machined. As for the fresh

specimens, they were tested in all the tests that occurred in the first week.

Table 4.2 outlines the number of specimens tested on each testing date.

Table 4.2 *Specimen distribution across the three storage protocols over the year timeframe.*

Time Frozen	MR	MF	FMF (2M)	FMF (11M)
0 Days	5			
2 Days	5	5		
4 Days	5	5		
1 Week	5	5		
2 Weeks		5		
1 Month		5		
2 Months		5	6	
4 Months		5	6	
6 Months		5	6	
8 Months		6	6	
10 Months			6	
11 Months				5
12 Months			6	
Total	20	46	36	5

4.4 Fresh Quasi-Static Compression

4.4.1 Data Capture

Prior to conducting any tests, each specimen was measured to determine diameter, height and mass. This allows for accurate stresses and strains to be calculated as well as for any data to be correlated to the density of the specimens. These measurements were performed using a vernier caliper, a micrometer and a digital mass scale.
Furthermore, due to the specimens being cut from the same parent cylinder using a lathe, the specimens featured small sprues protruding from the centre of their flat faces. As a result, prior to taking any measurements, or conducting any tests, the sprues were sanded down until the faces of the specimens were flat.
Once the plunger and sleeve were aligned in the loading frame of the Zwick, the crosshead was moved to allow the sleeve to self-aligned with the plunger. This process was repeated until the load cell read zero force, thus ensuring that there was no contact between the plunger and the sleeve, hence not frictional forces between the two components to effect the measured force.
As has been previously stated, the alignment of the two data streams, from the Zwick and the rig respectively, was the greatest issue with the data capture, but this was overcome by the use of a custom loading program on the Zwick. The Zwick software was setup to output time, displacement and force data in the form of a Microsoft Excel spreadsheet, used for data processing.
As for the data capture of the rig, it required significant post-processing before meaningful data could be interpreted. Although the magnetic sensor physically interpreting a magnetic flux, it outputted a digital, 12-bit signal, which was a number ranging from 0 to 4096. As the plunger, with the 2 mm pole-to-pole magnetic strips secured to it, moved down the collar, passed the magnetic sensor, the flux measured by the sensor would change from 0 and climb to 4096 and then go back to zero as a new pole-pair passed the sensor. Thus, this 12-bit signal could be interpreted as a differential displacement, by dividing the 2 mm by 4096.
The rig required three different software packages to fully capture and interpret data; namely the Arduino IDE, CoolTerm and MatLab. The Arduino IDE operated the microcontroller from which data from the sensor was interpreted and generated, and this software worked in tandem with the CoolTerm package, which simply captured the sensor data to a 'comma-separated values' file, or CSV. A MatLab code was used to convert the digital signal into a displacement and allowed for further data analysis.
The review by Zhao *et al.* [65] suggests that the lubrication of bone specimens during

compression is not a standard practice, although three studies were included where lubrication of trabecular bone specimens was reported to reduce the effect of friction. A separate study reported that the presence of an oil boundary between the specimens and the platens results in a significant load signal prior to full contact between the specimen and the loading platens. The authors presume that this refers to the 'take-up' phase of the loading process. Therefore, for the sake of consistency and to avoid an additional experimental variable, no specimen lubrication was used in any of the tests in this paper.

4.4.2 Data Processing

The data processing for the quasi-static tests was split into five major steps, and its primary objective was to align the two data streams. A common datum needed to be found in each case and the time intervals of the two different streams needed to be synchronized. The raw data needed to be compiled together and converted to the respective stress and strains.

The first step dealt with the refinement of the Zwick data, and by first locating the datum point at the initiation of the hold, where the cross-head of the Zwick was held at a constant height for a specific period of time. Excel was used to fit lines to the approach, the hold and the departure of the datum on the displacement-time data. Figure 4.6 shows the line fits used to determine the datum location in time. The two intersections between the hold, and the approach and departure lines, served as the datum points, from which the first would be the sync point between the two data streams and the second datum would prove the time capture of the Zwick was accurate. From this point, the data was reduced to only contain the sections from the datum to the end of the test. The data was interpolated to ensure consistent time steps between data points, so that the two data streams could be synchronized to each individual time step. The reason for this was due to the fact that the Zwick, although set to, did not capture data at consistent time steps, while the rig did.

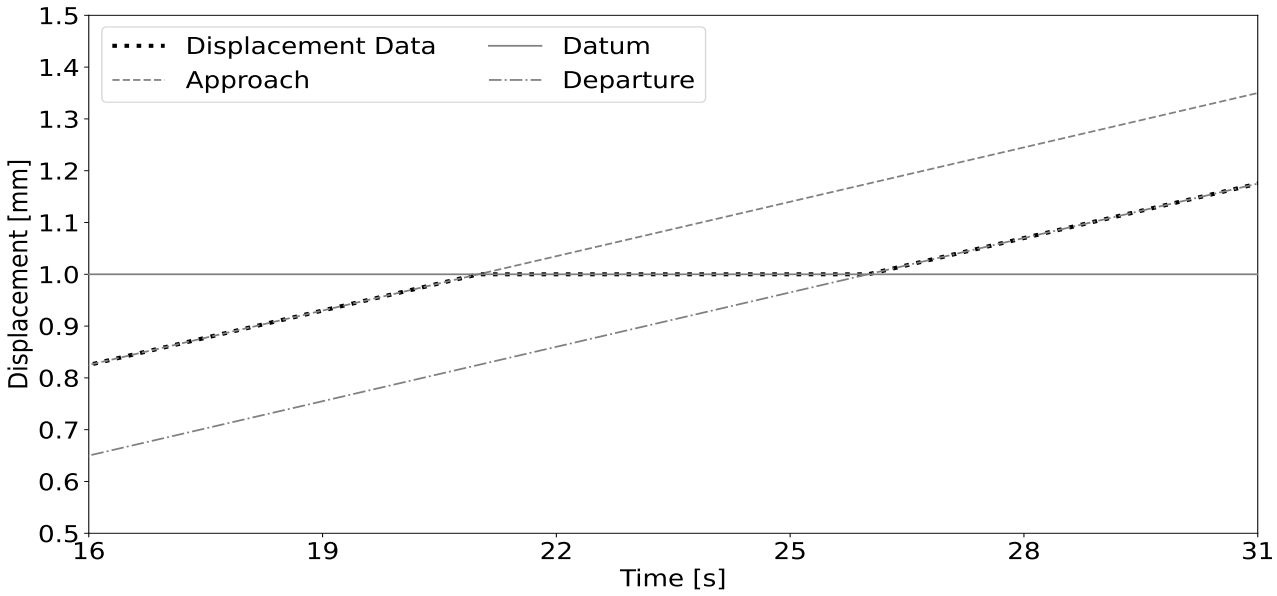

Figure 4.6 Line fits superimposed onto raw Zwick displacement vs time data used to define first datum.

The second step was concerned with the rig data, which generated a significantly larger dataset than the Zwick dataset. The reason for this was that the rig was capturing data every ten milliseconds, in order to have sufficient resolution capture data at the desired rate, while the Zwick was capturing at an average of every 100 milliseconds. Furthermore, due to the rig data capture starting before and ending after the Zwick data capture, this meant that it needed to be reduced at both the beginning and the end of the dataset. Thus, this datum identification needed to be repeated twice in the rig data analysis, and in the same manner as the Zwick data, but the second datum was different as there was no sharp point to definitely define the hold. This datum featured a curved edge, and as such the intersection of the line fits sat slightly off the actual curve, but the principle that was used for the first datum still held in this case. This whole process ensures that the two datasets are now fully synchronized and data is captured from the exact same point in time and ends at the exact same point in time.

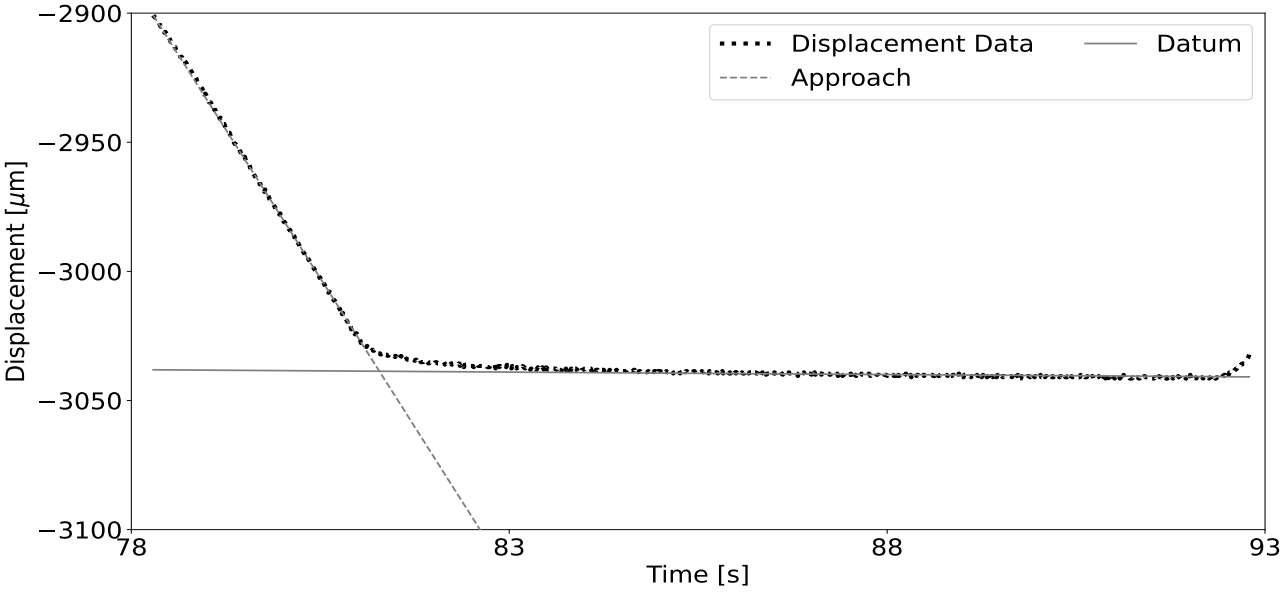

Figure 4.7 Line fits superimposed onto raw rig displacement vs time data used to define second datum.

From this point, the rig data was reduced further by averaging every ten data points to ensure that data was captured every 100 milliseconds. This also further increases the accuracy of the data as the concept of quantization was employed here as a result of the averaging, thus this step served a two-fold benefit [137].

The third step was to combine the two datasets, find the relevant stress and strain values and remove the free running data from before the plunger was in contact with the specimen. A similar line fit concept was used here, as before, to find the point of deviation between the Zwick data and the rig data. Data was reduced from this intersection point and zeroed.

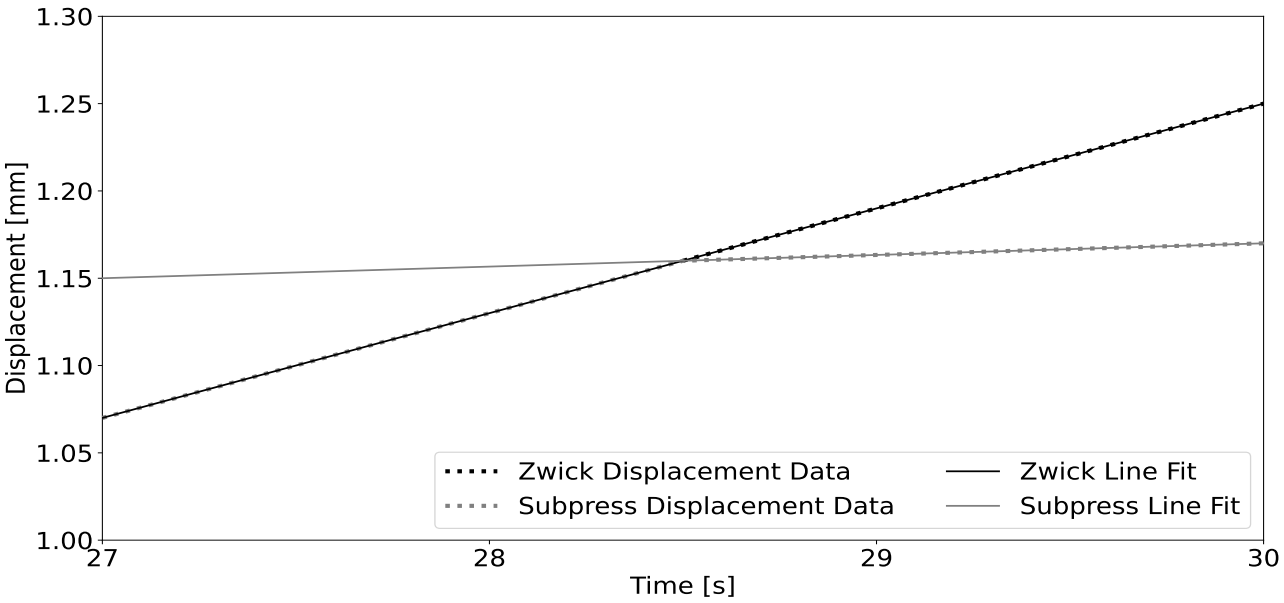

Figure 4.8 Line fits superimposed onto combined displacement vs time data used to define the deviation point.

This intersection of the Zwick data and the rig data further demonstrates the inherent inaccuracies of the integrated displacement measurement system of the Zwick. For the purpose of this study, where small deformations are recorded, the compliance of the Zwick has a significant effect on the measured displacements, and as such, this custom rig was necessary.

The fourth step involved finding the modulus of the specimens, compressive failure and ultimate, stresses and strains. These values were identified by plotting the strain rate and identifying two regions in particular; the first was a flat region, signifying the linear region of the stress-strain curve and the second was a sharply increasing region, which represented the failure of the specimen. Interpreted from this sharply increasing portion of the strain rate data is that the elastic energy built-up in the load train of the Zwick is being released as a result of the specimen failing. Linear line fits are plotted to these two regions of the strain rate plot and the intersection point between the two line fits is where failure initiation occurs. This is the point where the failure stresses and strains were recorded.
The ultimate stress is simply the maximum stress the specimen experienced and the strain at that point is considered as the ultimate compressive strain.

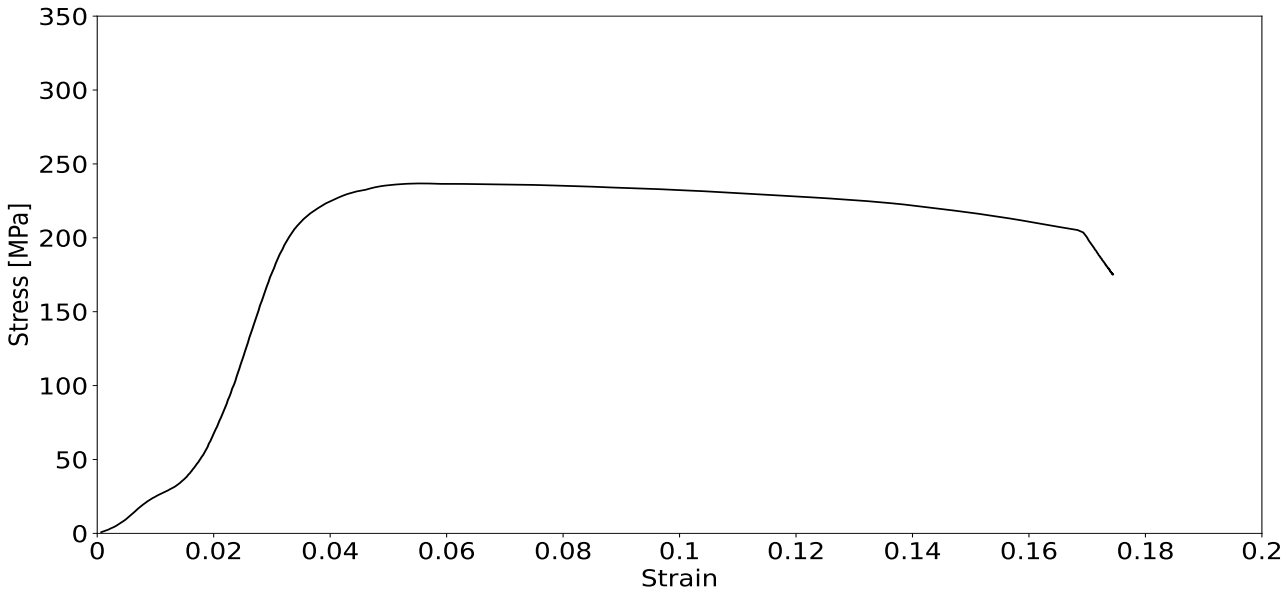

Figure 4.9 Raw stress vs strain curve from the subpress displacement data and the Zwick force data.

In order to identify the elastic modulus, it was decided that a linear line was to be fitted to the portions of the stress-strain curves that coincided with the flat portion of the strain rate data. Using a similar linear line fit technique to what was previously done to determine the failure initiation point, the true linear region was found and that was the region from which the modulus was recorded.

All of this was accomplished by observing the strain rate measured by the rig. It was found that a linear region of the strain rate coincided with the elastic region of the bone specimens with respect to time. Prior to this linear region, a decrease in the strain rate was observed and after this linear region, a sharp increase in the strain rate was observed, and this represented the failure of the specimen. Thus, using linear plots of these regions on the strain rate plot, their intersections would represent the elastic region, as well as the point of failure.

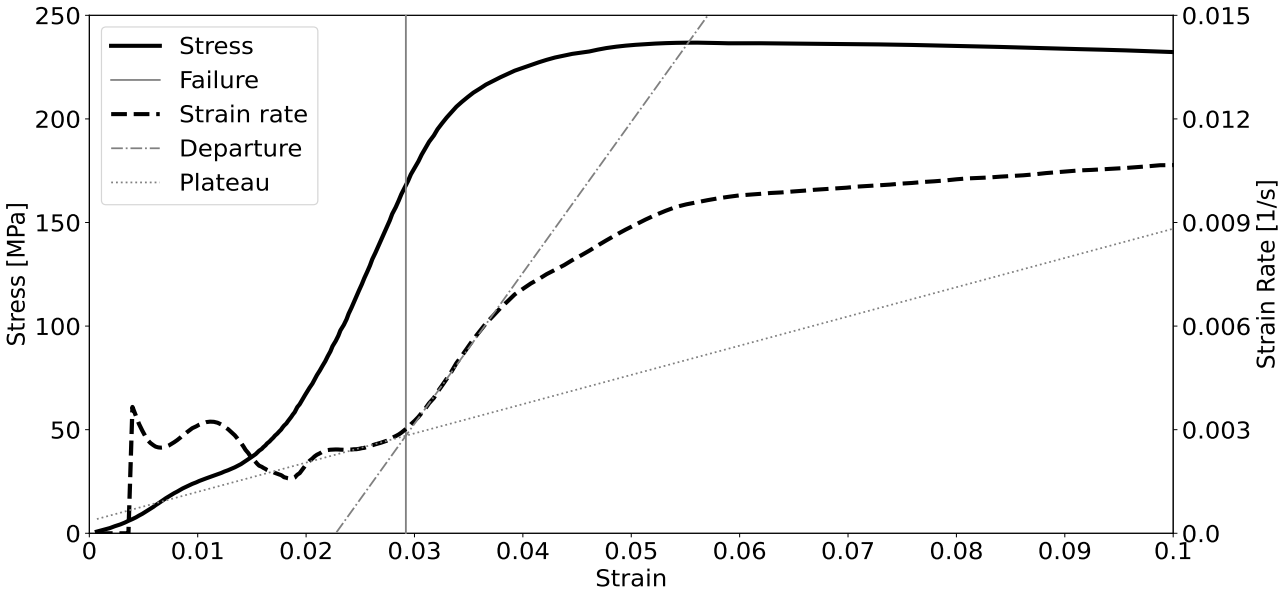

Figure 4.10 Line fits superimposed onto stress-strain curve used to determine the true modulus of the specimen.

A linear line was fitted to the stress-strain curve, using the aforementioned modulus, and the stress-strain curve was spliced with the linear fit to obtain the final, quoted stress-strain curves.

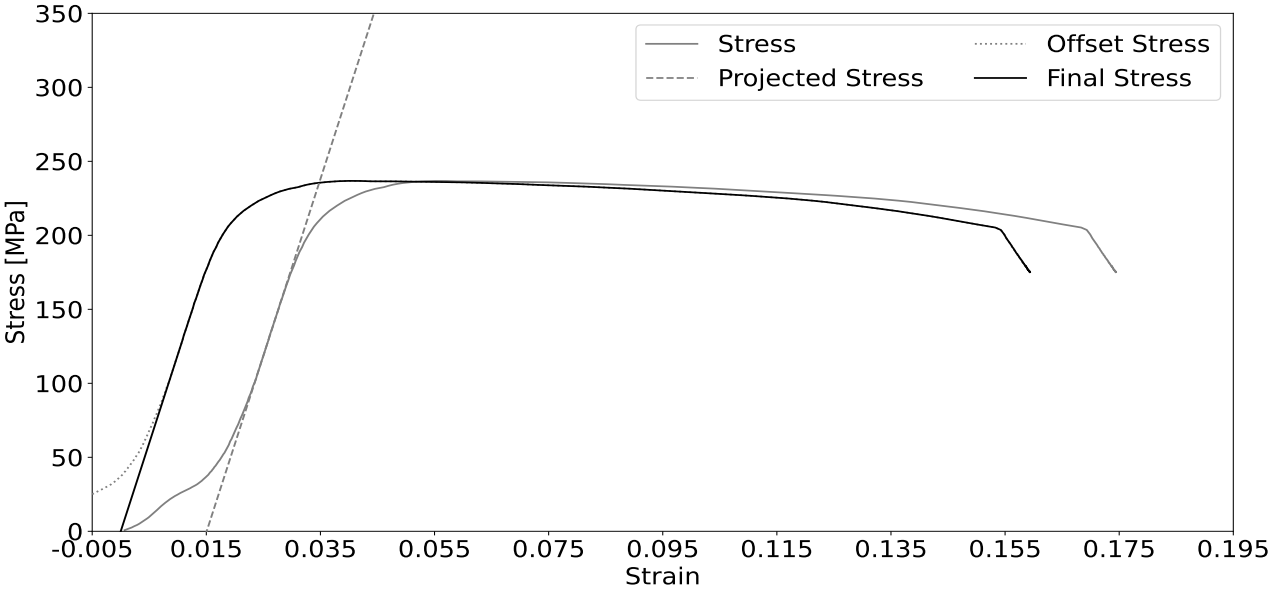

Figure 4.11 Linear line fit superimposed onto measured stress-strain data.

The final stress-strain curve would now appear is shown in Figure 4.12.

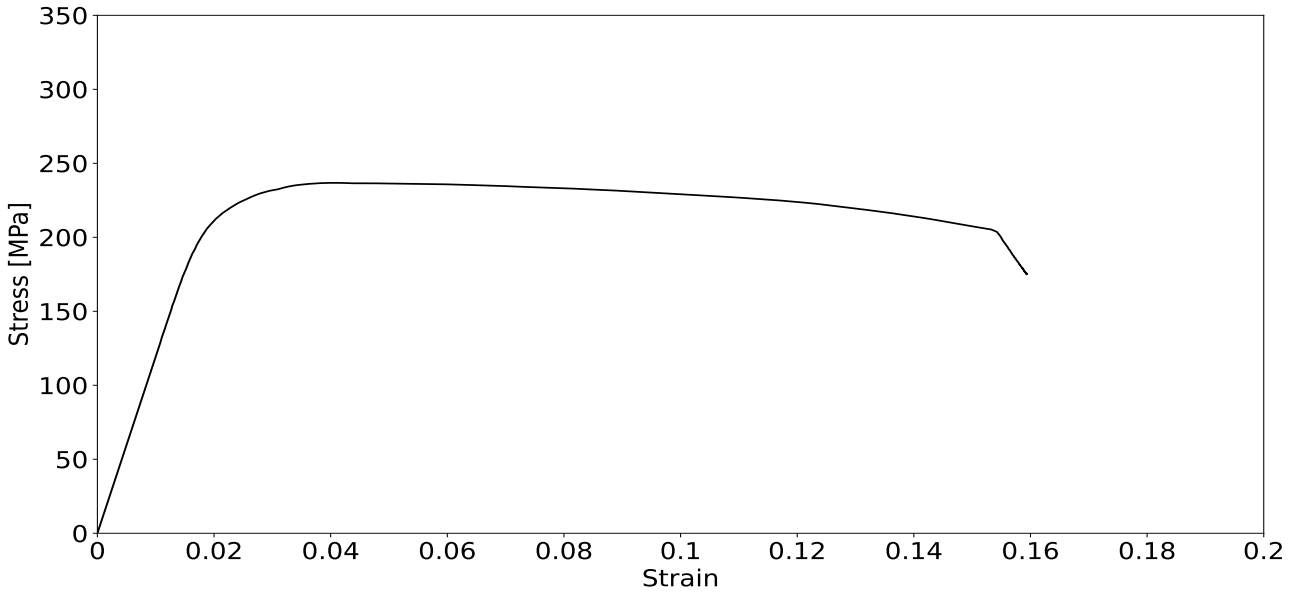

Figure 4.12 Final stress-strain curve.

4.5 Fresh Quasi-Static Bending

4.5.1 Data Capture

This configuration of tests was conducted using an Instron universal testing machine with no other data capture devices. A loading program was developed that moved the cross-head at a constant velocity, which was derived from the desired strain rate of 0.01 s^{-1}. A displacement and force limit for termination was imposed on the program, as well as a force-decrease limit, which was used to determine if the specimen had fractured. The test variables that were output by the Instron software were the time, force and displacement.

Prior to conducting any tests, each specimen was measured to determine its breadth, height, length and mass. This allows for accurate stresses and strains to be calculated as well as for any data to be correlated to the density. These measurements were done using a vernier caliper, a micrometer and a digital mass scale.

4.5.2 Data Processing

In order to account for the compliance of the machine, the Instron and the specimen were treated as two springs in series. The stiffness of the specimen was then calculated using:

$$k_{spec} = \left(\frac{1}{k_{test}} - \frac{1}{k_{Inst}} \right)^{-1} \tag{4.1}$$

The stiffness of the Instron was calculated previously using Equation 3.5 in Section 3.2. Having isolated the stiffness of the specimen, simple beam theory was used to process this data. The specimen was modelled as a simply supported beam with a force applied equidistant from the two outer supports. The maximum elastic modulus was calculated using:

$$E = \frac{l^3}{48I} \cdot k_{spec} \tag{4.2}$$

4.6 Dynamic Tests

4.6.1 Data Capture

A similar process was used for the data capture of the two SHB setups. A picoscope was used to record the stress history of the bars as a voltage-time history, while an oscilloscope was used to determine the velocity of the striker. When the electronics were set-up, the gas gun was primed and testing could begin. The picoscope software was set to capture 200 ms of data when a trigger of 1 V was reached in the input bar. This timeframe typically allowed for the incident and reflected waves to be completely capture in the input bar, with the start of the second reflected wave being captured as well. A full transmission wave could also be captured in this time.

Prior to any test, each specimen was measured for its diameter, height and mass, in the case of the compression specimens. The bending specimens were measured for their height, breadth, length and mass. During this process, care was taken to ensure that the specimens were being hydrated as much as possible to prevent drying out. Once the gas gun was fired, the time taken for the striker to break the two beams of the light trap was recorded using the oscilloscope. The picoscope software was checked to ensure that the data that was captured as intended and that all of the desired waves were free of noise and overlap.

4.6.2 Data Processing

A similar process was used here as the one outlined in Section 3.3. The raw voltage-time data was zeroed and shifted in time such that the incident wave coincided with the transmitted. The data was converted to stress-time using the K-factor for the respective bars, then converted to force-time data using the cross-sections of the bars. The force measured in the output bar is the force experienced by the specimen. Finally, the displacement-time data was obtained by converting the stress-time data, using Equation 3.6, to get velocity-time. This was then integrated to obtain the displacement history of the two bars, and the difference of which would be the displacement-time data of the specimen.

Considering the compression tests, having isolated the force-time and displacement-time data for the specimen, force-displacement curves could be converted to stress-strain using the geometry of the specimens. This allowed for the elastic modulus of the

specimen to be calculated. This differed from the bending tests as force-displacement data was then used in to determine the maximum stiffness of the specimen during the test. Simple beam theory was then applied in order to obtain the elastic modulus value of the specimen.

4.7 Cross-Section Tests

The same procurement protocol was used for the donor bones for the cross-section test as was outlined in Section 4.1. Donor bones were taken directly from the butchering facility to be machined. Specimens were machined using a band saw and a set of 'parallels' to ensure that the cutting faces of the specimens were parallel. The epiphyses (the heads of the bone) of the donor bones were removed after which the bone was pressed against the parallel and was cut perpendicular to the axis of the bone. Specimens were cut with a 10 mm thickness, and a total of eight specimens were machined from a single donor bone. The initial plan was to conduct these tests using the compression SHB setup, which was explained in Section 3.3, however, this SHB could not be used for two reasons. The first was that this SHB utilized maraging steel bars, and due to their high stiffness relative to the bone cross-section specimens, the signal measured in the output bar was too small to extract any meaningful data from. Additionally, due to the irregular circumferential surface of the cross-section specimens, the specimens slipped out from between the bars before being loaded. An example for this irregular surface is shown in Figure 4.13.

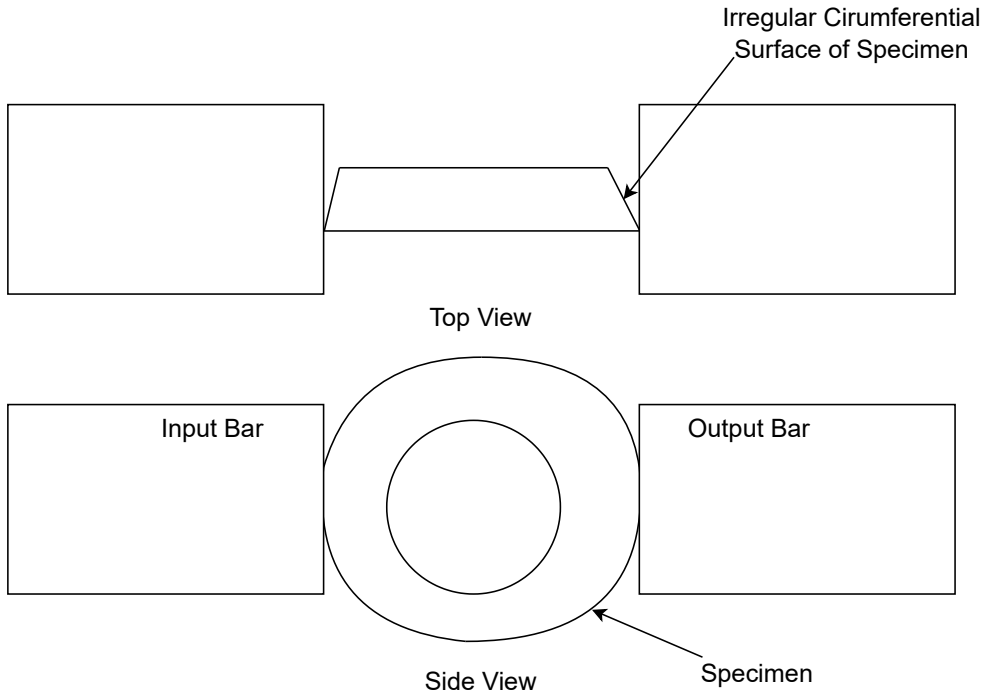

Figure 4.13 Schematic illustrating the irregular circumferential surface of the cross-section bone specimens with only two points of contact with the compression SHB bars.

Due to only being in contact with the input and output bars at one point respectively, the specimen could not be securely held by the bars upon impact of the input bar with the striker. The specimens were not able to be tested even with the application of a form of adhesive. Machining the circumference of the specimens to have better contact with the bars was avoided as a solution in an effort to maintain the natural cross-sectional shape of the specimens.
As a result, the decision was made to move the bone cross-section tests to the bending SHB setup explained in Section 3.4. This decision was based on the fact that the specimens could be held more securely with the three points of contact, and this setup already utilized a polymer output bar, which would allow for the transmitted signal to be recorded at a useful resolution. Furthermore, as the results from these tests were primarily being used to compare the complex geometry behaviour of the bone in the physical tests to the simulations, the type of loading (i.e. the move from pure axial compression with two points of contact to a three-point loading) was not a concern.

Due to the complex geometry of the specimens, obtaining an accurate stress-strain history for each specimen is near-impossible. As a result, only the force-displacement history of the cross-section specimens will be reported, and these will be obtained via the strain gauges (SG's) on the input tube and output bar of the SHB. Additionally, a high-speed camera was used to observe the deformation and potential failure of the specimens. A Phantom VEO 1310 series high-speed camera was used to capture the images at a frame rate of 27 000 frames per second (fps). Ideally a higher fps would be used, however with the size of the specimens, and therefore size of the image that needed to be captured, this was highest available fps option. The goal of the high-speed camera footage was to observe the deformation behaviour of the specimens as they were loaded, but also to observe crack propagation through the specimens should they fail.

The primary goal of these tests was to link small specimens tests with relatively simple geometry, such as the type of tests discussed previously in this chapter, to more complex tests, such as those conducted on whole bone specimens. Determining if the data extracted from material tests correlate with findings from more complex geometry tests is critical, particularly when attempting to simulate full bones in finite element analysis (FEA) software. However, before one conducts full bone tests, whether that be experimentally or computationally, accurate material parameters must have been determined, and that is done through the testing of small, simple specimens, where geometry does not have as significant of an influence on the observed behaviour. These cross-section tests act as an intermediary step in that process; small enough that

material characteristics still dominate material behaviour, but still introducing complex geometry. Additionally, these cross-section specimens allow for a reduced computational expense when attempting to simulate cortical bone in FEA software. When compared to full bone simulations, or even full skeletal simulations, these smaller specimens allow for significant computational savings, while still considering the effect of a more complex geometry.

4.8 Computational Simulations

4.8.1 SHB Operation

The initial focus of the simulation work was to have the model replicate the fundamental operation of a physical SHB. In an effort to reduce computational expense the entire SHB was not modelled. Rather, significantly shorter bars were modelled, coupled with infinite elements to remove any reflected waves. The striker was not modelled, but rather replaced by a pressure applied to an internal face of the input bar. This greatly reduced the computational expense and allowed for a finer mesh to be used without the penalty of a significantly increased simulation time.

As a result of simulating shortened bars, stress wave reflections off ends of the bars would make typical analysis of the SHB results impossible. As LS-Dyna does not have an integrated infinite elements option to absorb these reflections, a non-reflecting boundary condition was applied to the free-end of an extra sets of elements. This allowed for the shortened bars to simulate the actual operation of a full-length bar, where the overlaps of reflected stress waves could be avoided by placing the SG sufficiently far away from the ends of the bars. The non-reflecting boundary condition was applied by connecting a single row of elements to the respective free-ends of the bars via frictionless tied contact (TIED_SURFACE_TO_SURFACE) with the force transfer option activated. The cross-sectional mesh of this row of elements matched that of the bar exactly and this extra row of elements was constrained to prevent non-axial translation and rotation.

The striker was not modelled, but rather represented by an applied pressure boundary condition imparted in the input bar. As a result of the non-reflecting boundary condition being applied on the free-end of the input bar, the stress wave representing the striker impact had to be applied on the next available inner set of elements of the input bar. It was found that should the stress wave be applied too close to any other boundary condition, the stress wave would not propagate evenly through the cross-section of the bar. As a result, it was determined through a series of simulations that the stress wave needed to be applied at least one bar diameter away from any boundary condition.

For initial validation simulations, an artificial Gaussian-shaped pulse was used, similar to what is induced in the input bar when using pulse-shaping and a typical striker. The use of a smooth stress wave, rather than a square wave, allowed for the effects of dispersion to be greatly reduced.

A series of simulations were run in order to determine if the shortening of the simulated bars could in fact replicate the physical operation of the SHB. Input bars of 100 mm,

200 mm, 300 mm, 400 mm, 500 mm, 1000 mm and 1500 mm were modelled with a set of infinite elements on their respective free-ends. The mesh for these simulations had one element having an approximate edge length of 0.5 mm, and this mesh was kept constant for each simulations with a new bar length.

As a result of there being no overlap between the input and reflected waves in the 1500 mm, it was to be the baseline for this series of simulations. The goal of this series of simulations was to determine the shortest bar length that could be simulated, but which obviously resulted in the smallest error from what was effectively the physical equivalent in the form of the 1500 mm bar. All the bars had a smoothed Gaussian curve exerted on an internal cross-section, and this stress wave would propagate to the free-end, reflect off it and then propagate through the bar until it was absorbed by the infinite elements at the opposing free-end. In the cases where the input and reflected waves did overlap, the input wave could simply be subtracted from the stress history at the correct point in time to allow for the reflected wave to be plotted in isolation. The criteria used to determine the error between the various bar lengths was the peak value of the reflected wave compared to the baseline reflected wave, as well as the root mean square (RMS) error compared to the baseline reflected wave. This RMS error was calculated by superimposing the reflected wave over the baseline reflected wave and determining the RMS difference between the the stress values of the two waves at each time-step. Table 4.3 is a summary of the results from this series of simulations.

Table 4.3 *Summary of the results from the series of simulations used to determine the shortest possible length of bar for accurate SHB simulation.*

Bar Length	Run Time	Peak Err.	RMS Err.
[mm]	[min]	[%]	[MPa]
100	1.58	0.115	0.03
200	4.05	0.002	1.26
300	6.85	0.041	1.59
400	10.15	0.011	1.28
500	10.47	0.017	1.25
1000	18.20	0.132	1.25

From the data in Table 4.3, one can see that there is near negligible difference between the six bar length in terms of stress measurements, however a noticeable difference is

observed in the run times. As a result, the 100 mm bar length was chosen for these simulations.

With the minimum bar length established, and with the basic operation of the SHB satisfactorily replicated using the infinite elements, an output bar and specimen were added to the simulation. This series of simulations aimed to determine if a stress wave could propagate successfully through an input bar, then a specimen, and finally through an output bar. The contact between specimen and the two bars of the SHB was defined using automatic contacts (AUTOMATIC_SURFACE_TO_SURFACE) with the force transfer option activated. The frictional coefficients were set to zero in order to avoid any frictional effects in an effort to ensure full force transfer between the bars and specimen. This decision was based on work seen in literature [104–106, 138] and previous work done at BISRU by Hartley *et al.* [139], which determined that the error due to friction is approximately between 2% - 3%, provided specimens are lubricated. Simulations were conducted using perfectly elastic material models (MAT_001) for the maraging steel bars and the polymethyl methacrylate (PMMA) specimens. The bars had a daiamter of 20 mmwhile the cylindrical specimen had a 5 mm diameter and height. Elements for measurement were chosen at the locations identified in Figure 4.14. These elements were chosen as they should have near identical stresses if the simulation is operating correctly.

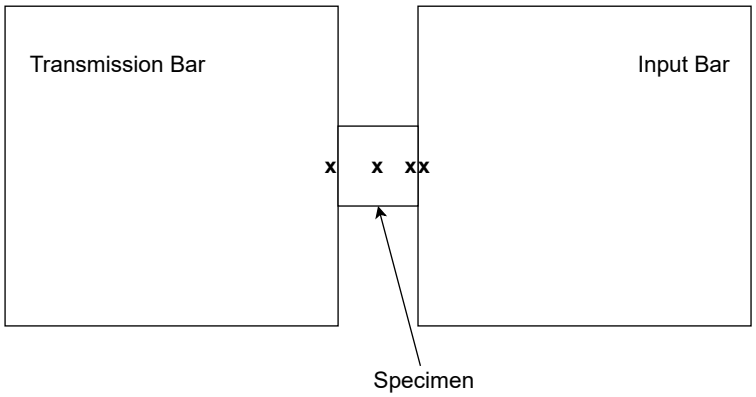

Figure 4.14 Schematic illustrating the locations of the measurement elements for the SHB stress wave propagation validation.

A stress wave similar to what would be exerted when using the Cone-in-Tube (CiT) striker was applied to the loading face of the input bar. Figure 4.15 shows the measured element stresses from the four chosen elements.

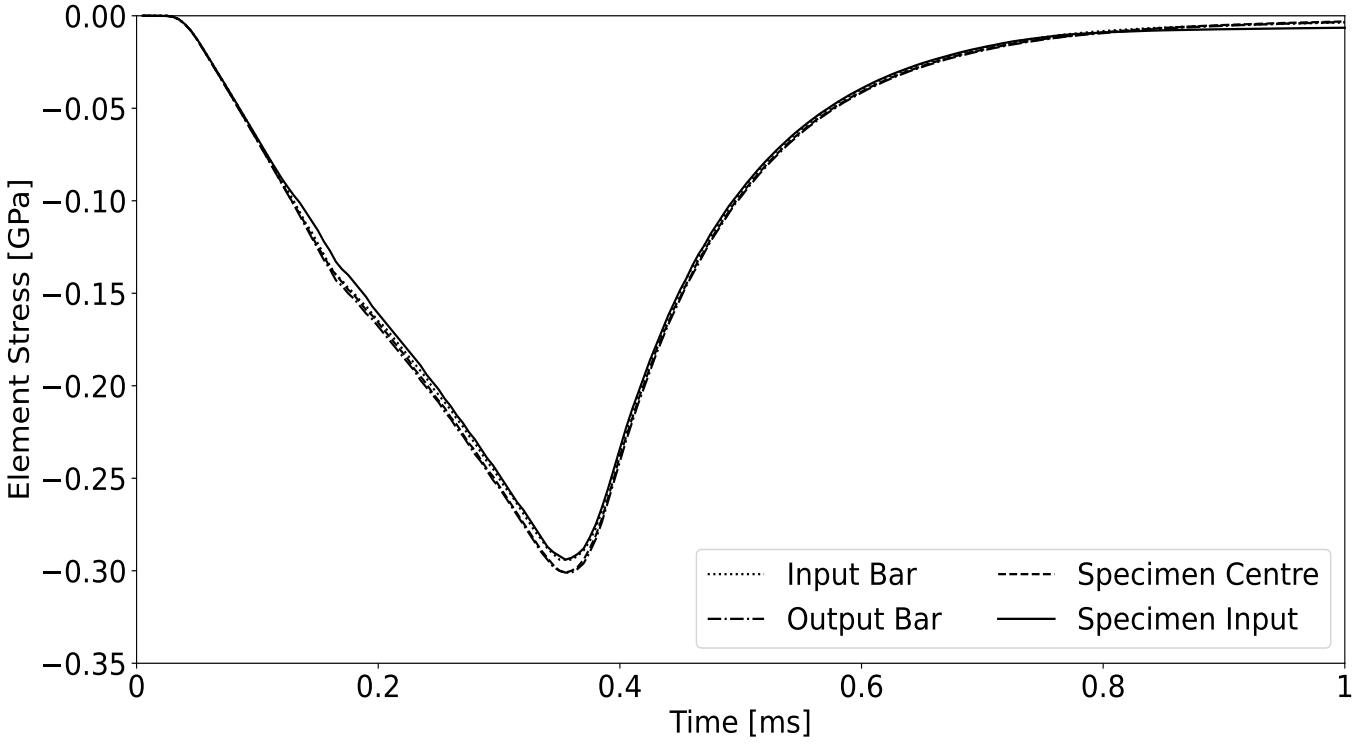

Figure 4.15 Stress vs time results from the SHB stress wave propagation validation.

Based on the near identical element stress histories shown in Figure 4.15, the operation of the simulation was validated. These results demonstrate that a stress wave can successfully propagate through all three components of a SHB with no critical loses, thus validating the operation of the simulation.

4.8.2 Mesh Convergence

Having verified that the FEA model could properly simulate the physical operation of the SHB with the shortened bars, a mesh convergence study was conducted. A series of simulations were run with the same bar and specimen geometry as used to verify the full operation of the SHB, however, each iteration of the simulation had a different mesh fineness.

When generating a solid cylinder in LS-Dyna, the options for mesh generation are the number of elements along the length of the cylinder and the number of elements around the circumference of the cylinder. Hence, four iterations of this mesh convergence study were run, with the respective mesh option parameters being summarized in Table 4.4.

Table 4.4 *Summary of the mesh fineness for the respective simulations in the mesh convergence study. Each value represents the length of each element in mm.*

	Coarsest		Coarse		Fine		Finest	
	Bar	Specimen	Bar	Specimen	Bar	Specimen	Bar	Specimen
Length	2	1	1	0.5	0.5	0.25	0.25	0.13
Circum.	3.93	2.24	2.24	1.12	1.12	0.56	0.56	0.28

In order to determine when convergence was met, displacement and stress parameters were measured. Three points of interest were chosen on each of the specimen-ends of the bars, with the first on the circumference of the bar, the second at the circumference of the specimen on the bar and the third at the centre of the bar. Four points were chosen on the specimen; on the input face, at the circumference and at the centre of the specimen, and the same two locations, but on the central plane of the specimen. Figure 4.16 illustrates the measurement locations which are marked with a 'x'.

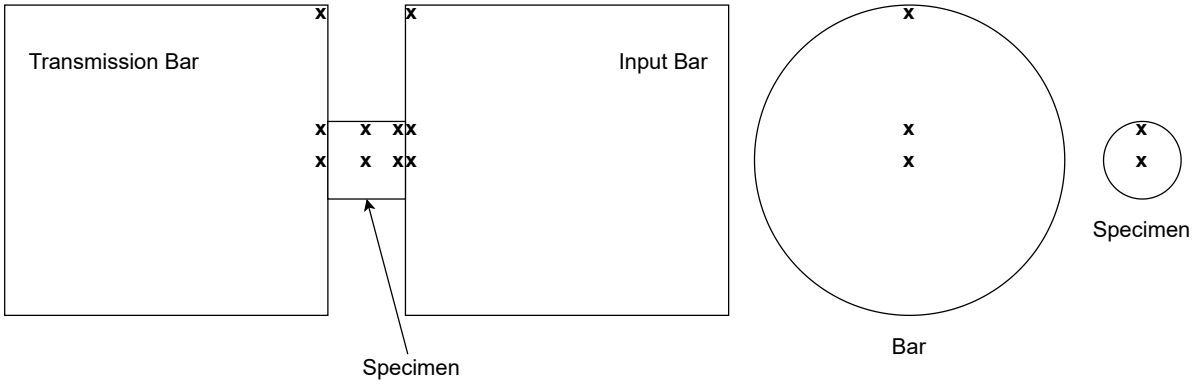

Figure 4.16 Schematic illustrating the locations of the measurement nodes/elements for the mesh convergence study.

From the displacement comparisons, it appeared that the 'Coarse' mesh had converged with the results from the 'Finest' mesh. Maximum displacements of all tested locations were within 0.015 mm when comparing the 'Coarse' mesh to the 'Finest' mesh. The displacement measurements from the input bar had the largest difference between meshes, with displacement measurements being far closer when considering the output bar and on the specimen itself. Figures 4.17 through 4.21 are examples of displacement vs time datasets recorded from the mesh convergence study. Examples are taken from the input bar as well as the specimen to demonstrate that the recorded displacements

are extremely close across the entire simulation. In particular, the displacements recorded in the specimen are near-identical, as shown in Figures 4.20 and 4.21, with essentially the same displacement-time histories being recorded for the 'Coarse', 'Fine' and 'Finest' meshes at the central face of the specimen.

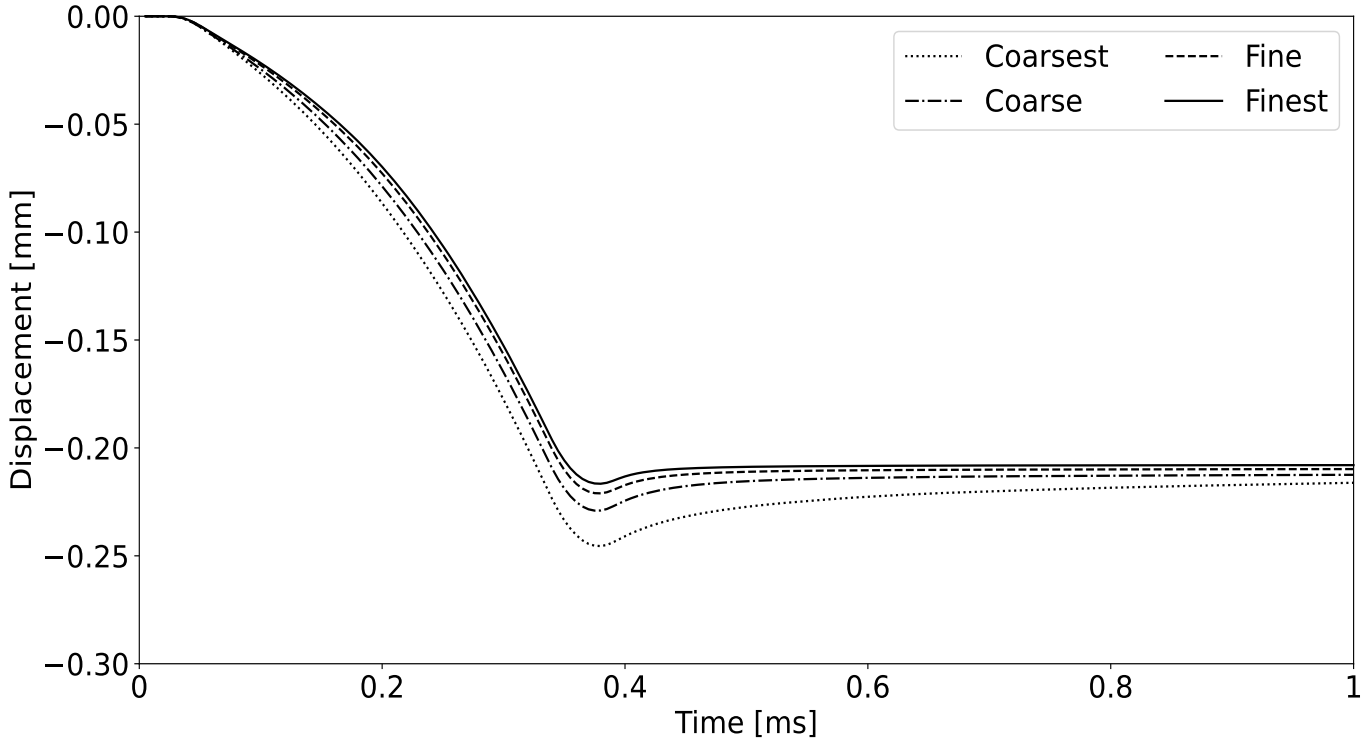

Figure 4.17 Displacement vs time results from the mesh convergence study for the circumferential location of the input bar.

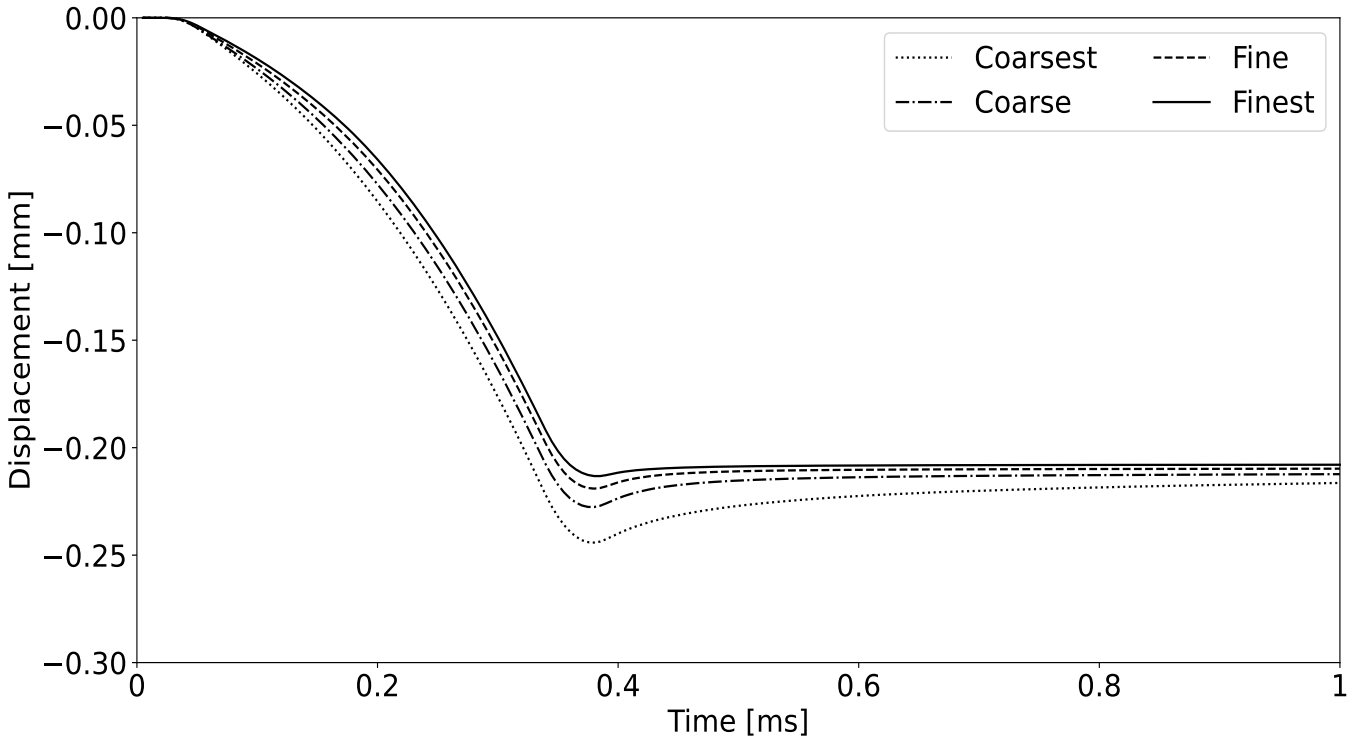

Figure 4.18 Displacement vs time results from the mesh convergence study for the circumferential location of the specimen on the input bar.

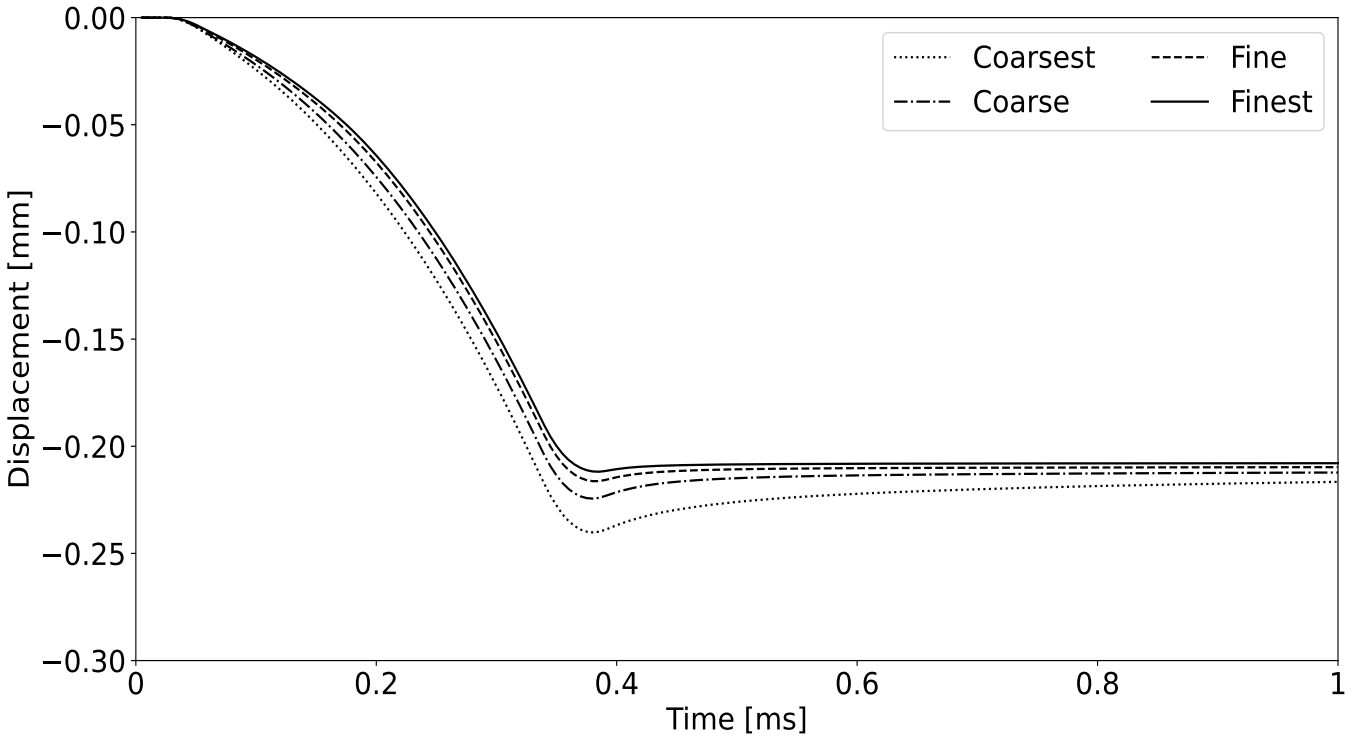

Figure 4.19 Displacement vs time results from the mesh convergence study for the central location of the specimen on the input bar.

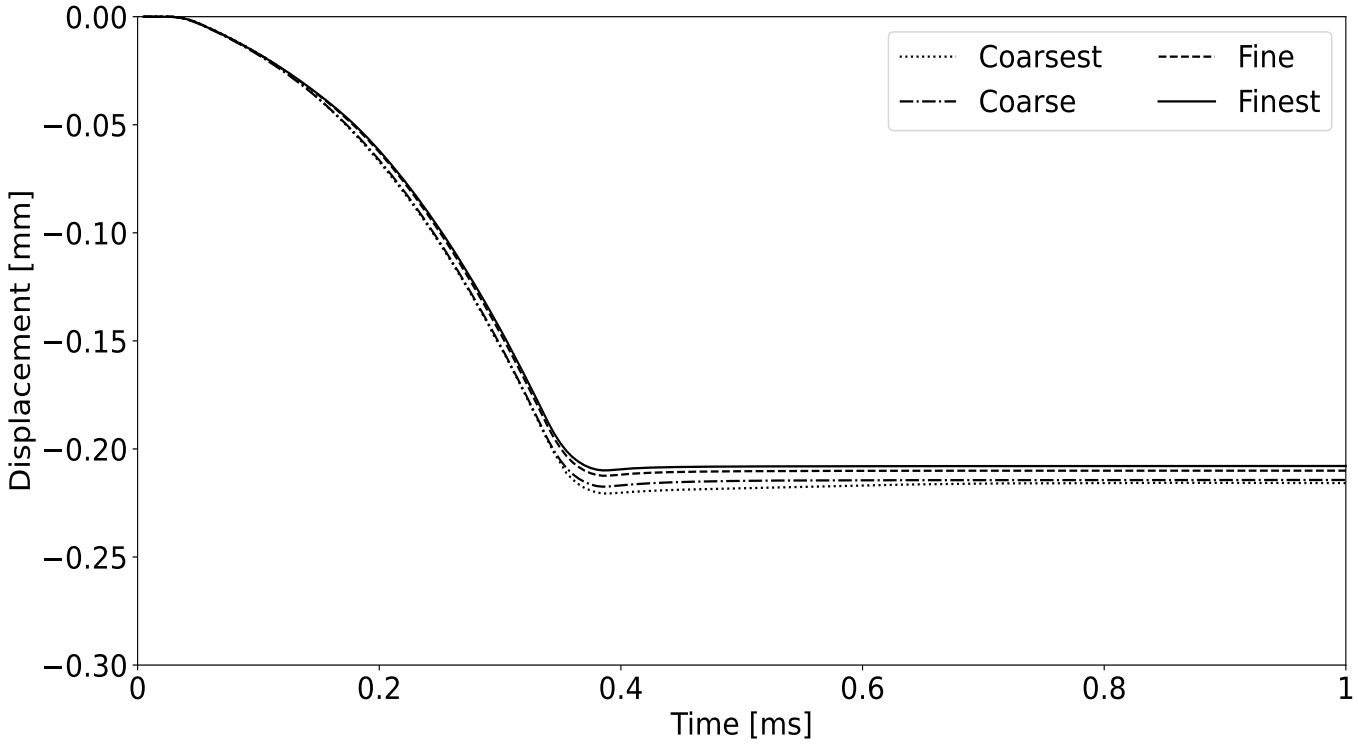

Figure 4.20 Displacement vs time results from the mesh convergence study for the central location of the specimen on the input face of the specimen.

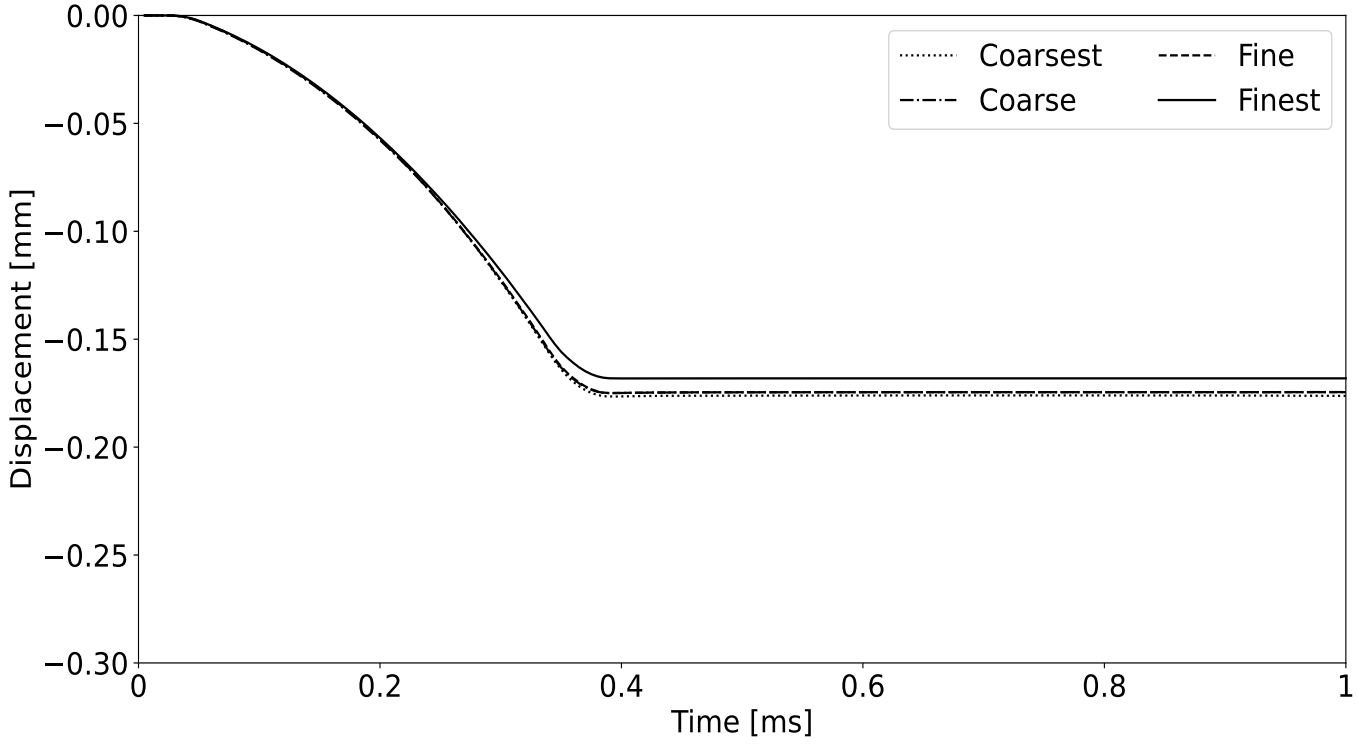

Figure 4.21 Displacement vs time results from the mesh convergence study for the central location of the specimen on the middle face of the specimen.

Based on these results, it would appear that the 'Coarse' mesh would be sufficiently accurate to run the simulations. However, the mesh convergence study did highlight that there was an improvement from the use of the 'Fine' mesh compared to the 'Coarse' mesh when considering the stresses recorded at these same locations. Figures 4.22 through 4.26 show the stress vs time results from these same simulations.

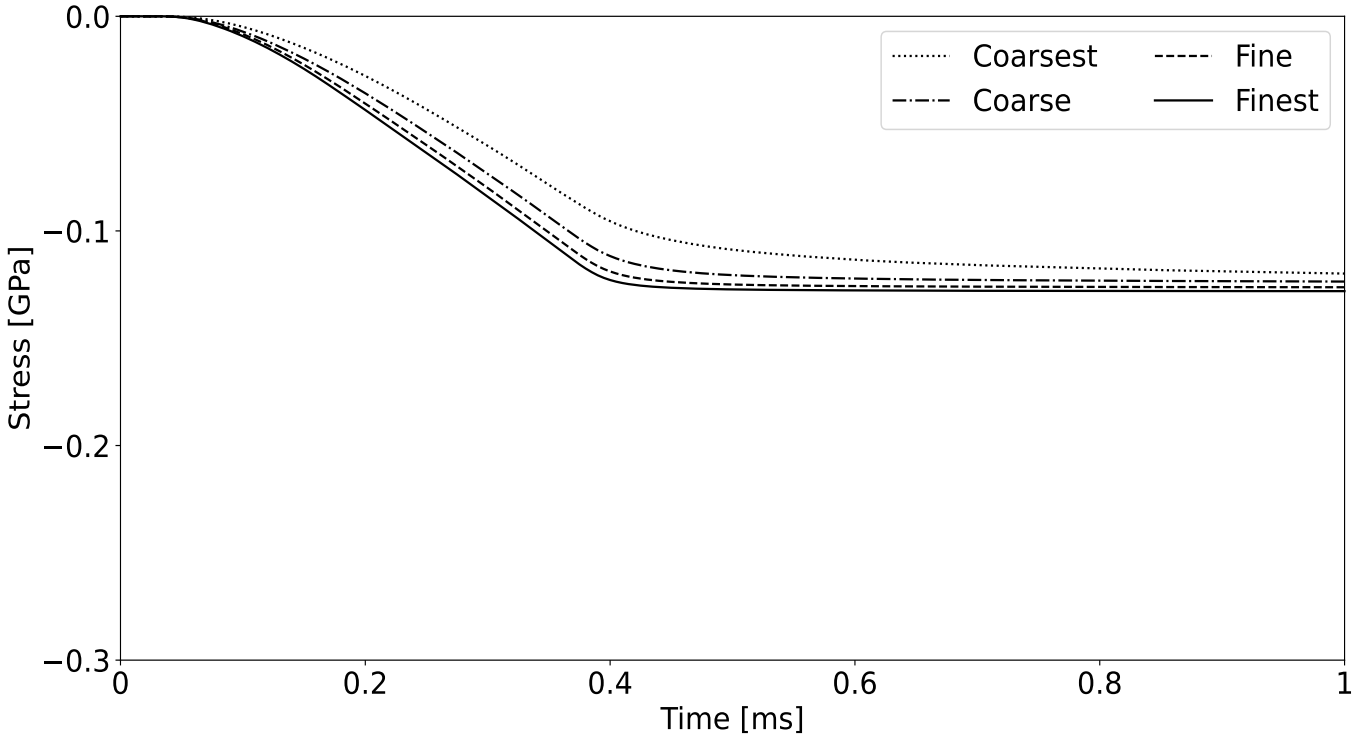

Figure 4.22 Displacement vs time results from the mesh convergence study for the circumferential location of the output bar.

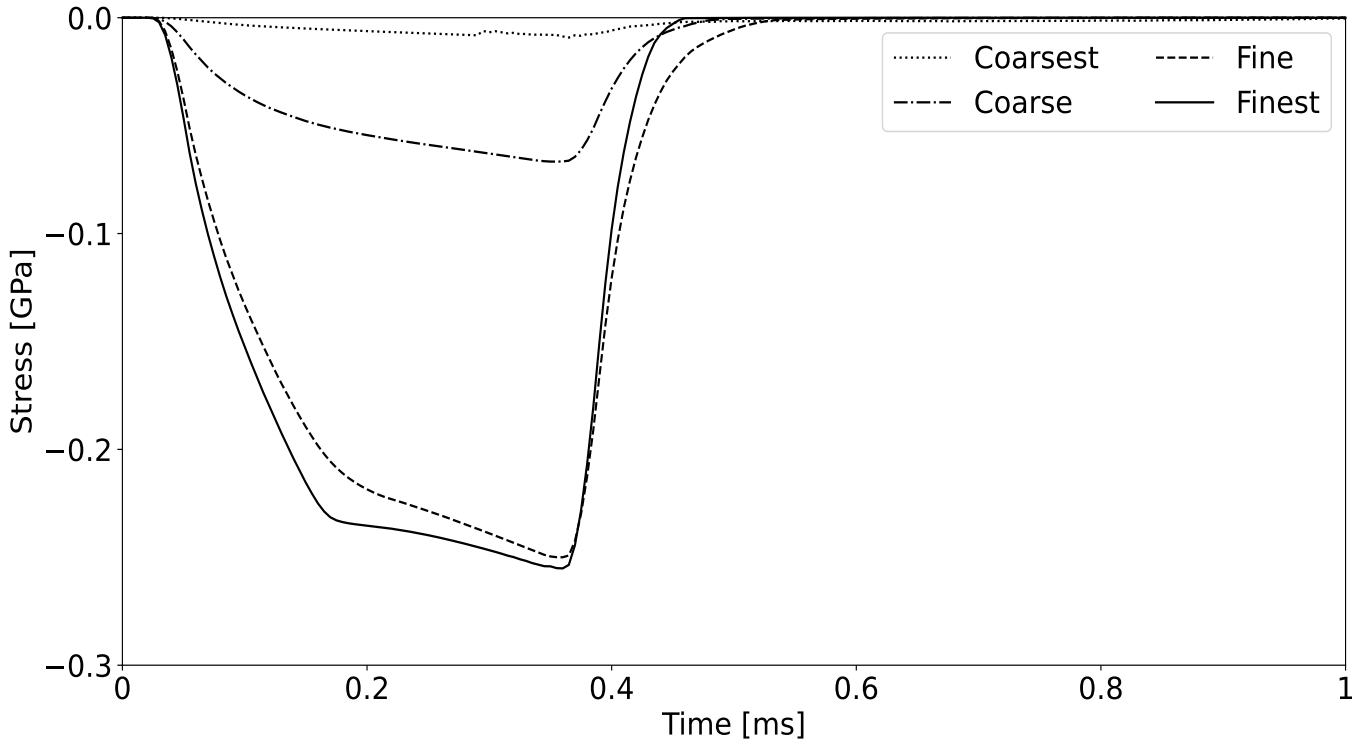

Figure 4.23 Displacement vs time results from the mesh convergence study for the circumferential location of the specimen on the output bar.

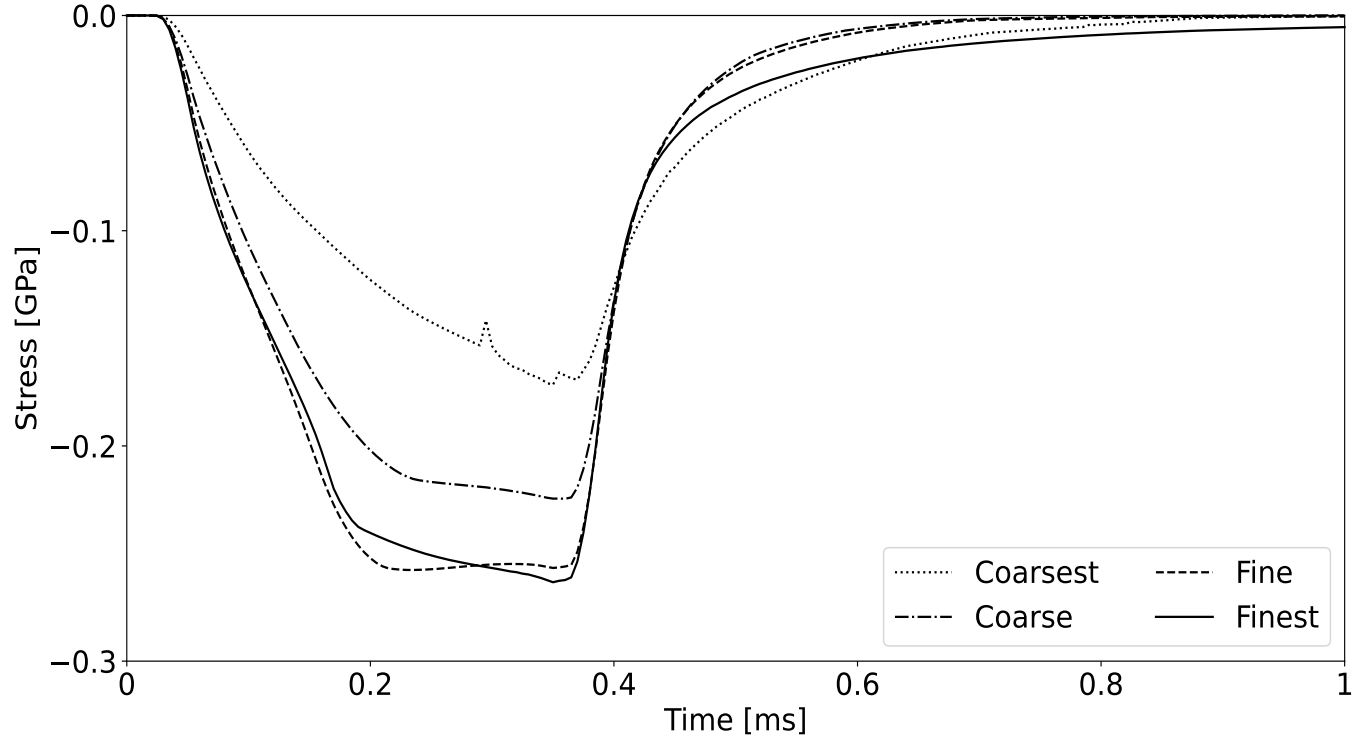

Figure 4.24 Displacement vs time results from the mesh convergence study for the central location of the specimen on the output bar.

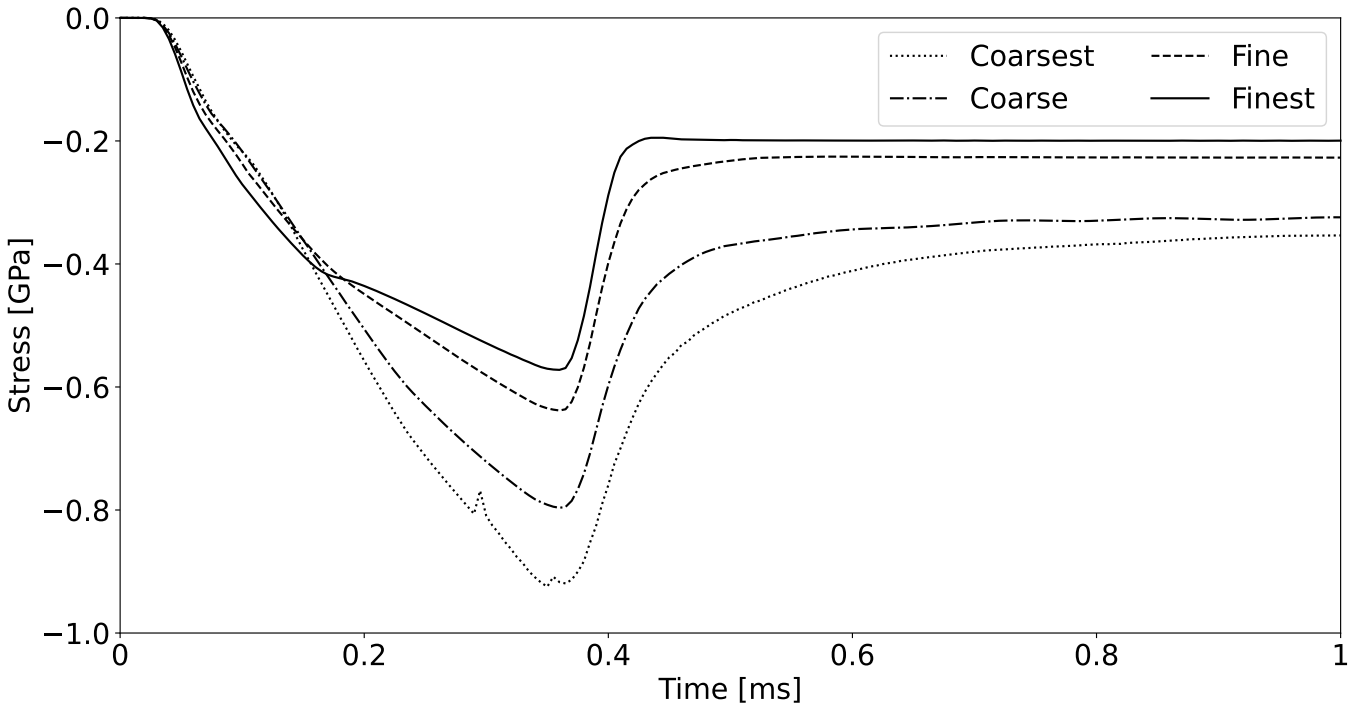

Figure 4.25 Displacement vs time results from the mesh convergence study for the circumferential location of the specimen on the input face of the specimen.

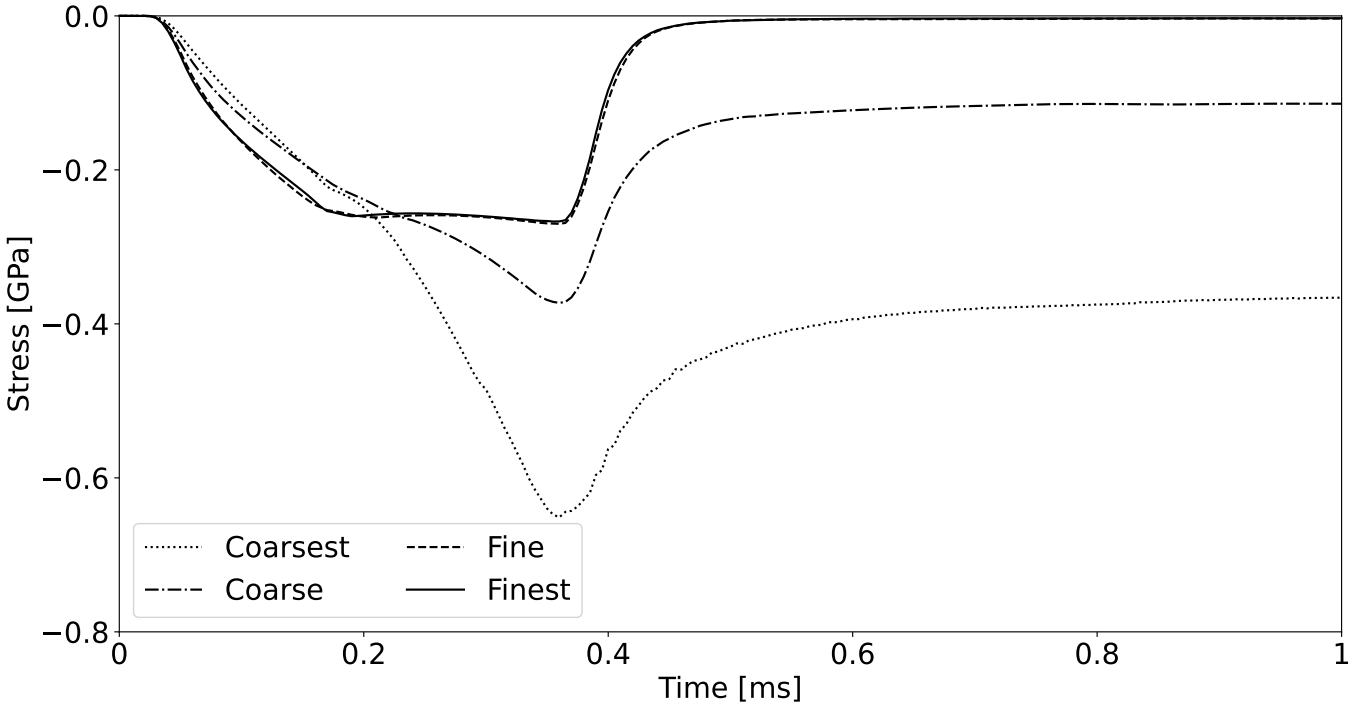

Figure 4.26 Displacement vs time results from the mesh convergence study for the circumferential location of the specimen on the middle face of the specimen.

The stress-time graphs shown in Figures 4.22 through 4.26 are taken from the locations on output bar and the specimen to demonstrate the mesh convergence with increased mesh density. Based on these results the 'Coarse' mesh simulation had not yet converged, while the 'Fine' mesh was significantly closer to convergence, with stresses in the bars being within 1 MPa of each other when comparing the 'Fine' and 'Finest' mesh results. However, one can see that although the 'Fine' mesh appeared to perform well in the bars, this mesh density would not be sufficient for the specimen. Despite the satisfactory specimen stress results shown in Figure 4.26, with the 'Fine' and 'Finest' meshes performing near-identically, the 'Fine' mesh results shown in Figure 4.25 were not acceptable.
The run times for the simulations are summarized in Table 4.5.

Table 4.5 *Summary of the run times of the simulations conducted in the mesh convergence study.*

Mesh	Coarsest	Coarse	Fine	Finest	
Run Time	~ 0.00	~ 0.08	1.70	20.06	[hrs]

Based on the results obtained through this mesh convergence study, the choice was made to use the 'Fine' mesh for the bars, with the 'Finest' mesh being used for the specimen. Another set of simulations were run in order to determine if this combination of meshes would retain the desired benefits of each individual mesh. The results from those simulations demonstrated that the combination mesh simulation retained the accuracy of the individual meshes for the respective parts, but significantly reduced the run time, at just under two and a half hours, when compared to the 'Finest' mesh simulation.
Figures 4.27, 4.28 and 4.29 show the final mesh used for the subsequent simulations.

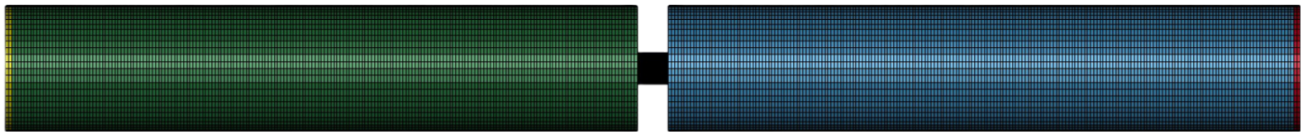

Figure 4.27 Side view of the final mesh used in the compression SHB simulations.

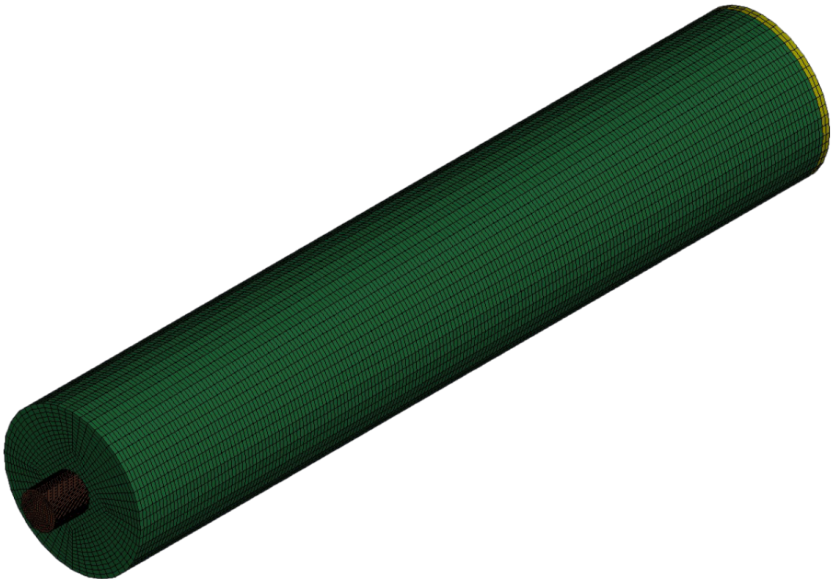

Figure 4.28 Isometric view of the final mesh of the specimen and output bar used in the compression SHB simulations.

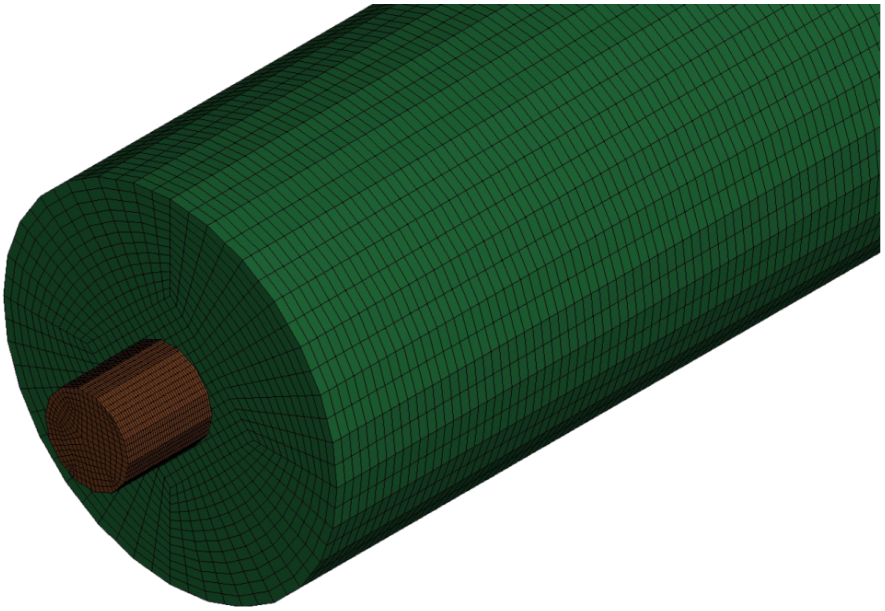

Figure 4.29 Zoomed isometric view of the final mesh of the specimen and output bar used in the compression SHB simulations.

4.8.3 SHB Simulation Setup

A simple compression SHB simulation was modelled in order to verify the specimen material model for the bone specimens. Both the input and output bars were modelled to a length of 100 mm instead of the 3 m and 2 m respective lengths in reality. The maraging steel bars were modelled using a simple elastic material model (MAT_001), as the experienced stresses in the physical tests would not deform the bars plastically. The mesh of the bars was set to 2 element per 1 mm along the length of the bar, and 1 element per 1.12 mm around the circumference of the cross-section of the bar (i.e. the 'Fine' mesh from the mesh convergence study). The specimen was modelled with a finer mesh with 1 element per 0.13 mm along its length and 1 element per 0.28 mm along the circumference of the cylindrical specimen (i.e. the 'Finest' mesh from the mesh convergence study).

Despite the success of the Objective Power Law (OPL) Model implemented by Bekker *et al.* [102], it was decided that this research would utilize material models already integrated into LS-Dyna. The reason for this was that the OPL Model was originally implemented in ABAQUS, and the implementation of the model into LS-Dyna was beyond the scope of this research. As a result, a strain-rate dependent plasticity material model (MAT_019) was used for this research. This model was chosen due to the option of defining the elastic modulus, failure stress and yield stress as a function of strain-rate. Based on the literature mentioned in Section 2.3.4 and previous work done at BISRU [101, 103, 136], this strain-rate dependency is vital when attempting to simulate the behaviour of cortical bone.
The strain rate dependency of this material model relies on a curve for the yield stress as a function of strain rate [140]. The strain rate sensitivity of this material model is described by:

$$\dot{\bar{\varepsilon}} = \left(\frac{2}{3}\dot{\varepsilon}'_{ij}\dot{\varepsilon}'_{ij}\right)^{\frac{1}{2}} \tag{4.3}$$

where the prime denotes the deviatoric component. Additionally, the elastic modulus can be defined as a function of strain rate, however this is not a requirement as is the case with the yield stress. This material model also features three options for material failure for solid elements. The first criteria being effective plastic strain, the second maximum principal stress and absolute minimum principal stress, and the third being maximum principal stress only. All three of these parameters can be defined as a

function of strain rate, and an element is deleted when it experiences stresses or strains which exceed these limits. The performance of this model will be compared to the piecewise linear plasticity material model (MAT_024) used for the cortical bone regions in the 'Total Human Model for Safety' (THUMS) model.
The parameters for the material model were determined through experimental tests, such as the degradation tests and the fresh bone tests. While these tests were conducted at constant strain rates, the results could be used in conjunction with the work done by Paul *et al.* [103] to define curves of these parameters over a range of QS, intermediate and dynamic strain rates. These curves were used as input in the material model.

Once the bone material model validation tests had been satisfactorily completed, simulations moved from testing of simple compressive specimens to bone cross-sections. The geometry of the bone cross-section was modelled using SolidWorks and dimensions were based upon measurements taken throughout the machining process of the cross-section specimens from the tests conducted prior to the simulations. Furthermore, as will be discussed in the upcoming Section 5.4, these cross-section experiments were conducted on the bending SHB. As a result, the geometry of the input tube and output bar needed to be modelled using SolidWorks and implemented into LS-Dyna with the 'infinite elements'. A similar preparation process was used with the bending SHB simulation as was used for the compression SHB simulation, however new bars lengths were used in order to allow for the stress wave to equilibrate in the more intricate geometry of the bending SHB. The input tube was modelled with a 500 mm length, while the transmission bar was modelled with a 200 mm length. The new specimen and SHB geometries were meshed using HyperMesh in order to retain the ability to simulate using solid elements in LS-Dyna. In the case of the cross-section simulations, stress results from the SHB bars were compared to the physical tests and deformation observed from the high-speed camera footage was compared element deformation data from the model.

Chapter 5

Results

In this chapter, the data obtained from the various tests will be outlined, summarized and critically analysed. Each set of results from their respective test will be dealt with individually, with a brief summary of all the results at the end of this chapter.

5.1 Apparatus Validation Tests

In an effort to confirm that the various apparatuses used in this study were operating as intended, a series of tests were conducted on polymethyl methacrylate (PMMA) and aluminium specimens. As has been stated previously, the use of these two materials is based upon the fact that their respective elastic moduli encompass the range of expected elastic moduli for cortical bone and these materials have a clearly observable elastic response. Additionally, being manufactured materials, it was anticipated that the specimens would behave in a consistent manner, therefore making them a reliable baseline to validate the operation of the various apparatuses.
These tests consisted of wave speed test series, tensile test series and then a series of tests on each of the four apparatuses previously mentioned in Chapter 3. A 2 m long rod of PMMA and a 2 m long rod of 6000 series aluminium were obtained for these tests. Both rods featured diameters of 20 mm. All specimens used in these tests were machined from the respective rods, therefore it is reasonable to assume that the respective results should all correlate.

5.1.1 Wave Speed Validation

In order to conduct these tests, the rods were treated as input bars of an SHB, and a calibration process was conducted as outlined in Section 3.3. Strain gauges were secured

to the rods and the recorded stress history allowed for an accurate modulus to be recorded for each of the rods.
Table 5.1 contains the average measured elastic moduli for the respective rods for the three tests conducted for each bar.

Table 5.1 *Summary of the average elastic moduli results from the wave speed apparatus validation tests.*

	Elastic Modulus [GPa]
PMMA	3.85
Aluminium	75.15

5.1.2 Tensile Validation

These tests involved using the Zwick in a tensile configuration, but conducting one set of tests using the internal measurement system of the Zwick and conducting a second set of tests using the VE to measure displacement.
Specimens for the Zwick-only tests were machined to have a 2 mm by 2 mm square cross-section and a length of 700 mm. By comparison, the VE specimens were machined to a length of 300 mm, but had the same cross-section. The reason for this length difference was to minimize the effect of the compliance of the load train of the Zwick on the overall measured displacement during the Zwick-only tests. Having a longer specimen would mean that the effect of the compliance of the load train of the Zwick would be minimized. Furthermore, the maximum specimen length that the VE is capable of measuring is approximately 250 mm due to the lenses and setup. But machine compliance was not as critical in this case, as the VE uses markers on the specimen itself to measure displacement, therefore machine compliance is not measured in the overall displacement measurements. Based on the results from the statistical analysis in Section 3.1.2, the VE was deemed sufficiently accurate and consistent for these long specimens and relatively large displacements. This is due to the VE being rated to an accuracy of 10 μm, therefore over the maximum visible distance the VE could measure, which was 250 mm, that would result in a maximum possible error of 0.004%.
In an attempt to maximize the number of smalls specimens that could be machined from the rods, thus limiting the stock available to machine these long specimens, along with the complexity of machining of these long specimens, only one specimen for each of

the respective tests could be manufactured.
Table 5.2 summarizes the measured elastic moduli from these tests.

Table 5.2 *Summary of the elastic moduli results from the tensile apparatus validation tests.*

	Zwick-Only Test [GPa]	VE Test [GPa]
PMMA	1.86	3.98
Aluminium	18.92	73.61

5.1.3 Quasi-Static Compression Validation

A series of tests were conducted using the subpress on specimens of 5 mm diameter and 5 mm height. The same loading program outlined in Section 4.4.2 was used in this series of tests.
Table 5.3 contains the average measured elastic moduli from the ten tests for the respective materials from the quasi-static (QS) compression validation tests.

Table 5.3 *Summary of the average elastic moduli results from the quasi-static compression apparatus validation tests.*

	Elastic Modulus [GPa]
PMMA	3.56
Aluminium	21.63

5.1.4 Quasi-Static Bending Validation

This series of tests were conducted on the Instron using the three-point bending attachments. Specimens were machined to have a height and breadth of 4 mm and a length of 40 mm. The same basic loading program was used in this series of test as was outlined in Section 4.5.1.
Table 5.4 contains the average measured elastic moduli, taking into account machine compliance using the spring theory method discussed in Section 3.2, from the five tests for the QS bending validation tests for the respective materials.

Table 5.4 *Summary of the averaged elastic moduli results from the quasi-static bending apparatus validation tests.*

	Elastic Modulus [GPa]
PMMA	3.45
Aluminium	74.78

5.1.5 Dynamic Compression Validation on Polymer Specimens

Previous work completed at BISRU has focused specifically on the dynamic behaviour of metals, with comparatively less work having been conducted pertaining to the dynamic behaviour of polymers. As a result, the focus of this validation process was on the PMMA specimens. As was discussed in Section 2.6.5, the testing of polymers in the ISR regime at near-constant strain rates is a challenge, and as such there appears to be a gap in the literature for PMMA in this strain rate regime. However, such tests were conducted with the use of the Cone-in-Tube (CiT) striker in the compression SHB setup. A series of tests were conducted using the compression SHB on specimens of 5 mm diameter and 5 mm height. As shown in Figure 5.1, the CiT striker was able to load the specimens are near-constant strain rates, significantly improving on tests that were claimed to have been conducted in this same strain rate regime in the literature, as shown in Section 2.6.5. Furthermore, the use of the CiT allowed for the test duration (i.e. the period of time when the specimen is being loaded) to be nearly doubled when compared to the tests conducted by Acharya *et al.* [98], which gives the specimen more time to reach a stress-state equilibrium.

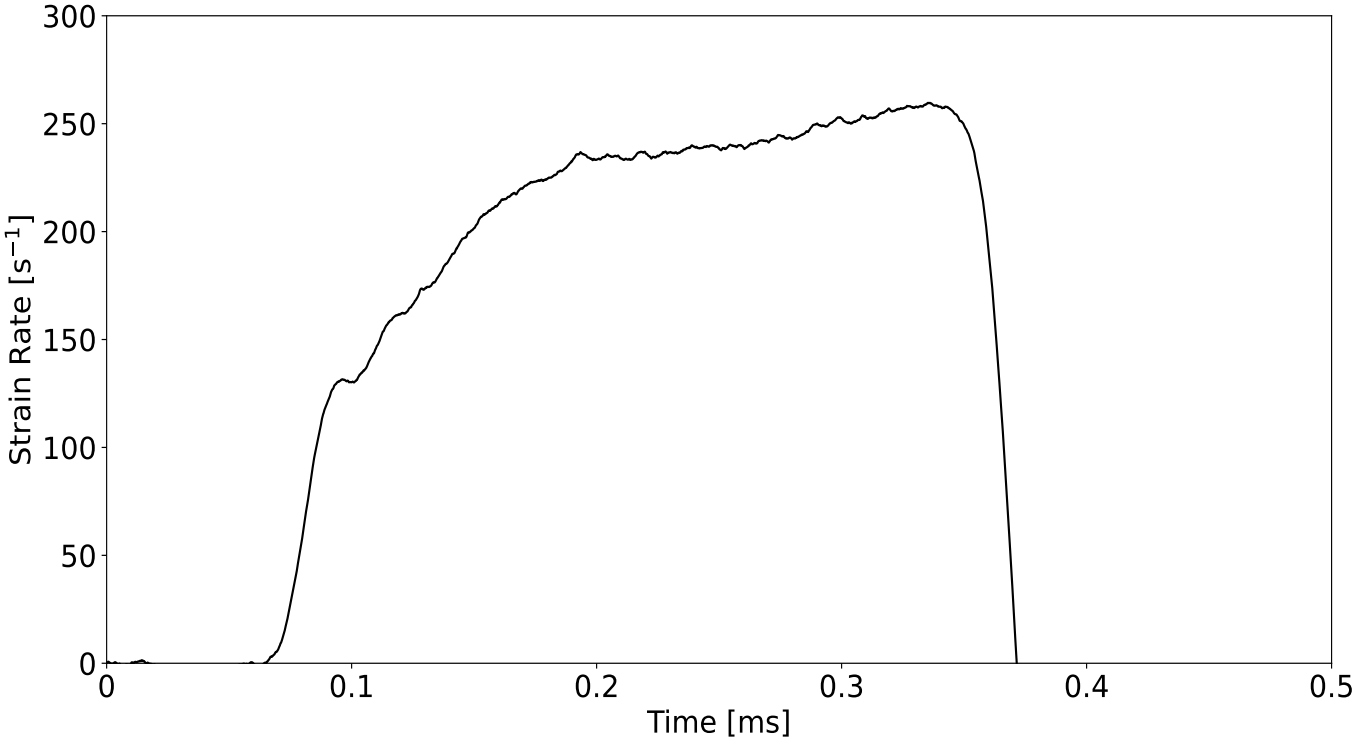

Figure 5.1 Typical graph of strain rate vs time for a compression SHB test when using the CiT striker to induce a near-constant strain rate when loading a PMMA specimen.

Through the use of this apparatus, tests were able to be conducted at average strain rates ranging from 93 s^{-1} to 248 s^{-1}, with all strain rate vs time graphs exhibiting a plateau during the test durations, as similar to what is shown in Figure 5.1. A summary of the results from this series of tests is shown in Table 5.5 and in Figure 5.2.

Table 5.5 *Summary of the apparent elastic moduli results from the dynamic compression apparatus validation tests on PMMA specimens at different strain rates.*

Test #	1	2	3	4	5
Strain Rate [1^{-1}]	93	121	183	240	248
Elastic Modulus [GPa]	4.3	6.2	3.9	6.7	5.8

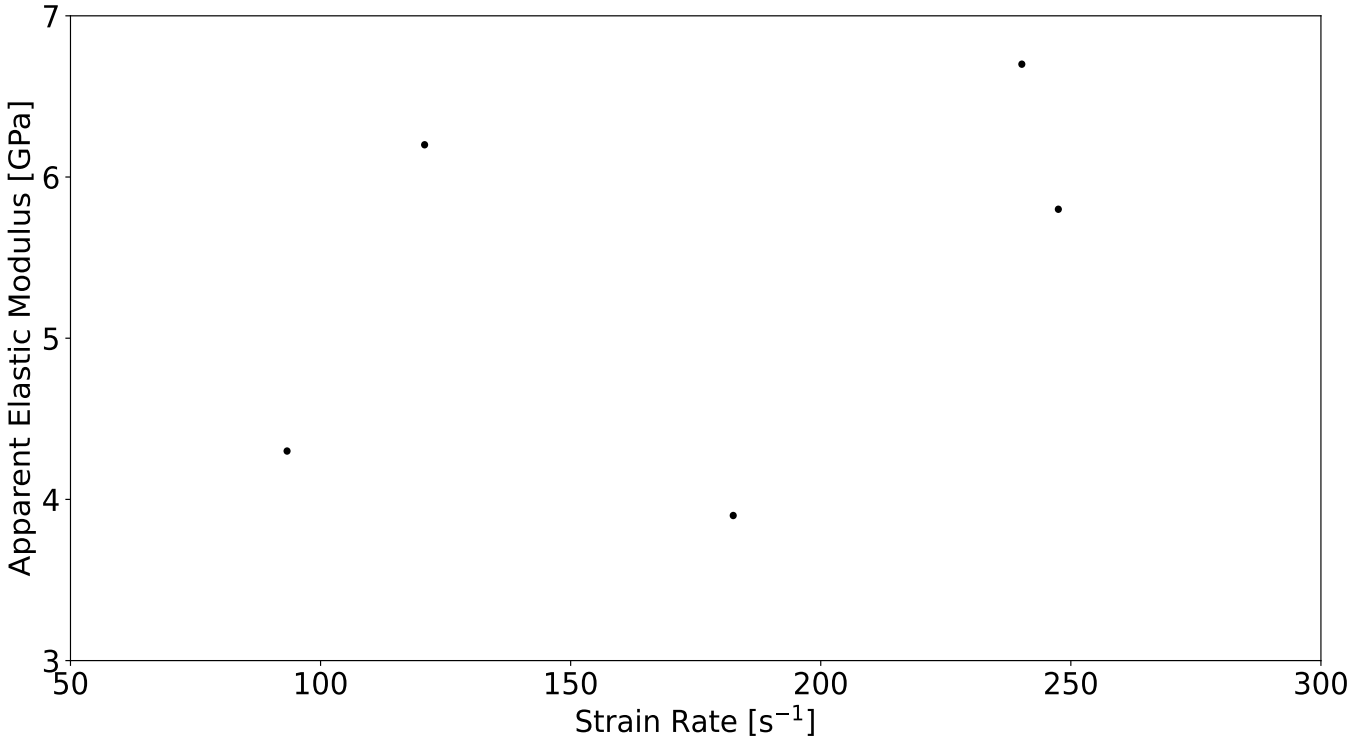

Figure 5.2 Graph of the results from the apparent elastic moduli vs strain rate for the dynamic compression of PMMA specimens.

Despite the scatter observed in Table 5.5, a clear increase in the apparent elastic modulus is noted at these intermediate strain rates when compared to those recorded during the QS validation tests.

5.1.6 Dynamic Bending Validation

A series of tests were conducted on the three-point bending SHB with two types of PMMA and aluminium specimens. The first type of specimens were 40 mm in length and had a 4 mm by 4 mm cross-section, while the second type of specimens featured the same length, but a 4 mm by 8 mm cross-section. Severe oscillations were observed in the loading of both the PMMA and aluminium specimens during preliminary tests on this SHB, as shown in Figure 5.3.

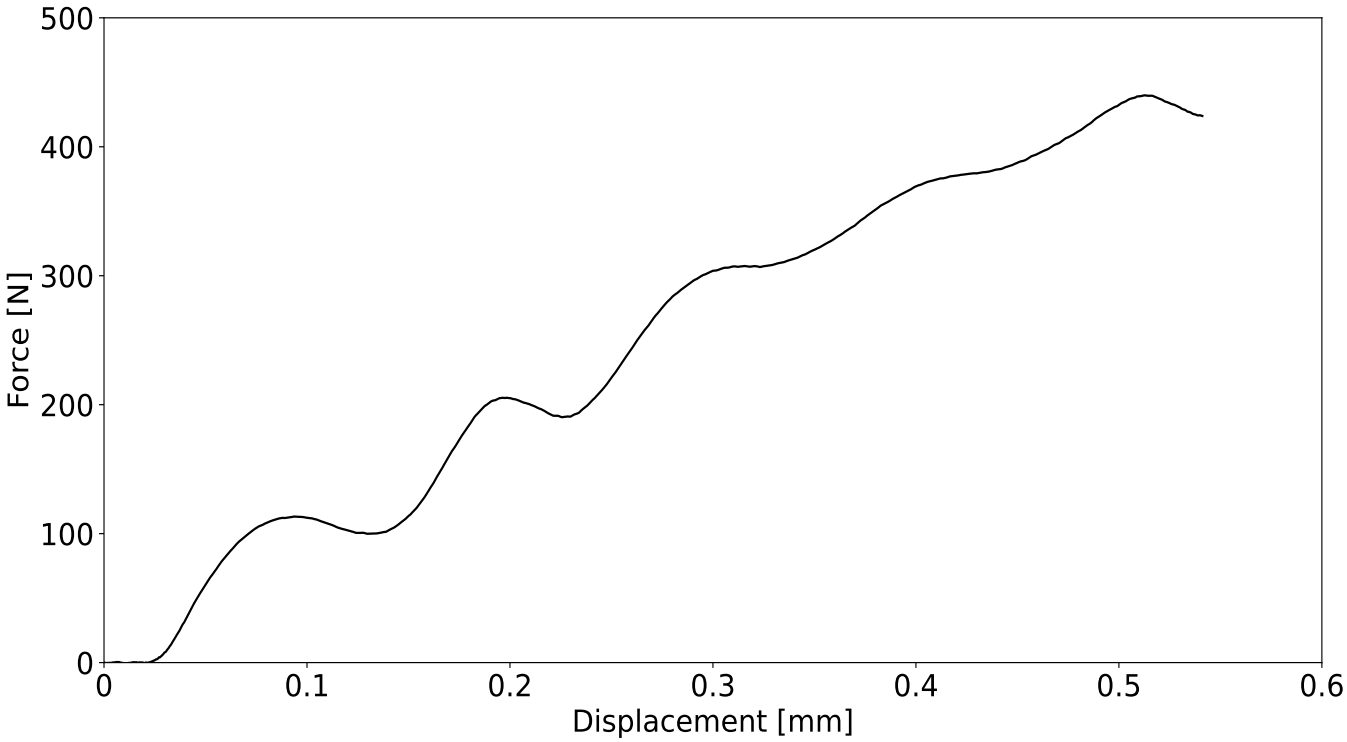

Figure 5.3 Graph of force vs displacement for the square cross-section PMMA beam specimen from the three-point bending SHB validation tests.

These oscillations prevented any meaningful material property data from being extracted from these results. Hence, the second type of specimens were manufactured with the intention that the increased cross-sectional area would increase the rigidity of the specimens, thus reducing the oscillations. These more robust specimens did not rectify the issue, nor did reducing the speed or magnitude of stress wave.
In an effort to confirm that these oscillations were in fact as a result of the specimen geometry, a series of calculations were done to determine the theoretical natural frequency [141] of the specimens using:

$$\omega_n = (\beta_n l)^2 \cdot \sqrt{\frac{EI}{\rho l^4}} \tag{5.1}$$

where ω_n, $\beta_n l$, $E\ I$, ρ and l are the natural frequency of the uniform beams, the normal mode of the uniform beams, the elastic modulus of the material, the second moment of inertia of the beam, the density of the material and the nominal length of the beam respectively. As a result of the three-point bending loading configuration, the beams could be bending in one of two ways; as a simply supported beam along the entire length of the

beam, or as a clamped-hinged beam along half of the length of the beam. Examples of these types of bending are shown in Figure 5.4.

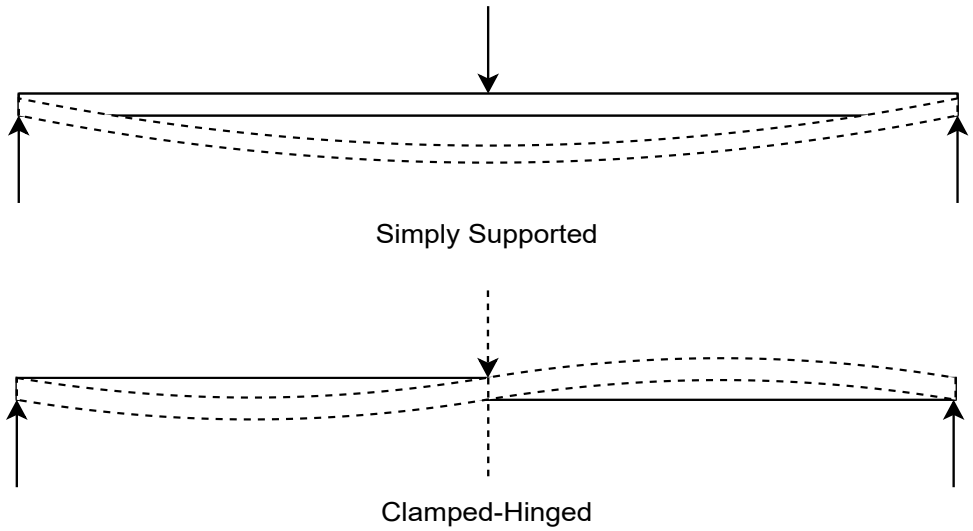

Figure 5.4 Schematics of the two potential bending types for specimens being loaded in the three-point bending SHB.

Through this analysis the frequency of the oscillations observed from the experiments matched with those calculated theoretically. In all cases, regardless of specimen geometry or material, the oscillations observed during experiments could be correlated to the natural frequencies of the beams, with a maximum difference between the experimentally measured to theoretical frequencies of 10%.

With it already being difficult to manufacture cortical bone beam specimens with the square cross-section geometry mentioned at the beginning of this section, further increasing the rigidity of the specimens by altering the geometry was not an option. Therefore, tests were conducted where the speed and intensity of the stress wave reduced in order to prevent the excitation of the specimens. This was done by reducing the speed of the striker on impact with the input tube, through reducing the firing pressure of the gas gun, as well as utilizing a number of forms of pulse shaping. While the combination of these two techniques did remove the oscillations, the specimens were simply not being loaded with sufficiently high force, nor were the specimens being deformed by a significantly large displacement, for meaningful data to be extracted from the results.

As a result of the inability to extract meaningful data from this apparatus, it was decided that dynamic bending tests could not be conducted on this apparatus. However, as will be discussed in Section 5.4, this SHB was used for the bone cross-section tests.

5.2 Degradation Tests

The goal of these tests was to identify a time period, after slaughter, wherein the bone could be considered fresh (i.e. harvested from the donor, machined and tested within 24 hours of the death of the donor). Ideally, material tests of bone would occur when the bone exhibits in-situ properties, and, as will be discussed, storing the bones, either as specimens or as whole bones, for prolonged periods of time does, in fact, degrade the properties of the material. These results have been summarized and presented in a journal article by Daras *et al.* [142], which has been referenced in Appendix A.

5.2.1 Statistical Analysis

In an effort to better interpret and appreciate the presented statistical data, an investigation was conducted into the meaning of the various statistical metrics that are quoted in the following results.

The first of these metrics is the coefficient of determination, or more commonly known as the R^2 value. According to Bryhn *et al.* [143], this metric, which ranges between zero and one, is used to measure the correlation between two variables, which in this degradation study are time in storage and the material characteristics, such as elastic modulus, strength and strain. Values of R^2 near zero imply that there is a low correlation between the two variables, while a value near to one implies a high correlation. The R^2 value is defined by:

$$R^2 = \frac{\left(\sum (x_i - x_{mean}) \cdot (y_i - y_{mean})\right)^2}{\sum (x_i - x_{mean})^2 \cdot \sum (y_i - y_{mean})^2} \tag{5.2}$$

The second metric is the p-value, which is a value used in statistical significance tests to describe the probability in which the null hypothesis is rejected, as defined by Bryhn *et al.* [143]. This is also a value ranging from zero to one, however a low value means that there is a statistically significant probability that the null hypothesis is rejected. Typically, a confidence level of 95% (i.e. p-value < 0.05) is used to deem a trend statistically significant, while a p-value higher than 0.05 results in a trend being deemed not statistically significant. In the case that p-value < 0.001, the trend is deemed to be highly significant. The means of determining the p-value is a well known process, and will not be outlined in this thesis, since derivations and explanations are readily available, for example in a paper by Frazer *et al.* [144].

These two metrics are obtained through a linear regression analysis of a dataset. In the case of a linear regression of a time series, which is simply a trend with respect to time, the null hypothesis, or basic assumption of a trend for statistical analysis, is that the data is stationary [145, 146]. Cryer *et al.* [146] define a time series to be stationary if the mean function does not change with respect to time (i.e. the mean does not change with time). When explaining the interpretation of the output from a linear regression analysis of a time series, Cryer *et al.* state that "In each case, the null hypothesis is that the corresponding unknown regression coefficient is zero." In other words, if the linear regression is thought of as a straight line with the equation $y = mx + c$, then the gradient value, or m, is zero, thus the data does not change with respect to time, therefore, it is stationary.
Hence, if a linear regression was conducted on a time series and the p-value from the analysis was less than 0.05, that implies that the mean of the data of that time series does not stay constant within a 95% confidence interval. We reject the null hypothesis at this confidence interval, and that results in the data being deemed as nonstationary.

5.2.2 Apparent Elastic Modulus

The MR specimens, including the day zero specimens, exhibited highly erratic behaviour throughout the study. Exhibiting an initial downward trend after the day-zero mode of 22 GPa to a minimum value of 15 GPa, then increasing to 28 GPa after a week of storage. A linear regression analysis was conducted on these MR results and generated a R^2 value of 0.342 and the data was deemed to have a highly statistical significant relationship with respect to time in storage ($p < 0.001$).

By contrast with the Mr specimens, the MF exhibited a distinctly stable behaviour for the first week of testing with apparent elastic modulus modes ranging between 21 GPa and 25 GPa. This range was consistent with the day-zero apparent elastic modulus and the linear regression trend had an R^2 value of 0.102 and was statistically insignificant ($p > 0.05$). After a week in storage, the MF specimens exhibited gradual degradation until the six month point, thereafter the degradation trend was more significant. By this six month point the MF specimens exhibited an apparent elastic modulus value of approximately 7 GPa and the modulus value appeared to stabilize at this value for the remainder of the tests. The linear regression trend for this selection of MF data had an R^2 value of 0.437 and was also highly statistically significant ($p < 0.001$).

The first results for the FMF (2M) specimens, which were obtained from tests conducted at the two month point, exhibited a noticeably high apparent elastic modulus mode of

approximately 24 GPa. This mode was consistent with the week-one average. However, by the next testing date, the FMF (2M) specimens had equilibrated with the MF specimens, and thereafter exhibited a similar degradation trend. By the six month point of the study the FMF (2M) specimens appeared to equilibrate at the same 7 GPa value as the MF specimens and remained at this value for the remainder of the study. The linear regression was the most successful with the FMF (2M) results as this trend had an R^2 value of 0.476 and was highly statistically significant ($p < 0.001$).

Finally, the FMF (11M) specimens were stored for 11 months prior to testing and these specimens exhibited a significantly low apparent elastic modulus value. This value was noticeably lower than any other measured value in this study.

5.2.3 Strength

The ultimate compressive strength values (UCS) reported in this section are the absolute maximum stress that was recorded throughout the entire test.

The MR specimens exhibited relatively stable behaviour in the first week of testing with modal values averaging approximately 260 MPa over the week. Scatter on each day did increase as the testing progressed through the week. The scatter can be noted in the R^2 value of 0.028 and this linear regression analysis did describe the trend as statistically insignificant ($p > 0.05$).

The MF specimens exhibited a similar behaviour to the MR specimens during the first week of testing, however the modal values were distinctly higher than the MR specimens, with average modal values for UCS being approximately 290 MPa. After the first week of testing the modal UCS for the MF specimens did not drop below 235 MPa until the month-six test, at which point a distinct decrease in UCS was noted. The decrease in modal UCS from the month-four test to the month-six test was approximately 50%, from 240 MPa to 111 MPa. Over the entire study, the data had an R^2 value of 0.552 and the trend was deemed to be highly significant ($p < 0.001$). However, if the first week is considered in isolation, this trend has a notably lower correlation, with an R^2 value of 0.002, but was deemed to be statistically insignificant ($p > 0.05$). The remaining MF data after week-one had a distinct increase in correlation, with an R^2 value of 0.425, and this trend was deems highly significant ($p < 0.001$).

The FMF (2M) specimens exhibited UCS values similar to those of the MF specimens tested on the same day. The significant decrease at the six-month point was noted with these specimens as well and beyond this point the UCS values remained relatively stable

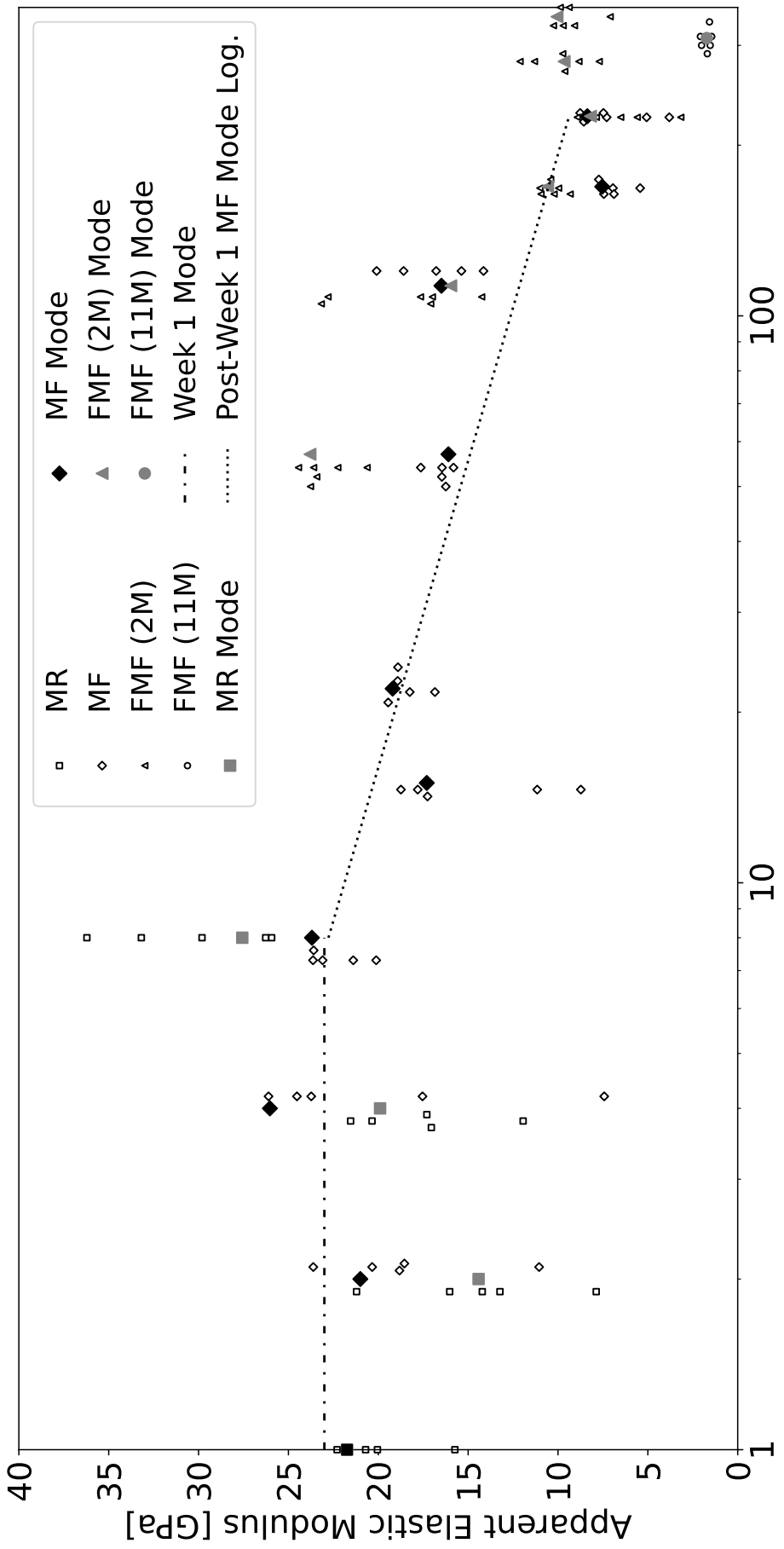

Figure 5.5 Graph of apparent elastic modulus vs storage time from the degradation tests with modal values from each testing day. Slight horizontal offsets are for clarity.

with low scatter on each testing day. The linear regression resulted in an R^2 value of 0.818 and was highly statistically significant ($p < 0.001$).

Finally, the FMF (11M) specimens exhibited a distinctly low modal UCS value of 70 MPa, with very low scatter.

5.2.4 Strain

The strain values quoted in this section are the corresponding strain for the UCS values quoted previously. Unlike with the apparent elastic modulus and the UCS, the strain at UCS, or UC strain, remained relatively constant regardless of storage protocol or time in storage. All specimens exhibited a UC strain value around 0.02 for the entire study. Scatter was also relatively small and consistent over the entire study, regardless of storage protocol.

The R^2 values for the MR, MF and FMF (2M) specimens over the entire study were 0.054, 0.017 and 0.034 respectively. For the first week of testing, the MF specimens exhibited an R^2 value of 0.114 and beyond the first week, the MF specimens exhibited an R^2 value of 0.054. The linear regression analysis for all protocols, on any time-frame, were deemed statistically insignificant ($p > 0.05$).

The only exception to this data was the FMF (11M) specimens, which exhibited a noticeably higher UC strain than the rest of the specimens. These specimens exhibited a modal UC strain value of approximately 0.07, with very low scatter being observed in this dataset.

5.2.5 Limitations

The subpress was designed with the intention of characterizing materials with relatively low elastic moduli, while reducing machine compliance to near-negligible levels. However, a combination of the small specimen geometry and a material much stiffer than the bone tested in this study could result in a specimen stiffness in the same order of the local deformation of the plunger and lower platen of the subpress. In this case, more significant local deformation would be expected on the surface of the plunger and lower platen, as well as global deformation of the plunger, between the specimen interface and the point on the plunger where the magnetic sensor is reading displacement.
Modifications could be made to the subpress to better account for these anticipated compliance effects. For example, the subpress could be manufactured from a material

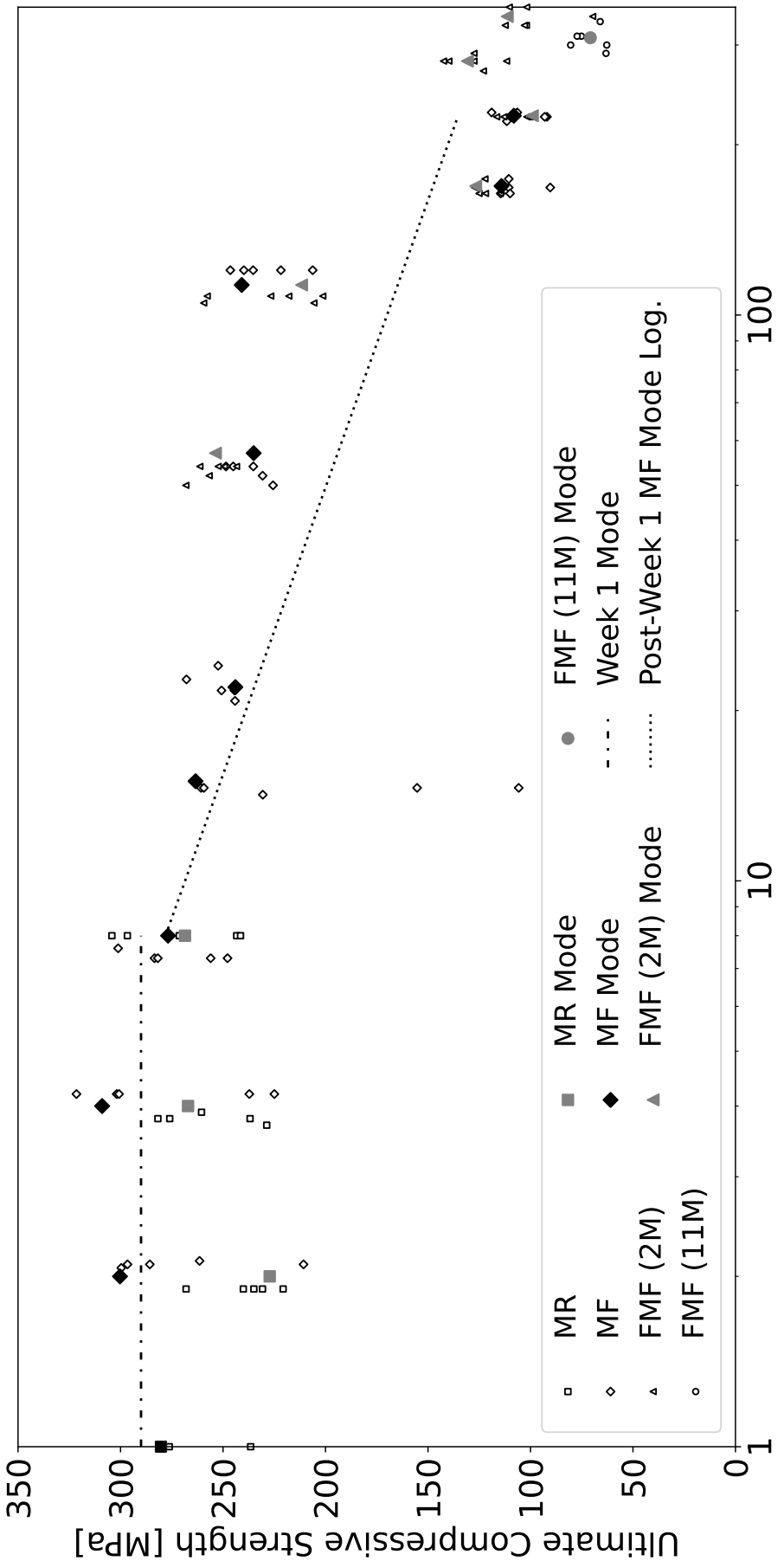

Figure 5.6 Graph of apparent UCS vs storage time from the degradation tests with modal values from each testing day. Slight horizontal offsets are for clarity.

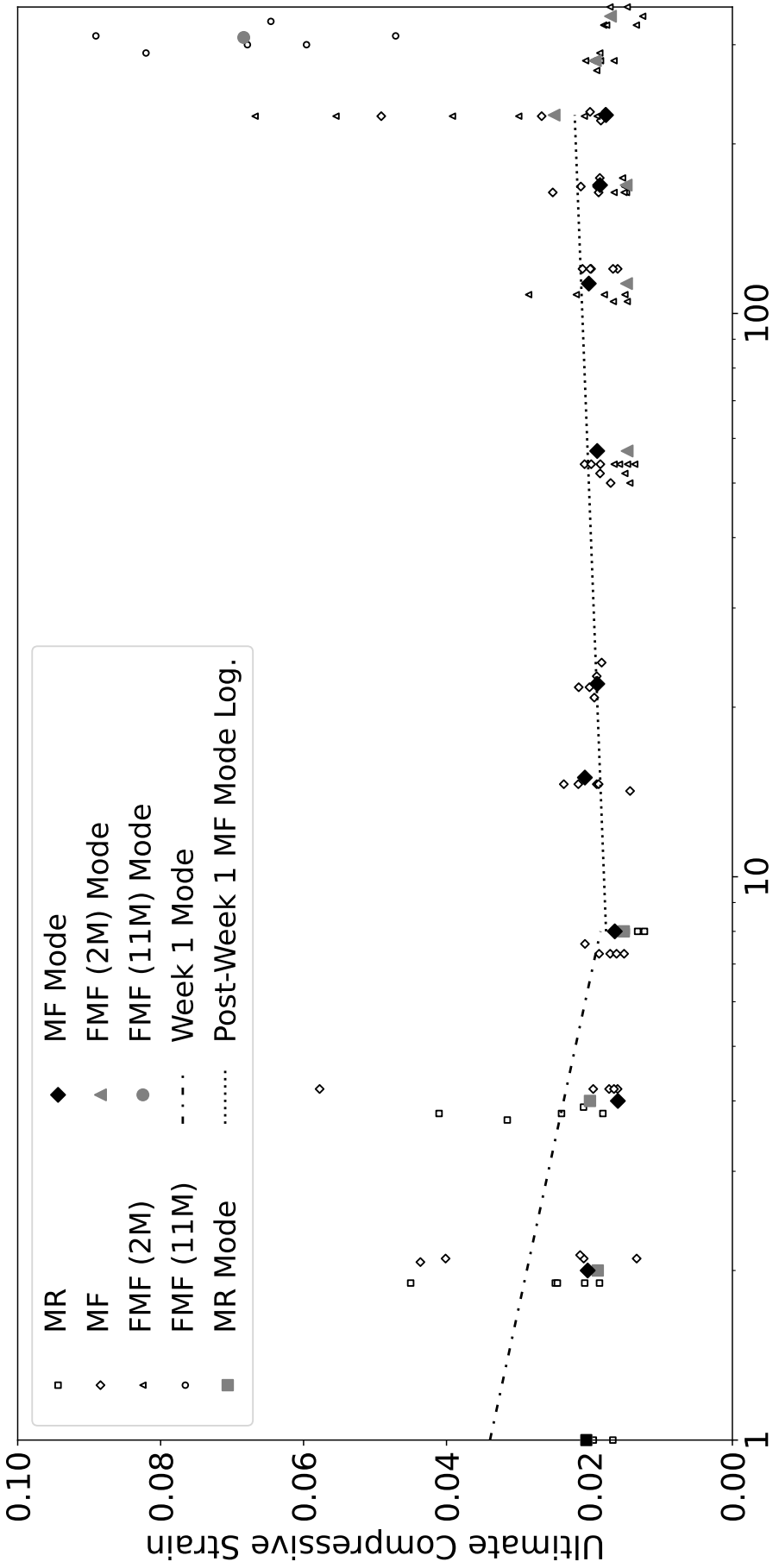

Figure 5.7 Graph of apparent UC Strain vs storage time from the degradation tests with modal values from each testing day. Slight horizontal offsets are for clarity.

stiffer than mild steel, such as tungsten, or inserts of stiffer materials can be integrated into the design of the subpress at the specimen interfaces. However, even with these modifications, the deformations as a result of the compliance could be reduced, but not removed entirely. Nevertheless, these compliance deformations are minimal, typically in the order of less than 10 microns, and can be accounted for theoretically should a stiffer material need to be tested using this subpress. For the cases stated in this study, the compliance as a result of local and global deformations did not emerge as a primary point of consideration.

Additionally, he time between donor death and the first series of tests was a limiting factor in the sense that the bones could not be retrieved any sooner than the timeline reported in this paper due to legal and medical constraints. While the results reported in this paper appear to be sufficient and representative, the ability to test bone prior to 12 hours post-mortem could provide valuable confirmation. Furthermore, this study was limited by the number of specimens that could be retrieved from a single donor bone. Hence, further testing is required from additional bovine donor bones to confirm these results.

5.3 Fresh Bone Tests

These sets of tests were conducted on specimens that were machined from bovine humeri that were deemed to be fresh, based on the results obtained from the degradation study, outlined in Section 5.2. These donor bones were retrieved within 24 hours of slaughter, frozen in a 0.9% concentrated saline solution at a temperature of $-32°C$. The next day the donor bones were allowed to thaw without any artificial interaction, and all of the specimens from those donor bones were machined and tested that same day. Based on the results from the degradation study, the freezing and thawing of the whole donor bones for one day after retrieval was deemed to have no effect on the measured mechanical properties of the bone specimens, and was hence considered representative of an in-vivo condition.
Two sets of fresh bone tests were conducted, each with their own respective donor bone. The first was a QS set of tests, wherein QS compression and bending were tested, and the second set of tests considered the QS and dynamic compression behaviour of the cortical bone specimens.

5.3.1 Quasi-Static Tests

These tests were conducted using the custom subpress, discussed in Section 3.1, and the QS three-point bending setup, discussed in Section 3.2. A total of 25 specimens were tested on this testing day, with 18 specimens tested in the QS compression configuration and 7 specimens tested in the QS bending configuration.
All 25 of the specimens underwent a visual inspection to identify any obvious defects, and none of the specimens appeared to exhibited any such anomalies. The compression specimens had an average density of 1999 kg/m^3, with a standard deviation of 83 kg/m^3, while the bending specimens had an average density of 2092 kg/m^3, with a standard deviation of 34 kg/m^3.
The specimens tested under the compression testing protocol exhibited an average apparent elastic modulus of 4.79 GPa with a standard deviation of 0.98 GPa. These specimens exhibited an average UCS of 142 MPa and a standard deviation of 26 MPa. The strain at which the UCS was recorded averaged 0.056 for all of the QS compression specimens, with a standard deviation of 0.010.
The seven bending specimens exhibited an apparent elastic modulus of 18.41 GPa with a standard deviation of 1.39 GPa. The average maximum bending stress experienced by these specimens was 228 MPa, and this metric had a standard deviation of 23 MPa. Finally, the average specimen midpoint deflection at which these specimens experienced

their respective maximum bending stresses was 0.001 mm, with a standard deviation of 0.0001 mm.
Tables 5.6 and 5.7 summarize the results from the QS fresh bone tests.

Table 5.6 *Summary of the results from the QS compression fresh bone tests.*

Elastic Modulus [GPa]	UCS [MPa]	UC Strain [N/A]	Density $[kg/m^3]$
4.23	112	0.0617	1872
4.38	132	0.0500	1921
3.30	127	0.0639	1849
4.51	129	0.0458	1964
4.65	170	0.0509	2065
5.53	139	0.0675	2020
4.87	159	0.0658	2067
6.30	159	0.0580	1998
6.35	166	0.0668	2032
4.41	141	0.0502	2052
6.52	172	0.0547	2072
5.40	169	0.0528	2079
3.80	121	0.0455	1976
4.64	139	0.0540	2041
2.88	83	0.0501	1816
4.64	176	0.0773	2019
4.72	151	0.0522	2064
5.04	104	0.0335	2074

5.3.2 Strain Rate Sensitivity

These tests were conducted using the custom subpress, discussed in Section 3.1, and the compression SHB, discussed in Section 3.3. A total of 30 tests were conducted on this testing day, with 15 specimens allocated to QS tests and the other 15 specimens

Table 5.7 *Summary of the results from the QS bending fresh bone tests.*

Elastic Modulus [GPa]	UBS [MPa]	UBS Deflection [mm]	Density $[kg/m^3]$
16.28	204	0.0010	2080
18.22	251	0.0011	2119
17.04	235	0.0013	2047
18.68	203	0.0008	2060
20.15	251	0.0010	2083
18.75	205	0.0009	2109
19.78	248	0.0010	2142

allocated to the dynamic tests.

All 30 specimens were checked for any obvious defects, with only one specimen was deemed to have a defect as a result of a large blood vessel canal. These specimens had an average density of 2085 kg/m^3, with a standard deviation of 34 kg/m^3.

The QS tests yielded an average apparent elastic modulus of 5.77 GPa, with a standard deviation of 0.85 GPa. The average UCS for these specimens was 154 MPa with a standard deviation of 15 MPa, and the average UC strain was 0.052, with a standard deviation of 0.013. No anomalies were noted during the running of any of the tests.

Due to the nature of dynamic testing, it can be difficult to ensure that all of the requirements are met to consider a test valid. As a result, not all 15 of the dynamic tests were considered valid, with only five of the tests meeting the requirements for a valid test. The requirement to have the specimen loaded at a near-constant strain rate was the reason for a majority of the specimens not being considered valid. This requirement manifests itself in the strain rate history plots as a flat plateau on the peak of the plots, as shown previously in Figure 5.1. Upon investigating the strain rate history of the specimen, no clear plateau would have been observed in the rejected cases, with most of the strain rate history of the specimens being similar to that shown in Figure 5.8.

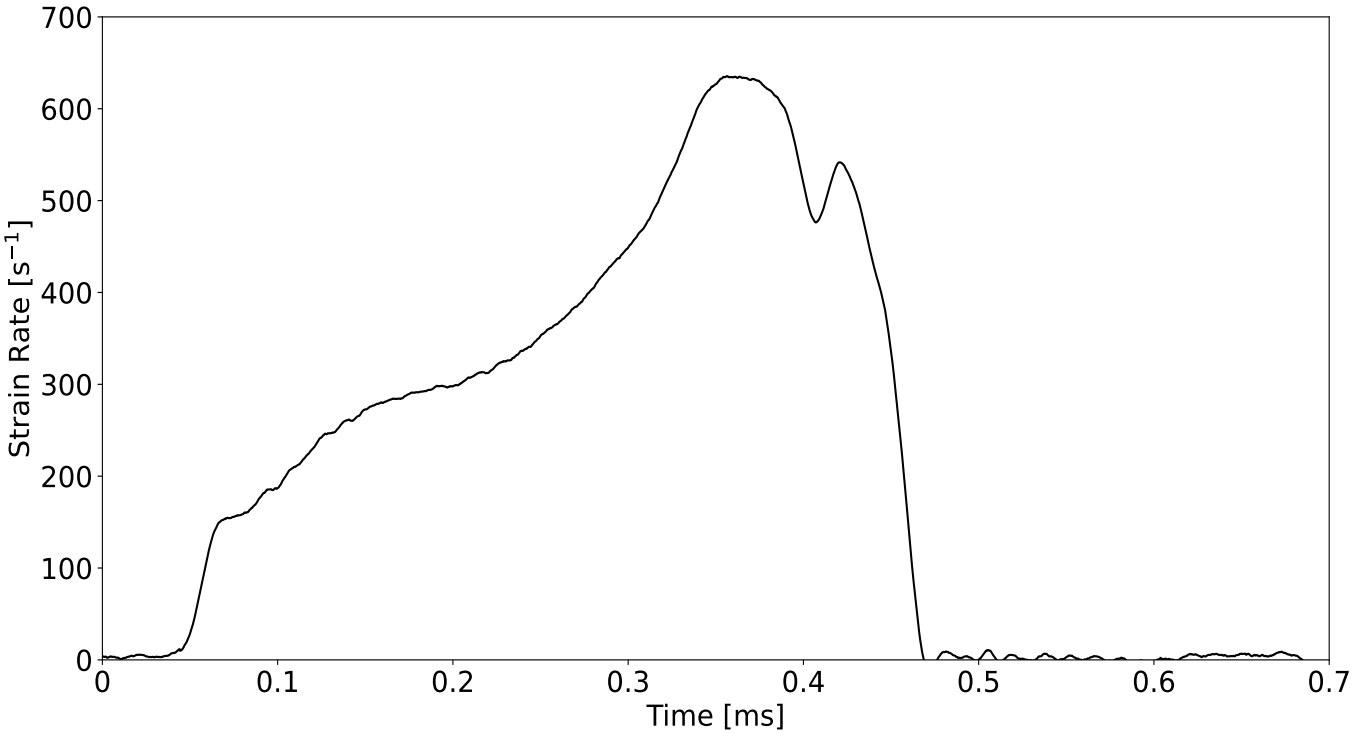

Figure 5.8 Typical strain rate history from a rejected dynamic compression test of a cortical bone specimen.

Additionally, specimens not being in a state of stress equilibrium deems a test to not be considered as valid, and a number of specimens in these tests did not achieve this stress state. This is evident by the stress histories of the SHB. The difference between the input and reflected waves in the input bar should be equal to the transmitted was in the transmission bar, however, in the case of some specimens, this requirement was not met. Therefore, based on these criteria, the average apparent elastic modulus of the cortical bone specimens for these dynamic tests was 9.88 GPa with a standard deviation of 1.40 GPa. The average UCS for these specimens was 214 MPa, with a standard deviation of 27 MPa. The average strain at which the UCS was experienced for these specimens was 0.042, with a standard deviation of 0.009. The valid results from these tests were all conducted in the strain rate range of between 141 s^{-1} and 181 s^{-1}.
Figure 5.9 shows the summarized results from these strain rate sensitivity tests.

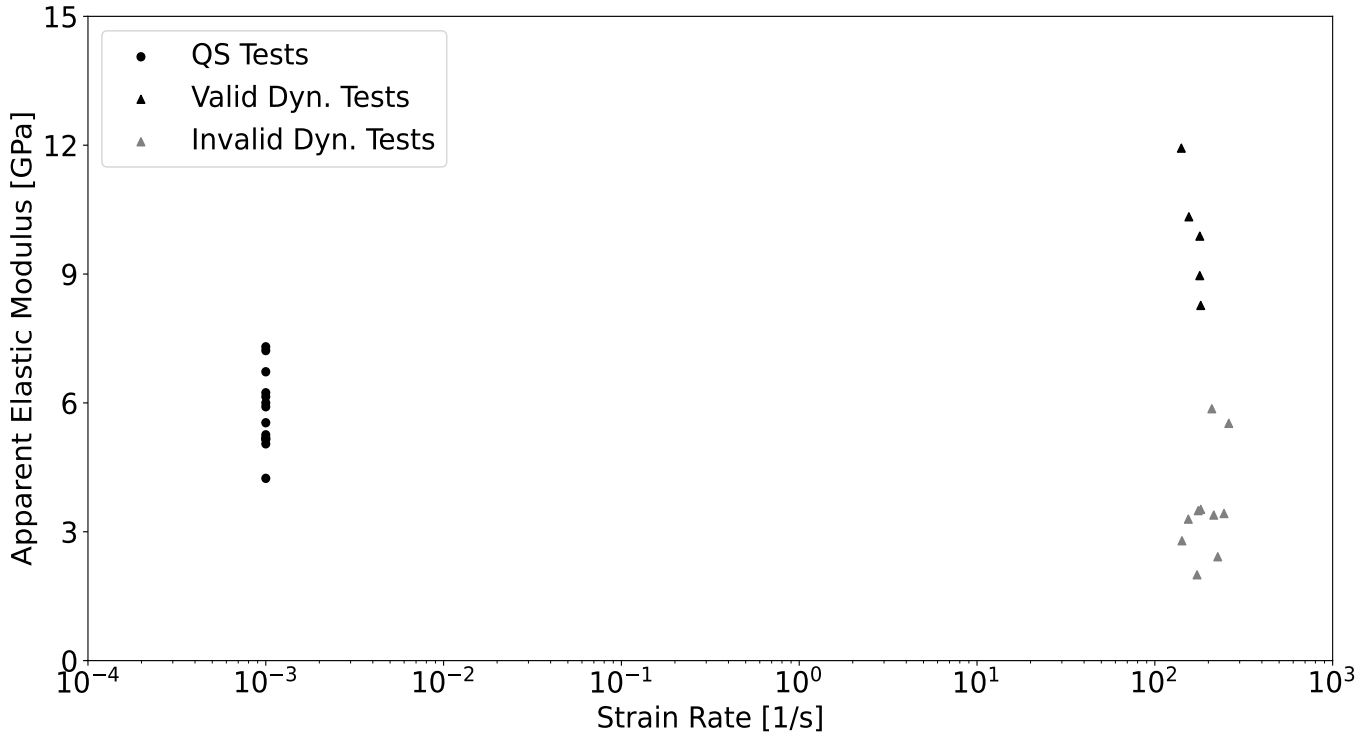

Figure 5.9 Graph of the apparent elastic modulus vs strain rate from the fresh bone strain rate sensitivity tests.

5.4 Bone Cross-Section Tests

The combination of the bending SHB and the high-speed camera successfully captured the quantitative force-displacement histories and the qualitative deformation and fracture information of the cortical bone cross-section specimens.
During the preliminary trial experiments for this testing technique, specimens were tested with alternating long axis orientations of the inner hole of the specimen (i.e.parallel then perpendicular) to the axis of the SHB. These tests were conducted on a donor bone used exclusively to refine this testing technique, with an additional donor bone being used for quantitative data that will be subsequently discussed. This technique refinement additionally was used to determine if the orientation of the specimen had an effect on the mechanical performance. Based on these tests, no such bias was identified, hence, it was decided that the long axis of the inner hole of the cross-section specimens was to be parallel with the axis of the SHB for the remaining tests. Figure 5.10 shows an example of the orientation of a cross-section specimen in the bending SHB.

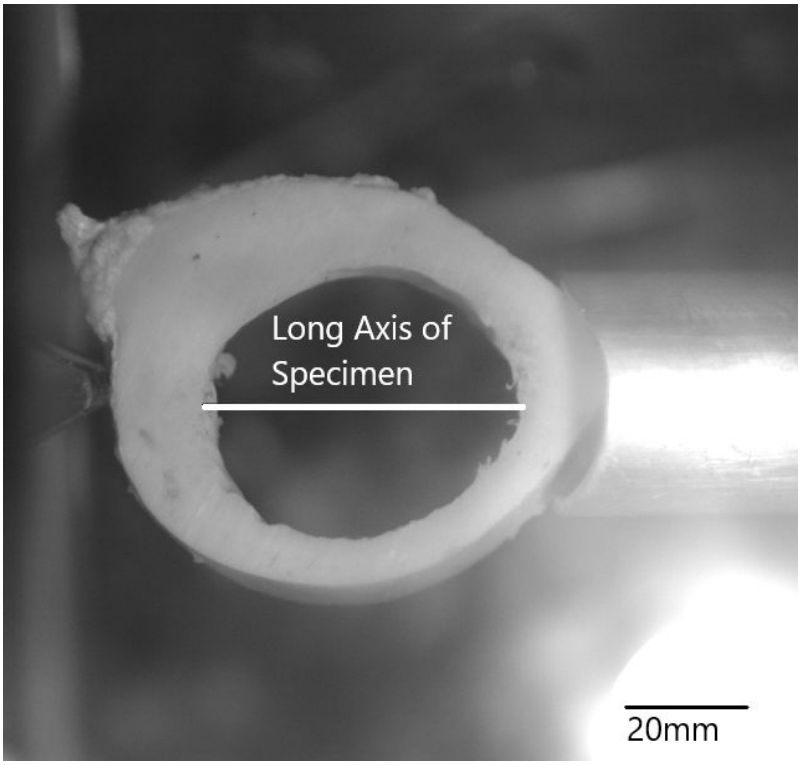

Figure 5.10 Image highlighting the long axis of the inner hole of the cross-section specimen used to identify the correct orientation of the specimen for testing.

Due to the inherent tapering of the donor bone, specimens featured varying levels of robustness. Hereafter, the term 'robustness' will refer to the complement (i.e. the complement of x would be $1 - x$) of the ratio of the total cross-sectional area of the internal hole relative to the total cross-sectional area of the specimen. For example, a perfectly circular specimen has a total cross-sectional area of 10 mm^2 and that same specimen has an internal hole with an area of 3 mm^2, the robustness of the specimen, under the definition given above, would be $1 - \frac{3}{10} = 70\%$. Figure 5.11 shows examples of specimens with 87.70% (Figure 5.11a) and 52.16% (Figure 5.11b) robustness respectively.

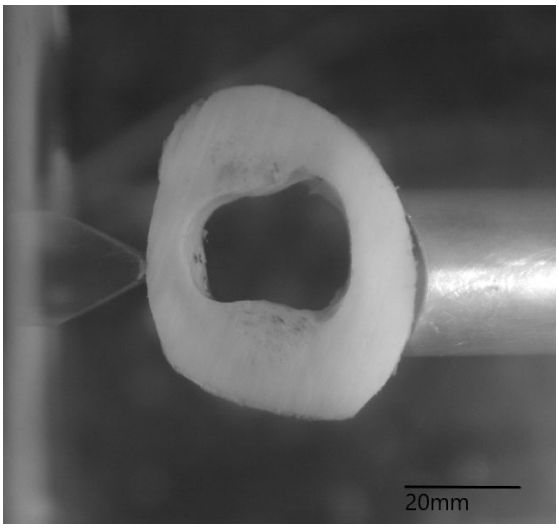

(a) Example of a more robust cortical bone cross-section specimen (Robustness = 81.7%) obtained from the distal (lower) region of the whole donor bone.

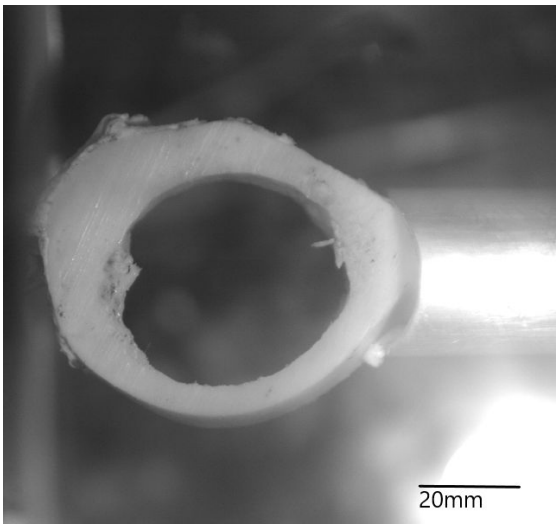

(b) Example of a less robust cortical bone cross-section specimen (Robustness = 52.2%) obtained from the proximal (upper) region of the whole donor bone.

Figure 5.11 Comparison of the varying levels of robustness of the cortical bone cross-section specimens.

A total of eight cross-section specimens were retrieved from the donor bone. Figure 5.12 illustrates the locations of the eight cross-section specimens from the donor bone.

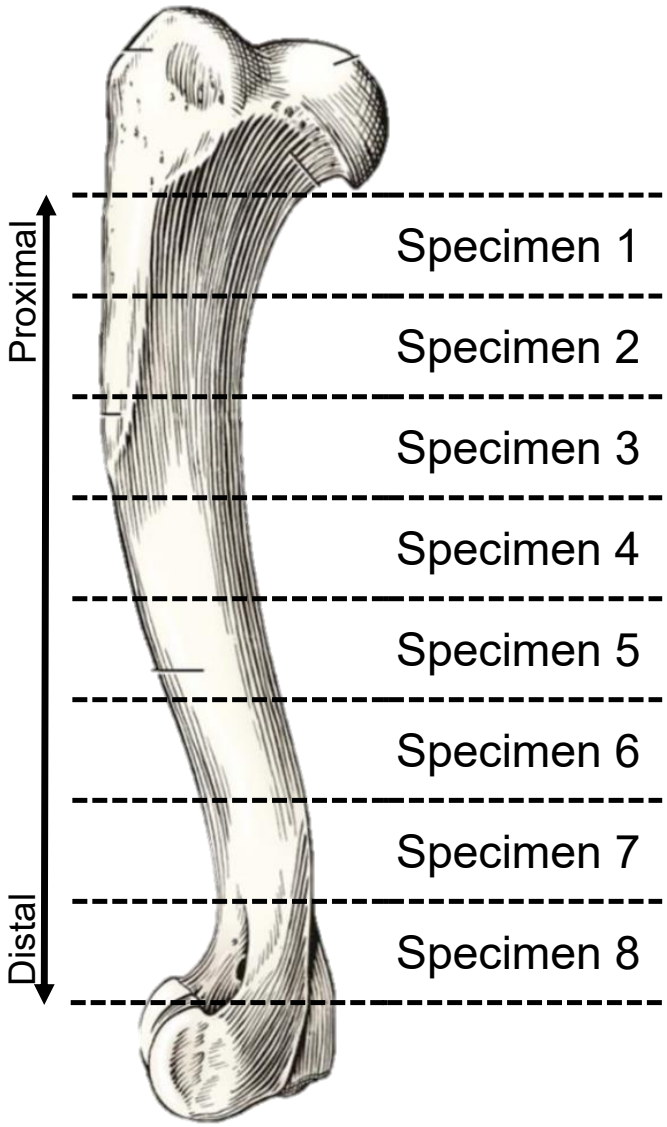

Figure 5.12 Locations along the donor bone from which cross-section specimens were retrieved.

The primary differentiator between these two types of specimens is the amount of cortical region relative to the outer circumference of the specimen. Specimens machined from the more distal (lower) regions of the donor bone featured far less bone marrow than the proximal (upper) specimens, and were more robust as a result. This difference was also observed in the force-displacement histories of the specimens. The more robust specimens exhibited higher load-bearing capabilities and were far less flexible than the more gracile specimens. Figures 5.13 and 5.14 are the respective force-displacement histories of the two specimens shown in Figures 5.11a and 5.11b.

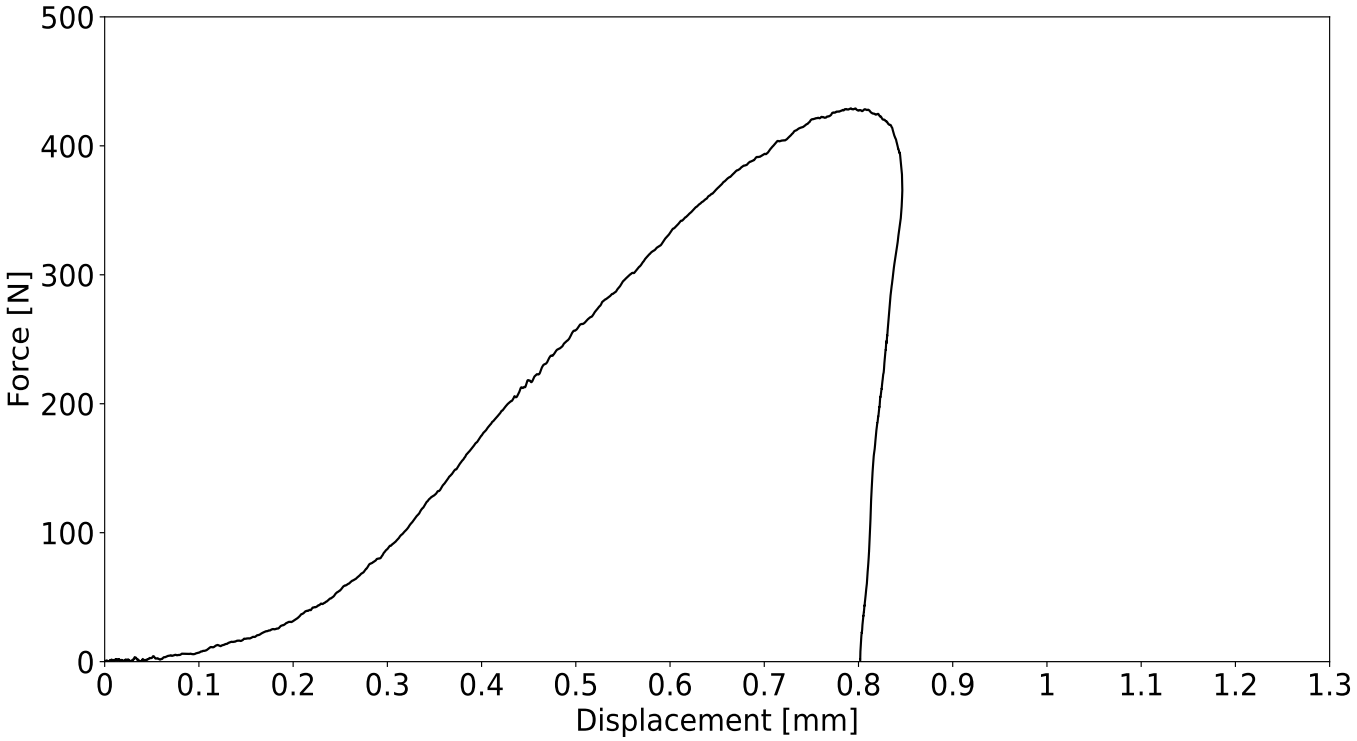

Figure 5.13 Graph of force vs displacement for a more robust cortical bone cross-section test.

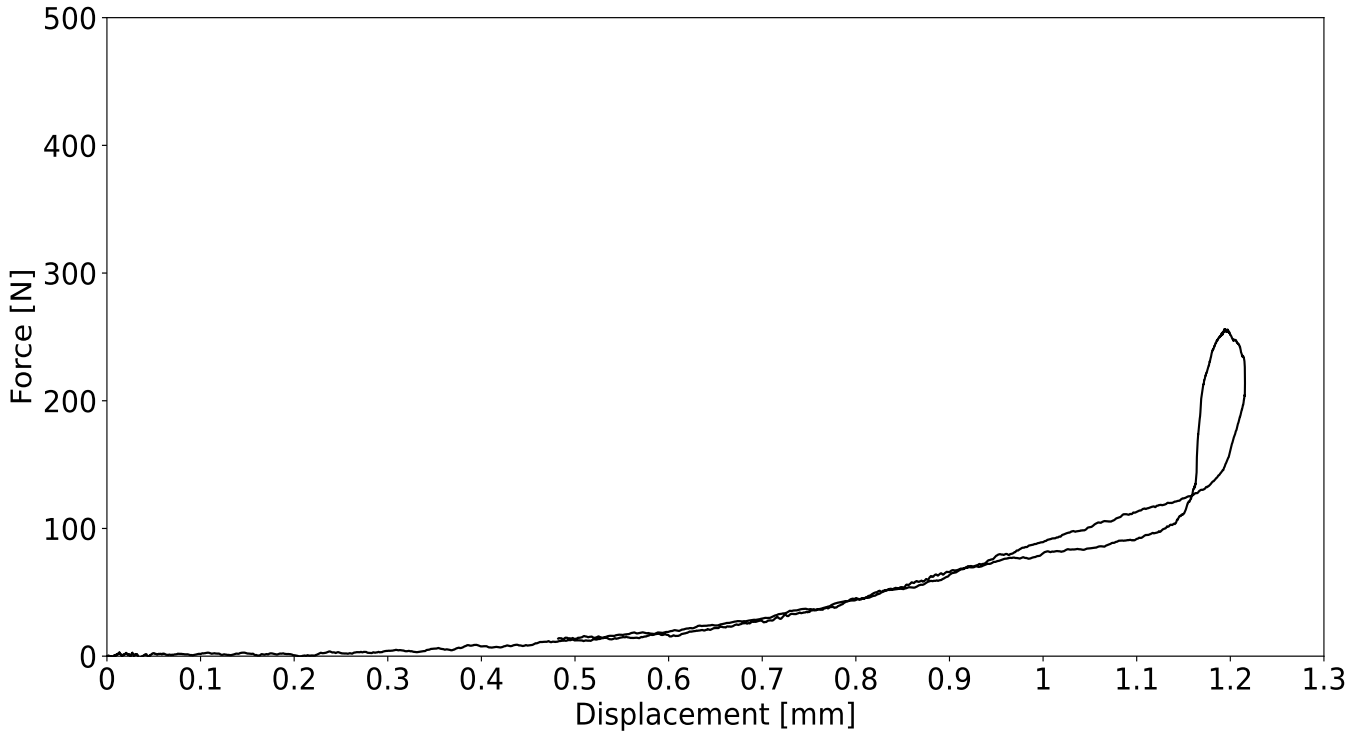

Figure 5.14 Graph of force vs displacement for a less robust cortical bone cross-section test.

The trends of increased strength and decreased flexibility with degree of distal positioning were clearly observed from these tests. Loading bearing capabilities reduced to approximately 40% when comparing the most distal and proximal specimens. The maximum displacement measured during these tests ranged from approximately 0.8 mm for the most distal specimen and 1.2 mm for the most proximal specimen. Furthermore, the SHB was able to clearly measure the rebound of the proximally located specimens after loading. This is shown in Figure 5.14 by the sharp increase in measured force as the elastic potential energy of the specimen reaches a maximum, and the drastic decrease in the measured displacement as the specimen rebounds back into the SHB. No specimen fracture or failure was recorded during these tests.
The high-speed camera was able to capture the deformation of the specimens during loading.

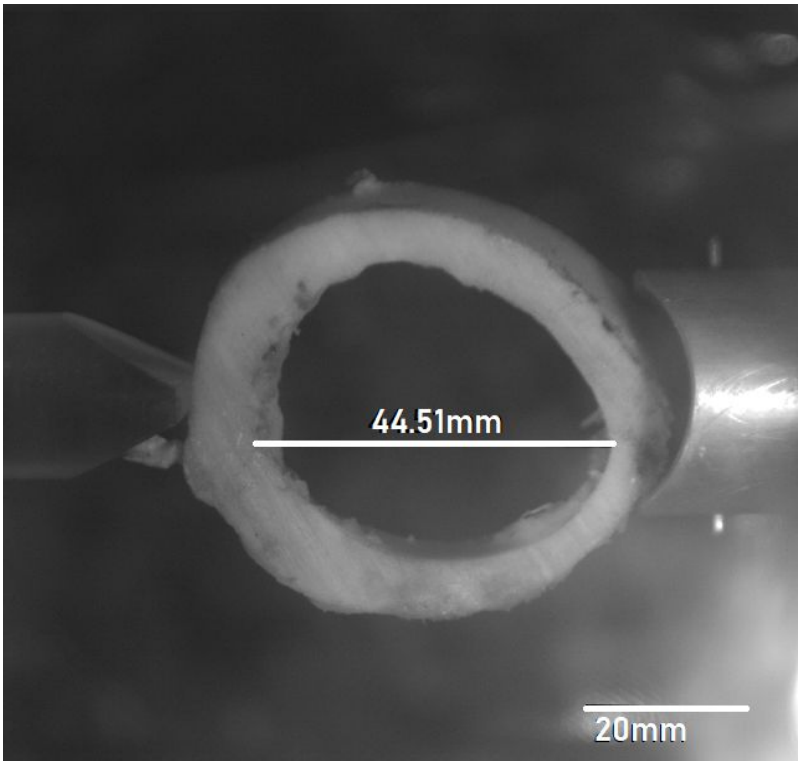

Figure 5.15 Image of a cortical bone cross-section specimen prior to loading with no deformation.

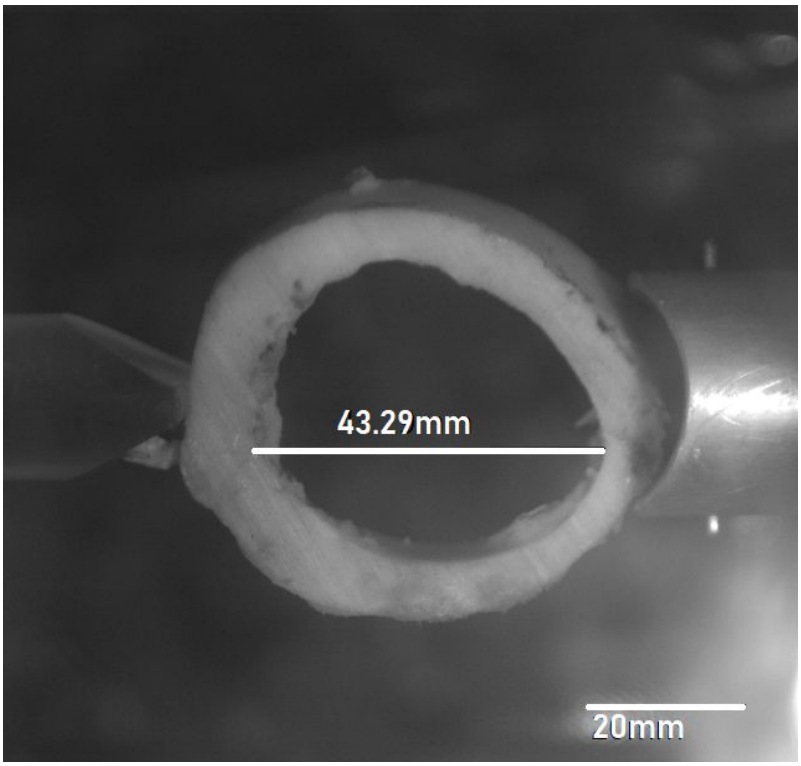

Figure 5.16 Image of a cortical bone cross-section specimen under maximum load and deformation at t=0.19 ms.

Stiffness of the specimens decreased with a decrease in robustness. A maximum stiffness of approximately 950 N/mm was recorded for the second most robust specimen and a minimum stiffness approximately 240 N/mm was recorded for the least robust specimen. Table 5.8 summarizes the measured properties of the cross-section specimens with the most distal specimen being listed on the far left moving towards the most proximal specimen being listed on the far right.

Table 5.8 *Summary of the material properties of cross-section specimens tested on the bending SHB ordered from most distal (left) to most proximal (right).*

Specimen #	1	2	3	4	5	6	7	8
Robustness [%]	81.7	76.8	74.3	75.3	67.9	64.6	58.3	52.2
Stiffness [N/mm]	902	945	808	793	684	556	457	237
Max. Force [N]	429	388	397	348	279	251	271	256
Max. Disp. [mm]	0.85	0.90	0.88	0.81	0.81	0.79	1.08	1.22

5.5 Computational Simulations

5.5.1 Dynamic Compression Specimen Simulations

The use of the strain-rate dependent plasticity material model (hereafter referred to as the SRD model), which was introduced in Section 4.8.3, resulted in distinct specimen behaviour when compared to the results from the use of the piecewise linear plasticity material model used in the THUMS simulation (hereafter referred to as the PL model). Both material models have the option to select a failure subroutine which dictates, firstly, if failure is considered, and secondly what criteria is used to determine if element failure has occurred. The PL model only offers an effective plastic strain failure flag, and this parameter was set to 0.0214 in the THUMS simulation. The SRD model offers three different failure subroutines. The first is the same effective plastic strain failure flag, the second is a maximum and an absolute minimum principal stress failure flag, and the final subroutine is a purely maximum principal stress failure flag. All three failure flags of the SRD model were considered in this comparison.

Initially, the material parameters for the SRD model simulations were based on the results obtained from the degradation study, however a further set of simulations were run with the results from the dynamic compression fresh bone tests, which were reported in Section 5.3.2. Simulations that utilized the degradation study parameters will be referred to as SRD (Deg) simulations, while simulations that utilized the fresh bone test parameters will be referred to as SRD (Fresh) simulations.

There was no discernible difference between the seven simulations when considering the exterior stress gradients. All simulations predicted a smooth stress gradient that increased towards the centre of the specimen, as shown in Figure 5.17a. In all simulations the specimens appeared to be in stress-state equilibrium when considering the axial profile of the specimens, as shown in Figure 5.17b.

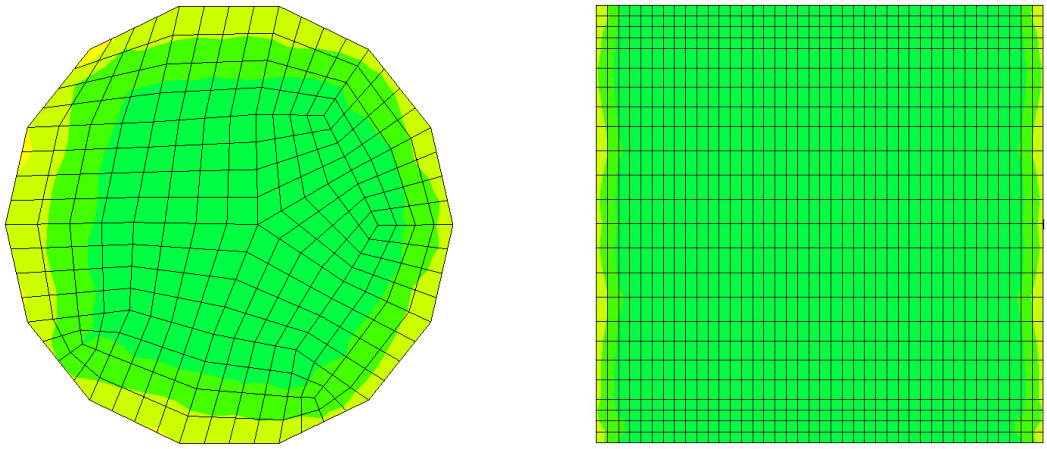

(a) Cross-sectional stress gradient. **(b)** Axial stress gradient.

Figure 5.17 Stress gradient results for the simulated dynamic compression cortical bone specimen with the SRD material model with the maximum and absolute minimum principal stress failure flag.

The SRD (Deg) model with the effective plastic strain failure flag was the only model that did not exhibit any element failure. The other two SRD (Deg) simulations and the PL simulation did exhibit failure exclusively on the surfaces that were in contact with the bars. This failure propagated towards the centre of the specimen as the simulations continued. Figure 5.18 shows an example of the type of failure observed during the simulations. However, the PL model, notably, exhibited failure far sooner into the simulation when compared to the other three simulations.

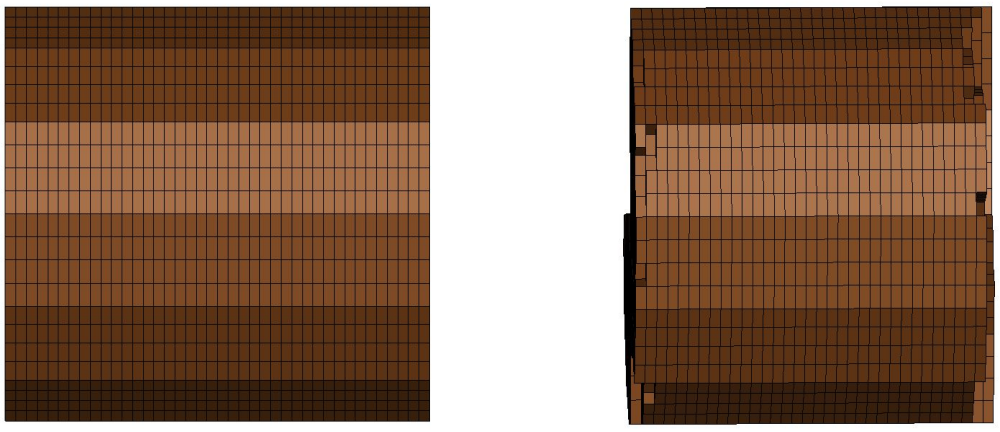

(a) Side-view of a simulated cortical bone specimen prior to failure. **(b)** Side-view of a simulated cortical bone specimen after failure.

Figure 5.18 Typical failure exhibited by the simulation. Element failure occurs exclusively on the faces of the specimen that were in contact with the bars.

All three of the SRD (Fresh) simulations exhibited specimen failure, in a similar way to the other simulations, however failure occurred far sooner into the simulation and failure was more catastrophic. Particularly in the SRD (Fresh) simulation with maximum principal stress failure flag activated, the observed failure in these SRD (Fresh) simulations propagated further into the specimen centre than the SRD (Deg) simulations.

Distinct differences were noted between the simulations when considering the planar cross-section of the specimens. The PL model exhibited a near-perfectly uniform stress distribution, however it must be noted that this was just prior to failure and that was only a quarter of the way through the simulation in this case. At this same point in time all of the specimens in the other simulations were in a stress-state equilibrium. The PL model exhibited a maximum specimen stress of 32 MPa at a strain of 0.017 prior to failure.

The SRD (Deg) model with the purely maximum principal stress failure flag activated exhibited a near-perfect stress-state across the specimen, with slightly higher stresses observed along the circumference of the specimen where it was in contact with the bars. Similar behaviour was observed with the SRD (Deg) material model with the maximum and absolute minimum principal stress failure flag activated. Both material models exhibited maximum specimen stresses of just over 40 MPa and both specimens exhibited highly brittle behaviour with failure occurring at strains less than 0.002.

The SRD (Deg) model with the effective plastic strain failure flag activated exhibited distinct behaviour when compared to the other simulations. It exhibited the highest maximum specimen stress, reaching a stress of 296 MPa at a strain of 0.022. Furthermore, the stress distribution with this simulation was the only one to not be uniform at the point of maximum compressive stress, but rather exhibited stress concentrations along the shear planes of the specimen. This resulted in an x-shaped stress distribution on the planar cross-section of the specimen at maximum load.

Figure 5.19 shows the planar cross-sections of the specimens from these simulations.

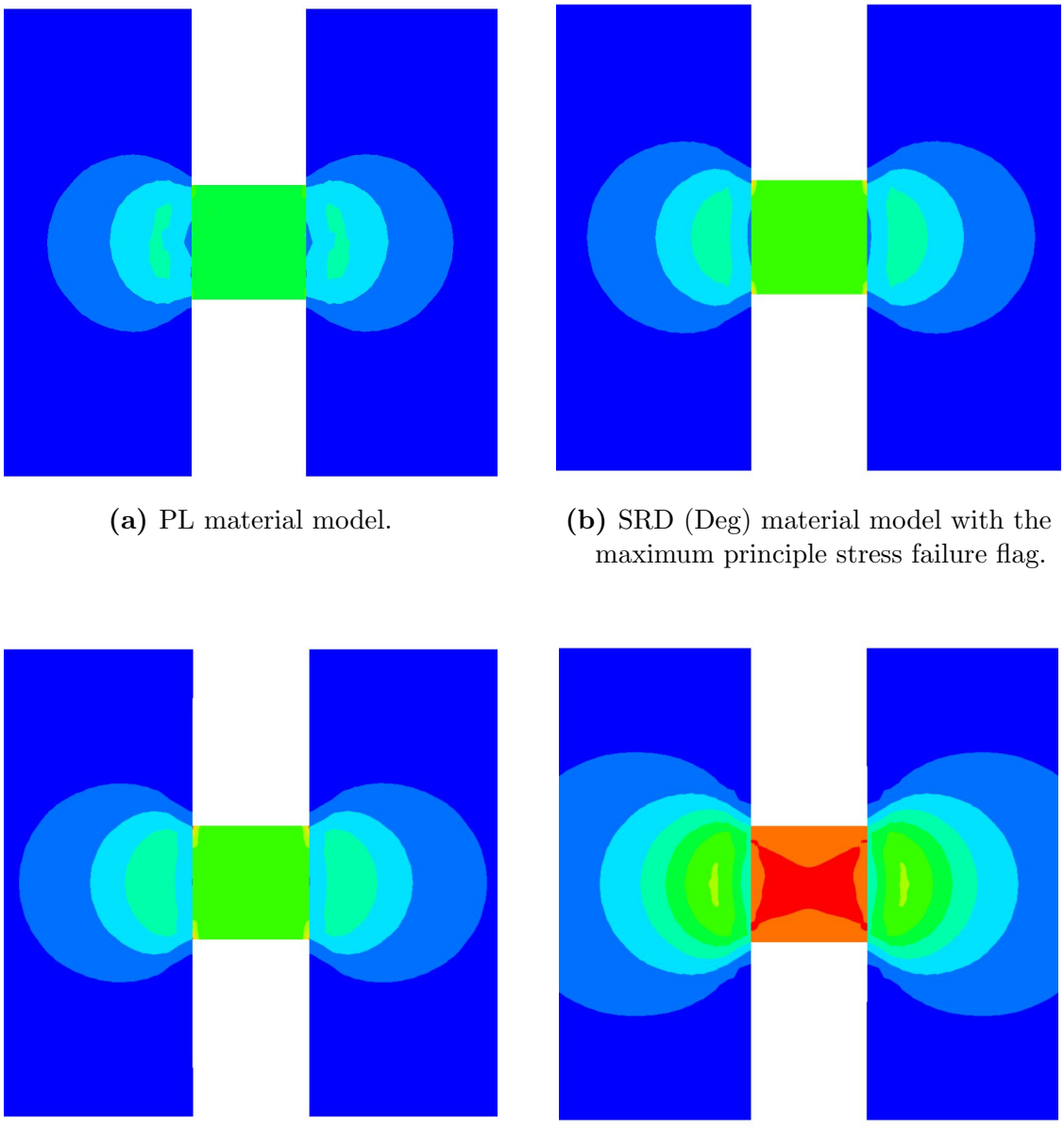

(a) PL material model.

(b) SRD (Deg) material model with the maximum principle stress failure flag.

(c) SRD (Deg) material model with the maximum and absolute minimum principle stress failure flag.

(d) SRD (Deg) material model with the maximum effective plastic strain failure flag.

Figure 5.19 Planar cross-section stress gradient results for the simulated dynamic compression degradation cortical bone specimen.

All of the SRD (Fresh) model simulations failed with a peak stress just above 25 MPa at a strain of approximately 0.0035. This highly weak and brittle behaviour is orders of magnitude lower than what was observed in the dynamic compression fresh bone tests reported in Section 5.3.2. These fresh specimen simulations exhibited similar planar

cross-section stress gradients to the SRD (Deg) simulations with the stress-based failure flag activated. Apart from minor stress concentrations around the circumferences of the specimens where they were in contact with the bars, the specimens were in a stress-state equilibrium. However, as was the case with the PL model simulations, these stress-states were observed just before failure, and at this point in the simulations, all of the specimens were in this stress-state.

Figure 5.20 shows the planar cross-sections of the specimens from the SRD (Fresh) simulations.

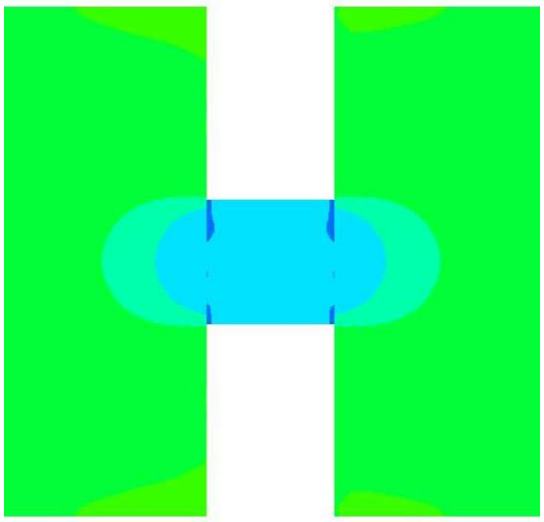

(a) SRD (Fresh) material model with the maximum principle stress failure flag.

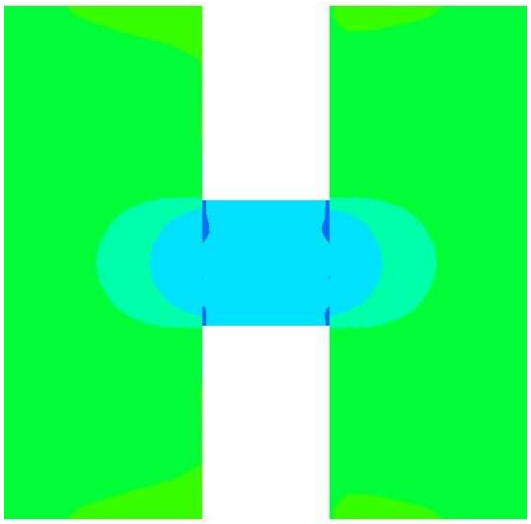

(b) SRD (Fresh) material model with the maximum and absolute minimum principle stress failure flag.

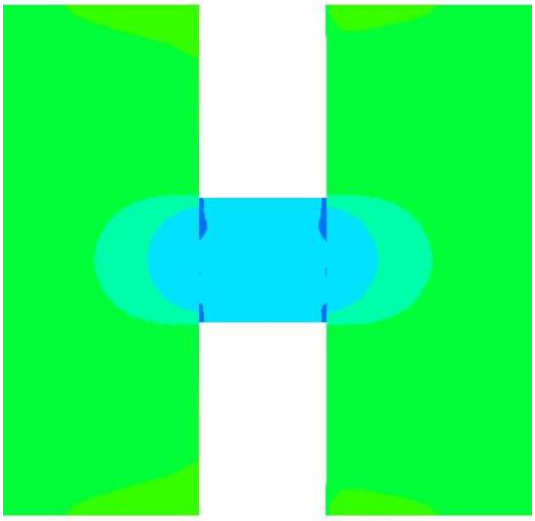

(c) SRD (Fresh) material model with the maximum effective plastic strain failure flag.

Figure 5.20 Planar cross-section stress gradient results for the simulated dynamic compression fresh cortical bone specimen.

5.5.2 Dynamic Cross-Section Simulations

Based on the results from the cross-section specimen experiments reported in Section 5.4, there is a clear trend with regards to cross-section specimen performance and level of robustness. As a result, two designs of cross-section specimen were simulated in these

dynamic cross-section simulations; type I II. Type I specimens would be categorized as the most robust, with a robustness of 68.50%, while type II was comparatively less robust with a robustness of 54.57%. The use of these two types of specimens allows the sensitivity of these materials models to be tested based on specimen robustness. As will be elaborated on in the discussion of the experimental cross-section tests, the level of robustness appears to have a high correlation with the apparent stiffness of the specimens in particular. Each specimen type will be simulated using the four material models mentioned in the previous section.

Upon initial runs of these simulations, severe oscillations were observed in the input tube as the reflected wave moved through the tube and as a result, the signals were not processable. Therefore, no meaningful specimen data could be extrapolated from the simulation if it were to be analysed as a physical SHB. Figure 5.21 shows an example of these oscillations.

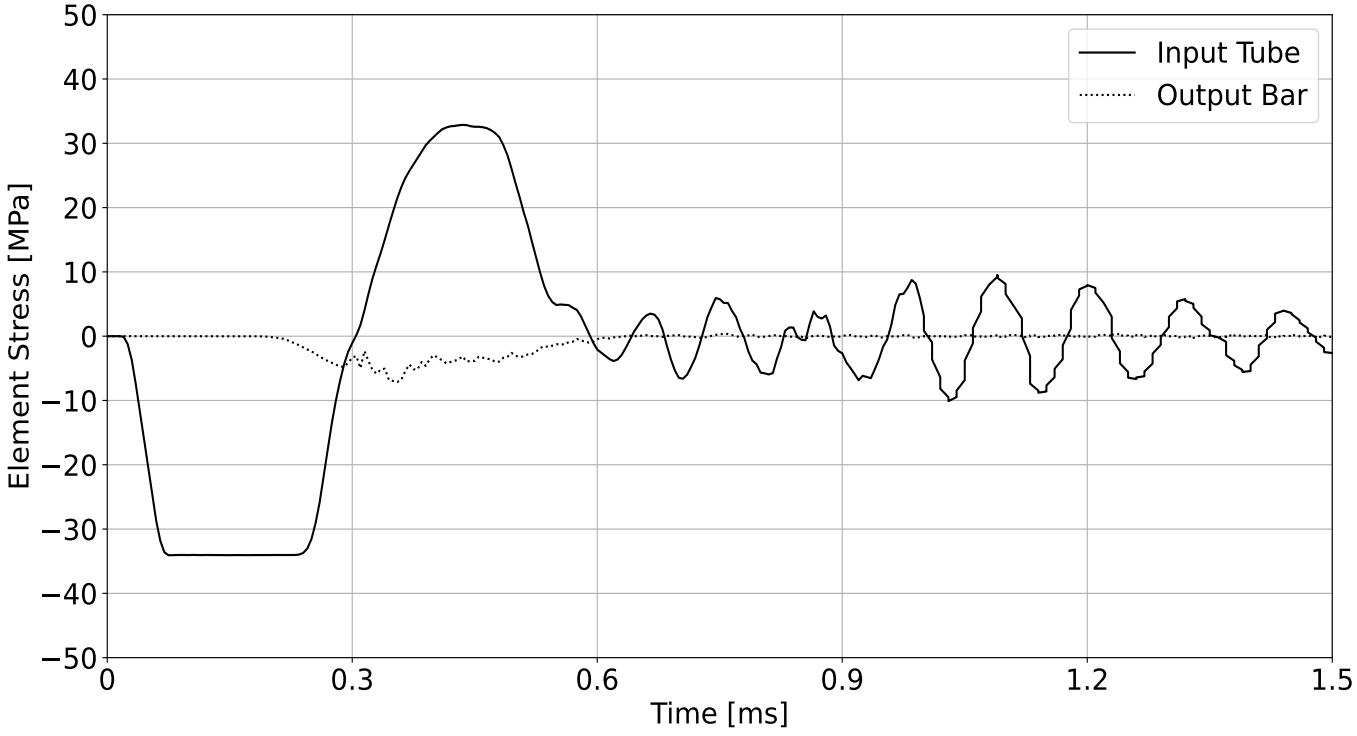

Figure 5.21 Graph of elemental stress vs time in the input tube and output bar for the dynamic cross-section simulations.

Upon further investigation, it was determined that these oscillations were originating when the input tube was not being loaded over its entire cross-section. Even when only one element was not loaded, minor oscillations were observed in the tube. As the loaded area decreased, for example to the point where cross-section of the input tube was only in

contact with the specimen, the oscillations became more severe. Hence, due to the input stress wave being applied to an entire internal face of the tube, these oscillations are not seen prior to the reflected wave. Figure 5.22 shows a front-view of the input tube with the loading regions of the specimen highlighted.

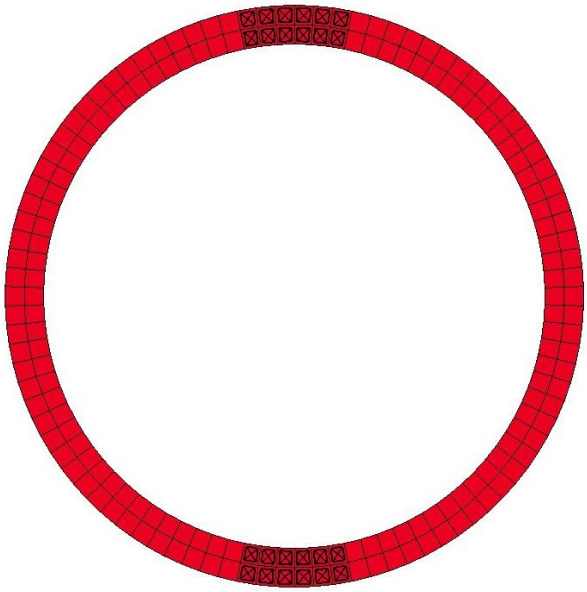

Figure 5.22 Front-view of the input tube from the dynamic cross-section simulations with the specimen would be in contact with the tube being highlighted.

It is hypothesized, based on the timing of what appears to be the start of the oscillations and the aforementioned investigation, that these oscillations originate as a result of the specimen unloading and pushing back into the input tube. Determining the mechanics behind why the oscillations occur at all is beyond the scope of this research.
In an effort to combat these oscillations it was decided that instead of applying an input stress to a particular face of the input tube, a prescribed displacement boundary condition was set on the tube which would result in the tube impacting the specimen. The force history of the specimen would then be interpreted from the output bar and the displacement could be measured directly from nodes on the specimen. This simplification could be done as the bending SHB does in fact impart a displacement on the specimens as a result of the stress wave traversing its length. Therefore, moving away from a stress-based input to a displacement-based input was a valid choice. This alternative did not yield the hoped results. Specimens would exhibit element failure, and hence deletion immediately as the input tube began to move, and this was not observed experimentally. Hence, this alternative was rejected and the original stress-based input was reimplemented.

As is the case with a physical SHB, the force history of a specimen is interpreted via the stress history of the transmission bar and displacement is interpreted via that of the input bar. Despite not being able to process the stress history of the input tube, nodal displacements are easily obtained and the stress history of the transmission bar was clear. Hence, the original setup could be used to interpret the response of the specimen after being dynamically loaded.

As a primary set of simulations, the bending SHB setup was simulated in order to determine where along the transmission bar the stress reading could be taken. Elements were measured at regular distances along the bar in order to determine at which point the stress wave had equilibrated. Based on these results, it was determined that the stress wave had equilibrated 180 mm from the specimen-end of the bar. This reinforced the decision to lengthen the transmission bar from 100 mm used in the dynamic compression simulations. Figures 5.23 and 5.24 show examples of the elemental stress histories of circumferential elements 100 mm and 180 mm away from the specimen-end of the transmission bar. The fact that the stress does not go back to zero in Figure 5.23 demonstrates that at that point in the bar, the stress wave has not yet equilibrated, hence, the stress reading must be taken further away from the specimen.

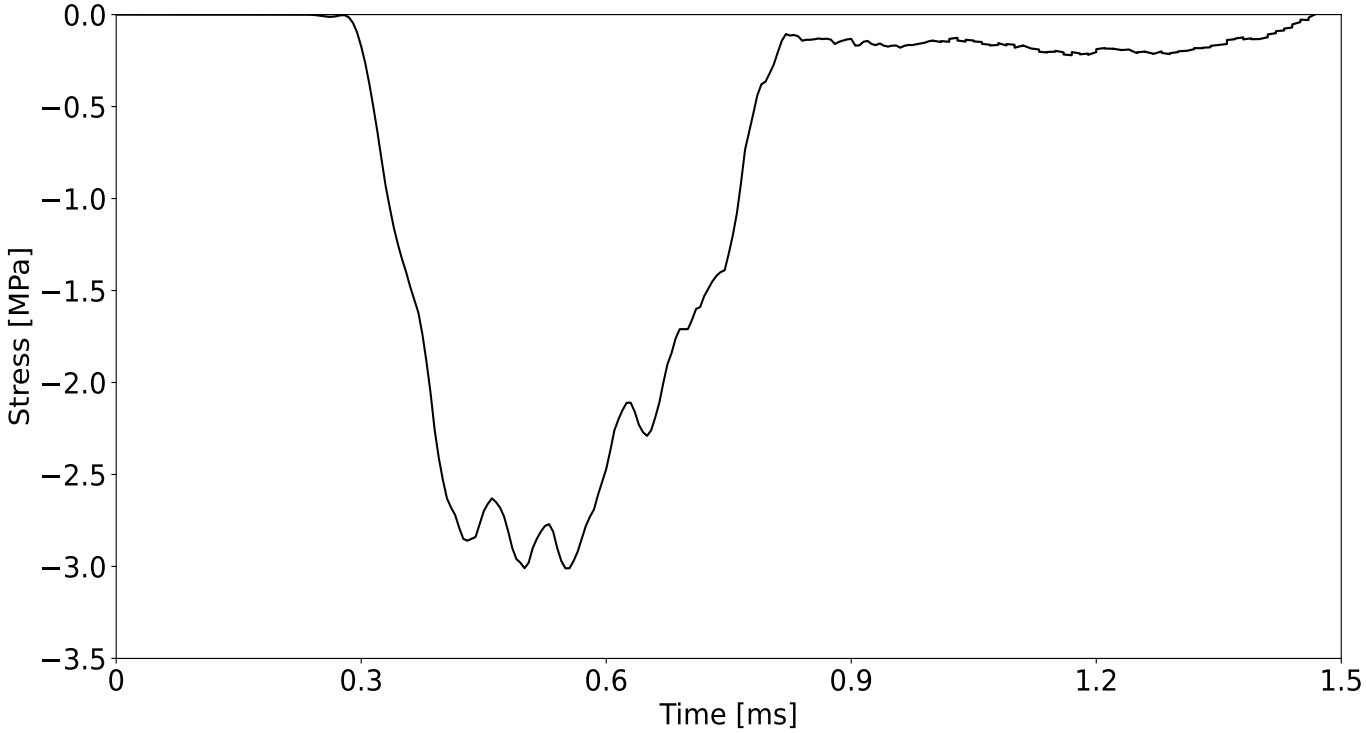

Figure 5.23 Graph of elemental stress vs time from a circumferential elemental 100 mm from the specimen-end of the transmission bar.

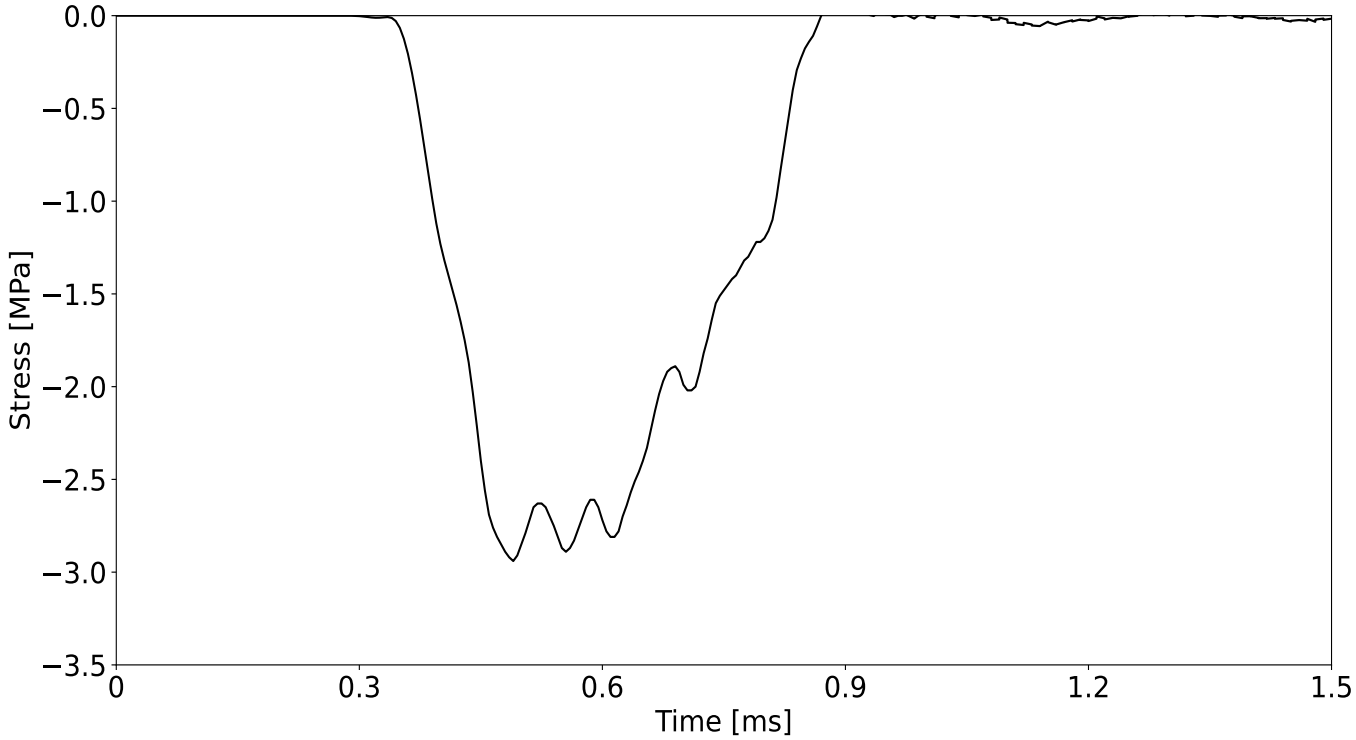

Figure 5.24 Graph of elemental stress vs time from a circumferential elemental 180 mm from the specimen-end of the transmission bar.

The transmission bar force history was obtained by dividing the individual elemental stress by their respective elemental areas for all of the elements of the cross-section at this distance away from the specimen. These individual elemental forces could then be averaged and plotted against time to obtain the force history of the transmission bar. The relative displacement of the specimen was obtained as the difference between the nodal displacement history at the points of contact of the input tube and output bar with the specimen. An example of the force-time graph from one of the simulation is shown in Figure 5.25.

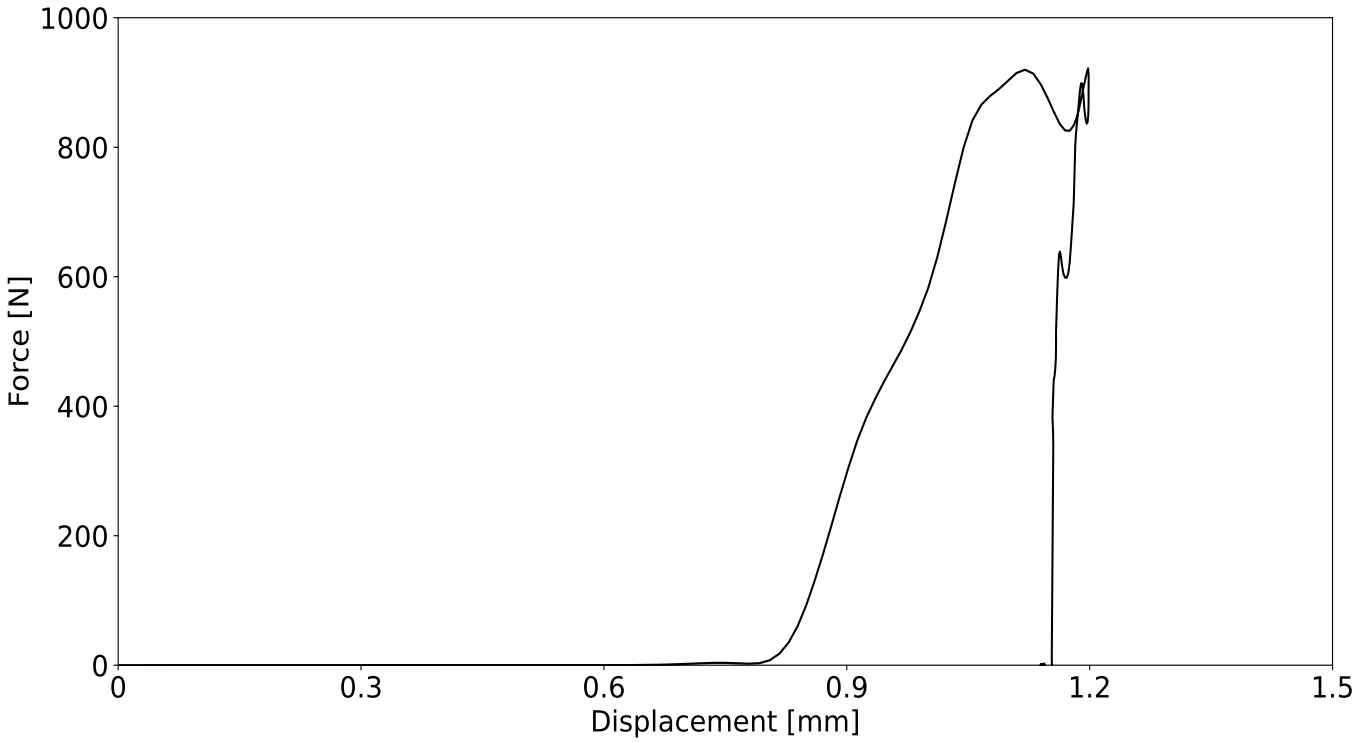

Figure 5.25 Typical force vs time for a specimen from the cross-section simulations.

As was with the dynamic compression specimens simulations, the PL model was compared to two variations of the SRD model. The first variation of the SRD model was parametrized using the material properties obtained from the degradation study, which will hereafter be referred to as SRD (Deg) simulations. The second variation of the SRD model simulations was parametrized using the material properties obtained from the fresh bone tests, which will hereafter be referred to as the SRD (Fresh) simulations. Furthermore, each of the three failure subroutine available for the SRD model were considered in this comparison.

From a qualitative perspective, the specimens with the SRD model, with the maximum and absolute minimum principle stress failure flag active, regardless of the model being parametrized with the degradation data or the fresh data, performed the least like the physical cross-section specimens. This material model exhibited elemental failure in three of the four simulations in which it was implemented. Beyond these elemental failures with this failure flag activated in the SRD model, the other material models occasionally exhibited minor element deformations at the interfaces of the specimen and the SHB.

Figure 5.26 shows an example of typical cross-section specimen failures.

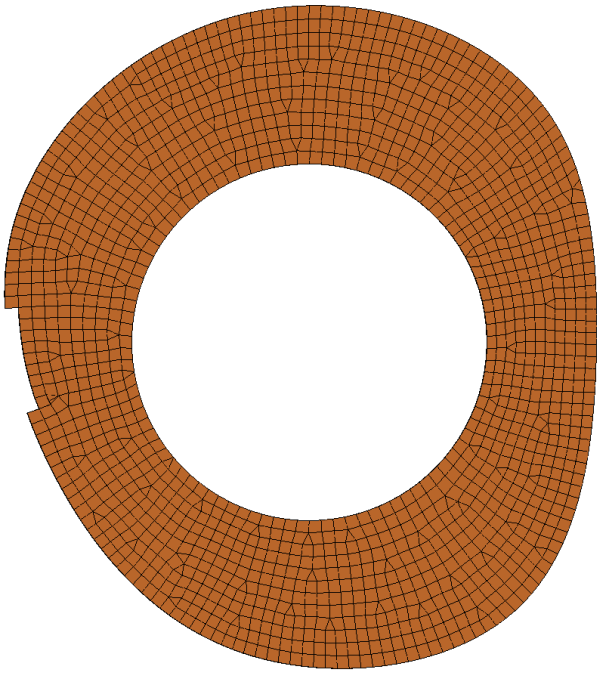

Figure 5.26 Typical cross-section specimen failure from the dynamic cross-section simulations.

From a quantitative perspective, none of the materials models were able to accurately recreate the material metrics that were obtained experimentally.
The PL model exhibited also exhibited this substantially stiffer than expected behaviour. Unlike the last two iterations of the SRD (Deg) model, the PL model followed the expected trend with the type I specimen being stiffer than the type II specimen. The type I specimen exhibiting a stiffness of 16825 N/mm, while the type II specimen exhibited a stiffness of 5955 N/mm. The PL material model exhibited similar maximum specimen forces to the SRD (Deg) model with the effective plastic strain failure flag activated. The type I specimen experienced a maximum force of 1834 N, and the type II specimen experienced a maximum force of 1553 N.

The SRD (Deg) model with the effective plastic strain failure flag active performed the least representatively of physical behaviour when compared to the other degradation-based simulations. This material model exhibited a specimen stiffness ranging from 14222 N/mm for the type I specimen to 7564 N/mm for the type II specimen. A similar trend of exhibiting a significantly stronger specimen was observed in the maximum forces the specimen experienced with this material model being used. The maximum forces experienced by the specimens in these simulations far exceeded those that were recorded experimentally. The forces ranged from 1874 N for the type I specimen to approximately 1581 N for the type II specimen.

The SRD (Deg) model with the maximum and absolute minimum principle stress failure flag active exhibited the next stiffest specimens and was still an order of magnitude greater than what was recorded experimentally. This simulation exhibited a specimen stiffness of approximately 6900 N/mm for the type I specimen and 7564 N/mm for the type II specimens, despite the type II specimens having a robustness 13% less than that of the type I specimen. As was with the previous material model, these simulations exhibited maximum forces far greater than the experimental data. Maximum forces ranged from 1581 N for the type II specimen, to 1398 N for the type I specimen. This material model did exhibit element failure, and hence deletion, where as none of the other simulation exhibited element failure.
The final iteration of the SRD (Deg) model, with the purely maximum principal stress failure flag active, exhibited the most erratic results out of the SRD (Deg) model iterations. This material model, as was with the previous, exhibited that the type I specimen would be less stiff than the type II specimen. Specimen stiffness for the type I specimen was 981 N/mm, while that type II specimen stiffness was 7564 N/mm. Despite these erratic results regarding stiffness, the maximum forces experienced by the specimens appeared more in-line with what was observed experimentally. The type I specimen appeared to bear the greatest load, with a maximum of 1883 N, while the type II specimen appeared to bear a load of 1581 N.

The SRD (Fresh) model with the effective plastic strain failure flag active exhibited near-instant element failure with the type I specimen, and as such, no numerical data could be obtained from that specimen. With regards to the type II specimen, this material model exhibited a specimen stiffness of 3225 N/mm and a maximum specimen force of 1471 N.
The SRD (Fresh) model with the maximum and absolute minimum principle stress failure flag active exhibited element failure for the type I specimen, and for this specimen exhibited a stiffness of 6473 N/mm and a maximum specimen force of 870 N. The type II specimen exhibited a stiffness of 3225 N/mm and a maximum specimen force of 1471 N.
The SRD (Fresh) model, with the purely maximum principal stress failure flag active, exhibited behaviour similar to the degradation-based variation of this model. The stiffness and maximum specimen force were higher for the type II specimen than the type I specimen. The type I specimen exhibited a stiffness of 870 N/mm and a maximum specimen force of 151 N, while the type II specimen exhibited a stiffness of 3225 N/mm and a maximum specimen force of 1471 N.
Table 5.9 summarizes the quantitative data from the cross-section simulations.

Table 5.9 *Summary of the material metrics from the cross-section specimen simulations.*

Mat. Mod. [N/A]	Fail. Flag [N/A]	Spec. Type [N/A]	Stiffness [N/mm]	Max. Force [N]	Max. Disp. [mm]
PL	-	1	1302	828	0.947
PL	-	2	649	950	0.978
SRD (Deg)	Plas.	1	14222	1874	0.515
SRD (Deg)	Plas.	2	7564	1581	0.589
SRD (Deg)	Max&Min	1	6879	1398	0.971
SRD (Deg)	Max&Min	2	7564	1581	0.589
SRD (Deg)	Max	1	981	1883	0.516
SRD (Deg)	Max	2	7564	1581	0.589
SRD (Fresh)	Plas.	1	0	0	0
SRD (Fresh)	Plas.	2	3225	1471	0.707
SRD (Fresh)	Max&Min	1	6473	870	1.075
SRD (Fresh)	Max&Min	2	3225	1471	0.707
SRD (Fresh)	Max	1	870	151	0.644
SRD (Fresh)	Max	2	3225	1471	0.707

A possible explanation for these extremely high specimen stiffnesses would be the fact that the specimens are not being loaded longitudinally with respect to the orientation of the original donor bone. Rather, these specimens are being loaded transversely and this would result in the anisotropy of the material needing to be accounted for. As discussed in Section 2.2.1, the literature reports that the apparent elastic modulus of cortical bone in the transverse direction can be approximately 40% of the axial apparent elastic modulus. Furthermore, based on distinctly low apparent elastic modulus values from the fresh bone results reported in Section 5.3.2, using the apparent elastic modulus value of 23 GPa from the degradation study might be contributing to extremely high specimen stiffnesses. As such, these same simulations were rerun using an apparent elastic modulus value of 3.95 GPa. This is 40% of the 9.88 GPa quoted in Section 5.3.2 as the dynamic apparent elastic modulus for that bone.

The SRD model with the effective plastic strain failure flag and the purely maximum principal stress failure flag activated both exhibited exactly the same behaviour for the two specimen types. For the type I specimen, both simulations exhibited a specimen stiffness of 1505 N/mm and a maximum specimen force of 114 N. The simulations with the type II specimens exhibited a specimen stiffness of 927 N/mm and a maximum specimen force of 1125 N.
The SRD model with the maximum and absolute minimum principle stress failure flag active was the only simulation to exhibit specimen failure with the type I specimen. This simulation with the type I specimen exhibited a stiffness of 5560 N/mm and a maximum force of 1292 was experienced by the specimen. The type II simulation exhibited the same results as the other two type II simulations with this fresh, transverse orientation elastic modulus. The type II specimen stiffness was 927 N/mm and the maximum specimen force was 1125 N.
Table 5.10 summarizes the quantitative data from the cross-section simulations.

Table 5.10 *Summary of the material metrics from the transverse orientation, fresh bone cross-section specimen simulations.*

Mat. Mod.	Fail. Flag	Spec. Type	Stiffness	Max. Force	Max. Disp.
[N/A]	[N/A]	[N/A]	[N/mm]	[N]	[mm]
SRD (Fresh)	Plas.	1	1505	114	0.742
SRD (Fresh)	Plas.	2	927	1125	0.870
SRD (Fresh)	Max&Min	1	5560	1292	0.868
SRD (Fresh)	Max&Min	2	927	1125	0.870
SRD (Fresh)	Max	1	1505	114	0.742
SRD (Fresh)	Max	2	927	1125	0.870

Chapter 6

Discussion

This chapter will include the in-depth analysis and investigation into the the results mentioned in the previous chapter. Thereafter, conclusions will be drawn based on the evidence that was made apparent in Chapter 5.

6.1 Apparatus Validation Tests

The wave speed tests served as the baseline value for the other apparatus validation tests. The reason for this is due to the fact that this testing method measures the behaviour of the material directly, through the use of the strain gauges, without inferring the material behaviour through other mechanisms, such as the crosshead displacement of a testing machine. Additionally, due to the nature of these tests, there is no possibility of machine compliance having an effect on the measure properties.
The tensile tests served as confirmation of the wave speed test results. As was expected, despite attempting to minimize the effects of machine compliance on the Zwick-only tests, the results were significantly offset. These results, along with those shown in Section 3.1.2, demonstrate that the current apparatus may not be capable of achieving the desired level of accuracy for this use case. However, the visual extensometer (VE) test results exhibited distinct improvements. Both the wave speed test results and the VE test results agreed within 3% of each other for both materials. Based on the previous work conducted on the VE, it was deemed that these results over this displacement were representative of the material when compared to those measured during the Zwick-only tests. Hence, the tensile tests confirmed the results obtained through the wave speed tests and the baseline was set for the remaining apparatus tests.
The quasi-static compression results highlighted interesting findings. The polymethyl

methacrylate (PMMA) results were slighting lower than the baseline measurement. This slight change could be attributed to the fact that these tests were conducted on different days, hence the ambient temperature was different on each day. With the temperature-dependent properties of polymers, such a change is plausible based on the reported literature [92–96]. Furthermore, the specimens were machined to the desired dimensions and through this process where high temperatures are experienced in the material, the polymer could have slightly altered at a molecular level. This could also account for the slight difference in results between the wave speed and tensile tests for the PMMA. Hence, with such a similar value, the quasi-static compression rig was deemed to operate satisfactorily on the polymer specimens. By contrast, the same cannot be said for the aluminium specimens. The custom rig measured an average apparent elastic modulus value for the aluminium less than a third of that of the baseline value. The hypothesis as to why such a low result was obtained is a combination of the stiffer material, along with the specimen geometry. The custom rig was designed with the intention of testing small specimens with maximum apparent elastic moduli values around 30 GPa, as is the case of cortical bone at these strain rates. The aluminium is over twice that value, hence the rig is operating outside of the intended range. Additionally, as a result of the small and robust specimen design, the specimens are stiffer than the plunger, hence the compliance of the rig begins to have an effect on the measured results. With the small specimen displacements that were being recorded for these tests, even the minimal machine compliance of the plunger can alter the results.

Attempts were made to conduct tests on lead specimens due to the material having a theoretical elastic modulus closer to 40 GPa. However, these specimens simply did not exhibit elastic behaviour for long enough for accurate apparent elastic modulus metrics to be extracted from the data. Hence, based on the results obtained in Section 3.1.2 and the PMMA results obtained from these tests, the custom rig was deemed to operate satisfactorily well for the case of tests conducted on cortical bone specimens, however, improvements must be made for it to be used to test stiffer materials.

The quasi-static bending validation tests yielded near-identical results to the baseline values. As was the case with the PMMA quasi-static compression results, the slight difference between these and the baseline values could be attributed to the temperature-dependence of the material. Both the quasi-static compression and bending tests were conducted on the same day and both results are closer to each other than to the baseline value, hence suggesting that the temperature-dependence could explain the difference to the baseline. Furthermore, the aluminium results agree with the baseline values within 0.5%, further suggesting that the PMMA is a volatile material to test. It

must be noted that these results were obtained after taking into account the compliance of the machine through the process outlined in Section 4.5.2. These results demonstrate that this spring theory technique for accounting for machine compliance works as intended and can be used to quantify, and therefore help account for, machine compliance from measured results. Finally, the quasi-static bending rig was deemed to operate satisfactorily for the testing of cortical bone specimens, provided that machine compliance is accounted for.

The dynamic compression validation tests were focused entirely on the testing of the PMMA specimens. Furthermore, through the use of the Cone-in-Tube (CiT) striker, these tests were conducted exclusively in the intermediate strain rate (ISR) regime. Due to the viscoelastic nature of the PMMA, it was expected that the apparent elastic moduli measured during these tests would be higher than that measured during the quasi-static tests. A clear increase in the apparent elastic modulus of the material was observed during these tests. At the lowest dynamic strain rate tested, 93 s^{-1}, the measured apparent modulus increased by approximately 11% from the baseline, and nearly doubled at the higher strain rates that were tested. The trend of increasing apparent elastic modulus with increasing strain rate is not perfectly linear in the results obtained from these tests. A possible explanation for this could simply be due to the small sample size of experiments conducted for these tests and due to the inherent volatility of the material, as has been discussed previously. Nevertheless, a notable increase in the measured apparent elastic modulus is clearly observed in the results from these tests. Furthermore, the CiT striker allowed for consistent and repeatable dynamic material tests to be conducted in the ISR regime. Hence, the dynamic compression apparatus was deemed to operate satisfactorily for the testing of cortical bone specimens.

Finally, the dynamic bending validation tests did not yield any successful results. Despite attempting to reduce the oscillations through a more robust specimen geometry and altering the test conditions, through manipulating the length of the input stress wave, lowering the firing speed of the striker and using pulse shaping techniques, no meaningful material property data could be extracted from the results. Using vibration theory, it was proven that the oscillations were in fact as a result of the specimens resonating due to the loading by the dynamic bending rig. The oscillations were reduced with a combination of the striker speed had been lowered to the lowest possible speed the gas gun could produce and a pulse shaping technique to smooth the loading stress wave, but under these conditions the induced force and displacement on the specimens was too small for any true material data to be extracted from the results. An input tube that would allow for greater specimen displacement while also increasing the length of

the input wave would potentially be able to reduce the oscillations. A possible option for such a solution would be a polymer tube, however sourcing such a piece of stock would be difficult, and, secondly, the wave dispersion would need to be corrected for, as it would be amplified by using the polymer input tube.

Apart from the dynamic bending apparatus, the results from these tests demonstrate that cortical bone specimens can be tested over a range of strain rates and loading types. The successful use of wave speed tests to obtain the inherent material properties of material stock demonstrates a novel and robust means of determining a baseline for further specimen tests for apparatus validation. Furthermore, the implementation of the spring theory method of determining machine compliance proved to be a unique and simple means of greatly increasing the accuracy of results from material property testing, particularly when considering small specimens. Finally, the successful dynamic compression testing of PMMA specimens in the ISR regime through the use of the CiT striker demonstrates that the apparatus serves as a valuable contribution to the notable void in existing literature for polymers in this strain rate regime.

6.2 Degradation Study

The refrigerated specimens (MR) exhibited highly erratic behaviour during the first week of testing. This was not only observed in the modal values, but the individual tests conducted on a particular day also exhibited significant scatter. The first day of testing exhibited the least scatter of the MR tests, with other testing days having apparent elastic moduli values ranging between ± 7 GPa. This erratic behaviour strongly suggests that these MR specimens underwent degradation within a day after being harvested from the donor animal. This erratic behaviour was not only observed with the scatter, but also with the trend of the modal values. These specimens appeared to have a decrease in apparent elastic modulus during the first days of storage, and then an increase towards the end of the week. From the linear regression analysis, the relationship between the apparent elastic modulus and storage duration for the MR specimens was highly statistically significant, suggesting that there is a significant change of the modulus as storage time increases. A summary of the apparent elastic moduli for the specimens stored under the MR protocol is shown in Figure 6.1.

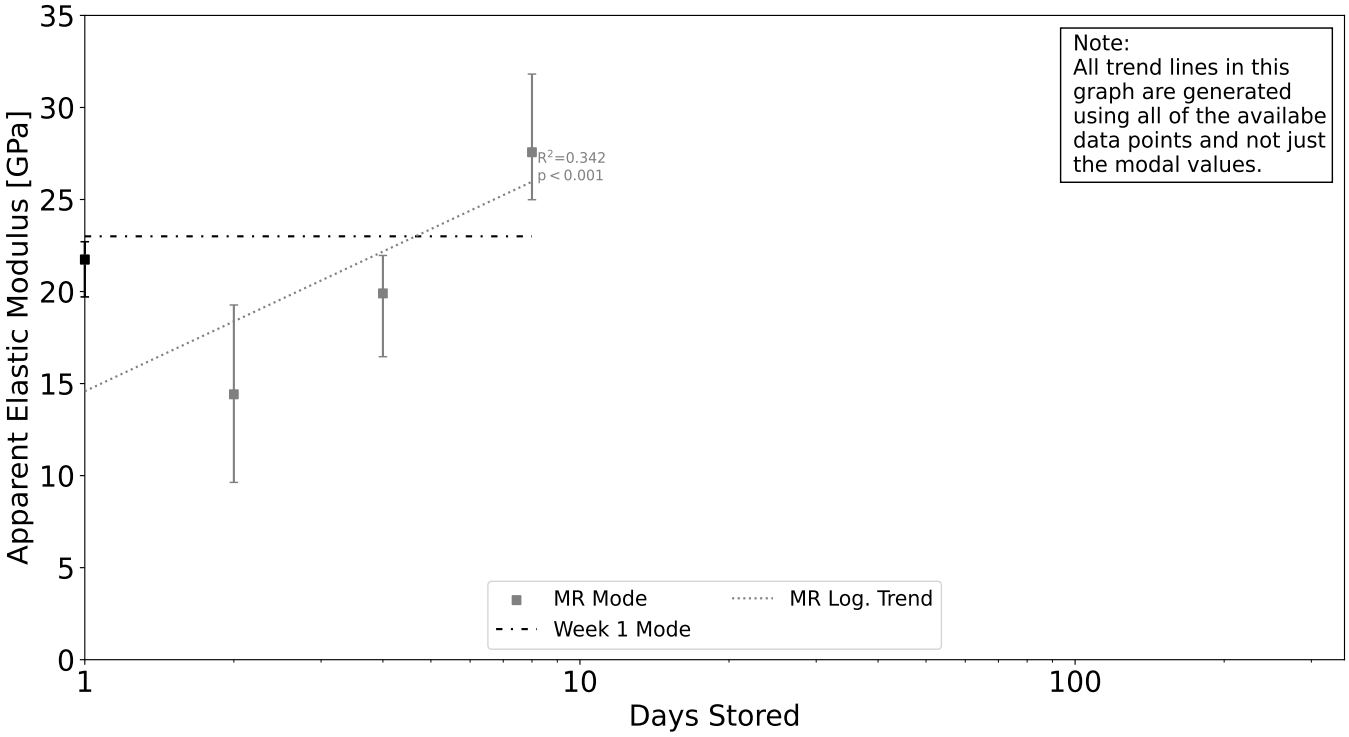

Figure 6.1 Graph of modal apparent elastic moduli vs time in storage for the MR protocol. Error bars indicate one standard deviation from the mean for the logged data in order to highlight the skewness of the datasets.

The UCS of these MR specimens was distinctly more stable than the apparent elastic modulus, however the initial weakening then gradual strengthening was also observed in the UCS values. The scatter of the MR specimens was drastically reduced for the UCS values when compared to the individual apparent elastic moduli values. Regarding the UC strain for the MR specimens, it remained extremely stable throughout the entire week of MR testing. The UC strain remained approximately 2% for all tests with a slight decrease towards the end of the testing week. A summary of the UCS and UC strain data for the specimens stored under the MR protocol is shown in Figures 6.2 and 6.3.

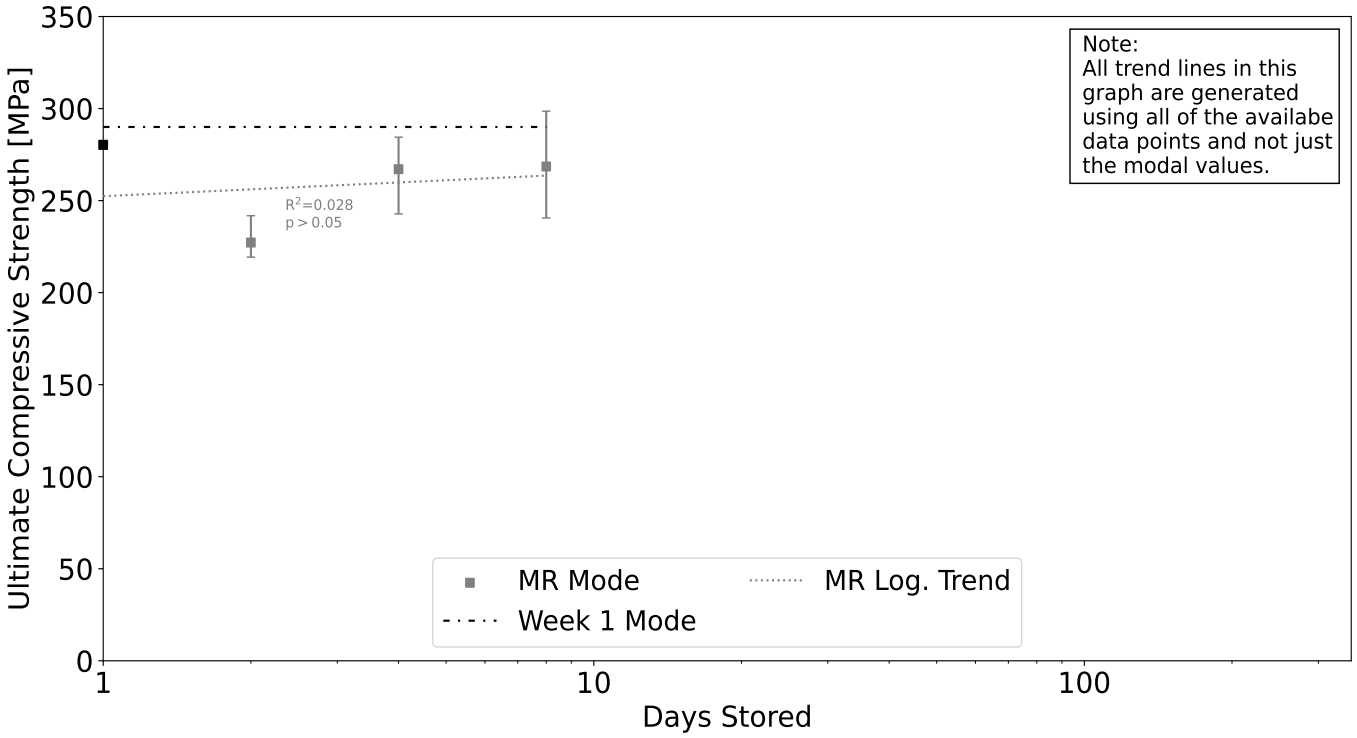

Figure 6.2 Graph of modal UCS vs time in storage for the MR protocol. Error bars indicate one standard deviation from the mean for the logged data in order to highlight the skewness of the datasets.

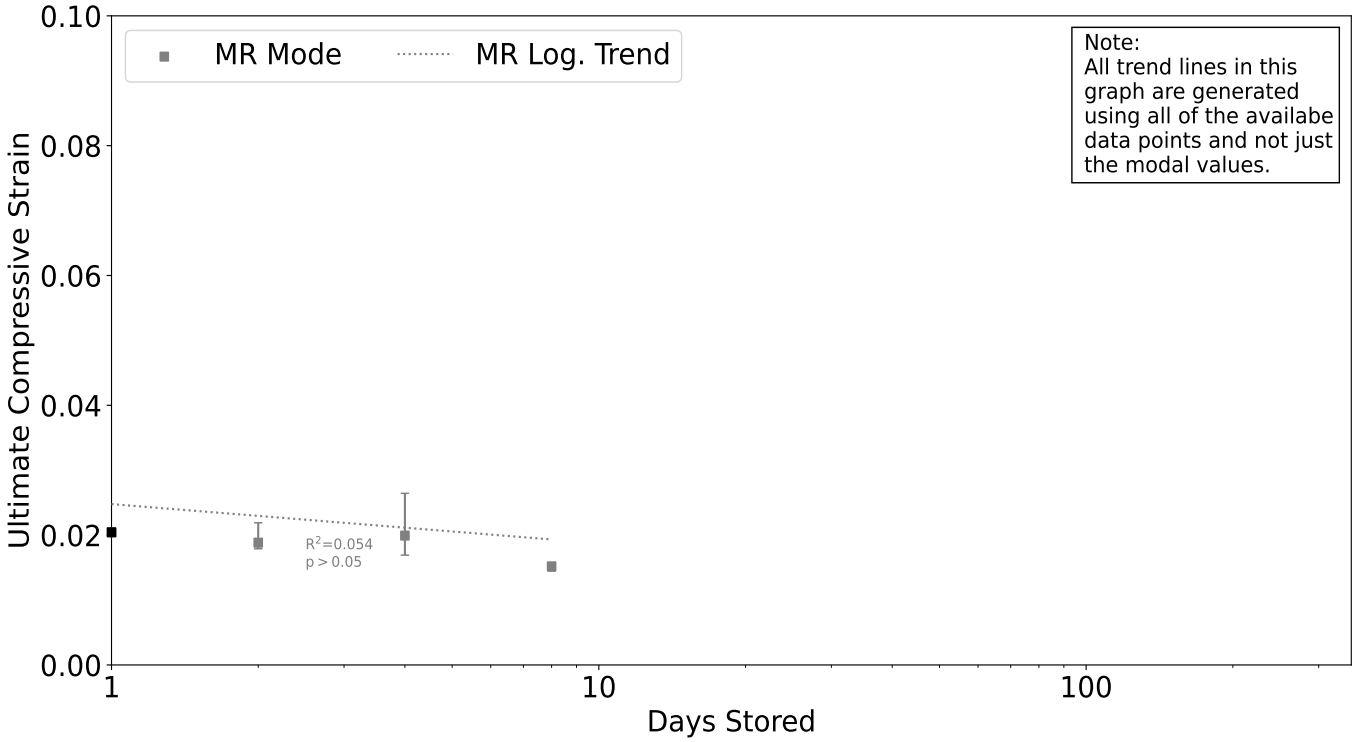

Figure 6.3 Graph of modal UC strain vs time in storage for the MR protocol. Error bars indicate one standard deviation from the mean for the logged data in order to highlight the skewness of the datasets.

What can be drawn from these finding is that the testing of fresh, never-frozen bone specimens should only be conducted within 24 hours of retrieval from a living host. Beyond this point, the bone appears to degrade and exhibit behaviour that is not representative of in-vivo conditions. The determining of the mechanism of this degradation behaviour is beyond the scope of this research.

The freshly machined then frozen specimens (MF) also exhibited scatter during the first week of testing, as was observed with the MR specimens, however the scatter appeared to reduce as the storage duration increased. Furthermore, the MF specimens exhibited far more stable behaviour during the first week of testing than the MR specimens, with the week-one modal average being approximately 23 GPa. This average was consistent with the day-zero results, which had a modal average just below 23 GPa. However, beyond the week-one point the MF specimens exhibited highly significant degradation with an approximate 20% decrease. By the six-month point the apparent elastic modulus of the MF specimens had reduced to a third of the week-one average. A summary of the apparent elastic moduli for the specimens stored under the MF protocol is shown in Figure 6.4.

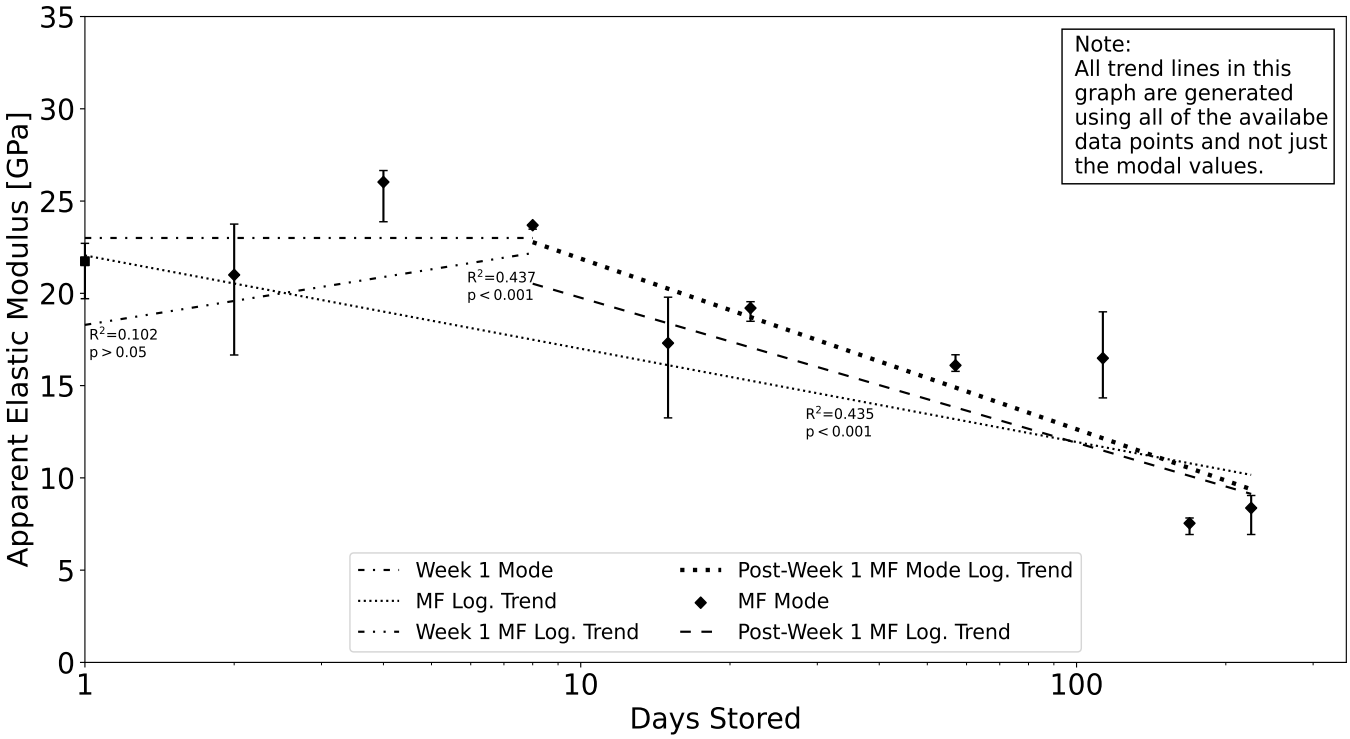

Figure 6.4 Graph of modal apparent elastic moduli vs time in storage for the MF protocol. Error bars indicate one standard deviation from the mean for the logged data in order to highlight the skewness of the datasets.

This trend is also noted when considering the UCS values of the MF specimens. The modal values for the UCS of the MF specimens were within 10% of day-zero tests, even up to the week-two point. However, beyond two weeks in storage, the MF specimens began to exhibit degradation, and by the six-month point, the specimens exhibited UCS values less than half of the week-one average. No such degradation was observed for the UC strain values. A summary of the UCS and UC strain data for the specimens stored under the MF protocol is shown in Figures 6.5 and 6.6.

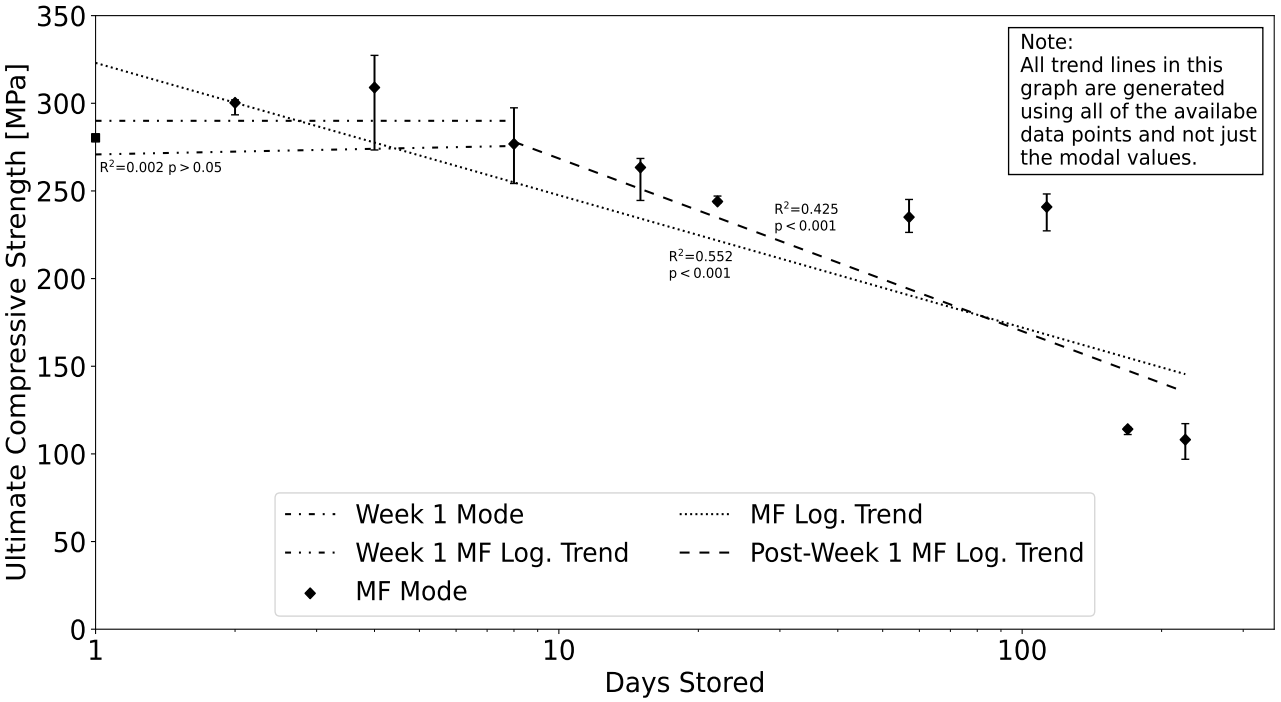

Figure 6.5 Graph of modal UCS vs time in storage for the MF protocol. Error bars indicate one standard deviation from the mean for the logged data in order to highlight the skewness of the datasets.

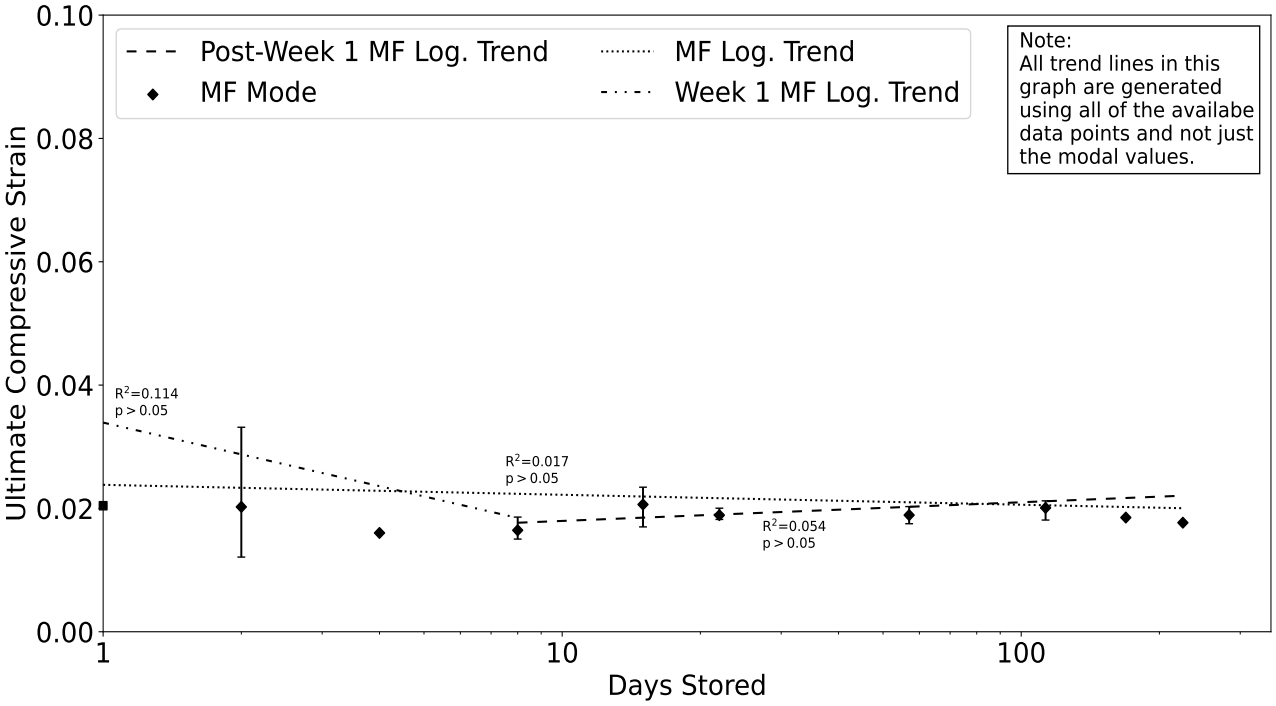

Figure 6.6 Graph of modal UC strain vs time in storage for the MF protocol. Error bars indicate one standard deviation from the mean for the logged data in order to highlight the skewness of the datasets.

What these results would suggest is that the MF specimens exhibit two distinct phases of mechanical performance during the year-long storage duration. The first phase is during the first week after retrieval from the living host, while the second phase is beyond the week-one point. In this first phase, the MF specimens appear to retain their fresh characteristics and perform similar to what was observed by the day-zero specimens. However, beyond the week-one tests, these specimens began to exhibit significantly weaker material characteristics. This finding is further reinforced by the linear regression analysis with the week-one and post-week-one trendlines exhibiting different statistical significances than the trendline for the entire MF dataset. For both the apparent elastic modulus and the UCS, the relationship between these material characteristics and storage duration were deemed to be statistically insignificant for the first week in isolation, while beyond the week-one point, this relationship was deemed to be highly statistically significant. If the MF data was analysed without considering this split at the week-one point, the relationships between apparent elastic modulus and UCS are deemed to be highly statistically significant. In other words, the drastic degradation beyond the week-one point masks the week-one stability. Therefore, based on these findings, it would appear that the testing of specimens machined from fresh donor bones that are frozen directly after machining can be conducted up to one week after retrieval from a living host, and still be considered representative of an in-vivo condition.

The specimens that were machined from a donor bone that was frozen whole and stored for two months prior to machining (FMF (2M) specimens) exhibited a high modal value on the first day of testing for this protocol. This modal value was within 1 GPa of the week-one average, at a value of 24 GPa. However, by the next testing date, the FMF (2M) specimens appeared to equilibrate with the MF specimens, and by the six-month point these specimens exhibited a modal apparent elastic modulus of 10 GPa. Beyond this point, the FMF (2M) specimens stabilized at approximately 9 GPa until the end of the study. What was of interest regarding these specimens was that the scatter they exhibited throughout the study was reduced compared to the initial scatter observed with the other two storage protocols. A summary of the apparent elastic moduli for the specimens stored under the FMF (2M) protocol is shown in Figure 6.7.

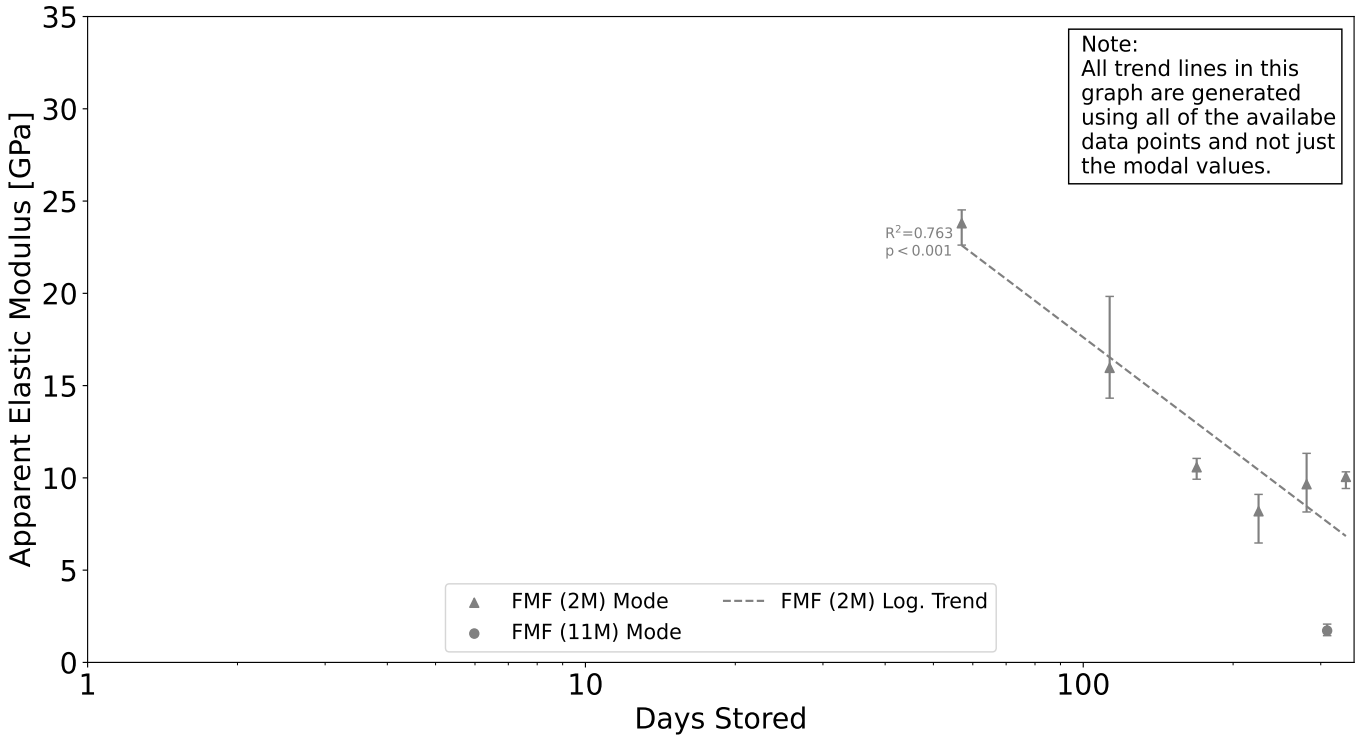

Figure 6.7 Graph of modal apparent elastic moduli vs time in storage for the FMF (2M) protocol. Error bars indicate one standard deviation from the mean for the logged data in order to highlight the skewness of the datasets.

A similar trend was observed for the UCS values of these specimens, however the initial UCS values were notably closer to the MF specimens than the apparent elastic modulus. Again, by the six month point, significant degradation had occurred with the UCS dropping from the initial 253 MPa to 127 MPa over this timeframe. The UC strain remained consistent with the prior UC strain data for all FMF (2M) tests. A summary of the UCS and UC strain data for the specimens stored under the MF protocol is shown in Figures 6.8 and 6.9.

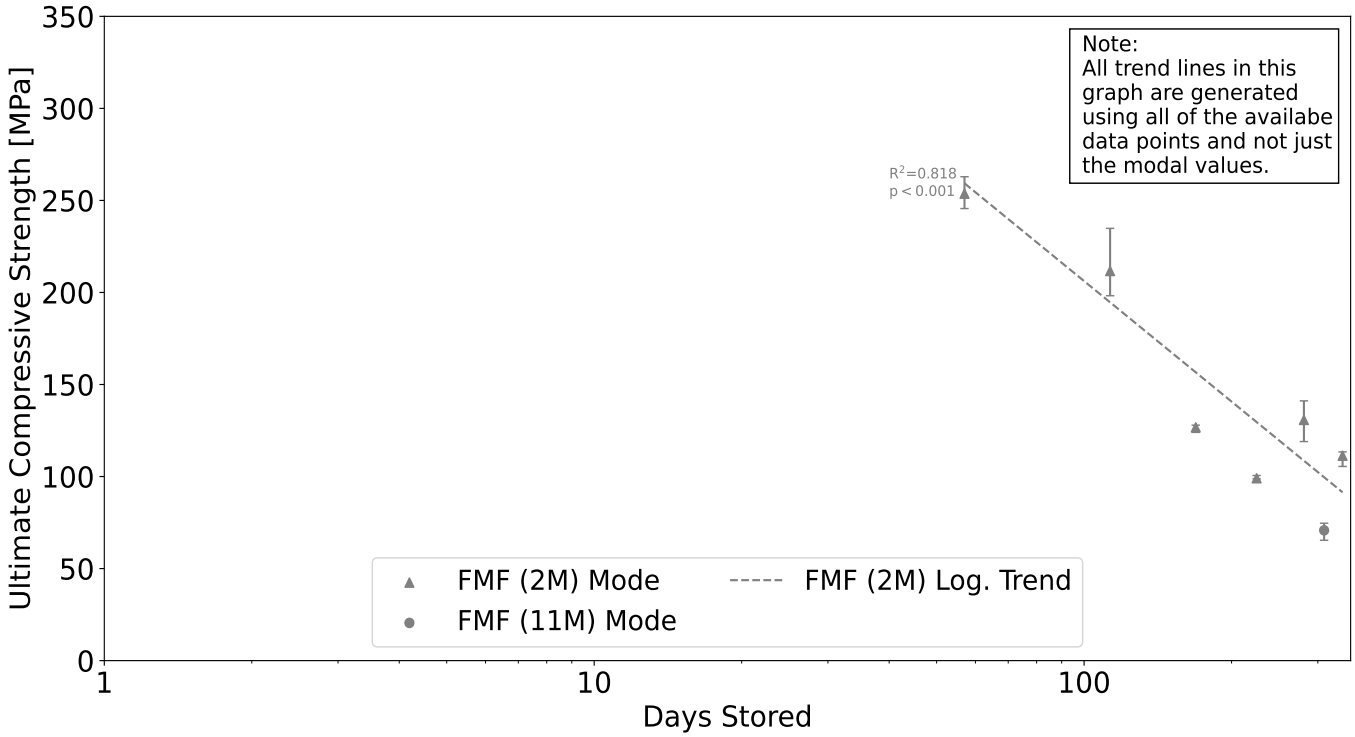

Figure 6.8 Graph of modal UCS vs time in storage for the FMF (2M) protocol. Error bars indicate one standard deviation from the mean for the logged data in order to highlight the skewness of the datasets.

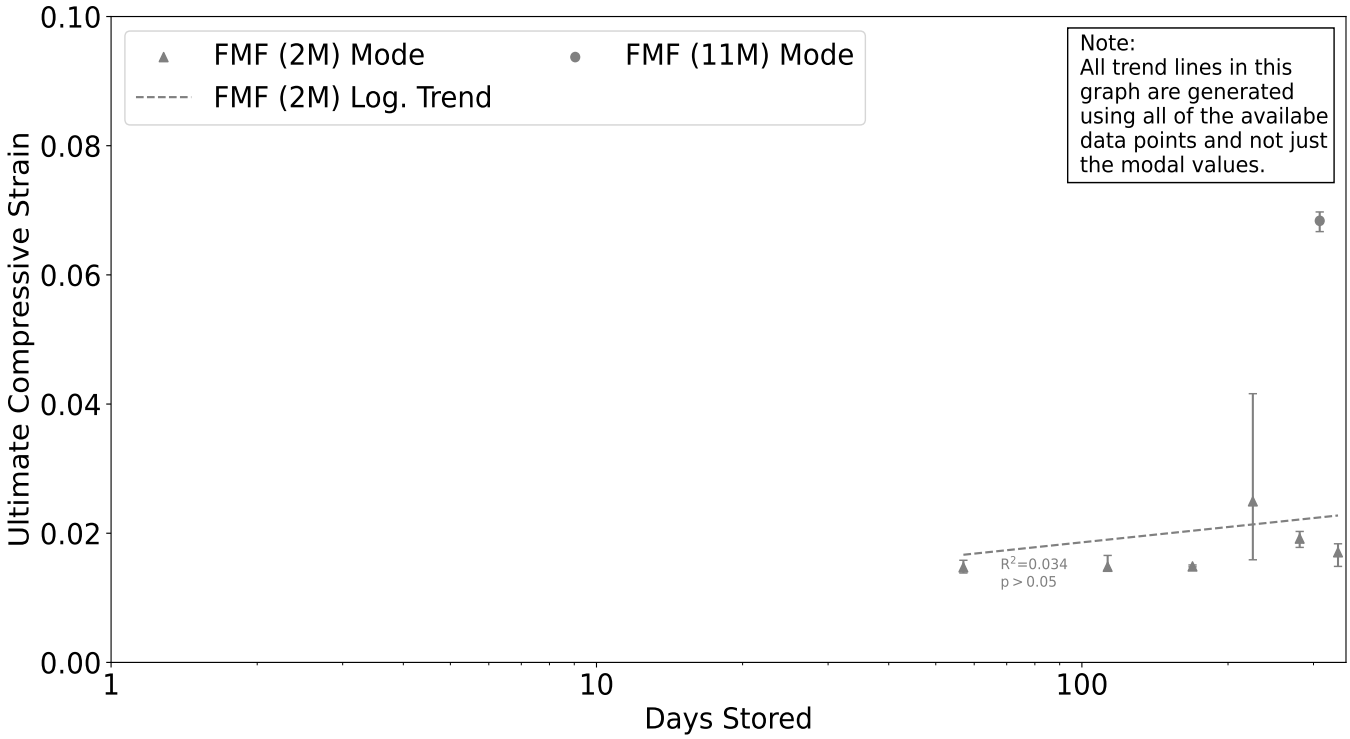

Figure 6.9 Graph of modal UC strain vs time in storage for the FMF (2M) protocol. Error bars indicate one standard deviation from the mean for the logged data in order to highlight the skewness of the datasets.

What these findings suggest is that the frozen storage of whole donor bones can potentially prolong the useful storage life of the bone, however, any bone specimen that has been stored for six months or more, regardless of storage protocol cannot be considered remotely representative of an in-vivo state.

Finally, the specimens that were machined from a donor bone, which was frozen whole for 11 months prior to machining (FMF (11M)) exhibited an extremely low first data point with a modal apparent elastic modulus value of 1.7 GPa. This extremely weak material characteristic is mirrored in both the UCS and UC strain values. These specimens exhibited an average UCS value of 70 MPa and a UC strain value of 6.8%. All of these material characteristics reinforce the conclusion that the storage of bones specimens does have an effect on the measured mechanical properties of the bone. Notable degradation does occur in the bone, and other results would suggest that this typically occurs roughly six months after removal from the living host, regardless of storage protocol of the bone; whether that be as a specimen or as a whole bone.

A summary of the results from this study can be seen in Figures 6.10, 6.11 and 6.12. It must also be noted that the apparent elastic modulus, UCS and UC strain are all plotted against a logarithmic scale, which is intended for clarity when observing the results.

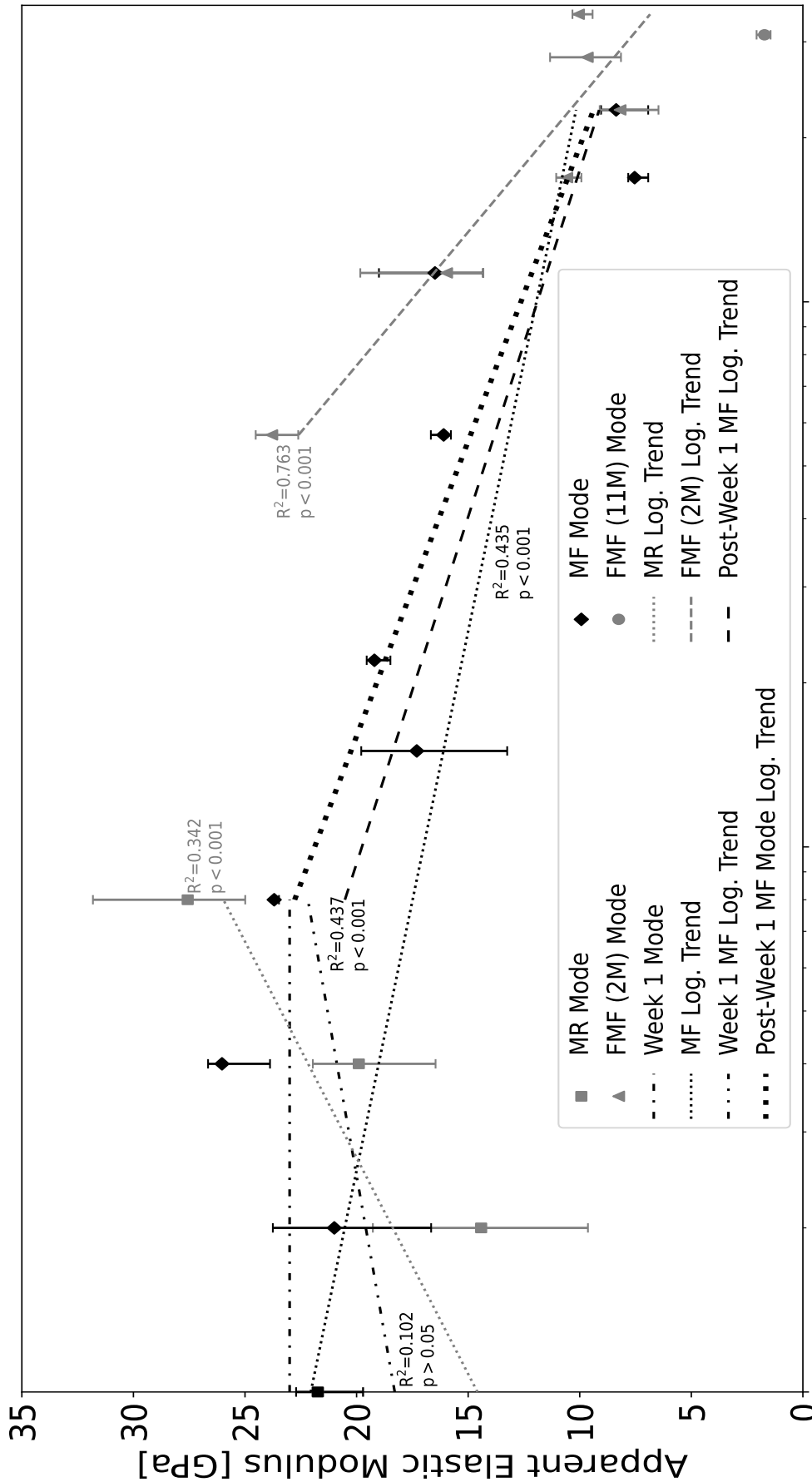

Figure 6.10 Graph of modal apparent elastic moduli vs time in storage for all the test series of this study. Error bars indicate one standard deviation from the mean for the logged data in order to highlight the skewness of the datasets. Slight horizontal offsets are for clarity.

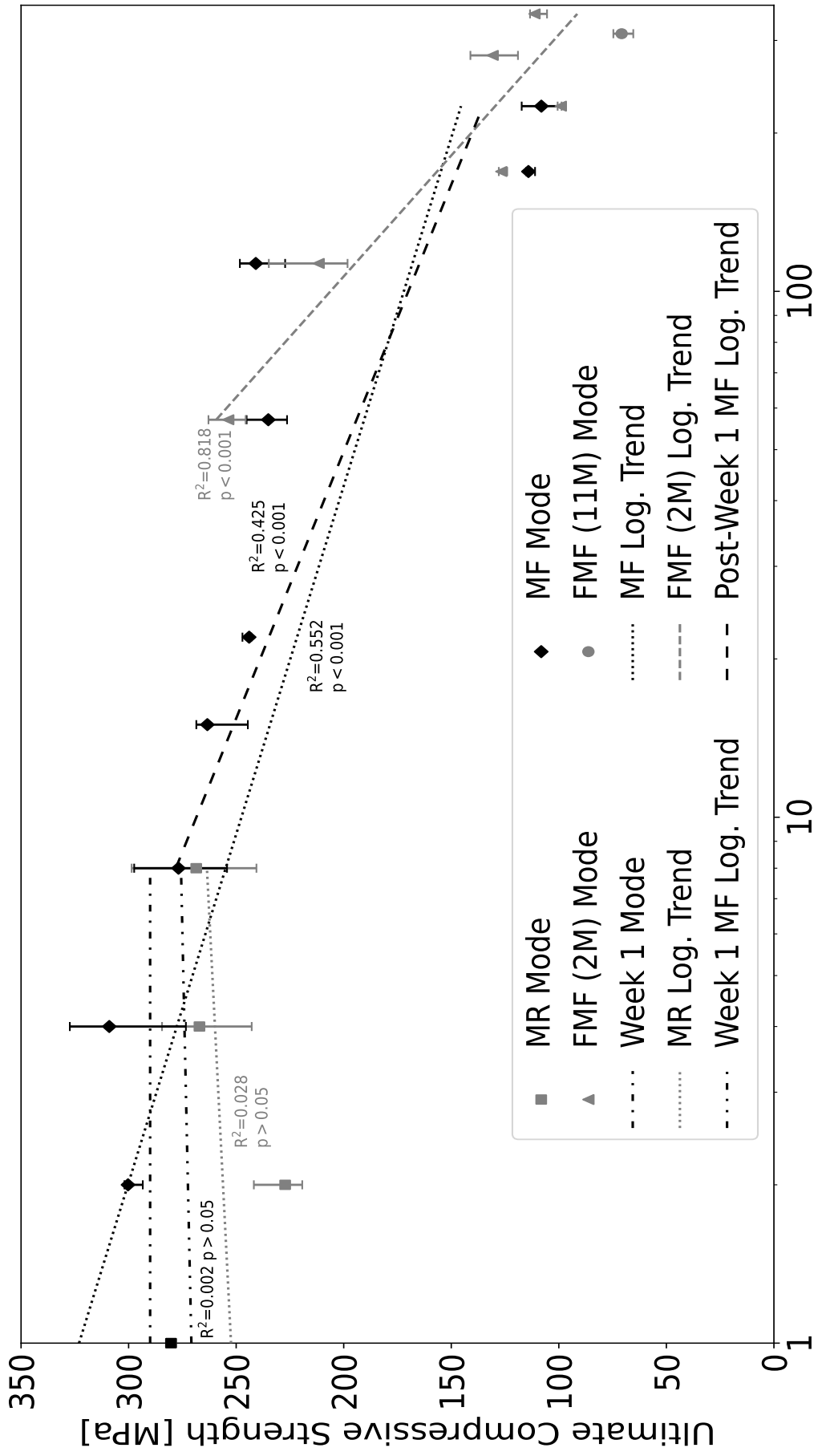

Figure 6.11 Graph of modal UCS vs time in storage for all the test series of this study. Error bars indicate one standard deviation from the mean for the logged data in order to highlight the skewness of the datasets. Slight horizontal offsets are for clarity.

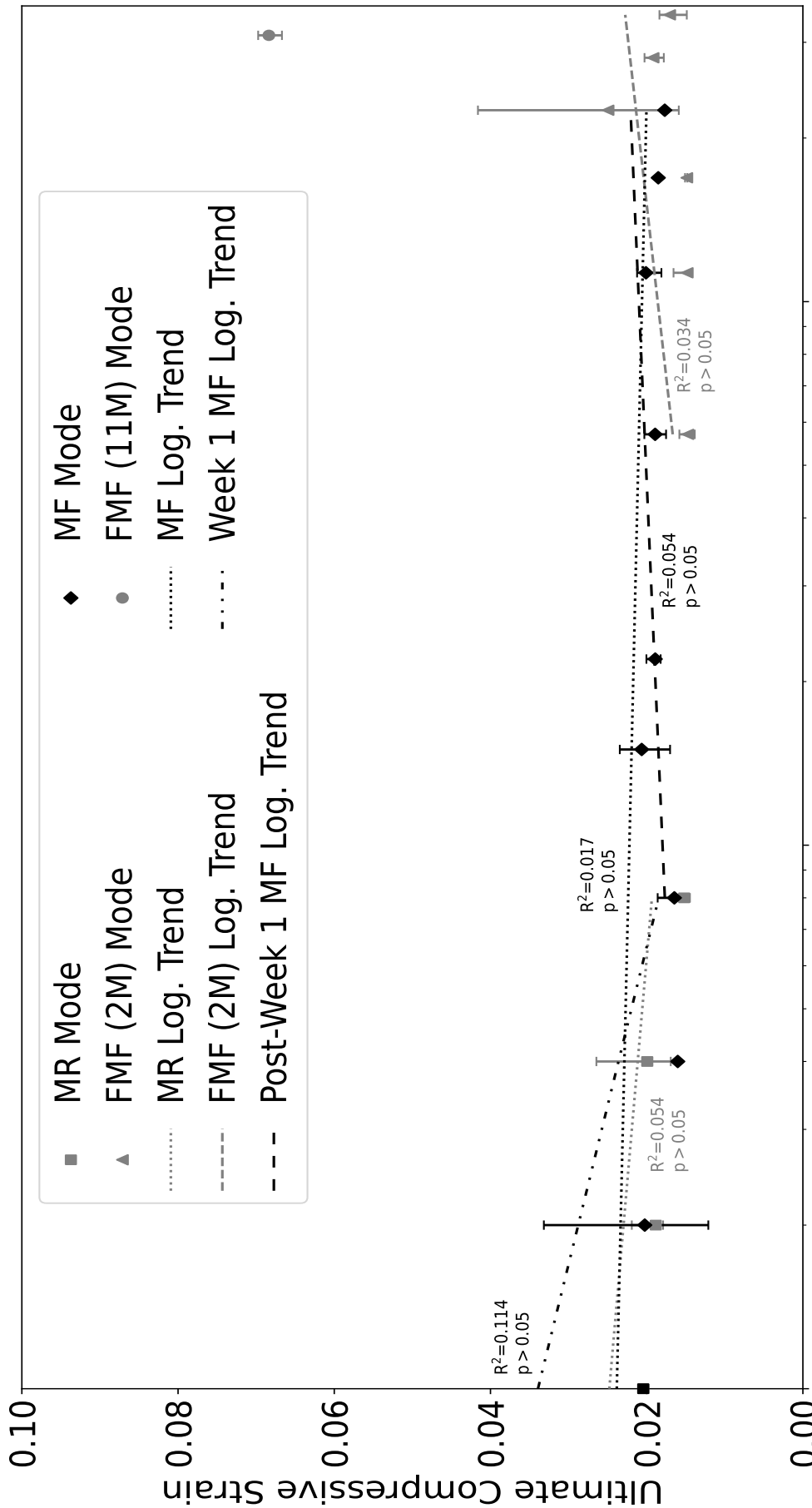

Figure 6.12 Graph of modal UC strain vs time in storage for all the test series of this study. Error bars indicate one standard deviation from the mean for the logged data in order to highlight the skewness of the datasets. Slight horizontal offsets are for clarity.

As stated previously, based on the data in Figures 6.10 and 6.11, it would appear that bone degrades in two distinct phases when being stored under a frozen protocol with distinct week-one behaviour and post-week-one behaviour. Simply refrigerating bone specimens in saline has highly significant effects on its measured mechanical properties even if only stored for a single day. Freezing as a machined specimen in saline does appear to allow the specimen to retain its in-vivo characteristics, but only if the specimen is stored for a maximum of one week. The storage of whole donor bones in saline also appears to allow the bone to retain its in-vivo mechanical properties, however more repeated tests must be conducted before this finding can be definitive.
Due to the fact that the degradation was not linear, assigning a degradation parameter of loss in GPa per day would not be representative of the data. Rather, the use of a half-life is more applicable in this instance. A half -life is simply the amount of time it takes for a parameter to drop to half of its initial value. Over the entire study, the MF specimens had an approximate half-life of 150 days, while the FMF (2M) specimens had an approximate half-life of 195 days. Considering the MF specimens after the first week of testing, these specimens had a half-life of 110 days. What this data would suggest the MF specimens after the week-one point have distinct degradation behaviour than week-one MF specimens. This is as a result of the entire MF data set taking longer to degrade to half its original stiffness than the MF data post-week-one does. Furthermore, this half-life metric further reinforces that fact the FMF (2M) specimens exhibit unique degradation behaviour than the MF specimens.
In contrast to the apparent elastic modulus and UCS data, the UC strain data was extremely stable over the entire study regardless of storage protocol, excluding the FMF (11M) results. This was confirmed through the various linear regression analyses, which all resulted in the relationships between UC strain and storage duration being statistically insignificant regardless of storage protocol. This finding would suggest that the use of a strain-based failure criteria when modelling cortical bone could offer a more robust and consistent failure criteria than the use of the stress-based option.

Inserting the most and least fresh data from this study into the graph by Johnson *et al.* [2], one can see that most fresh data from this study lies above the literature data at its given strain rate, while the least fresh lies near the bottom of the previously reported data. What Figure 6.13 would suggest is that degradation alone could be considered as a major contributing factor to the scatter observed in the literature. This does not suggest that degradation is solely to blame for all of the observed scatter, rather, it could account for a substantial portion of what scatter is shown in Figure 6.13.

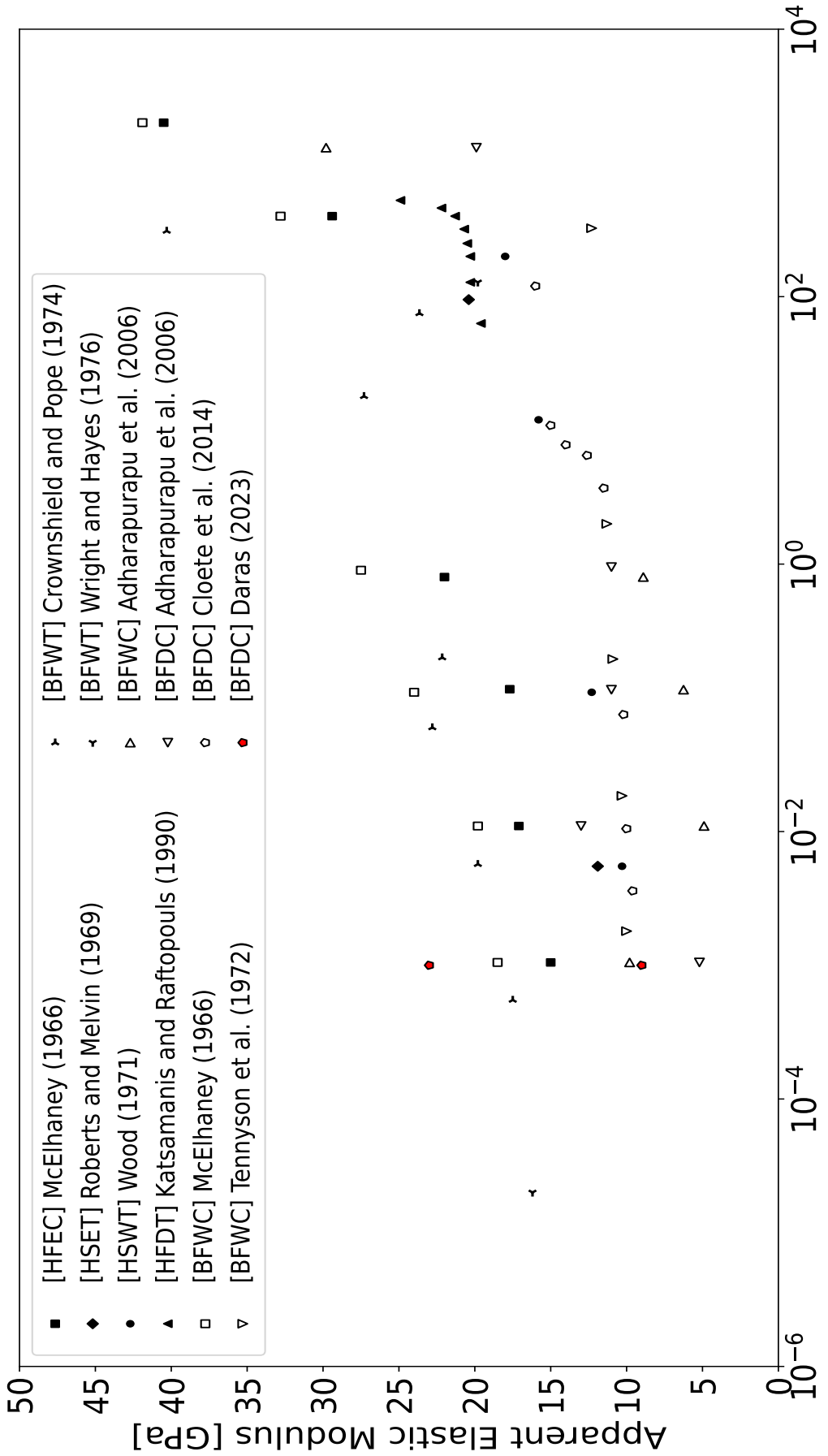

Figure 6.13 The graph generated by Johnson *et al.* [2] demonstrating the relationship between the apparent elastic modulus and strain rate adapted to include the most and least fresh results from this study.

Additionally, the fresh specimens exhibited a unique failure mode to the less fresh specimens. Before the month-one point specimens exhibited failure on what appeared to be shear planes and the specimens remained relatively intact post-test. An example of a specimen that exhibited this failure is shown in Figure 6.14.

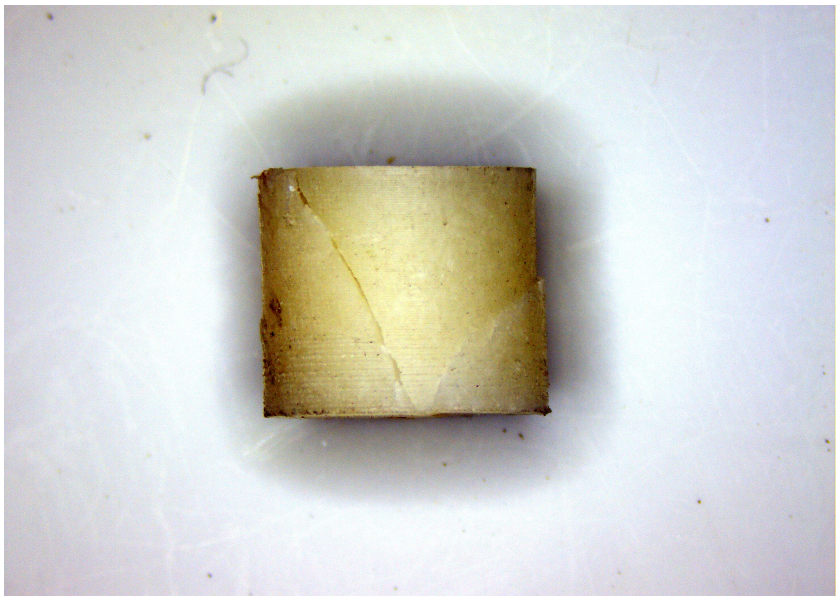

Figure 6.14 Image of a post-test fresh specimen (Day 0) with failure occurring along shear planes of the specimen, forming a V-shaped crack.

There did not appear to be any bias in the number of tests where the cracks met at the top or bottom surfaces of the specimen. This failure mode was consistent for all specimens that were tested before the month-one point in the degradation study. From the month-one point onwards, specimens appeared to fail along the axis of loading and specimens exhibited significant flaking, which became more severe with an increase in storage time. An example of a specimen that exhibited this failure is shown in Figure 6.15.

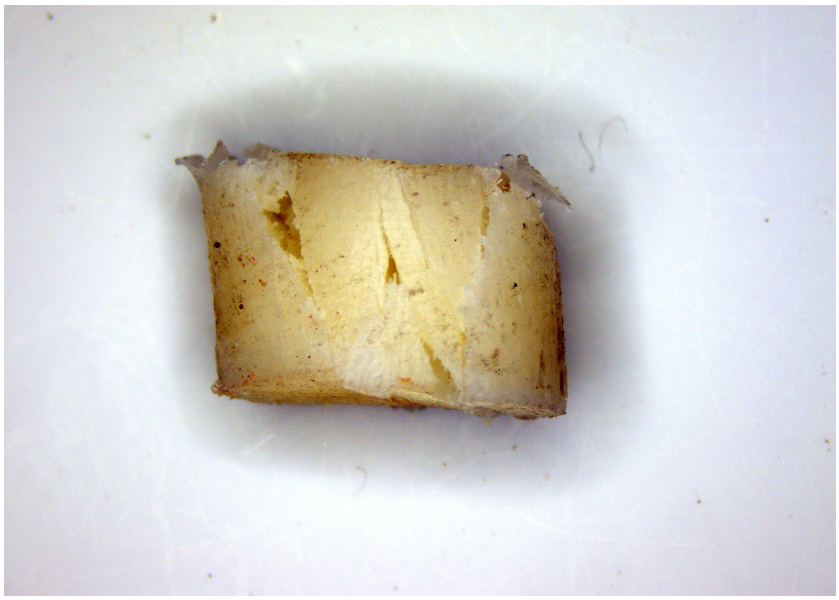

Figure 6.15 Image of a post-test non-fresh specimen (Month 2) with failure occurring along the axis of loading, with moderate flaking.

These less fresh specimens clearly exhibit unique failure modes to the fresher specimens. Far more cracks formed in the older specimens and the failure manifested in a more ductile manner than the fresher specimens. While the specimen in Figure 6.15 does not exhibit severe flaking, many of the older specimens broke apart into many individual flakes post-test. This failure mode was consistent for all specimens that had a storage life of more than one month, with flaking becoming more severe and regular as storage life increased.

6.3 Fresh Bone Tests

It is evident that the specimens tested in the fresh bone tests were distinctly weaker and more ductile than the fresh specimens tested in the degradation study. The donor bones tested in the fresh bone tests were obtained from the same source and underwent the same specimen preparation, machining and storage protocols that the donor bones from the degradation study underwent. In addition to this, the sex, age group and feed of the donor animals for the fresh bone tests were matched to those of the donor animals from the degradation study. As a result, no clear difference could be identified in the sourcing of the bones, nor the specimen preparation, machining, storage and testing protocols. All of the influential factors that could be controlled for these fresh bone tests were matched to those of the degradation study. A chemical analysis or a microstructural analysis of the two sets of donor bones might allow for the difference to be identified, however that extends beyond the scope of this thesis, and potentially beyond the realm of mechanical engineering. As such, an explanation of the observed difference in reported mechanical properties between the fresh bone tests and the degradation study will not be pursued.

With that being said, it is believed, based on the consistency with the literature, and repeatability of the tested specimens, that mechanical properties reported in the degradation study are more representative of in-vivo conditions. Furthermore, long duration storage does appear to have a significant effect on the measured mechanical properties of bovine cortical bone, and this aspect alone does contribute to the scatter observed in the literature. However, degradation alone does not account for all of the scatter observed in the literature. Clearly, based on the fresh bone test results, cortical bone is a complex and inherently inscrutable material for which mechanical tests alone are not capable of truly characterizing.

Nevertheless, these results were recorded and are thus reported in this thesis. As was mentioned in Sections 5.5.1 and 5.5.2, these lower value results appeared to correlate better with the experimental data than the simulations with the material properties obtained from the degradation study, and hence are still valuable in the pursuit of the tangential numerical goals of this thesis.

6.3.1 Quasi-Static Tests

When comparing compression to bending of a quasi-brittle material, one would expect to see a difference in the measured mechanical properties of the material between the two tests. However, in the case of these QS fresh bone tests, the difference appears to be

the reverse of what is expected. One would anticipate that the three-point bending would induce a tensile failure in the specimens, as cortical bone has been reported as being weaker under tension than compression, however the bending specimens exhibited a much higher average apparent elastic modulus and ultimate strength than the compression specimens. It is worth noting that the compression specimens had an average density of approximately 100 kg/m^3 less than the bending specimens, but this difference would not account for the large discrepancies in the material properties.

The only possible explanation for this drastic difference in mechanical performance between the two testing methods would be the failure would be the mode of failure of the specimens. Both Zysset *et al.* [24] and Wirtz *et al.* [4] reported that cortical bone has an approximate apparent shear modulus of 3.3 GPa, which is lower than the reported elastic modulus in the literature, which is approximately 17 GPa in the longitudinal direction according to Morgan *et al.* [3] and Rho *et al.* [5]. With the compression specimens from these fresh bone tests also exhibiting the same diagonal failure planes as those discussed in the closing portions of Section 6.2, attributing the lower measured modulus to the potential shear failure could explain the noted difference.

6.3.2 Strain Rate Sensitivity

The strain rate sensitivity tests demonstrated the clear viscoelastic properties of bovine cortical bone. The QS apparent elastic moduli ranged from 4.24 GPa to 7.31 GPa, which sits near the bottom of the reported values in the summarized data by Johnson *et al.* [2], while the valid dynamic apparent elastic moduli ranged from 8.27 GPa to 11.93 GPa, which places these specimens slightly below the literature data at the tested strain rates. Nevertheless, there is a distinct increase in the apparent elastic modulus of the cortical bone specimens when tested at a higher strain rate, which is consistent with what is observed in the literature.

This roughly 5 GPa increase in apparent elastic modulus is also consistent with previous strain rate sensitivity tests conducted in BISRU by Paul [103] who conducted tests in the QS strain rate regime and recorded an apparent elastic modulus of 9 GPa. This same study reported an approximate apparent elastic modulus of 15 GPa in the ISR regime. Notwithstanding the fact that the upper and lower limits of the apparent elastic moduli reported by Paul *et al.* are different to the limits reported in this study, the viscoelastic behaviour (i.e. rate sensitivity) of the material appears to be consistent. This can be noted by the similar increase in apparent elastic modulus between the QS tests and the dynamic tests being similar between the two studies.

In both the QS and the dynamic tests, the specimens exhibited the same diagonal failure

planes that were considered indicative of the fresh specimens from the degradation study. The approximately 1 GPa increase in the QS compression tests from this strain rate sensitivity analysis and the QS tests could be attributed to the slight increase in density of the specimens tested in the strain rate sensitivity tests, however such a small difference could also simply be due to natural variation one would expect when working with cortical bone.

6.4 Bone Cross-Section Tests

The use of the bending SHB for the dynamic testing of cortical bone cross-section specimens proved to be a successful testing technique. Specimens remained in position for the duration of the test and a satisfactory degree of deformation was able to be induced in the specimens. Furthermore, the use of the polymer output bar allowed for the transmission wave to have a large enough signal for meaningful data to be extracted. With the addition of the high-speed camera, this bending SHB setup was able to record force and displacement data of the cross-sectional specimens at a high resolution. Furthermore, tests were able to be conducted rapidly and in a highly repeatable manner. This system demonstrates promise as the desired intermediary step between small cortical bone specimen testing and whole bone testing.

The particularly interesting finding from this section of research was the drastic difference in the performance between the specimens with differing levels of robustness. The concept of 'robustness' in the context of this thesis was defined in Section 5.4. A highly statistically significant ($p < 0.001$) linear relationship was observed between the apparent stiffness of the specimens and the level of robustness, as shown in Figure 6.16.

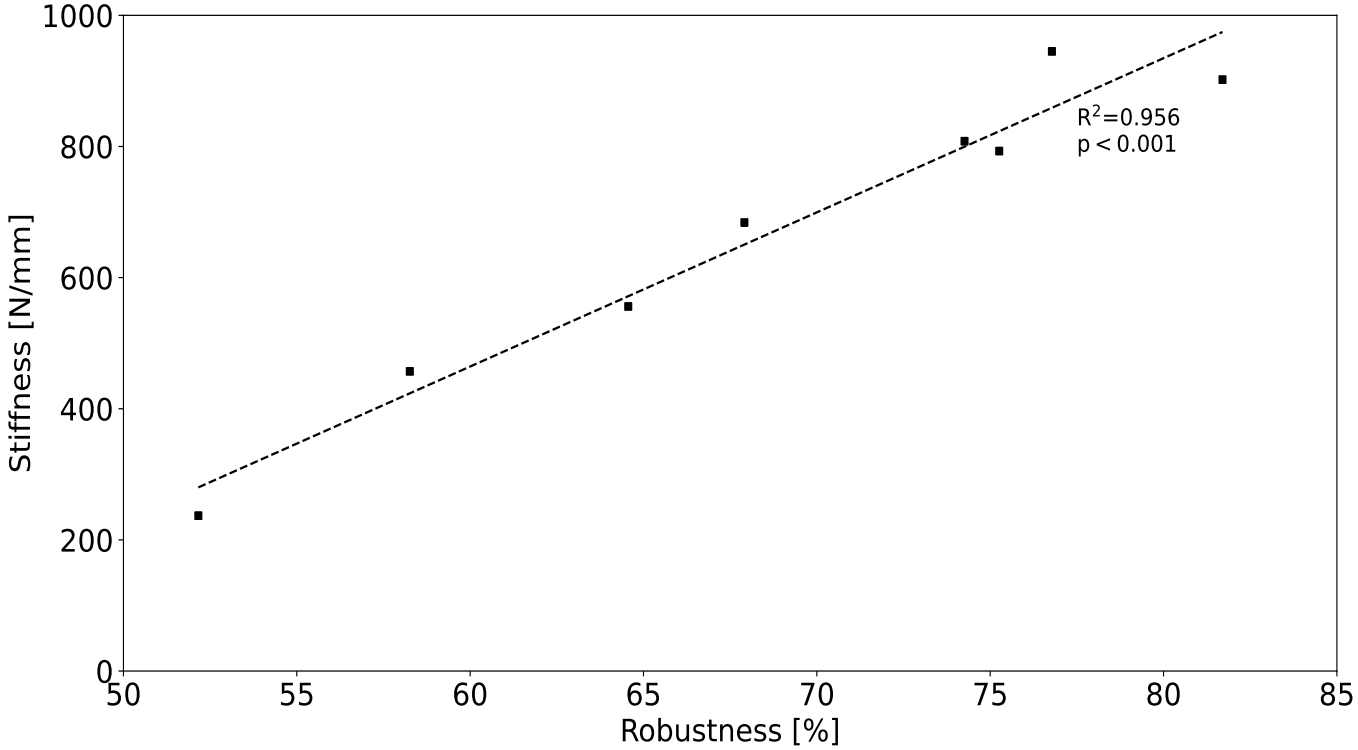

Figure 6.16 Graph of apparent stiffness vs robustness for the cross-sectional cortical bone specimens.

A linear regression resulted in an R^2 value of 0.956, thus implying that these two factors are highly correlated. This level of robustness was explored further by comparing it to the maximum force experienced by the cross-section specimens, as well as the maximum deflections that the specimens experienced during testing. The force-robustness relationship exhibited a statistically significant exponential-like trend, with the maximum force experienced by the specimens starting at an asymptotic value of approximately 250 N, but gradually rising to approximately 400 N as the robustness increases. With an R^2 value of 0.723, the relationship between force and robustness is not as highly correlated as stiffness is to robustness, but still demonstrates that these two aspects are closely linked. Figure 6.17 shows this relationship.

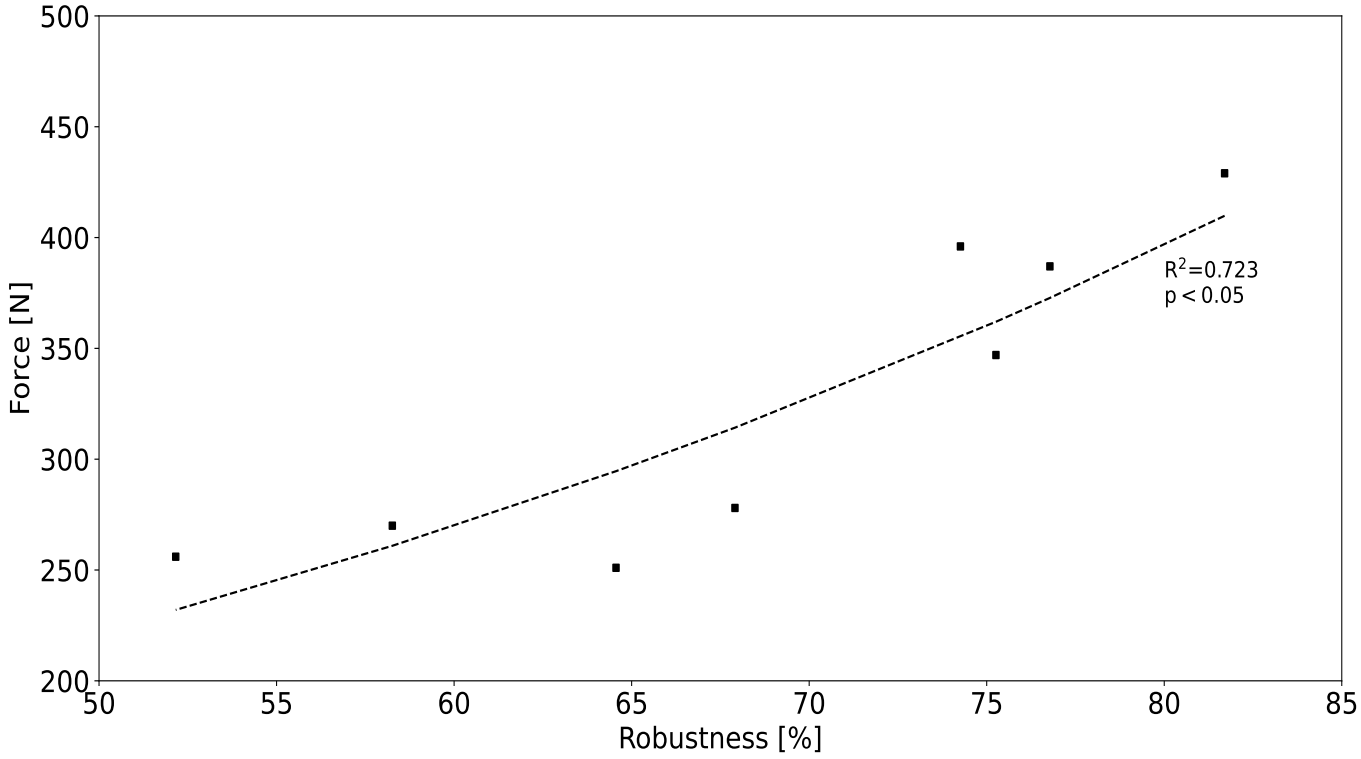

Figure 6.17 Graph of maximum recorded force vs robustness for the cross-sectional cortical bone specimens.

By contrast, the deflection-robustness relationship exhibits a statistically significant ($p < 0.05$) negative logarithmic-like trend. When considering the entire dataset, the regression analysis results in an R^2 value of 0.622, which is comparatively lower than the other two relationships. The specimens with robustness levels higher than 65% appear to have a relatively stable maximum deflection, remaining at approximately 0.8 mm to 0.9 mm. A sharp increase in maximum deflection is observed with specimens with robustness levels lower than 65%. As a result, it would appear that this relationship

would be better represented by a piecewise linear function.

When considering a piecewise linear function however, the specimens with a robustness level above 65%, the relationship between maximum deflection and robustness is statistically insignificant ($p > 0.05$) with an R^2 value of 0.322. The low correlation factor could be improved with a greater sample size, but the statistical insignificance suggests that in this robustness regime, the deflection is not changing significantly. By contrast, the linear regression analysis of the specimens with robustness levels below 65% resulted in a statistically significant ($p < 0.05$) relationship, with an R^2 value of 0.967. This regression analysis demonstrates that this piecewise linear function could be more representative of the deflection-robustness relationship.

With this being said, a greater sample size would result in greater reliability of results. As these experiments were aimed at refining a new testing technique, as well as being used as computational simulation verification results, more tests were not conducted. Despite this, these results demonstrate that the testing of cortical bone cross-section specimens can be used to illuminate new perspectives and means of characterizing bone specimens.

6.5 Computational Simulations

To systematically document the various simulation configurations discussed in this section, Figure 6.18 has been created to illustrate the detailed breakdown of simulation variations.

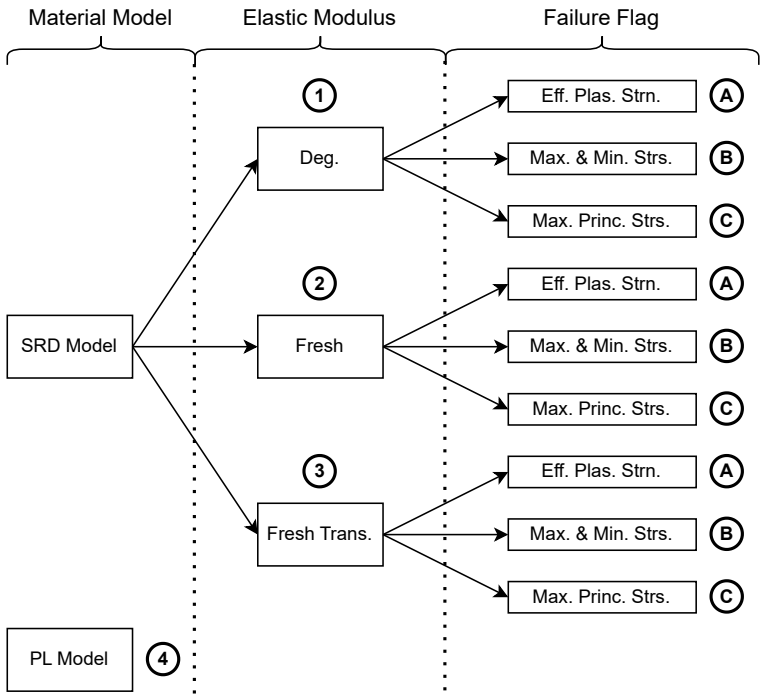

Figure 6.18 Breakdown of the variations of the material models tested in the computational simulations.

To summarize the material model variations, piecewise linear plasticity material model (PL model) is directly imported from the 'Total Human Model for Safety' (THUMS) and only has one variation shown as 4 in Figure 6.18. The strain rate dependent material model (SRD model) has three variations, each with a unique elastic modulus, each labelled 1 through 3 in Figure 6.18. The elastic modulus for the first SRD model variation, labelled 1 in the figure, is obtained from the fresh results from the degradation study, and is therefore referred to as the (Deg) model. The elastic modulus for the second variation of the SRD model, labelled 2 in the figure, is obtained from the dynamic compression fresh bone tests, and is hence referred to as the (Fresh) model. Finally, the elastic modulus for the third variation of the SRD model, labelled 3 in the figure, is obtained by estimating the elastic modulus in the transverse direction based on the results from the dynamic compression fresh bone tests, and is therefore referred to as the (Fresh Trans.) model. Each of the three SRD model variations was individually simulated with the three different failure flags activated, labelled A through C in Figure 6.18.

6.5.1 Dynamic Compression Specimen Simulations

The failure exhibited by the specimens in these simulations was not observed during experimental testing. During experimental testing, failure was observed along the shear planes of the fresh specimens, in both the QS and dynamic tests from the degradation study and the fresh bone tests. Failure along axial planes was exclusively observed in the case of the degraded specimens of the degradation study. By contrast, the simulations exhibited failure exclusively on the faces of the specimens that were in contact with the bars. Hence, this failure mode predicted by the simulations does not appear to be representative of the physical behaviour of cortical bone. Furthermore, SRD (Deg) model with the plastic strain failure flag was the only simulation that did not exhibit any failure. This is also not representative of physical testing as, based on this study and previous BISRU testing, small cortical bone specimens do fail when subjected to such dynamic stresses.

However, based on the planar cross-section stress gradients, which are shown in Figure 5.19, it would appear than the SRD (Deg) model, with the plastic strain failure flag activated, is the most representative of the physical stresses that such specimens experience under compressive loading. The presence of peak stresses in the specimen being along the shear planes, as shown as the x-shaped stress distribution in the specimen, correlates more closely to the fresh failure observed during physical testing. The other simulations exhibited near-constant stress gradients prior to element failure, with minor stress concentrations around the circumference of the specimens on the faces that were in contact with the bars. This constant stress gradient throughout the specimen does confirm that the specimens are in a state of stress equilibrium, however, the premature failure of these specimens, essentially going directly from a stress-state equilibrium to failure does not appear representative of the physical behaviour of the material.

Considering the specimen stresses, the experimental results from the fresh bone dynamic compression specimens exhibited an average UCS of 214 MPa. By contrast, the fresh results from the degradation study exhibited a UCS of approximately 290 GPa, which was conducted in the quasi-static strain rate regime. The PL model exhibited a UCS of 32 MPa, which is well below the observed experimental results. The SRD (Deg) model with the plastic strain failure flag activated, appeared to be more representative of the physical behaviour of cortical bone with a UCS value of 296 MPa, however a higher UCS value would be expected due to these higher strain rates. Similar UCS values were exhibited by the simulations with the remaining SRD (Deg) and SRD (Fresh) models as that observed with the PL model. All of these specimens exhibited a UCS of

approximately 25 MPa just prior to failure, which is a tenth of the observed experimental results.

Based on the degradation results, it was anticipated that the UC strain should remain stable near approximately 0.02, as this trend is clearly observed in those results. By comparison, the dynamic compression fresh bone tests exhibited an average UC strain of 0.042. The PL model exhibited a UC strain value of 0.017, however, as mentioned, the PL model exhibited a UCS value of 32 MPa, which is clearly lower than the UCS values observed in the degradation study and the fresh bone tests. The SRD (Deg) model with the plastic strain failure flag activated exhibited a UC strain value of 0.022. Both of these simulation results are well within the observed scatter in the experimental results regarding UC strain from the degradation study. Similar to the observed stresses in the simulations, the remaining SRD (Deg) and SRD (Fresh) model simulations were drastically different to experimental results, with these simulations exhibiting UC strains values of 0.002 and 0.0035, respectively.

Despite the SRD (Deg) model with the plastic strain failure flag activated appearing to be the ideal material model for this application, its post-elastic behaviour does not appear to be representative of the physical behaviour of cortical bone. The stress-strain graph of the specimen with this material model, shown in Figure 6.19, appears as a bi-linear piecewise function, which contrasts the smooth curve that is observed in physical testing. Despite the SRD model allowing for such smooth curves to be generated, under these conditions it does not appear to be able to accurately simulate the behaviour of the cortical bone. With that being said, this material model did generate the most typically shaped stress-strain graph for a ductile material. By contrast, the SRD model with both of the other failure flags activated exhibited brittle failure at the previously reported low stresses. The PL model did generate a typically shaped stress-strain graph for a ductile material, however the UCS was also much lower than expected.

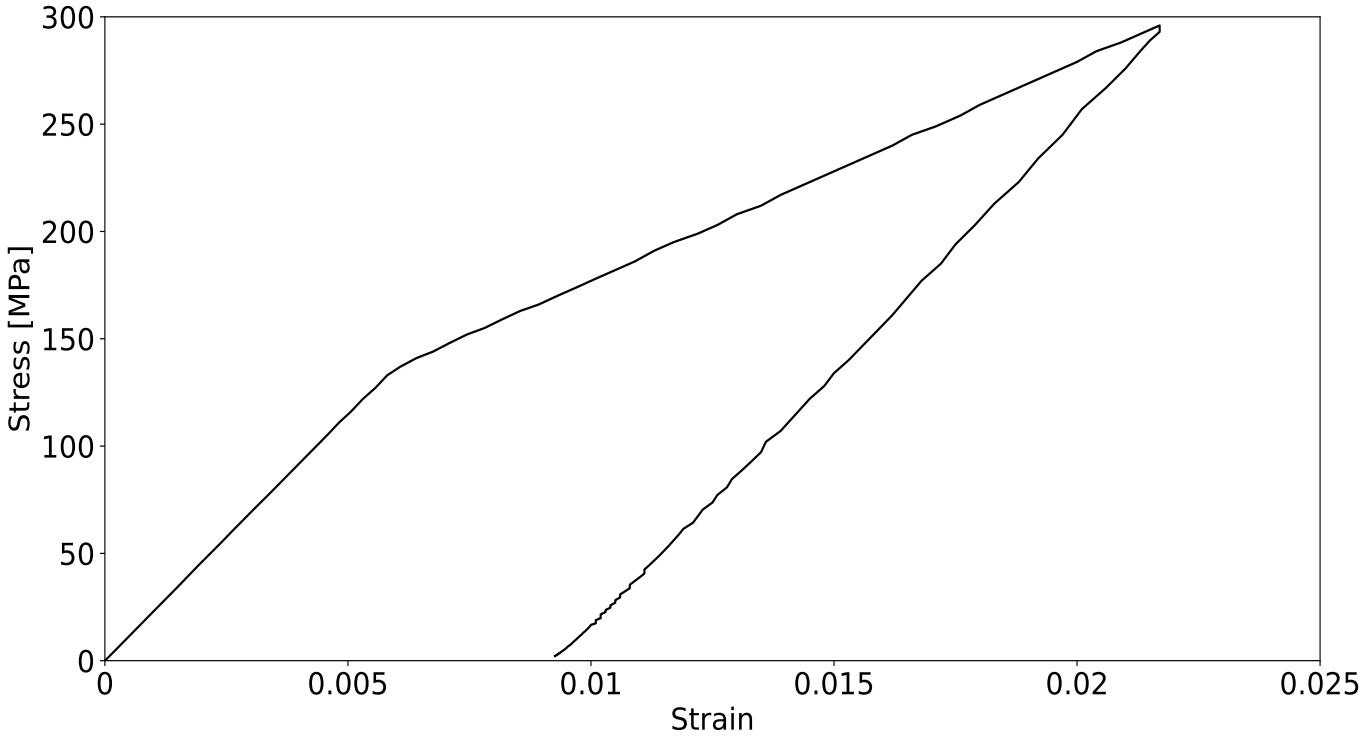

Figure 6.19 Graph of stress vs strain for the simulated SRD model specimen with the effective plastic strain failure flag activated.

Hence, it would appear that the PL model, which is implemented in the commonly used THUMS to simulate cortical bone, does not appear to accurately represent the behaviour of cortical bone at a small specimen scale. The SRD model simulations produce encouraging results, however the performance of the model is highly dependent of the failure flag that is activated, and material model parameters have drastic implications on the results of the simulations. Furthermore, none of the failure flag options appear to allow for accurate representation of the observed failure of small cortical bone specimens during experiments. Hence, the development of this material model to incorporate a more representative failure criteria would potentially make it a more suitable option for the simulation of cortical bone.

6.5.2 Dynamic Cross-Section Simulations

Element failure was exclusively observed in the type I specimen simulations with both the (Deg) and (Fresh) SRD model, and the maximum and absolute minimum principle stress failure flag active. No other combination of material model and specimen type exhibited this element failure, which is consistent with the lack of specimen failure seen experimentally. A point of interest noted with this element failure was that it occurred

exclusively at the point of contact with the polymer transmission bar, and not the harder, aluminium input tube. What this may suggest is that the contact condition imposed between the specimen and the SHB may not be ideal, despite this type of contact being used in other SHB simulations [104–106, 108]. It would be expected that the input tube would be the cause of the element failure as it is far stiffer than the polymer of the transmission bar and the energy going through the input tube has not been dampened by the compliance of the specimen. Therefore, contact types should be investigated further to improve the reliability of the simulations and to make the simulations more representative of the physical behaviour of the cross-section specimens.

Regardless of the material models used, all of the simulations exhibited specimens stiffnesses higher than what was observed experimentally. Furthermore, the simulations exhibited a dependency on specimen robustness, however this relationship was inconsistent between each of the material models. The PL model, all of the SRD (Fresh Trans.) model, SRD (Deg) model with the effective plastic strain failure flag active and the SRD (Fresh) model with the maximum and absolute minimum principle stress failure flag active exhibited specimen stiffness and robustness relationships similar to what was observed experimentally. The other simulations exhibited an increase in specimen stiffness with a decrease in robustness, which was not observed in the physical tests.

Only the SRD (Fresh Trans.) models were remotely representative of the observed experimental results, with the only exception being the type I specimen simulation with the maximum and absolute minimum principle stress failure flag active. Although these simulations exhibited specimen stiffness for the type II specimens being approximately similar to the type I specimens tested experimentally, these simulations results appear to be nearly representative of the physical specimens when compared to the other material models. What this also might suggest is that the donor bone used for the cross-section tests might have been of comparable material properties to the donor bones from the fresh bone tests and not from the degradation study. However, further physical tests need to be conducted to determine if the weaker donor bone tested in the fresh bone tests, and potentially in the cross-section tests, were simply an anomaly.

Figure 6.20 compares all of the numerical results and trendline of the experimental results, while Figure 6.21 is simply a rescaling of Figure 6.20 to highlight the region more representative of the experimental results.

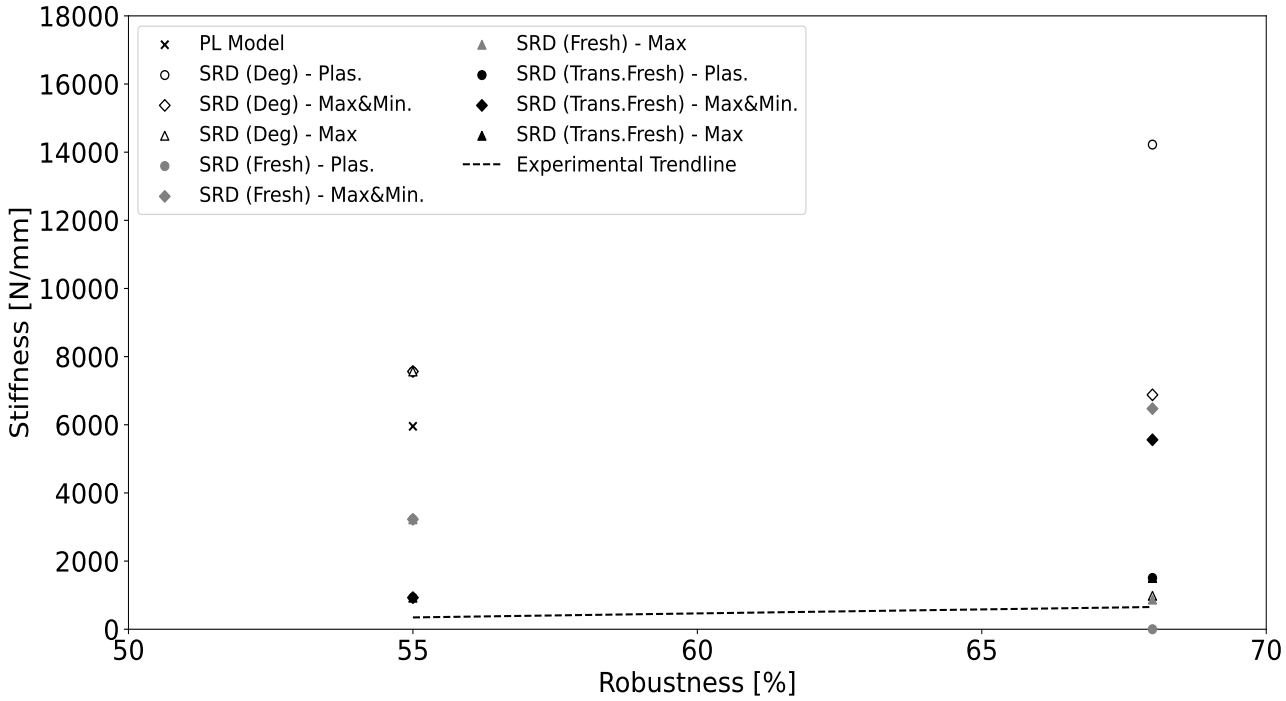

Figure 6.20 Graph of apparent stiffness vs robustness for the cross-sectional cortical bone simulations.

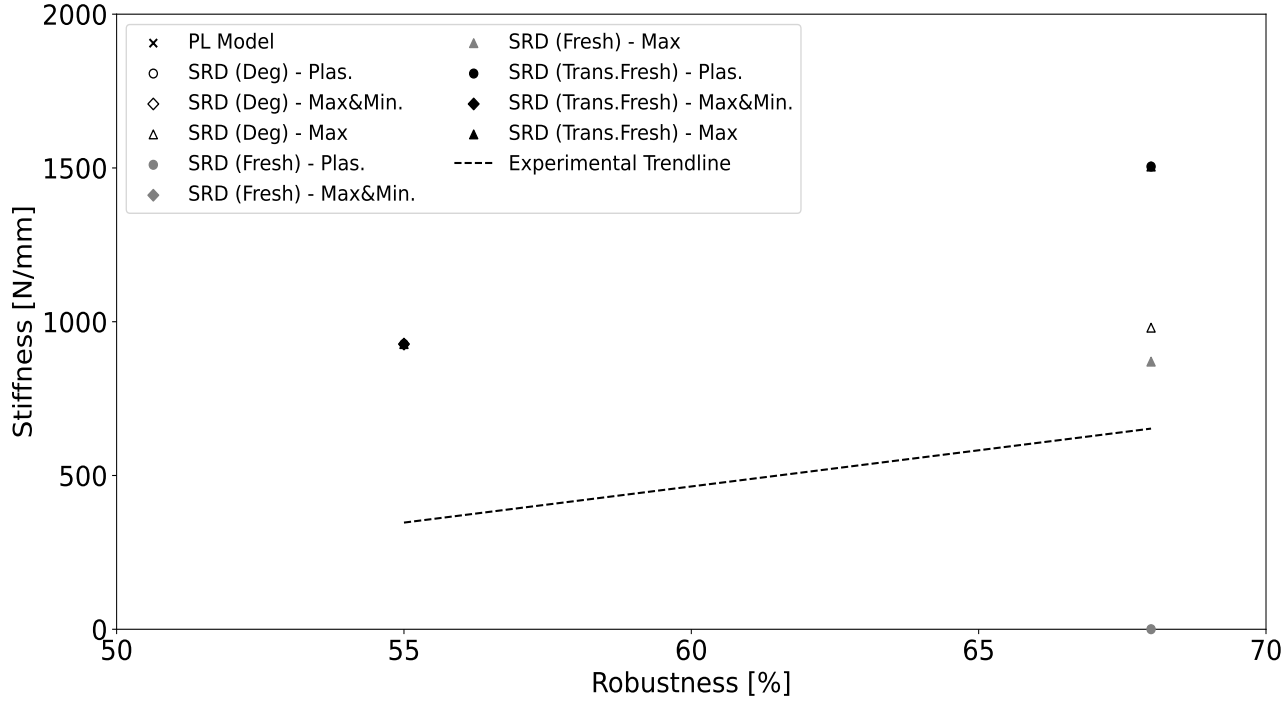

Figure 6.21 Graph of apparent stiffness vs robustness for the cross-sectional cortical bone simulations scaled to be more representative of the experimental results.

The maximum force experienced by the simulated specimens were, on average, much higher than what was observed experimentally, particularly when considering the type II specimens. Based on the experimental result, a maximum type II specimen force of approximately 250 MPa is to be expected, however the lowest simulated type II specimen force was 1125 MPa. Furthermore, only the PL model, two of the SRD (Deg) models and the SRD (Fresh Trans.) model, with the maximum and absolute minimum principle stress failure flag active, actually exhibited a lower maximum specimen force with a lower specimen robustness. The other simulations failed to exhibit this clear trend from the experimental results. Regardless, none of the material models used to simulate the cross-section specimens offered representative metrics of the physical specimens. The SRD (Fresh) model, with the maximum and absolute minimum principle stress failure flag active, does appear to represent the type I specimen rather well, however the behaviour of the type II specimen was not remotely similar to what was observed experimentally.

Figure 6.22 compares all of the numerical results and trendline of the experimental results, while Figure 6.23 is simply a rescaling of Figure 6.22 to highlight the region more representative of the experimental results.

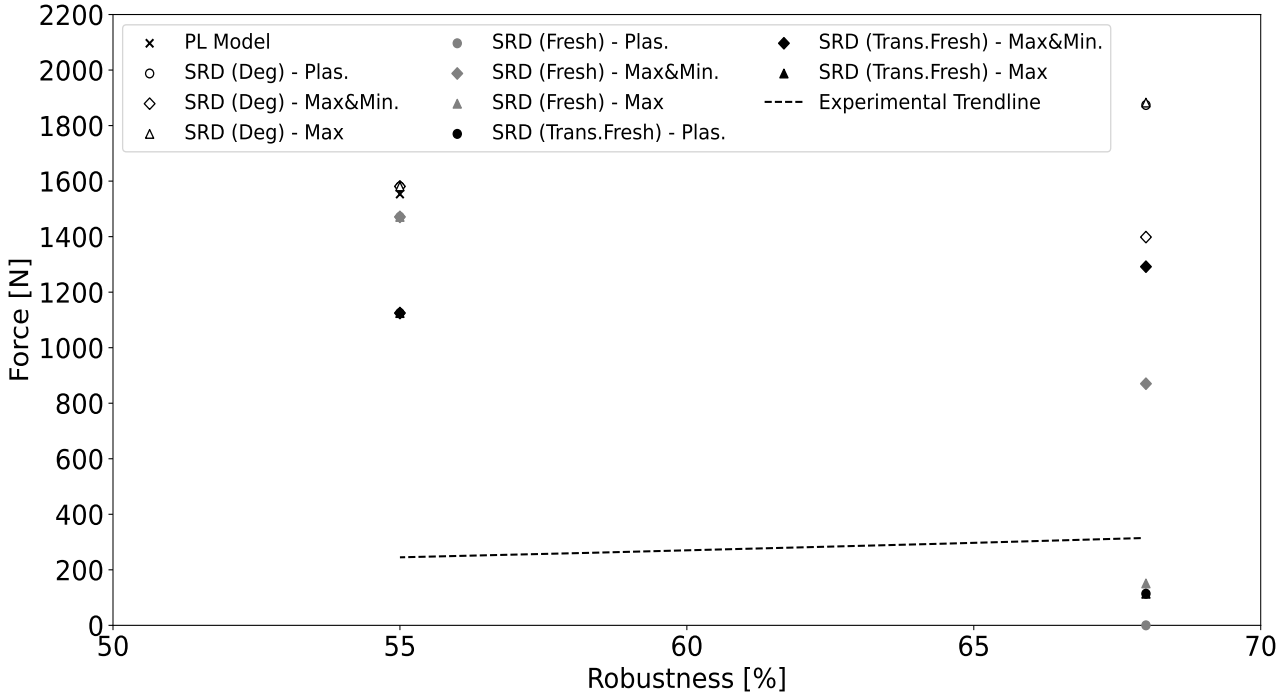

Figure 6.22 Graph of maximum recorded force vs robustness for the cross-sectional cortical bone simulations.

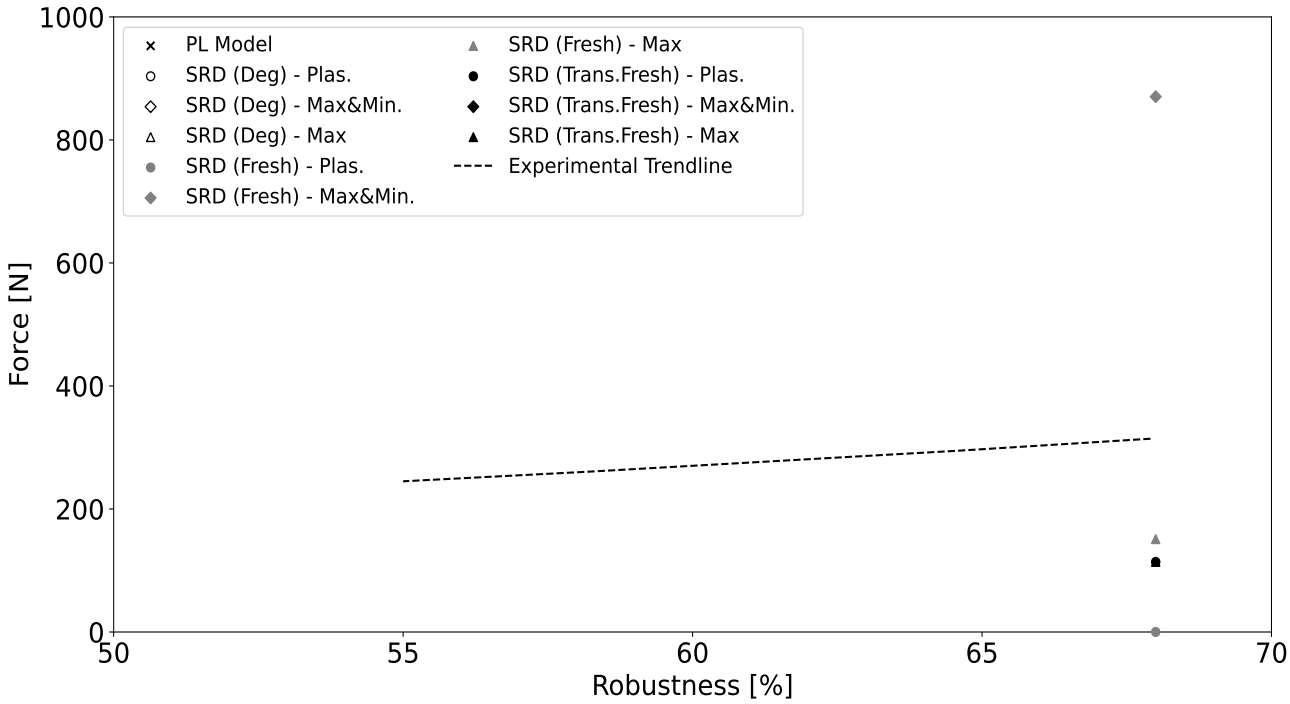

Figure 6.23 Graph of maximum recorded force vs robustness for the cross-sectional cortical bone simulations scaled to be more representative of the experimental results.

In terms of the maximum recorded displacements, the SRD model, with the maximum and absolute minimum principle stress failure flag active, was the only material model that exhibited less overall displacement for the less robust type II specimens. All of the other material models exhibited the observed increased specimen displacement with decrease robustness, to varying degrees. However, as was with the specimen stiffness and maximum specimen force, the simulated maximum specimen displacements were not capable of satisfactorily representing the physical behaviour of the cross-section specimens. Based on the experimental results, the type I specimen should have a maximum deflection of approximately 0.8 mm and the type II specimen, approximately 1.1 mm. Although the scatter from the simulation results were around the expected value, the majority of the simulations were far below, with only the SRD (Fresh) models being approximately 0.05 mm either side of the expected 0.8 mm. The highest type II specimen deformation from the simulations was 0.87 mm, which is well below the expected. 1.1 mm. Therefore, as was with the maximum specimen forces, the type I specimen behaviour was closer to the experimental results, while the type II specimen behaviour was comparatively worse. Figure 6.24 compares all of the numerical results and trendline of the experimental results.

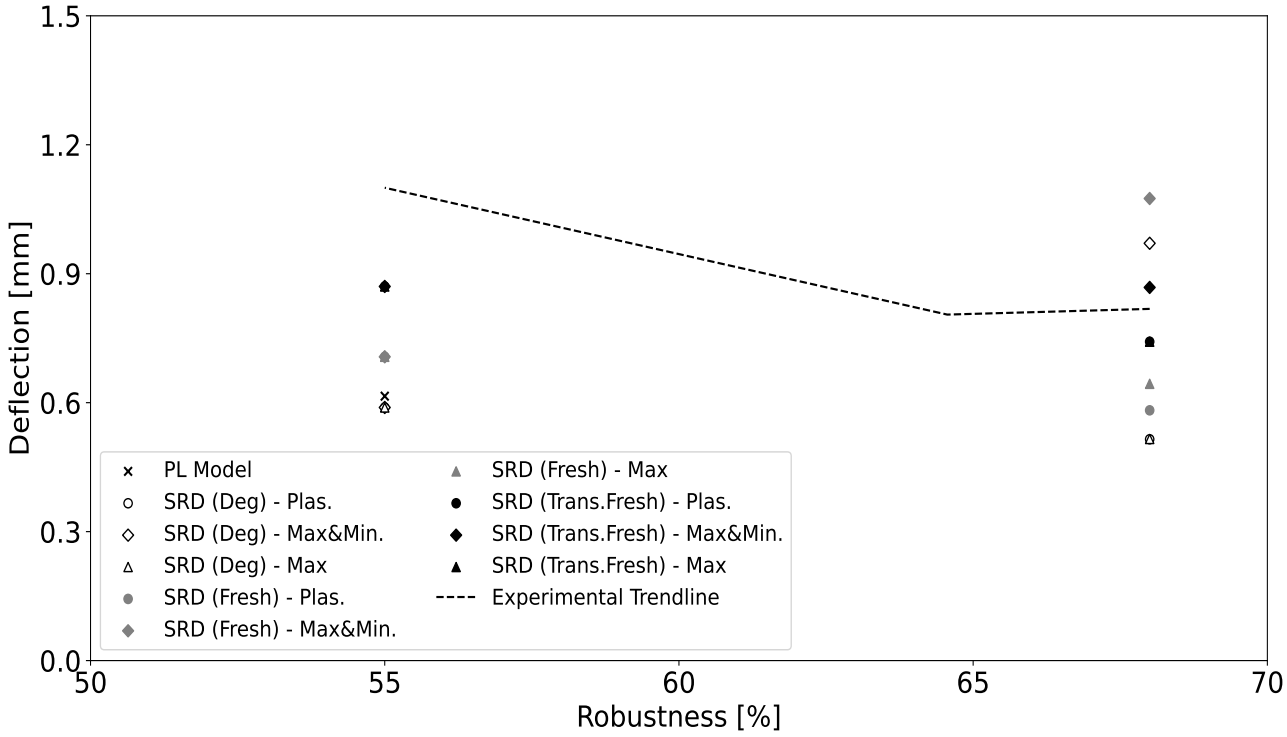

Figure 6.24 Graph of maximum recorded displacement vs robustness for the cross-sectional cortical bone simulations.

Therefore, in summary, the PL model does not appear to satisfactorily represent the experimental data obtained in the cross-section bone tests. Although it does exhibit the observed experimental trends, the final values are, particularly in the case of the specimen stiffness and maximum force, drastically over-estimating the mechanical performance of the specimens. The SRD model, depending on the failure flag that is activated, shows benefits over the PL model when considering the specimen performance, however in this form it is by no means the ideal solution. The presence of element failure when using the maximum and absolute minimum principle stress failure flag, which was not observed in the experiments, renders that variation of the material model inappropriate for the simulation of cortical bone. The other two options for the SRD model do produce encouraging results, appearing more representative of the physical specimens, however material model parameters need to be refined further if the accuracy of the simulations are to be improved. The same could be said for the PL model, however, the inherent inability of the material model to account for strain rate dependency could be the major disadvantage of this model.

Chapter 7

Conclusions and Recommendations

7.1 Conclusions

The results obtained through the research conducted in this study aimed to address a number of limitations in the current literature pertaining to the mechanical behaviour of cortical bone. The critical limitations in the literature that were filled by this research include:

- The development and commissioning of an accurate displacement measurement subpress for the testing of small, quasi-brittle compression specimens, which will exhibit failure strains in the order of magnitude where machine compliance of easily available testing machine will have an effect on the measured results.
- A characterization of the degradation behaviour of bovine cortical bone specimens, in the form of specimens and whole bones, when stored under different storage protocols; in this case short-term refrigeration as a specimen and long-term freezing as a specimen and a whole bone.
- The use of cortical bone cross-section specimens as an intermediary step between material characterization specimen tests and whole bone tests for the material characterization and behaviour of cortical bone.
- The lack of strain-rate dependency of the current 'gold standard' 'Total Human Model for Safety' (THUMS), commonly used to simulate cortical bone.

A general summary of the conclusions will be outlined, followed by a summary of the conclusions that were made for the individual objectives of this study. The conclusions

will be concluded with closing remarks emphasizing the importance of the findings from this work, after which a number of recommendations will be made for future research that will follow-on from this study.

7.1.1 General Conclusion

This work has demonstrated that bovine cortical bone does in fact exhibit distinct degradation behaviour after two weeks in frozen storage. With the most common storage method in the literature being a frozen protocol, this degradation behaviour must be accurately understood, and its effect should be considered when conducting mechanical tests on cortical bone. The long-term frozen storage of cortical bone, be that in the form of a specimen or as a whole bone, has effects on the mechanical properties of cortical bone that cover the scatted range of reported results in the literature. The degradation behaviour observed from the results of this study appear to be a contributing factor to the scatter observed in the literature.

7.1.2 Quasi-Static Subpress

Based on the comparison of the currently available testing machines and the custom quasi-static subpress developed and used in this study, the need for a more accurate and easily repeatable testing apparatus for the testing of small cortical bone specimens is apparent. The comparison of the three displacement measurement systems demonstrated the advantages of the custom subpress over the other two systems. These advantages are even more pronounced when considering the testing of small compression cylinders made of quasi-brittle materials, where minimal yield and failure deformations are expected (i.e. in the order of a millimetre). Through the use of high accuracy magnetic strips, Hall effect sensors, with sufficiently high sampling rates, the subpress was demonstrated to be accurate to the order of a micron.

The subpress met the design and operational requirements, however its ability to test materials stiffer than cortical bone is a point of potential development. The subpress offers a highly repeatable, accurate and consistent displacement measurement system that removes the effect of machine compliance. For the use case of conducting material testing on small cortical bone specimens, the subpress demonstrates significant improvements and benefits over the currently available testing apparatuses.

7.1.3 Machine Compliance

The effect on machine compliance can have a negative effect on the measured properties of cortical bone specimens. Machine compliance must be accounted for and the effects of machine compliance on the measured material properties must be mitigated where possible. The spring theory technique, which was discussed in Section 3.2, that was developed and implemented in this study offers a novel means of determining machine compliance. Based on the results discussed in Section 5.1.4, this technique allowed for the compliance of the Instron testing machine to be quantified and accounted for in the results used to obtain the apparent elastic modulus of polymethyl methacrylate (PMMA) and aluminium three-point bending specimens.

The relative simplicity and repeatability of this technique circumvents the need for complicated and expensive alternatives. The implementation of this technique on future cortical bone specimen tests will allow for more accurate and reliable results.

7.1.4 Degradation Study

With this being the primary aspect of the study, a number of conclusion were drawn of the results from the degradation study. The primary conclusion is that cortical bone specimens undergo significant degradation when stored under a long-term frozen storage protocol. Based on these results, it would appear that degradation effects become apparent after two weeks in frozen storage, with significant degradation occurring after six months in frozen storage. The long-term storage of cortical bone specimens under a refrigerated protocol is not viable. It would appear that the long-term frozen storage of whole bones in saline, from which specimens are machined closer to testing, could prolong the storage life of the specimens, however further research is required to confirm this observation.

Therefore, the testing of refrigerated cortical bone specimens is not recommended if the specimens are stored for longer than 24 hours after retrieval from the donor. The testing of frozen specimens, machined from fresh donor bones, can reliably be conducted up to one week after retrieval from the donor. Specimens that are stored for longer than two weeks in frozen storage have begun to undergo degradation, and any form of bone, be that specimen or whole bone, appears to undergo significant degradation after six months in frozen storage. As a result, for material tests on cortical bone specimens to be considered representative of an in-vivo state, it is advised that specimens be machined from fresh donor bone (i.e. retrieved from the donor within the prior 24 hours) and frozen in saline for a maximum of one week.

Based on these results, fresh bovine cortical bone has an apparent elastic modulus of 23 GPa when tested in quasi-static strain rate regime. This appears to be the closest possible approximation to in-vivo state from an excised bone specimen, under the circumstances and limitations that comply with the ethical testing of biological materials. The most and least fresh results from this degradation study encompass the scatter observed in the literature, at this strain rate, suggesting that degradation contributes to this scatter. This reinforces the need for a standard testing protocol that can be used when conducting material tests of cortical bone. With the seeming lack of consistency in the literature regarding retrieval processes, specimen preparation, storage and testing protocols, such significant scatter is probable.

7.1.5 Cross-Section Tests

The use of cortical bone cross-section tests offer an intermediary step between small, material characterization specimen tests and full bone tests. With small specimens being ideal for material property characterization, due to their inherent simplicity and manufacturability, and full bone tests being significantly geometry-dependent, the cross-section tests offer a balance between the two. The cross-section specimens are small and simple enough to have many machined from a single donor bone relatively easily, and yet complex enough, where the geometry of the specimen begins to offer insight into how a full bone would react under load.

The combination of the three-point bending split Hopkinson bar (SHB) and the high-speed camera yielded results, which were both data-rich quantitatively and qualitatively. The SHB captured the force and displacement history of the specimens, while the high-speed camera captured the overall deformation of the specimens during loading and allowed for the relative cross-sectional area of the cortical region to be quantified, which allowed for the useful 'robustness' metric to be determined. These tests demonstrated a clear relationship between specimen stiffness and robustness, which is a useful benchmark to which numerical results can be compared.

The benefits of the cross-section tests become more apparent when considering the numerical validation of material models for cortical bone. The cross-section specimens are significantly smaller than whole bone models, and are thus less computationally expensive to simulate. However, these cross-section specimens still retain the natural complex geometry of bone, therefore allowing for a more realistic alternative to simulating small, material characterization specimens, where geometry does not have as large of a role.

7.1.6 Numerical Results

Based on the numerical work presented in this thesis, it would appear that the strain rate dependent material model (SRD model) in LS-Dyna has advantages over the piecewise linear plasticity material model (PL model), which is implemented in the 'Total Human Model for Safety' (THUMS). Firstly, the ability for the SRD model to account for the strain rate sensitivity of cortical bone is advantageous as this is far more representative of the biomaterial. Secondly, based on the dynamic compression simulation, the SRD model was the only simulation capable of generating numerical results similar to what was observed experimentally. Finally, with regards to the cross-section simulations, although the PL model was capable of recreating the general trends with relation to specimen robustness, the SRD model, depending on the chosen failure criteria and the material parameters, was able to far closer recreate what was observed experimentally.
Further work is required before these material models and overall simulations can be considered acceptably representative of cortical bone. As has been discussed, the chosen material parameters are crucial in the performance of the simulation. Based on the distinct difference in the measured material properties of the cortical bone when comparing the degradation study results to the fresh bone test results, further experimental tests would greatly help in the refinement of the chosen material parameters.

7.2 Recommendations

The work completed in this study has resulted in a number of useful and important conclusions, particularly with regards to the degradation behaviour of bovine cortical bone. However, like most academic pursuits, answering one question inevitably raises another. As such, this work has, along with its conclusions, brought to light other avenues of research that were beyond the scope of this study, but are still deemed to be worth pursuing further.

7.2.1 Long-Term Storage of Full Bones

While the data from the degradation study did yield a number of useful results, one finding could be enhanced by further, dedicated research. This finding is the degradation behaviour of full bones that are stored under the same long-term storage protocol as the ones in this study. With the FMF (11M) specimens from the degradation study in this research exhibiting such a high initial modulus after two months in storage as a whole bone, this shows promise in extending the viable storage life of cortical bone specimens. However, with only one donor bone in this study being stored under this protocol, further research is required to confirm this conclusion.

7.2.2 Identification of Degradation Mechanism

Although the degradation behaviour of the cortical bone specimens was observed, and general trends and conclusions were made, the mechanism behind this behaviour lies, potentially, beyond the scope of the engineering field, but certainly beyond the scope of this thesis. Should this research be repeated, a microstructural analysis of the specimens could be conducted before each test in order to observe any structural difference in the specimens as they degrade in storage. An electron microscope, micro-CT or synchrotron could offer the resolution required to observe the microstructures that could be the cause of the degradation. Another potential option could be the dyeing of the specimens in order to observe the microstrucutres of the specimens. However, in an effort to truly understand the exact mechanisms behind this degradation, a biological analysis of the specimens through the degradation process might offer an improved alternative to the microstructural analysis. Mineral content analysis would be the most likely to bring to light the chemical mechanism behind the degradation, from which an improved means of prolonging specimen storage life could be identified, perhaps through the use of buffered storage solutions.

7.2.3 Multi-Species Degradation Behaviour

An investigation into bone degradation behaviour across a number of different species would prove useful in an effort to infer human bone degradation, as fresh (i.e. retrieved and tested within 24 hours of death of the donor) human bones cannot be readily accessed, due to ethical restrictions. Characterizing the bone degradation behaviour of a number of different species could allow for a generalized behaviour to be identified. If a sufficiently diverse set of species can be shown to have similar degradation behaviour, it would be reasonable to assume the same behaviour for human bones.

7.2.4 Dedicated Numerical Work

With the numerical work being a minor aspect of this study when compared to the other experimental aspects, a dedicated numerical project focused on the work initiated in this thesis would yield valuable results. In particular, the implementation of the Objective Power Law (OPL) model, developed in BISRU, into LS-Dyna would allow for greater control over the strain-rate dependent nature of cortical bone. Bekker [102] demonstrated the capabilities of this material model when simulating cortical bone. Furthermore, the refinement of the SHB model in LS-Dyna with finer meshes and improved contact definitions could yield improved results, which would more accurately simulate cortical bone.

7.2.5 Bending SHB Redesign

Although the three-point bending SHB was used for the cross-section tests, it was not capable of conducting tests of small beam specimens. The observed dynamic oscillations in the specimens did not allow for any meaningful data to be extracted. As such, it would be recommended that this apparatus be redesigned, taking into account the findings from this study. Potentially using different materials, with slower material wave speeds, such as polymers, could be used to reduce the oscillations, however the sourcing of long polymer tubes with the necessary dimensions could prove difficult. However, if performed, that would allow for a full suite of material tests to be conducted (i.e. both quasi-static and dynamic compression tests or bending tests).

References

[1] James. H. McElhaney, "Dynamic response of bone and muscle tissue.", *J. Appl. Physiol.*, vol. 21, (1966), pp. 1231–1236.

[2] Timothy P.M. Johnson, Simona. Socrate & Mary C. Boyce, "A viscoelastic, viscoplastic model of cortical bone valid at low and high strain rates", *Acta Biomater.*, vol. 6, (2010), pp. 4073–4080.

[3] Elise F. Morgan, Ginu U. Unnikrisnan & Amira I. Hussein, "Bone Mechanical Properties in Healthy and Diseased States", *Annu. Rev. Biomed. Eng.*, vol. 20, (2018), pp. 119–143.

[4] Dieter Christian Wirtz, Norbert Schiffers, Raimund Forst, Thomas Pandorf, Dieter Weichert & Klaus Radermacher, "Critical evaluation of known bone material properties to realize anisotropic FE-simulation of the proximal femur", *J. Biomech.*, vol. 33, (2000), pp. 1325–1330.

[5] Jae Y. Rho, Ting Y. Tsui & George M. Pharr, "Elastic properties of human cortical and trabecular lamellar bone measured by nanoindentation", *Biomaterials*, vol. 18, (1997), pp. 1325–1330.

[6] Nicolas H Hart, Sophia Nimphius, Timo Rantalainen, Alex Ireland, Aris Siafarikas & Robert U. Newton, "Mechanical basis of bone strength: influence of bone material, bone structure and muscle action", *J. Musculoskelet. Neuronal Interact.*, vol. 17, (2017), pp. 114–139.

[7] Emil H. van Haaren, Babette C. van der Zwaard, Albert J. van der Veen, Ide C. Heyligers, Paul I. J. M. Wuisman & Theo H. Smit, "Effect of long-term preservation on the mechanical properties of cortical bone in goats", *Acta Orthop.*, vol. 79, (2009), pp. 708–716.

[8] Elias D. Sedlin & Carl Hirsch, "Factors affecting the determination of the physical properties of femoral cortical bone", *Taylor Fr.*, vol. 37, (1966), pp. 29–48.

[9] Caroline Öhman, Enrico Dall'Ara, Massimiliano Baleani, Serge Van Sint Jan & Marco Viceconti, "The effects of embalming using a 4% formalin solution on the

compressive mechanical properties of human cortical bone", *Clin. Biomech.*, vol. 23, (2008), pp. 1294–1298.

[10] David L. Kopperdahl & Tony M. Keaveny, "Yield strain behavior of trabecular bone", *J. Biomech.*, vol. 31, (1998), pp. 601–608.

[11] Masami Iwamoto, Yoshikatsu Kisanuki, Isao Watanabe, Katsuya Furusu & Kazuo Miki, "Development of a finite element model of the total human model for safety (THUMS) and application to injury reconstruction", in: "IRCOBI Conf.", 2002, pp. 30–42.

[12] Masami Iwamoto, Yuko Nakahira & Hideyuki Kimpara, "Development and Validation of the Total HUman Model for Safety (THUMS) Toward Further Understanding of Occupant Injury Mechanisms in Precrash and During Crash", *Traffic Inj. Prev.*, vol. 16, (2015), pp. S36–S48.

[13] Jae Y. Rho, Liisa Kuhn-Spearing & Peter Zioupos, "Mechanical properties and the hierarchical structure of bone", *Med. Eng. Phys.*, vol. 20, (1998), pp. 92–102.

[14] Maria Fatima, Helena Canhao & Joao Eurico, "Bone: A Composite Natural Material", in: "Bone A Compos. Nat. Mater.", September, InTech, 2011.

[15] Bart Clarke, "Normal Bone Anatomy and Physiology", *Clin. J. Am. Soc. Nephrol.*, vol. 3, (2008), pp. S131–S139.

[16] Trevor J. Cloete, Graeme Paul & Ernesto B. Ismail, "Hopkinson bar techniques for the intermediate strain rate testing of bovine cortical bone", *Philos. Trans. R. Soc. A Math. Phys. Eng. Sci.*, vol. 372.

[17] Susan M. Ott, "Cortical or Trabecular Bone: What's the Difference?", *Am. J. Nephrol.*, vol. 47, (2018), pp. 373–375.

[18] Fan Liu, Chen Liu, Qiuhong Chen, Qiang Ao, Xiaohong Tian, Jun Fan, Hao Tong & Xiaohong Wang, "Progress in organ 3D bioprinting", *Int. J. Bioprinting*, vol. 4.

[19] Sugandha Chahal, Anuj Kumar & Fathima Shahitha Jahir Hussian, "Development of biomimetic electrospun polymeric biomaterials for bone tissue engineering. A review", *J. Biomater. Sci. Polym. Ed.*, vol. 30, (2019), pp. 1308–1355.

[20] Yasser Ahmed, Mohamed Abdelsabou & Fatma Khalil, "Absence of Typical Haversian System from the Compact Bone of Some Reptile and Bird Species", *Asian J. Biol. Sci.*, vol. 10, (2017), pp. 98–103.

[21] John D. Currey, "The many adaptations of bone", *J. Biomech.*, vol. 36, (2003), pp. 1487–1495.

[22] Zilan X. Lin, Zhi H. Xu, Yuehuei H. An & Xiaodong Li, "In situ observation of fracture behavior of canine cortical bone under bending", *Mater. Sci. Eng. C*, vol. 62, (2016), pp. 361–367.

[23] Christopher R. Ethier & Craig A. Simmons, *Introductory Biomechanics: From Cells to Organisms*, Cambridge University Press, 2007.

[24] Philippe K. Zysset, Edward X. Guo, Edward C. Hoffler, Kristin E. Moore & Steven A. Goldstein, "Elastic modulus and hardness of cortical and trabecular bone lamellae measured by nanoindentation in the human femur", *J. Biomech.*, vol. 32, (1999), pp. 1005–1012.

[25] Christian Huet & C Huett, "Application of variational concepts to size effects in elastic heterogeneous bodies", *J. Mech. Phys. Solids*, vol. 38.

[26] Tony M. Keaveny, Edward F. Wachtel, Catherine M. Ford & Wilson C. Hayes, "Differences between the tensile and compressive strengths of bovine tibial trabecular bone depend on modulus", *J. Biomech.*, vol. 27, (1994), pp. 1137–1146.

[27] Charles H. Turner, Anand Chandran & Ramana M. V. Pidaparti, "The Anisotropy of Osteonal Bone and Its Ultrastructural Implications", *Bone*, vol. 17, (1995), pp. 85–89.

[28] Cinzia Zannoni, Raffaella Mantovani & Marco Viceconti, "Material properties assignment to finite element models of bone structures: a new method", *Med. Eng. Phys.*, vol. 20, (1998), pp. 735–740.

[29] Ziheng Wu, Timothy C. Ovaert & Glen L. Niebur, "Viscoelastic Properties of Human Cortical Bone Tissue Depend on Gender and Elastic Modulus", *J. Orthop. Res.*, vol. 30, (2012), pp. 693–699.

[30] Naoki Sasaki, Tsutomu Nozoe, Ryoji Nishihara & Akimasa Fukui, "Effect of mineral dissolution from bone specimens on the viscoelastic properties of cortical bone", *J. Biomech.*, vol. 41, (2008), pp. 3511–3514.

[31] David P. Fyhrie & Blaine A. Christiansen, "Bone Material Properties and Skeletal Fragility", *Calcif. Tissue Int.*, vol. 97, (2015), pp. 213–228.

[32] Dennis R. Carter & Wilson C. Hayes, "Bone compressive strength: the influence of density and strain rate", *Science*, vol. 194, (1976), pp. 1174–1176.

[33] Marta E. Szabó & Philipp J. Thurner, "Anisotropy of bovine cortical bone tissue damage properties", *J. Biomech.*, vol. 46, (2013), pp. 2–6.

[34] Xu Feng, "Chemical and Biochemical Basis of Cell-Bone Matrix Interaction in Health and Disease", *Curr. Chem. Biol.*, vol. 3, (2009), pp. 189–196.

[35] Fergal J. O'Brien, David Taylor & T. Clive Lee, "Bone as a composite material: The role of osteons as barriers to crack growth in compact bone", *Int. J. Fatigue*, vol. 29, (2007), pp. 1051–1056.

[36] Hélène Beaupied, Eric Lespessailles & Claude Laurent Benhamou, "Evaluation of macrostructural bone biomechanics", *Jt. Bone Spine*, vol. 74, (2007), pp. 233–239.

[37] H. Spatz, E. J. O'leary & Julian F. V. Vincent, "Young's Moduli and Shear Moduli in Cortical Bone", *Biol. Sci.*, vol. 263, (1996), pp. 287–294.

[38] Harold M. Frost, "Bone's mechanostat: A 2003 update", *Anat. Rec. Part A Discov. Mol. Cell. Evol. Biol.*, vol. 275A, (2003), pp. 1081–1101.

[39] Harold M. Frost, "A 2003 Update of Bone Physiology and Wolff's Law for Clinicians", *Angle Orthod.*, vol. 74.

[40] Diane M. Cullen, R. T. Smith & Mohammed P. Akhter, "Bone-loading response varies with strain magnitude and cycle number", *J. Bone. Joint. Surg. Am.*, vol. 66, (1984), pp. 397–402.

[41] Yeou-Fang Hsieh & Charles H. Turner, "Effects of Loading Frequency on Mechanically Induced Bone Formation", *J. Bone Miner. Res.*, vol. 16, (2001), pp. 918–924.

[42] Stuart J. Warden & Charles H. Turner, "Mechanotransduction in the cortical bone is most efficient at loading frequencies of 5–10 Hz", *Bone*, vol. 34, (2004), pp. 261–270.

[43] David B. Burr, Alexander G. Robling & Charles H. Turner, "Effects of biomechanical stress on bones in animals", *Bone*, vol. 30, (2002), pp. 781–786.

[44] Stefan Judex & Ronald F. Zernicke, "High-impact exercise and growing bone: relation between high strain rates and enhanced bone formation", *J. Appl. Physiol.*, vol. 88, (2000), pp. 2183–2191.

[45] David M. L. Cooper, Chantal E. Kawalilak, Kim D. Harrison, Bryan D. Johnston & James D. Johnston, "Cortical Bone Porosity: What Is It, Why Is It Important,

and How Can We Detect It?", *Curr. Osteoporos. Reports 2016 145*, vol. 14, (2016), pp. 187–198.

[46] John D. Currey, "Incompatible mechanical properties in compact bone", *J. Theor. Biol.*, vol. 231, (2004), pp. 569–580.

[47] Richard W. McCalden, J. A. McGlough, M. B. Barker & Charles M. Court-Brown, "Age-related changes in the tensile properties of cortical bone. The relative importance of changes in porosity, mineralization and microstructure", *J. Bone Jt. Surg. - Ser. A*, vol. 75, (1993), pp. 1193–1205.

[48] Klaus Engelke, Cesar R. Libanati, Thomas P. Fuerst, Philippe K. Zysset & Harry K. Genant, "Advanced CT based In Vivo Methods for the Assessment of Bone Density, Structure, and Strength", *Curr. Osteoporos. Reports 2013 113*, vol. 11, (2013), pp. 246–255.

[49] John D. Currey, "Effects of differences in mineralization on the mechanical properties of bone", *Philos. Trans. R. Soc. London. B, Biol. Sci.*, vol. 304, (1984), pp. 509–518.

[50] Eve Donnelly, Dan X. Chen, Adele L. Boskey, Shefford P. Baker & Marjolein C. H. van der Meulen, "Contribution of Mineral to Bone Structural Behavior and Tissue Mechanical Properties", *Calcif. Tissue Int. 2010 875*, vol. 87, (2010), pp. 450–460.

[51] Ting Wang & Zude Feng, "Dynamic mechanical properties of cortical bone: The effect of mineral content", *Mater. Lett.*, vol. 59, (2005), pp. 2277–2280.

[52] Dan Faibish, Susan M. Ott & Adele L. Boskey, "Mineral Changes in Osteoporosis A Review", *Clin. Orthop. Relat. Res.*, vol. 443, (2006), p. 28.

[53] Jae Y. Rho & George M. Pharr, "Effects of drying on the mechanical properties of bovine femur measured by nanoindentation", *J. Mater. Sci. Mater. Med.*, vol. 10, (1999), pp. 485–488.

[54] Raghavendra R. Adharapurapu, Fengchun Jiang & Kenneth S. Vecchio, "Dynamic fracture of bovine bone", *Mater. Sci. Eng. C*, vol. 26, (2006), pp. 1325–1332.

[55] Prasit Lucksanasombool, William A. J. Higgs, Robin J. E. D. Higgs & Michael V. Swain, "Fracture toughness of bovine bone: influence of orientation and storage media", *Biomaterials*, vol. 22, (2001), pp. 3127–3132.

[56] Jasmine A. Nirody, Karen P. Cheng, Robin M. Parrish, Andrew J. Burghardt, Sharmila Majumdar, Thomas M. Link & Galateia J. Kazakia, "Spatial distribution of intracortical porosity varies across age and sex", *Bone*, vol. 75, (2015), pp. 88–95.

[57] Zacharie Toth, Ashley Ward, Simon Y. Tang & Sarah Mcbride-Gagyi, "Sexual differences in bone porosity, osteocyte density, and extracellular matrix organization due to osteoblastic-specific Bmp2 deficiency in mice", *Bone*, vol. 150, (2021), pp. 8756–3282.

[58] Henry T. Montoye, John F. McCabe, Helen L. Metzner & Stanley M. Garn, "Physical Activity and Bone Density", *Hum. Biol.*, vol. 48, (1976), pp. 599–610.

[59] Nils Dalén & Karl E. Olsson, "Bone Mineral Content and Physical Activity", *Acta Orthop. Scand.*, vol. 45, (2009), pp. 170–174.

[60] Vincent Ebacher, Cecelia Tang, Heather McKay, Thomas R. Oxland, Pierre Guy & Rizhi Wang, "Strain redistribution and cracking behavior of human bone during bending", *Bone*, vol. 40, (2007), pp. 1265–1275.

[61] Jong-Hoen Kim, Mitsuo Niinomi, Toshikazu Akahori & Hiroyuki Toda, "Fatigue properties of bovine compact bones that have different microstructures", *Int. J. Fatigue*, vol. 29, (2007), pp. 1039–1050.

[62] Satoshi Yamada, Shigeru Tadano & Koichi Fukasawa, "Micro-cantilever bending for elastic modulus measurements of a single trabecula in cancellous bone", *J. Biomech.*, vol. 49, (2016), pp. 4124–4127.

[63] Zhigang Li, Jinjin Wang, Guanghui Song, Cheng Ji & Xinfeng Han, "Anisotropic and strain rate-dependent mechanical properties and constitutive modeling of the cancellous bone from piglet cervical vertebrae", *Comput. Methods Programs Biomed.*, vol. 188, (2020), p. 105279.

[64] Robert E. Borchers, Lorna J. Gibson, Hans Burchardt & Wilson C. Hayes, "Effects of selected thermal variables on the mechanical properties of trabecular bone", *Biomaterials*, vol. 16, (1995), pp. 545–551.

[65] Sarah Zhao, Matthew Arnold, Richard L. Abel, Justin P. Cobb, Shaocheng Ma, Ulrich Hansen & Oliver Boughton, "Standardizing Compression Testing for Measuring the Stiffness of Human Bone", *Bone Jt. Res.*, vol. 7, (2018), pp. 524–538.

[66] B Sanborn, C A Gunnarsson, & M Foster & T Weerasooriya, "Quantitative Visualization of Human Cortical Bone Mechanical Response: Studies on the

Anisotropic Compressive Response and Fracture Behavior as a Function of Loading Rate", *Exp. Mech.*, vol. 95, (2016), pp. 56–81.

[67] Tusit Weerasooriya, Brett Sanborn, Allan C. Gunnarsson & Mark Foster, "Orientation dependent compressive response of human femoral cortical bone as a function of strain rate", *J. Dyn. Behav. Mater.*, vol. 2, (2016), pp. 74–90.

[68] Mary B. Gustafson, Rod B. Martin, V. A. Gibson, David H. Storms, Ssusan M. Stover, Jeffery C. Gibeling & Lanny V. Griffin, "Calcium buffering is required to maintain bone stiffness in saline solution", *J. Biomech.*, vol. 29, (1996), pp. 1191–1194.

[69] James C. H. Goh, Eng J. Ang & Kamal Bose, "Effect of preservation medium on the mechanical properties of cat bones", *Acta Orthop. Scand.*, vol. 60, (2009), pp. 465–467.

[70] Unger Stefan, Blauth Michael & Schmoelz Werner, "Effects of three different preservation methods on the mechanical properties of human and bovine cortical bone", *Bone*, vol. 47, (2010), pp. 1048–1053.

[71] John D. Currey, Kevin Brear, Peter Zioupos & Gwendolen C. Reilly, "Effect of formaldehyde fixation on some mechanical properties of bovine bone", *Biomaterials*, vol. 16, (1995), pp. 1267–1271.

[72] Woowon Lee & Iwona Jasiuk, "Effects of freeze-thaw and micro-computed tomography irradiation on structure-property relations of porcine trabecular bone", *J. Biomech.*, vol. 47, (2014), pp. 1495–1498.

[73] Bryan Kaye, Connor Randall, Daniel Walsh & Paul Hansma, "The effects of freezing on the mechanical properties of bone", *Open Bone J.*, vol. 4, (2012), pp. 14–19.

[74] Manh-Tu Nguyen, Jean-Marc Allain, Hakim Gharbi, Christophe Desceliers & Christian Soize, "Experimental multiscale measurements for the mechanical identification of a cortical bone by digital image correlation", *J. Mech. Behav. Biomed. Mater.*, vol. 63, (2016), pp. 125–133.

[75] B Pereira, J Xavier, F Pereira & J Morais, "Identification of transverse elastic properties of the diaphysis of cortical bone", *J. Mech. Eng. Biomech.*, vol. 2, (2018), pp. 50–55.

[76] Marianne Prot, Trevor J. Cloete, Dominique Saletti & Sebastien Laporte, "Intermediate strain rate behaviour of cancellous bone: Links between

microstructural and mechanical properties", *EPJ Web Conf.*, vol. 94, (2015), p. 03006.

[77] Ch-Kranthi Teja, Anoop Chawla & Sudipto Mukherjee, "Determining the strain rate dependence of cortical and cancellous bones of human tibia using a Split Hopkinson pressure bar", *Int. J. Crashworthiness*, vol. 18, (2013), pp. 11–18.

[78] Tim Svensson & Filip Tell, *Stress Wave Propagation Between Different Materials*, Ph.D. thesis, Chalmers University Of Technology, 2015.

[79] Adnan I .O. Zaid, "Stress Waves in Solids, Transmission, Reflection and Interaction and Fractures Caused by Them: State of the Art", *Int. J. Theor. Appl. Mech.*, vol. 1, (2016), pp. 155–164.

[80] Kaiwen Xia & Wei Yao, "Dynamic rock tests using split Hopkinson (Kolsky) bar system – A review", *J. Rock Mech. Geotech. Eng.*, vol. 7, (2015), pp. 27–59.

[81] Fengchun Jiang, Kenneth S. Vecchio & Aashish Rohatgi, "Analysis of modified split Hopkinson pressure bar dynamic fracture test using an inertia model", *Int. J. Fract.*, vol. 126, (2004), pp. 143–164.

[82] Fengchun Jiang & Kenneth S. Vecchio, "Dynamic Effects in Hopkinson Bar Four-Point Bend Fracture", *Metall. Mater. Trans. A*, vol. 38, (2007), pp. 2896–2906.

[83] Robert E. Chen, Kaiwen Xia, Feng Dai, Fangyun Lu & Shengnian N. Luo, "Determination of dynamic fracture parameters using a semi-circular bend technique in split Hopkinson pressure bar testing", *Eng. Fract. Mech.*, vol. 76, (2009), pp. 1268–1276.

[84] Hongbo Du, Feng Dai, Kaiwen Xia, Nuwen Xu & Yuan Xu, "Numerical investigation on the dynamic progressive fracture mechanism of cracked chevron notched semi-circular bend specimens in split Hopkinson pressure bar tests", *Eng. Fract. Mech.*, vol. 184, (2017), pp. 202–217.

[85] Shigeo M. Tanaka, Imranul Alam & Charles H. Turner, "Stochastic resonance in osteogenic response to mechanical loading", *FASEB J.*, vol. 17, (2003), pp. 313–314.

[86] Brad L. Boyce & Morris F. Dilmore, "The dynamic tensile behavior of tough, ultrahigh-strength steels at strain-rates from 0.0002 s-1 to 200 s-1", *Int. J. Impact Eng.*, vol. 36, (2009), pp. 263–271.

[87] Charles M. Court-Brown, S. Rimmer, Udai Prakash & Margaret M. McQueen, "The epidemiology of open long bone fractures", *Injury*, vol. 29, (1998), pp. 529–534.

[88] Kun Hwang, Sun H. You & In A. Sohn, "Analysis of orbital bone fractures: A 12-year study of 391 patients", *J. Craniofac. Surg.*, vol. 20, (2009), pp. 1218–1223.

[89] Kun Hwang & Sun H. You, "Analysis of facial bone fractures: An 11-year study of 2,094 patients", *Indian J. Plast. Surg.*, vol. 43, (2010), pp. 42–48.

[90] Ron C. Cannon & Robert A. Jahrsdoerfer, "Temporal Bone Fractures: Review of 90 Cases", *Arch. Otolaryngol.*, vol. 109, (1983), pp. 285–288.

[91] Kenneth S. Vecchio & Fengchun Jiang, "Improved pulse shaping to achieve constant strain rate and stress equilibrium in split-Hopkinson pressure bar testing", *Metall. Mater. Trans. A Phys. Metall. Mater. Sci.*, vol. 38 A, (2007), pp. 2655–2665.

[92] Petra Christöfl, Caterina Czibula, Michael Berer, Gernot Oreski, Christian Teichert & Gerald Pinter, "Comprehensive investigation of the viscoelastic properties of PMMA by nanoindentation", *Polym. Test.*, vol. 93, (2021), p. 106978.

[93] Makrem Nasraoui, Pascal A. Forquin, Larbi Siad & Alexis Rusinek, "Influence of strain rate, temperature and adiabatic heating on the mechanical behaviour of poly-methyl-methacrylate: Experimental and modelling analyses", *Mater. Des.*, vol. 37, (2012), pp. 500–509.

[94] Wenjun Hu, Hui Guo, Yongmei Chen, Ruoze Xie, Hua Jing & Peng He, "Experimental investigation and modeling of the rate-dependent deformation behavior of PMMA at different temperatures", *Eur. Polym. J.*, vol. 85, (2016), pp. 313–323.

[95] Lijun Li, Yiben Zhang, Lingyu Sun & Huipeng Hu, "Effects of strain rate and temperature on the mechanical behavior of polymethyl methacrylate (PMMA)", *Polym. Bull.*, vol. 80, (2023), pp. 8685–8702.

[96] J. Richeton, Said Ahzi, Kenneth S. Vecchio, Fengchun C. Jiang & Raghavendra R. Adharapurapu, "Influence of temperature and strain rate on the mechanical behavior of three amorphous polymers: Characterization and modeling of the compressive yield stress", *Int. J. Solids Struct.*, vol. 43, (2006), pp. 2318–2335.

[97] Tao Jin, Zhiwei Zhou, Xuefeng Shu, Zhihua Wang, Guiying Wu & Zhenguo Liu, "Effects of strain rate on PMMA failure behavior", *Appl. Phys. A*, vol. 122.

[98] Saikat D. Acharya & Anoop K. Mukhopadhyay, "High strain rate compressive behavior of PMMA", *Polym. Bull.*, vol. 71, (2014), pp. 133–149.

[99] Timothy J. Holmquist, Jermaine M. Bradley, Ajmer K. Dwivedi & Daniel T. Casem, "The response of polymethyl methacrylate (PMMA) subjected to large strains, high strain rates, high pressures, a range in temperatures, and variations in the intermediate principal stress", *Eur. Phys. J. Spec. Top.*, vol. 225, (2016), pp. 343–354.

[100] Victor P. W. Shim, L. M. Yang, Jianfei F. Liu & Peter V. S. Lee, "Characterisation of the dynamic compressive mechanical properties of cancellous bone from the human cervical spine", *Int. J. Impact Eng.*, vol. 32, (2005), pp. 525–540.

[101] Anriette van der Westhuizen, *The strain rate dependent mechanical properties and modelling of bovine cortical bone in compression*, Ph.D. thesis, University of Cape Town, 2008.

[102] Anriëtte Bekker, Schalk Kok, Trevor J. Cloete & Gerald N. Nurick, "Introducing objective power law rate dependence into a visco-elastic material model of bovine cortical bone", *Int. J. Impact Eng.*, vol. 66, (2014), pp. 28–36.

[103] Graeme Paul, "The Strain Rate Dependent Properties of Bovine Cortical Bone", Tech. Rep. April, University of Cape Town, 2014.

[104] Mayank Bagaria, *Experimental and numerical simul al and numerical simulation of split hopkinson pressure bar test on borosilicate glass*, Ph.D. thesis, Michigan Technological University, 2019.

[105] Shou Chen, "Numerical simulation of split-hopkinson pressure bar test on high-density polyethylene", *Chem. Eng. Trans.*, vol. 66, (2018), pp. 271–276.

[106] Erik Söderström, *Characterisation and Modelling of Mechanical Properties for Granite and Diabase*, Ph.D. thesis, Luleå University of Technology, 2016.

[107] Emmanuel A. Flores-Johnsond & Qingming Li, "Structural effects on compressive strength enhancement of concrete-like materials in a split Hopkinson pressure bar test Split Hopkinson pressure bar Structural effects Concrete-like materials Dynamic increase factor Finite-element modelling", *Int. J. Impact Eng.*, vol. 109, (2017), pp. 408–418.

[108] Man Xu & Kay Wille, "Numerical Investigation of the Effects of Pulse Shaper, Lateral Inertia, and Friction on the Calculated Strain-Rate Sensitivity of UHP-FRC Using a Split Hopkinson Pressure Bar", *J. Mater. Civ. Eng.*, vol. 28.

[109] Wanhui Feng, Baiyu Chen, Yunchao Tang, Wenbo Wei, Weiming He & Yongmin Yang, "Structural effects and real strain-rate effects on compressive strength of sustainable concrete with crumb rubber in split Hopkinson pressure bar tests", *Arch. Civ. Mech. Eng.*, vol. 22, (2022), p. 136.

[110] Claire Kammerer & Alain Neme, "Plane behaviour at high strain rates of a quasi-unidirectional E-glass/polyester composite: Application to balistic impacts", *Eur. J. Mech. A/Solids*, vol. 17, (1997), pp. 461–477.

[111] Claire Kammerer & Alain Neme, "Plane behavior of an E-glass/polyester composite at high strain rates", *Compos. Sci. Technol.*, vol. 58, (1998), pp. 717–725.

[112] José A. Loya & Jose Fernández-Sáez, "Three-dimensional effects on the dynamic fracture determination of Al 7075-T651 using TPB specimens", *Int. J. Solids Struct.*, vol. 45, (2008), pp. 2203–2219.

[113] Dan Givoli, "High-order local non-reflecting boundary conditions: A review", *Wave Motion*, vol. 39, (2004), pp. 319–326.

[114] Matthew Weyer, *An Experimental and Theoretical Study on the Effect of Strain Rate on Ductile Damage*, Ph.D. thesis, University of Cape Town, 2016.

[115] Jamila Rahmoun, Audrey Auperrin, Rémi Delille, Hakim Naceur & Pascal Drazetic, "Characterization and micromechanical modeling of the human cranial bone elastic properties", *Mech. Res. Commun.*, vol. 60, (2014), pp. 7–14.

[116] Zhigang Li, Jian Wang, Jiawei Wang, Jinjin Wang, Cheng Ji & Guangliang Wang, "Experimental and numerical study on the mechanical properties of cortical and spongy cranial bone of 8-week-old porcines at different strain rates", *Biomech. Model. Mechanobiol.*, vol. 19, (2020), pp. 1797–1808.

[117] Zahra Asgharpour, Peter Zioupos, Matthias Graw & Steffen Peldschus, "Development of a strain rate dependent material model of human cortical bone for computer-aided reconstruction of injury mechanisms", *Forensic Sci. Int.*, vol. 236, (2014), pp. 109–116.

[118] Masami Iwamoto, Yuko Nakahira & Atsutaka Tamura, "Development of Advanced Human Models in Thums", in: "6th Eur. LS-DYNA Users' Conf. Dev.", 2007, pp. 47–56.

[119] Masami Iwamoto, Atsutaka Tamura, Katsuya Furusu, Chiharu Kato, Kazuo Miki, Junji Hasegawa & King H. Yang, "Development of a Finite Element Model of the

Human Lower Extremity for Analyses of Automotive Crash Injuries", *J. Passeng. Cars Mech. Syst. J.*, vol. 109, (2000), pp. 846–853.

[120] Takao Matsuda, Maoya Kobayashi, Noriyuki Fujita & Yuichi Kitagawa, "Development of a Human Body Model (Thums Version 7) To Simulate Kinematics and Injuries of Reclined Occupants in Frontal Collisions.", in: "27th Int. Tech. Conf. Enhanc. Saf. Veh. Natl. Highw. Traffic Saf. Adm.", 2023, pp. 1–29.

[121] Kai A. Forster, "High Precision Bone Specimen Loading Fixture", Tech. rep., University of Cape Town, 2020.

[122] Adina Piovesana & Graeme Senior, "How Small Is Big: Sample Size and Skewness", *Assessment*, vol. 25, (2018), pp. 793–800.

[123] Robert A. Wannamaker, Stanley P. Lipshitz, John Vanderkooy & J. Nelson Wright, "A theory of nonsubtractive dither", *IEEE Trans. Signal Process.*, vol. 48, (2000), pp. 499–516.

[124] John Vanderkooy & Stanley P. Lipshitz, "Resolution Below the Least Significant Bit in Digital Systems With Dither.", *J. Audio Eng. Soc.*, vol. 32, (1984), pp. 106–113.

[125] Roberto Etchenique & Jorge Aliaga, "Resolution enhancement by dithering", *Am. J. Phys.*, vol. 72, (2004), p. 159.

[126] "ASTM D695 - Standard test method for compressive properties of rigid plastics", 2023.

[127] "ISO604 - Plastics - Determination of compressive properties", 2002.

[128] Claire V. Rampersadh, Lee-Anne Welgemoed & Trevor J. Cloete, "A multispecies investigation of the strain rate sensitivity of the modulus of cortical bone", in: "EPJ Web Conf.", , vol. 2502021, p. 06003.

[129] Nicholas Daras, Trevor J. Cloete & Gerald N. Nurick, "A novel quasi-static compression test set-up with micron order accuracy for small specimens", *J. Brazilian Soc. Mech. Sci. Eng.*, vol. 46.

[130] Sebastian Henschel & Lutz Krüger, "Dynamic crack initiation measurements in a four-point split Hopkinson bending device", *Eng. Fract. Mech.*, vol. 133, (2015), pp. 62–75.

[131] Alpana A Thorat & Raj Suryanarayanan, "Characterization of Phosphate Buffered Saline (PBS) in Frozen State and after Freeze-Drying", *Pharm. Res.*, vol. 36, (2019), pp. 1–11.

[132] Rodrigo J. Aristizabal, *Estimating the Parameters of the Three-Parameter Lognormal Distribution*, Ph.D. thesis, Florida International University, 2012.

[133] Prasanta Basak, Indrani Basak & N Balakrishnan, "Computational Statistics and Data Analysis Estimation for the three-parameter lognormal distribution based on progressively censored data", *Comput. Stat. Data Anal.*, vol. 53, (2009), pp. 3580–3592.

[134] Eckhard Limpert, Werner A. Stahel & Markus Abbt, "Log-normal distributions across the sciences: Keys and clues", *Bioscience*, vol. 51, (2001), pp. 341–352.

[135] A. Clifford Cohen & Betty Jones Whitten, "Estimation in the three-parameter lognormal distribution", *J. Am. Stat. Assoc.*, vol. 75, (1980), pp. 399–404.

[136] Lee-Anne Welgemoed, "An experimental investigation of interspecies variation in mechanical properties of cortical bone", Tech. rep., University of Cape Town, Cape Town, 2018.

[137] Robert M. Gray & David L. Neuhoff, "Quantization", *IEEE Trans. Inf. Theory*, vol. 44, (1998), pp. 2325–2383.

[138] Xudong C. Limei, Ge Jikai & Zhou S. Wu, "Dynamic brazilian test of concrete using split hopkinson pressure bar", *Mater. Struct.*, vol. 50, (2017), pp. 1–15.

[139] Ross S. Hartley, Trevor J. Cloete & Gerald N. Nurick, "An experimental assessment of friction effects in the split Hopkinson pressure bar using the ring compression test", *Int. J. Impact Eng.*, vol. 34, (2007), pp. 1705–1728.

[140] Patrick Jonsson, Pär Jonsén, Patrik Andreasson, Staffan Lundström & Gunnar I. Hellström, *LS-DYNA Keyword User's Manual Volume II - Material Models*, ANSYS, Livermore, CA, 15th edn., 2024.

[141] Singiresu S. Rao, *Mechanical Vibrations*, Pearson Education, Inc., New Jersey, fifth edn., 2011.

[142] Nicholas Daras, Gerald N. Nurick & Trevor J. Cloete, "Degradation of the mechanical properties of cortical bone due to long duration storage", *J. Mech. Behav. Biomed. Mater.*, vol. 157.

[143] Andreas C. Bryhn & Peter H. Dimberg, "An operational definition of a statistically meaningful trend", *PLoS One*, vol. 6, (2011), p. 19241.

[144] Donald A. S. Fraser & Judith Rousseau, "Studentization and deriving accurate p-values", *Biometrika*, vol. 95, (2008), pp. 1–16.

[145] Ricardo Gimeno, Benjamin Manchado & Roman Minguez, "Stationarity tests for ÿnancial time series", *Physica A*, vol. 269, (1999), pp. 72–78.

[146] Jonathan D. Cryer & Kung-Sik Chan, *Time series analysis*, Springer Science+Business Media, New York, second edn., 1986.

Additional Readings

This chapter provides a compilation of journal articles that, although not directly cited in the text, provided supplementary insights and facilitated additional avenues for exploration.

[1] Albert H. Burstein, Donald T. Reilly, and Marc Martens. "Aging of bone tissue: mechanical properties.", *The Journal of Bone & Joint Surgery*, vol. 58, (1976), pp. 82-86.

[2] Evans, F. Gaynor. "Mechanical properties and histology of cortical bone from younger and older men.", *The Anatomical Record*, vol. 185, (1976), pp. 1-11.

[3] Monika Martiniakova, Birgit Grosskopf, Radoslav Omelka, Maria Vondrakova, and Maria Bauerova. "Differences among species in compact bone tissue microstructure of mammalian skeleton: use of a discriminant function analysis for species identification.", *Journal of Forensic Sciences*, vol. 51, (2006), pp. 1235-1239.

[4] Ingrid Ott, Reinhold Kienzler, and Roswitha Schröder. "Aging in the cortical bone: a constitutive law and its application.", *Archive of Applied Mechanics*, vol. 80, (2010), pp. 527-541.

[5] Esther J. Tanck, Jasper Homminga, Harry G. van Lenthe, and Rik Huiskes. "Increase in bone volume fraction precedes architectural adaptation in growing bone.", *Bone*, vol. 28, (2001), pp. 650-654.

[6] Amanda M. Agnew, Kevin Moorhouse, Yun-Seok Kang, Bruce R. Donnelly, Kiel Pfefferle, Angela X. Manning, Alan S. Litsky, Rod Herriott, Mahmoud Abdel-Rasoul, and John H. Bolte. "The response of pediatric ribs to quasi-static loading: mechanical properties and microstructure.", *Annals of Biomedical Engineering*, vol. 41, (2013), pp. 2501-2514.

Appendices

Appendix A

List of Publications

This appendix contains a list of the published journal papers and conference proceedings that stem from the work reported in this thesis.

A.1 Journal Articles

A.1.1 In Press

1. Daras, N., Cloete, T. J. and Nurick, G. N., A Novel Quasi-Static Compression Test Set-up With Micron Order Accuracy for Small Specimens, In the *Journal of the Brazilian Society of Mechanical Sciences and Engineering*, Accepted in May 2024, BMSE-D-24-00195.
   This introduces the need for the novel subpress through the comparison of the displacement measurement capabilities of the subpress, a universal testing machine and a visual extensometer. Results from a number of tests conducted on polymer specimens and cortical bone specimens validate the operation of the subpress. The polymer test comparison is discussed in Section 3.1, while the cortical bone tests are discussed in Section 6.2. Reference [129].

2. Daras, N., Nurick, G. N. and Cloete, T. J., Degradation of the Mechanical Properties of Cortical Bone due to Long Duration Storage, In the *Journal of the Mechanical Behavior of Biomedical Materials*, Accepted in June 2024, JMBBM-D-24-00509.
   This article presents the results obtained from the degradation study where the effects of storage duration on the mechanical properties of cortical bone were studied, as discussed in Section 6.2. Reference [142].

A.2 Conference Proceedings

1. Daras, N., Cloete, T. J. and Nurick, G. N., Influence of long duration storage on the material characterization data of bovine cortical bone, In *The 7th International Conference on Material Modelling (ICMM7)*, Cape Town, South Africa, December 2022.
   This presentation represents the first publication of the results obtained from the degradation study where the effects of storage duration on the mechanical properties of cortical bone were studied, as discussed in Section 6.2.

2. Daras, N., Cloete, T. J. and Nurick, G. N., Storage duration effects on the properties of cortical bone - modelling implications, In *Symposium on Computer Methods in Biomechanics and Biomedical Engineering (CMBBE)*, Paris, France, May 2023.
   This presentation represents an investigation in to the modelling implications of the effects of storage duration on the modelling of cortical bone specimens, as discussed in Sections 6.2 and 6.5.1.

Appendix B

Log Normal Distribution

Due to the data obtained in this research being skewed, in order to determine the true mean, mode and median of the data, a log normal distribution was used. If a data set has a log normal distribution, equation B.1 will result in the data set's normal distribution.

$$Y = ln(X + C) \tag{B.1}$$

The reason for this choice, as can be seen in the plots below, is that a log normal distribution more accurately describes a skew data set than a normal distribution. This is made evident by the fact that the mode, which is represented by the tallest bar of the histogram, it outside of the data range of the normal distribution. However, the log normal distribution more accurately accounts for this extreme skewness.

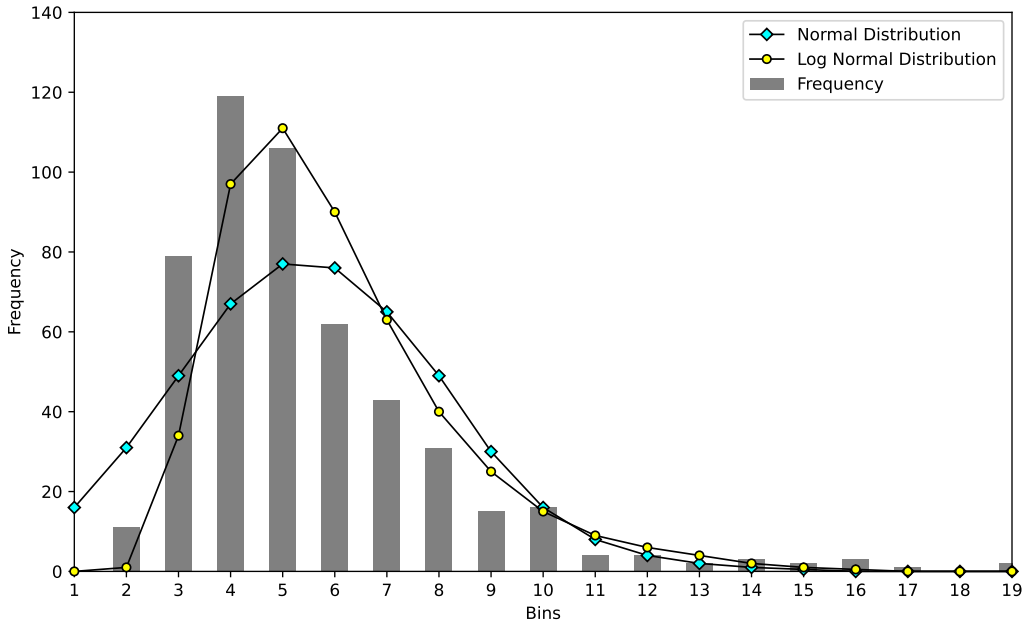

From this log normal distribution, one can determine the mean, mode and median of the otherwise difficult to analyse data. These three critical values are determined using the Equations B.2, B.3 and B.4.

$$Mean(X) = C + e^{\mu + \frac{\theta^2}{2}} \tag{B.2}$$

$$Mode(X) = C + e^{\mu - \theta^2} \tag{B.3}$$

$$Median(X) = C + e^{\mu} \tag{B.4}$$

In the three equations seen above, μ and θ are the mean and standard deviation of the Y data set respectively. The constant C is the threshold parameter, and it is a constant that is chosen independent of the data, and it simply ensures that not values of the log normal data are negative. If there were negative values, the log normal function would result in an error.

Appendix C

Ethics Clearance Form

ETHICS APPLICATION FORM

Please Note:
Any person planning to undertake research in the Faculty of Engineering and the Built Environment (EBE) at the University of Cape Town is required to complete this form **before** collecting or analysing data. The objective of submitting this application *prior* to embarking on research is to ensure that the highest ethical standards in research, conducted under the auspices of the EBE Faculty, are met. Please ensure that you have read, and understood the **EBE Ethics in Research Handbook** (available from the UCT EBE, Research Ethics website) prior to completing this application form: http://www.ebe.uct.ac.za/ebe/research/ethics1

APPLICANT'S DETAILS		
Name of principal researcher, student or external applicant		Nicholas Daras
Department		Mechanical Engineering
Preferred email address of applicant:		DRSNIC002@myuct.ac.za
If Student	Your Degree: e.g., MSc, PhD, etc.	PhD
	Credit Value of Research: e.g., 60/120/180/360 etc.	360
	Name of Supervisor (if supervised):	Prof. Gerald N. Nurick
If this is a researchcontract, indicate the source of funding/sponsorship		N/A
Project Title		Strain Rate Sensitivity of the Mechancial Properties of Fresh Porcine Cortical Bone

I hereby undertake to carry out my research in such a way that:

- there is no apparent legal objection to the nature or the method of research; and
- the research will not compromise staff or students or the other responsibilities of the University;
- the stated objective will be achieved, and the findings will have a high degree of validity;
- limitations and alternative interpretations will be considered;
- the findings could be subject to peer review and publicly available; and
- I will comply with the conventions of copyright and avoid any practice that would constitute plagiarism.

APPLICATION BY	Full name	Signature	Date
Principal Researcher/ Student/External applicant	Nicholas Daras	Daras.	24/03/2022
SUPPORTED BY	Full name	Signature	Date
Supervisor (where applicable)	Prof. Gerald N. Nurick		12/04/2022

APPROVED BY	Full name	Signature	Date
HOD (or delegated nominee) Final authority for all applicants who have answered NO to all questions in Section 1; and for all Undergraduate research (Including Honours).			
Chair: Faculty EIR Committee For applicants other than undergraduate students who have answered YES to any of the questions in Section 1.	Prof. H. von Blottnitz	H. von Blottnitz	21/06/2022

To Whom It May Concern

Dear Sir/Madam

This purpose of this letter is to confirm the ethical process by which we, Bill Riley Meat cc, have provided biological material for research to be conducted by Mr Nicholas Daras and Dr Trevor Cloete at the University of Cape Town.

The biological material provided by us for the purpose of research was all by-product of the standard operations at our facility and no harm was done to any animal specifically for the purpose of research.

Heinrich Kuntenbach

BILL RILEY MEAT (PTY) LTD
2 STEENBRAS ST.
BROOKLYN
TEL: 021 511-5522